A MICROANALYTICAL ISOTOPIC STUDY OF ARCHEAN ANORTHOSITES

AMANDA KATE SOUDERS

A Microanalytical Isotopic Study of Archean Anorthosites

by

© Amanda Kate Souders

A dissertation submitted to the

School of Graduate Studies

in partial fulfillment of the

requirements for the degree of

Doctor of Philosophy

Department of Earth Sciences

Memorial University of Newfoundland

May 2011

St. John's Newfoundland

ABSTRACT

This thesis focuses on developing and applying in-situ microanalytical methods to study Archean mantle evolution using radiogenic isotope tracers. The timing and mechanism of Archean crust-mantle differentiation is uncertain. Much of our knowledge of the geochemical composition of Archean mantle is through whole rock analysis of mantle-derived magmatic rocks or analysis of minerals separated from these rocks. Pervasive metamorphism and secondary alteration have affected almost all Archean rocks making bulk rock analyses unreliable. Because of this, isotopic analysis of preserved igneous domains of minerals is preferred.

In this work, isotopic analyses of Lu-Hf in zircon and Pb-Pb in plagioclase are made on coarse-grained, Archean anorthosites. An advantage of these two minerals is both have low parent-daughter ratios and therefore analyses require minimal correction for radiogenic in-growth. LA-MC-ICPMS methods for measuring Lu-Hf in zircon are well established but in-situ measurement of Pb isotopes in Pb-poor minerals required significant analytical development work. Chapters two and three document LA-MC-ICPMS methodology of Pb isotope measurements in Pb-poor silicate glasses, feldspars and sulfides and evaluate any potential biases due to sample matrix. Results demonstrate accurate and precise Pb isotope ratios can be obtained using silicate glass reference materials as calibration standards, despite differences in physical and chemical properties between samples and standards. Average accuracies for Pb-poor feldspars are within 0.40% of the preferred values with external precisions better than 0.60% (RSD, 1σ). Chapter four applies the in-situ Pb isotope method to igneous plagioclase megacrysts

from Fiskenæsset and Nunataarsuk anorthosite complexes of south West Greenland. Lead isotope data from each anorthosite complex are used to determine timing of crust extraction from the mantle. This information is coupled with Lu-Hf LA-MC-ICPMS analysis of zircon, from the same rocks, to constrain the $^{176}Lu/^{177}Hf$ and characterize the composition of the crustal end member. Results show the ~ 2936 Ma Fiskenæsset and ~ 2914 Ma Nunataarsuk anorthosite complexes crystallized from mantle-derived melts that had interacted with ancient (Eoarchean to Hadean) mafic crust, which could still be present in south West Greenland today.

TABLE OF CONTENTS

LIST OF TABLES

CHAPTER 4

LIST OF FIGURES

CHAPTER 1

CHAPTER 2

CHAPTER 3

CHAPTER 4

CO-AUTHORSHIP STATEMENT

This dissertation incorporates material that is the result of collaborative research under the supervision of Professor Paul Sylvester. Chapters 2 and 3 of this thesis were published in the Journal of Analytical Atomic Spectrometry. Chapter 4 has been submitted to Geochimica et Cosmochimica Acta and is currently in review. A. Kate Souders is the primary author and researcher for all manuscripts/chapters including experimental design, data collection, synthesis and interpretation of data and manuscript preparation.

Professor Paul Sylvester is a co-author on all manuscripts included in this dissertation, (chapters 2 – 4). Paul provided insight and direction during the initial stages of each experiment (paper/chapter), especially the development of the LA-MC-ICPMS method presented in chapter 2. Paul was involved in discussing issues involving both data collection and interpretation. He also played a significant role reviewing and editing each manuscript.

Dr. John Myers is a co-author on the third manuscript, chapter 4, in this dissertation. John provided the geologic context for the study including all samples analyzed, unpublished mapping and geologic observations at Nunataarsuk, and first-hand observations he had made during his previous mapping at Fiskenæsset.

Chapter 1: Overview

1.1 INTRODUCTION

The Earth's mantle is a complex reservoir, chemically heterogeneous due to the dynamic interplay between it and Earth's other major geochemical reservoirs. Long-lived radiogenic isotopes are power tracers of geochemical processes and are used to track changes in the geochemical composition of the mantle through geologic time directly through the isotopic analysis of peridotites brought to the Earth's surface or indirectly through the analysis of mantle-derived material such as mid-ocean ridge basalts (MORB), ocean island basalts (OIB), juvenile granites, or individual minerals, such as pyroxene (Nd isotopes) and zircon (Hf isotopes), separated from these rocks (*e.g.* Bennett et al., 1993; Layahe et al., 1995; Vervoort and Blichert-Toft, 1999; Chauvel and Blichert-Toft, 2001; Kamber et al., 2003; Hiess et al., 2009).

The isotopic composition of the Archean mantle is poorly defined. Much of our knowledge of the geochemical composition of the Archean mantle is based on bulk rock analyses of mafic volcanics or juvenile granites (*e.g.* Bennett et al., 1993; Layahe et al., 1995; Bowring and Housh, 1995; Vervoort and Blichert-Toft, 1999; Kamber et al., 2003; Polat et al., 2003; Blichert-Toft et al., 2004; Hoffmann et al., 2010) or zircons separated from these rocks (*e.g.* Vervoort et al., 1996; Vervoort and Blichert-Toft, 1999; Amelin, 2000; Harrison et al., 2005, 2008; Blichert-Toft and Albarade, 2008; Hiess et al., 2009; Kemp et al., 2009, 2010; Zeh et al., 2010). The interpretation of radiogenic isotope data for a suite of whole rocks is complex due to the range of isotope ratios typically found, and the multiple processes that have commonly affected those compositions. It is

important, for instance, to distinguish between primary and secondary isotope signatures of samples. Often, bulk analyses represent a summation of open system processes and/or radiogenic in-growth of daughter isotopes after crystallization, obscuring the primary isotopic compositions of interest. Hadean and Archean age rocks consist of only ~ 7 % of the exposed rock record yet represent > 50 % of Earth's history (Hawkesworth et al., 2010) and many of the > 2.5 Ga rocks exposed at the surface have been intensely altered and deformed and no longer preserve their initial isotopic signatures (Bennett, 2003). Determination of initial isotope ratios of mantle-derived material, especially for Hadean and Archean samples, is critical to tracing the isotopic composition of the mantle through time, but difficult where secondary processing is pervasive or intense.

Archean anorthosite complexes represent a minor, yet distinct rock type found within most Archean cratons of the world (Figure 1-1). Traditional whole rock isotopic studies have concluded that Archean anorthosites were derived from chondritic or depleted mantle derived melts yet a range of isotopic compositions have been determined for each anorthosite complex investigated. For example, Nd isotope data from various studies (Ashwal et al., 1985, 1989; Barton, 1996; Bhasker Rao et al., 1996, 2000; Fletcher et al., 1988; Polat et al., 2010) plotted in Figure 1-2 show that the sources of Archean anorthosites have initial ε_{Nd} values that range over 2 or more units for each complex. It is unclear, however, whether this range represents mantle heterogeneities, crustal contamination or a summation of open system processes. Most Archean anorthosites are intensely deformed and metamorphosed yet preserved igneous minerals such as plagioclase megacrysts and zircon crystals have been identified within several

complexes (*e.g.* Ashwal et al., 1983; Myers, 1985; Myers 1988; Fletcher et al., 1988). These minerals are ideal targets for in situ isotopic analysis and further characterizing the source of Archean anorthosites and the isotope composition of the Archean mantle. An in situ approach is especially advantageous when investigating highly deformed rocks with complex deformation and metamorphic histories because the analysis is focused on previously identified pristine domains within an individual crystal.

This thesis consists of both analytical development of a laser ablation multi-collector inductively coupled plasma mass spectrometry (LA-MC-ICPMS) method to measure Pb isotope ratios in Pb-poor materials (Chapters 2 and 3; published as Souders and Sylvester, 2008a, 2010) and the application of the method to characterize the source of Archean anorthosites and the isotope composition of the Archean mantle (Chapter 4; Souders et al., in review). The rocks of the study are from two Archean anorthosite complexes in south West Greenland, Fiskenæsset and Nunataarsuk. A companion paper to Chapter 2 (published as Souders and Sylvester, 2008b), giving more details on the analytical procedures and the principles behind them is included in the Appendix at the end of the thesis.

1.2. BACKGROUND

1.2.1 Crust – Mantle Evolution and Initial Pb Isotope Ratios

The Pb isotope compositions of a rock or mineral changes over time based on the radioactive decay of ^{238}U to ^{206}Pb, ^{235}U to ^{207}Pb and ^{232}Th to ^{208}Pb and the parent daughter ratio of the system. The U and Th parent isotopes have half-lives ranging from 0.7 – 14 Ga, long enough to have produced large variations in parent-daughter ratios that

can be used to constrain models of crust-mantle evolution on Earth (*e.g.* Stacey and Kramers, 1975; Kramers and Tolstikhin, 1997). Pb isotope ratios are also sensitive indicators of heterogeneities within source regions of igneous rocks as a result of crustal contamination and magma mixing due to large concentration differences between U, Th and Pb in the mantle, mantle-derived magmas and the crust (Oversby, 1975; Housh and Bowring, 1991).

Lead isotope analyses of modern basalts provide information about the composition and heterogeneities of the mantle today (Hofmann, 2004 and references therein; GEOROC database http://georoc.mpch-mainz.gwdg.de/georoc/). Application of the Pb isotope method to trace mantle composition through time using ancient mantle-derived rocks requires knowledge of the initial Pb isotope composition of these rocks. When a volume of mantle undergoes partial melting, the melt inherits the Pb isotope composition of the entire system. Combining the initial Pb isotope compositions of mantle-derived rocks of various ages provides information about the composition and differentiation history of the mantle.

Determination of the initial Pb isotope composition for ancient rocks is hindered by the high mobility of U during low temperature hydrothermal alteration and high-grade metamorphism (Rosholt et al., 1973; Rudnick et al., 1985) and knowledge of the crystallization age of the sample. Any disturbance of the parent-daughter ratio (U/Pb, Th/Pb) prohibits back-calculation of the initial Pb isotope ratios from the present-day measured values. A potential solution to this problem is to measure Pb isotope compositions of individual minerals with low U/Pb such as feldspars and galena (*e.g.*

Doe, 1962; Stacey and Kramers, 1975; Ludwig and Silver, 1977; Housh and Bowring, 1991). In theory, the Pb isotope composition of these minerals should be unaffected by U-mobility and radiogenic in-growth and should reflect the initial Pb isotope composition of the melt they crystallized from.

1.2.2 In-situ Pb Isotope Analysis

Advances in analytical instrumentation over the past ~20 years have provided analysts with the capabilities to make elemental and isotopic measurements in-situ, rather than by traditional bulk methods. LA-ICPMS and secondary ion mass spectrometry (SIMS) allows the scientist to target specific domains (10s – 100s of μm) within minerals of interest for further characterization. Typically, these areas of interest are identified prior to in-situ analysis by optical microscopy and back-scattered electron (BSE) and cathodoluminescence (CL) imaging by scanning electron microscopy. Potential sources of radiogenic Pb, such as in cracks, grain boundaries and mineral inclusions, that had hampered Pb leaching procedures for feldspars (Housh and Bowring, 1991; Connelly and Thrane, 2005) can be avoided by combined imaging and in-situ analysis.

1.2.2.1 LA-MC-ICPMS Pb Isotope Analysis

LA-MC-ICPMS has been demonstrated to be able to document isotopic variations on tiny objects of geologic interest at high spatial resolution. In-situ measurements of common Pb isotope compositions in minerals with low U/Pb and Th/Pb have become increasingly important for a variety of applications. Lead isotope ratio measurements by LA-MC-ICPMS have been applied to a range of problems including accessory mineral geochronology (*e.g* Horn et al., 2000; Willigers et al., 2002; Simonetti et al., 2005; Vry

and Baker, 2006); analysis of melt inclusions (*e.g* Paul et al., 2005); isotopic tracing in silicate and sulfide magmatic systems (*e.g* Mathez and Waight, 2003; Gagnevin et al., 2005; Mathez and Kent, 2007); sedimentary provenance investigations (*e.g* Tyrrell et al., 2006; Connelly and Thrane, 2005); and environmental studies for contaminant source apportionment (*e.g.* McGill et al., 2003; Novak et al., 2010). With improvements in instrumentation, the range of problems and matrices analyzed by the laser ablation technique continues to expand.

Despite advances of the technique, the measurement of Pb isotope ratios by LA-MC-ICPMS is not without difficulties. Unlike most radiogenic isotope systems (*e.g.* Sm-Nd, Lu-Hf), the Pb isotope system does not have an invariant isotope pair with which to internally correct for instrumental mass bias. Alternative external corrections methods such as aspirating a Tl tracer solution during laser analysis to monitor Pb fractionation (*e.g.* Horn et al., 2000; Kosler et al., 2002) or standard – sample – standard bracketing with silicate glass reference materials of known Pb isotope composition (*e.g.* Willigers et al., 2002; Simonetti et al., 2005) must be employed instead. The latter method is used in Chapter 2 (published as Souders and Sylvester, 2008a). As with any external correction method, the potential for mass bias variations as a function of matrix composition must be carefully evaluated. In Chapter 3 (published as Souders and Sylvester, 2010), potential biases in measured Pb isotope ratios as a function of sample matrix for feldspar and sulfide minerals are tested by calibration against a silicate glass reference material. It is found that a silicate glass is an appropriate standard to correct for mass bias when measuring Pb isotope ratios in Pb-poor (< 40 ppm total Pb) feldspars and sulfides.

A further limitation of Pb isotope ratio measurements by LA-MC-ICPMS is instrument sensitivity and measurement of the stable ^{204}Pb isotope. Not only is ^{204}Pb the least abundant of all Pb isotopes (~ 1.4% of all common Pb), it also suffers from an isobaric interference from ^{204}Hg. The ability to measure Pb isotope ratios involving the minor ^{204}Pb isotope becomes progressively more difficult as the total Pb concentration of a material decreases. Measurement precision is strongly dependant on ion beam intensities (Paul et al., 2005; Kent, 2008; Chapter 2, published as Souders and Sylvester, 2008a). In order to measure materials with low total Pb concentrations (< 20 ppm Pb), compromises between spatial resolution and precision must be made.

MC-ICPMS instruments allow for the simultaneous measurement of all isotopes of interest. Early LA-MC-ICPMS Pb isotope measurements were made using multiple Faraday detectors (*e.g.* Mathez and Waight, 2003) or multiple Faraday detectors plus an axial multiplier for the low intensity 204-mass signal (*e.g* Willigers et al., 2002; Horstwood et al., 2003). There are many advantages to using Faraday detectors including high efficiency and uniform response time; yet the precision is severely compromised by resistor noise when measuring low intensity signals such as ^{204}Pb (Longerich, 2008). Not all investigations require the measurement of ^{204}Pb, yet most natural variation is recorded in the ^{206}Pb/^{204}Pb, ^{207}Pb/^{204}Pb and ^{208}Pb/^{204}Pb ratios.

In order to accommodate the limitations of the Faraday collector configuration and enable the measurement of ^{204}Pb, previous LA-MC-ICPMS studies focused on Pb-rich materials with total Pb concentrations greater than ~ 80 ppm Pb (*e.g.* apatite, monazite, Pb-rich sulfides; Willigers et al., 2002; Horstwood et al., 2003 Mathez and

Waight, 2003) or analysis of minerals with moderate to low Pb concentrations using a large laser beam (100 – 200 μm) rastered across the surface of the mineral (*e.g.* K-feldspar, plagioclase; Mathez and Waight, 2003; Connelly and Thrane, 2005; Gagnevin et al., 2005). For many of these investigations, data for all 4 Pb isotopes were collected (^{204}Pb, ^{206}Pb, ^{207}Pb and ^{208}Pb), yet only the ^{207}Pb/^{206}Pb and ^{208}Pb/^{206}Pb proved useful due to low ^{204}Pb ion beam intensities resulting in imprecise ^{204}Pb isotope ratio measurements.

Recently, multiple ion counters have been installed within the collector array of MC-ICPMS instruments (*e.g.* Figure 1-3). The addition of multiple ion counters within the MC-ICPMS collector array has significantly increased the precision with which the low intensity ^{204}Pb ion beam is measured and extended the method to include measurement of Pb-poor materials (*e.g.* plagioclase; < 20 ppm Pb) with improved spatial resolution (40 – 99 μm laser spots). At ^{204}Pb ion beam intensities < 50,000 cps, use of parallel Faraday cup – ion counting systems improves the internal precision on the ^{206,207,208}Pb/^{204}Pb ratios by 1 – 2 orders of magnitude (Kent, 2008).

Increased spatial resolution and improved precision and accuracy for Pb isotope ratio measurements of Pb-poor minerals are both advantages of Pb isotope ratio measurements using multiple ion counters, but there are also drawbacks. Ion counters are less stable than Faraday detectors and changes in ion counter gains, or drift, will occur due to degradation of the ion counter surface by exposure to the ion beam. This drift occurs over time periods as short as a single analytical session (Souders and Sylvester, 2008b). Therefore, when using ion counters, it is important to keep count rates low (< 300,000 cps) to minimize detector drift and potential dead-time correction errors

associated with pulse pile up. Reducing the ion beam intensity will also prolong the life span of the detector. Additional effort is also required to cross calibrate the detectors when using ion counting systems, especially when dealing with mixed Faraday – ion counter collector configurations, due to differences in relative response times between the two types of detectors (Cottle et al., 2009).

1.2.3 Anorthosites

Anorthosites are rocks made up of ≥ 90 % plagioclase feldspar (Streckeisen, 1976). They are found throughout the Earth's geological record since at least 3700 Ma (Kinney et al., 1988). Anorthosites are only a minor component of the Earth's crust yet they comprise a dominant portion of the lunar surface and possibly Mercury and also occur as meteorites (Strom and Sprague, 2003; Taylor, 2009). Anorthosites have been classified most recently by Ashwal (1993) into 6 basic types: (1) Archean megacrystic anorthosite (*e.g.* Fiskenæsset Complex, south West Greenland; Manfred Complex, Western Australia; Bad Vermillion Lake Complex, Ontario), (2) Proterozoic (massif-type) anorthosites (*e.g.* Lac-Saint-Jean Complex, Quebec; Nain Plutonic Suite, Labrador; Laramie Anorthosite Complex, Wyoming), (3) Anorthosites of layered mafic complexes (*e.g.* Bushveld Complex, South Africa; Stillwater Intrusion, Montana), (4) Anorthosites of oceanic settings (within ophiolites), (5) Anorthosite inclusions in other rock types (*e.g.* xenoliths or plagioclase accumulations) and (6) Extraterrestrial anorthosites (*e.g.* Lunar highlands, meteorites). The classification is based on distinctive features such as age, composition, texture, geologic setting and geological associations. Some overlap between categories is recognized and some anorthosites are difficult to characterize; yet all known

occurrences fit, generally, into one of these 6 categories. This thesis focuses on Archean anorthosites. A detailed description of the features of Archean anorthosite complexes follows.

1.2.3.1 Archean Anorthosite Complexes

Anorthosites are a minor yet distinctive feature of many Archean terranes, found in association with mafic supracrustal rocks (Figure 1-1). Archean anorthosites are characterized by equidimensional, calcic ($>An_{85\pm10}$), plagioclase megacrysts, 0.5 – 30 cm in diameter, within a mafic groundmass (Figure 1-4). The characteristic composition and texture of these anorthosites are generally only found within Archean terranes. Along with komatiites, Archean anorthosites represent the only rock type largely restricted to the Archean (Ashwal, 1993, and references therein).

Although massive bodies of megacrystic anorthosite do occur (*e.g.* Shawmere anorthosite, Ontario; Simmons et al., 1980), Archean anorthosites commonly form sheet-like bodies originally emplaced as sills (*e.g.* Fiskenæsset, SW Greenland; Sittampundi, India; Messina layered intrusion, South Africa; Bird River and Pipestone Lake, Canada). Many Archean anorthosites (*e.g.* Fiskenæsset, Messina, Sittampundi) have subsequently been fragmented and deformed by the intrusion of granitoids and subsequent tectonic activity yet still maintain their sheet-like structure (Windley et al, 1973; Barton et al, 1979; Myers, 1985;). These anorthosites are commonly found in layers associated with leucogabbro, gabbro, and ultramafic units of similar origin. The contact relationships between anorthosite complexes and surrounding country rock are most often obscured due to deformation and metamorphism ranging from lower greenschist to granulite facies.

Primary relationships between the anorthosite complex and the mafic metavolcanic country rocks have been described at Fiskenæsset (Greenland) (Escher and Myers, 1975) (Figure 1-5) and in the Bad Vermilion Lake complex (Wood et al., 1980).

Megacrystic, Ca-plagioclase surrounded by a mafic matrix is common to most Archean anorthosite complexes. The degree to which these megacrysts retain both igneous texture and composition depends on the severity of deformation (Figure 1-6). Inclusions of amphibole $\pm$ pyroxene $\pm$ rutile are common in some igneous plagioclase megacrysts (Ashwal et al., 1983; Myers and Platt, 1977; Myers, 1985). Recrystallized megacrysts tend to be free of inclusions. There is little compositional heterogeneity within individual relict plagioclase megacrysts or entire anorthosite complexes (Myers and Platt, 1977; Phinney et al., 1988). Relict igneous plagioclase megacrysts are generally $An_{80\pm10}$. More sodic plagioclase compositions ($< An_{70}$) are explained by the removal of Ca to form epidote group minerals, calcite, or hornblende, common secondary minerals in anorthosite complexes (*e.g.* epidote/calcite (Bad Vermilion Lake, Manfred Complex): Ashwal et al., 1983; Fletcher et al., 1988; hornblende (Messina): Barton, 1996). Very high An-values (An_{90-100}) found in some high-grade anorthosite complexes could be the result of the removal of albite (Na) components by partial melts (Ashwal, 1993).

The mafic mineral matrix surrounding the plagioclase megacrysts can be coarse or fine-grained and makes up between 0 – 50% of the groundmass (Ashwal, 1993). The bulk composition of the matrix is generally basaltic and has been interpreted to represent the trapped liquid of the anorthosite parent magma (Ashwal et al., 1983). Amphiboles

dominate the mafic matrix, which also includes relict igneous pyroxenes as well as olivine, plagioclase, spinel, chromite and magnetite. Barton et al. (1979) documented an inverse relationship between the An-content in plagioclase and amphibole abundance within the Messina layered intrusion suggesting the amphibole formed as a product of a metamorphic reaction between plagioclase and anhydrous mafic silicates.

The igneous or metamorphic origin of amphibole within Archean anorthosite complexes is a topic of ongoing debate. This interpretation has further implications on the water content of the anorthosite parent melt. At Fiskenæsset, Weaver et al. (1981) found no geochemical evidence for primary amphibole crystallization in samples from the Fiskenæsset complex and Myers (1985) found no petrographic evidence for primary amphibole at Majorqap qava. In contrast, Keulen et al. (2009) reported clinopyroxene – hornblende sills intruding a layered dunite sequence within the Majorqap qava region, suggesting the Fiskenæsset complex contained a hydrous batch of magma that intruded the early olivine cumulates. Windley et al. (1973) documented interlayering of hornblende-bearing and hornblende-free assemblages and millimeter-scale layers of hornblende within ultramafic rocks at Qeqertarssuatsiaq. They also noted equilibrium intergrowth textures between olivine and hornblende in Qeqertarssuatsiaq ultramafic rocks, all considered evidence for primary igneous amphibole. Polat et al. (2009) described hornblendite veins consisting of magmatic amphiboles on Qeqertarssuatsiaq Island. Rollinson et al. (2010) interpreted amphibole inclusions within chromites from this same location within the Fiskenæsset complex to be igneous in origin. Each of the

three investigations at Qeqertarssuatsiaq concluded that Fiskenæsset formed from hydrous parent magmas.

Traditionally, primary magmas for Archean anorthosite complexes have been thought to be anhydrous (Ashwal, 1993). Yet, experimental evidence documents that elevated water content in mafic magmas results in the crystallization of high-Ca plagioclase (*e.g.* Sisson and Grove, 1993; Tagaki et al., 2005). A hydrous parent magma could possibly explain the high Ca-composition of plagioclase megacrysts within Archean anorthosite complexes as it does for the high-Ca compositions of anorthosites incorporated into Proterozoic island arcs (*e.g.* Burg et al., 1998; Gibson and Ireland, 1999), yet the megacrystic texture, characteristic of Archean anorthosites, is missing from the younger high-Ca anorthosites (Ashwal, 2010).

Determining the bulk composition and source of Archean anorthosites is a difficult task and ongoing problem in petrology (Phinney et al., 1988). No single attempt at determining the anorthosite parent melt composition has been considered entirely successful, yet many attempts have been made (Ashwal, 1993). There are several general methods to estimate the parent melt composition of Archean anorthosites. One approach is to look for, find and analyze melt inclusions or chilled margins of the intrusion and assume that they represent the original parent magma composition. Unfortunately, these features are very rare within Archean anorthosite complexes due to secondary alteration and deformation. Alternative approaches to determine the parent magma composition must be considered. Other approaches that have been used include: (1) Estimating the bulk composition of a single anorthosite complex by adding the average geochemical

composition of each unit, weighted by the surface area that each unit is exposed (*e.g.* Windley et al., 1973; Barton et al., 1979; Polat et al., 2011). This method assumes that the present relative proportions are representative of the original proportions of each lithology, all major lithological units are present, nothing has been lost by tectonic or magmatic processes and the entire sequence crystallized from one batch of magma; (2) Assuming associated dikes, sills and flows are comagmatic with the anorthosite complex and taking the most primitive composition of these units as being representative of the parent melt composition of the anorthosite (*e.g.* Weaver et al., 1981, 1982; Ashwal et al., 1983; Phinney et al., 1988); and (3) Using crystal-melt distribution coefficients to calculate equilibrium melt compositions from geochemical analysis of bulk samples and cumulate mineral separates (*e.g.* Henderson et al., 1976; Simmons et al., 1980; Weaver et al., 1981; Phinney and Morrison, 1990). The results of using partition coefficients have been mixed and success rests heavily on assuring the best-preserved mineral separates and bulk rocks are analyzed and appropriate partition coefficients are used (Ashwal, 1993). Regardless of the method, all investigations have reached a similar conclusion: the parent magma of Archean anorthosites was (broadly) basaltic (Ashwal, 1993).

Emplacement into oceanic crust is assumed for most Archean anorthosite complexes based on geochemical similarities and/or the spatial association of anorthosite complexes with mafic supracrustal rocks of greenstone belt affinity (Windley et al., 1973; Escher and Myers, 1975; Ashwal et al., 1983; Peck and Valley, 1996; Polat et al., 2009, 2011). The exact ocean environment is currently unresolved and debated. Recently both Polat et al. (2009) and Rollinson et al. (2010) proposed an oceanic arc setting for the

Fiskenæsset complex based on bulk rock trace element chemistry and chromitite geochemistry, respectively. They proposed that Al-, Ca- Sr- and LREE-enrichment was due to metasomatism of the depleted mantle wedge by slab-derived melts. An early model for Archean anorthosite complexes proposed by Phinney (1982) suggested that mafic, mantle-derived melts ponded at or near the base of oceanic crust where, upon cooling, the crystallization of mafic silicates commenced and the magma was enriched in both Ca and Al. After sufficient cooling time to allow for the formation of large, Ca-rich, compositionally homogeneous plagioclase megacrysts, the less-dense plagioclase crystals were separated from the mafic material and carried upward through the crust along with varying amounts of remaining melt and emplaced at near-surface depths as flows, sills, and dikes.

Modifications to the original multi-stage emplacement model of Phinney (1982) were made by Phinney et al. (1988) to account for new experimental results (Morrison et al., 1985). The modified model calls for the crystallization and accumulation of mafic phases at depth within a high-pressure magma chamber. When the density of the melt is low enough, the fractionated melt will rise from the base of the crust to a low-pressure magma chamber within the crust where Ca-rich plagioclase will crystallize as the primary liquidus phase as a result of depressurization. The crystallized ultramafic material remains at depth (Stolper and Walker, 1980). Replenishment of melt from depth to the low-pressure magma chambers would produce high-concentrations of Ca-rich, cumulate plagioclase seen in Archean anorthosite complexes and force melts, with varying

concentrations of plagioclase cumulates, towards the surface as flows, dikes and sills (Phinney et al., 1988).

1.2.4 Previous Isotopic Studies of Archean Anorthosites

There have been numerous isotopic studies of the Sm-Nd, Rb-Sr and Pb-Pb systems in bulk rocks and mineral separates from Archean anorthosite complexes. In addition, several recent studies have reported U-Pb and Pb-Pb zircon ages and Hf isotopic compositions of zircon grains from Archean anorthosites and leucogabbros (*e.g.* Kinney et al., 1988; Mouri et al., 2009; Zeh et al., 2010; Keulen et al., 2010). The Sm-Nd, Pb-Pb, U-Pb and Lu-Hf isotopic studies are summarized in Table 1-1. A number of the previous isotopic studies have been concerned with Fiskenæsset anorthosites (Black et al., 1973; Gancarz, 1976; Moorbath and Pankhurst, 1976; Pidgeon and Kalsbeek, 1978; Kalsbeek and Pidgeon, 1980; Taylor et al., 1980; Ashwal et al., 1989; Keulen et al., 2010; Polat et al., 2010, 2011) but none have dealt with Nunataarsuk anorthosites.

There have been no previous reports on Archean anorthosites that included in situ analyses of the Pb isotope composition of plagioclase and only one report of the Hf isotope composition of zircon. In the latter, Zeh et al. (2010) analyzed ~3350 Ma zircon grains from two anorthosite samples from the Messina Layered Intrusion, South Africa, for Hf isotopes by LA-MC-ICPMS. Initial εHf (ca. 3350 Ma) for the anorthosites are + 1.4 ± 1.8 and + 0.1 ± 1.9, respectively, which was interpreted as reflecting slight enrichment of depleted mantle-derived melts by crustal contamination.

1.2.4.1 Previous Pb Isotope Studies of Archean Anorthosites

Previous studies of Pb isotopes in bulk rocks and mineral separates by TIMS have been reported for 3 anorthosites in south West Greenland (Fiskenæsset, Storoø and Ivnajaugtoq; Black et al., 1973; Gancarz, 1976; Polat et al., 2010), the Messina Layered Instrusion, South Africa (Barton et al., 1983, 1996) and the Manfred complex, Western Australia (Fletcher et al., 1988). Most studies focused on determining the crystallization and/or metamorphic age of the anorthosite and only a few investigations (Gancarz, 1976; Barton, 1996) were aimed at determining initial Pb isotope ratios in order to characterize the source of the anorthosites. A range of Pb isotope ratios is presented in each investigation, largely the result of radiogenic in-growth of Pb, yet without knowledge of initial Pb isotope ratios, variations due to magmatic or secondary processes are ambiguous. Previous Pb isotope investigations of Archean anorthosites are summarized below.

Anorthosites from south West Greenland

Black et al. (1973) reported the first Pb isotope data from 5 anorthosites and 1 gneiss from the Fiskenæsset complex. A Pb-Pb isochron age of 2810 +/- 70 Ma (2σ) was determined and interpreted to represent a regional granulite facies metamorphic event. Polat et al. (2010) presented Pb-Pb data from 46 granulites (20 anorthosites, 6 leucogabbros, 4 gabbros, 6 ultramafic rocks) from Qeqertarssuatsiaq, located on the western edge of the Fiskenæsset complex. The Pb-Pb isochron for all samples yielded an age of 2945 ± 36 Ma (MSWD = 44) and intersects the Stacey and Kramers (1975) growth curve at 3036 Ma. Polat et al. (2010) interpreted the ~ 2945 Ma isochron age to be within

error of the crystallization age of the Fiskenæsset complex. Gancarz (1976) was focused on determining initial Pb isotope ratios in order to characterize the reservoir from which the Fiskenæsset anorthosite was derived. Pb isotope ratios of plagioclase and hornblende mineral separates and a bulk leucogabbro sample from the Majorqap Qava area of the Fiskenæsset complex were measured. Cores of plagioclase megacrysts were generally less radiogenic than analyzed rims and were considered most representative of the initial Pb isotope composition of the Fiskenæsset complex. Biotite, hornblende and epidote separates analyzed all had more radiogenic Pb isotope compositions. The analyzed mineral separates define a Pb-Pb isochron, colinear with that of Black et al. (1973) yielding an age of ~2800 Ma and corresponding to a source μ-value of ~ 8. Gancarz (1976) also analyzed plagioclase megacryst separates from two other anorthosites, Storø and Ivnajaugtoq, within the Godthabsfjord region of south West Greenland. At both Storø and Ivnajaugtoq, the rims of each plagioclase megacryst analyzed were found to be more radiogenic than the corresponding core. A precise age for the Storø and Ivnajaugtoq anorthosites could not be determined due to insufficient spread in the measured Pb isotope ratio yet the data for each anorthosite are consistent with an age of ~2800 Ma and source μ-values of 5.4 (Storø) and 7.6 (Ivnajaugtoq). All three anorthosites were similar in age yet each had a different initial Pb isotope composition suggesting that the 3 anorthosites are not cogenetic and each anorthosite has a unique source history.

Messina Layered Intrusion, South Africa

Barton et al. (1983) presented Pb-Pb whole rock data for 8 quartz-hornblende-plagioclase gneiss samples from the Messina Layered Instrusion, South Africa. The

samples defined an isochron corresponding to an age of ~ 3270 Ma, interpreted to be the timing of emplacement of the complex. Barton (1996) analyzed the Pb isotope composition of plagioclase megacrysts, megacryst fragments and recrystallized plagioclase separated from the quartz-hornblende-plagioclase gneisses previously analyzed. The Pb isotope compositions measured from the igneous (grey) plagioclase megacrysts and fragments define a trend, distinct from the trend defined by the Pb isotope ratios of the metamorphic plagioclase and whole rock samples. The isochron age corresponding to the trend of Pb isotope compositions measured for the igneous plagioclase is greater than the age of the Earth and was interpreted to be a mixing line between a low μ depleted mantle source and a high μ source with a Pb isotope composition similar to the surrounding country rock of the intrusion. The range of Pb isotope data suggests assimilation of surrounding rocks with the mantle derived anorthosite magma prior to crystallization of the anorthosite.

Manfred complex, Western Australia

Pb isotope geochronology of gabbros, leucogabbros, anorthosites and ultramafic units from the Manfred Complex was presented in Fletcher et al. (1988). Pb isotope analyses were made on both whole rocks and mineral separates. Analyses were divided into 3 groups: least radiogenic, moderately radiogenic and highly radiogenic. The 6 samples that make up the least radiogenic group are generally accessory mineral free and define a linear array corresponding to an isochron age of 3689 +/- 146 Ma (MSWD = 8.7) with an apparent source μ = 10.2 +/- 0.4. The Pb-Pb isochron age is within error of the U-

Pb zircon crystallization age of 3730 +/- 6 Ma (Kinney et al., 1988) and the 3680 +/- 70 Ma Sm-Nd isochron age determined for the Manfred complex.

1.3. THESIS OVERVIEW

LA-MC-ICPMS analysis has provided Earth scientists with the ability to determine precise isotopic ratios of major and minor elements in minerals in-situ. Most studies have focused on isotopes that are sufficiently abundant in the sample (*e.g.* Mg in olivine; S, Fe and Cu in sulfides; Nd in monazite; Hf in zircon) and employed the use of Faraday detectors. Integration of ion counters into the collector configuration of multi-collector ICPMS instruments has opened the possibility of determining precise isotope ratios of trace elements in minerals. Instead of trying to understand isotopic variations on the scale of a whole rock sample, isotopic variations on the mineral scale can now be evaluated and interpreted.

Previous LA-MC-ICPMS Pb isotope investigations measured all Pb isotopes in Faraday cups or a combination of Faraday cups and ion counters. Most of these in-situ investigations were limited by sensitivity, both for reducing the laser spot size in Pb - 'rich' materials (> 70 ppm total Pb) and for extending the technique to measure Pb - 'poor' materials such as plagioclase feldspar and melt inclusions. The integration of ion counters into the traditional Faraday cup configuration of MC-ICPMS instruments greatly improves precision on low intensity signals (Paul et al., 2005; Kent, 2008; Souders and Sylvester, 2008b). Many previous LA-MC-ICPMS Pb isotope investigations do not report Pb isotope ratios involving the minor ^{204}Pb isotope (~ 1.4 % of all natural Pb) due to difficulties in precisely measuring this relatively low-abundance isotope.

Chapter 2 (Souders and Sylvester, 2008a) presents a new LA-MC-ICPMS technique to measure Pb isotopes in Pb-'poor' silicate glasses (< 15 ppm total Pb). The method allows for the static, concurrent measurement of ^{204}Pb, ^{206}Pb, ^{207}Pb, ^{208}Pb as well as ^{202}Hg in 5 Channeltron ion counters installed within the Thermo-Scientific NEPTUNE collector array. The accuracy and precision of the method is evaluated by replicate analysis of several MPI-DING reference glasses made from natural silicate rocks with well-characterized Pb isotope ratios and chemical compositions and total Pb concentrations ranging from ~1 – 11 ppm total Pb (Jochum et al., 2000, 2005). Minimum laser spot sizes for LA-MC-ICPMS measurements are between 40 – 69 μm, improving spatial resolution over previous in-situ investigations reporting ^{204}Pb. Average measured Pb isotope ratios for the MPI-DING reference glasses T1-G (11.6 ppm total Pb) and ATHO-G (5.67 ppm total Pb) agree within 0.10 % and 0.15 % respectively of the preferred values using the 40 μm spots. For MPI-DING KL2-G (2.07 ppm total Pb) and ML3B-G (1.28 ppm total Pb) measured ^{206,207,208}Pb/^{204}Pb isotope ratios agree within 0.75 % of the accepted values with typical precisions of < 0.85 % (RSD) using 69 μm spots; measured ^{207}Pb/^{206}Pb and ^{208}Pb/^{206}Pb are within 0.25% of preferred values with precisions of < 0.25% (RSD). These results demonstrate improvement over previous LA-MC-ICPMS data in terms of both quantification limits and spatial resolution, while retaining similar levels of accuracy and precision.

Unlike other radiogenic isotope systems of geological interest (*e.g.* Rb-Sr, Sm-Nd, Lu-Hf), the Pb isotope system lacks an invariant Pb isotope ratio that can be used for internal mass bias corrections of measured Pb isotope ratios. Instead, an external

normalization method such as aspirating a thallium tracer solution during laser analysis to monitor lead isotope fractionation (*e.g.* Horn et al., 2000; Kosler et al., 2002) or standard – sample – standard bracketing with reference materials of known lead isotope compositions (*e.g.* Willigers et al., 2002; Paul et al., 2005; Souders and Sylvester, 2008a) must be employed. The technique to measure lead isotopes in lead-'poor' materials presented in Chapter 2 uses standard – sample – standard bracketing to externally correct for mass bias. Standard – sample – standard bracketing can only be used if drift of the measured isotope ratios of the standards is linear over the course of the analytical period and there is no difference in mass discrimination between the standard matrix relative to the sample matrix.

Measured LA-MC-ICPMS ratios differ from true isotope ratio values due to mass-dependant processes such as instrumental mass bias and isotopic fractionation. Mass discrimination plays a limiting role in the accuracy of isotope ratio measurements and proper correction procedures must be ensured, especially when external normalization methods are used. Isotopic fractionation can be influenced by instrument parameters, laser ablation parameters and differences in chemical and physical properties between standards and samples, or matrix effects. The effect of sample matrix can result in variable ablation rates, particle size formation, particle composition, particle transport efficiency and mass loading in the Ar-plasma (Sylvester, 2008 and references therein). Therefore the potential for mass bias variation as a function of sample matrix must be carefully evaluated.

Several high-precision LA-MC-ICPMS investigations using external normalization procedures have identified significant sample matrix-related biases (Mason et al., 2006; Norman et al., 2006). The study presented in Chapter 3 (Souders and Sylvester, 2010) evaluates the need for matrix matching for LA-MC-ICPMS lead isotope measurements of lead-'poor' (< 40 ppm total Pb) feldspar and sulfide minerals using standard – sample – standard bracketing to correct for mass discrimination. Feldspar minerals and sulfides, two materials with large differences in matrix composition and ablation behavior, were chosen to determine the quality of data possible when calibrating samples with standards having different physical and chemical characteristics. The Pb isotope ratios of the 3 different feldspar minerals were calibrated against NIST 612, NIST 614 and BCR2-G. Each feldspar analyzed had different chemical composition, physical characteristics and total lead concentration. The average $^{206,207,208}Pb/^{204}Pb$ and $^{207,208}Pb/^{206}Pb$ ratios measured for all 3 feldspars, independent of calibration standard, are within 0.40 % of the preferred average values determined by thermal ionization mass spectrometry (TIMS) as part of this investigation. External precisions for the lead isotope measurements of feldspar by LA-MC-ICPMS are better than 0.60 % (RSD, 1σ). Lead isotope ratios of three different sulfides were determined by LA-MC-ICPMS using NIST 612 or PB-1, a synthetic sulfide glass, as the external standard. Two sulfides, PB-1 and B41, contained little to no measurable mercury. The mean $^{206,207,208}Pb/^{204}Pb$, $^{206,207}Pb/^{206}Pb$ are accurate within 0.40 % of the TIMS results with only subtle differences in results between matrix-matched (PB-1) by and non-matrix-matched (NIST 612/614). The final results suggest that accurate and precise Pb isotope ratios measured for lead-

'poor' minerals can be obtained by LA-MC-ICPMS using available silicate glass reference materials regardless of differences in the physical and chemical properties between standards and samples.

Traditional isotope and geochemical investigations have concluded that Archean anorthosites were derived from depleted mantle melts (*e.g.* Ashwal et al., 1983, 1989; Barton, 1996; Polat et al., 2009, 2010, 2011; Rollinson et al., 2010) and isotopic analysis of preserved igneous minerals could provide a window into the differentiation of the Archean mantle. A limiting factor in the isotopic analysis of Archean anorthosites, and other ancient rocks, is the pervasive metamorphism and secondary alteration that has affected most Archean rocks present at the surface of the Earth today. An advantage of in-situ isotopic analysis by methods such as LA-MC-ICPMS is that preserved igneous regions of individual minerals can be targeted for analysis, avoiding more recrystallized or altered domains.

Igneous plagioclase megacrysts preserved within Archean anorthosites make excellent targets for in-situ Pb isotopic analysis by LA-MC-ICPMS yet low Pb concentrations (~ 2 – 10 ppm Pb) and abundant mineral inclusions within preserved igneous domains hinder in-situ analysis. The incorporation of ion counters within the collector configuration of MC-ICPMS instruments and further development of the analytical method extends LA-MC-ICPMS Pb isotope measurements to Pb-poor materials (< 20 ppm Pb) with significantly improved spatial resolution (40 – 99 μm laser spots depending on Pb concentration) (*e.g.* Chapters 2 and 3; published as Souders and Sylvester, 2008, 2010). The new technique is applied to plagioclase megacrysts from

Archean anorthosite complex and investigations of Archean mantle evolution in Chapter 4 (Souders et al., *in review*).

The Fiskenæsset and Nunataarsuk anorthosite complexes of south West Greenland (Figure 1-8) are two of the best-preserved examples of Archean anorthosites in the world. Little geochemical information is known about Nunataarsuk but Fiskenæsset is thought to have a mantle source (Ashwal et al., 1989; Polat et al., 2009). Like most Archean rocks, the Fiskenæsset and Nunataarsuk anorthosites have been intensely deformed and metamorphosed yet locally preserve igneous minerals within low-strain regions of each anorthosite complex. These pristine domains of interest can be identified through thin section petrography using an optical microscope, back-scattered electron (BSE) imaging using a scanning electron microscope (SEM) and then further characterized by in situ geochemical (EPMA and LA-ICPMS) and isotopic analysis (LA-(MC)-ICPMS) (Figure 1-7). The expectation is that magmatic isotope systematics are most likely to be preserved within these domains, where parent-daughter ratios have not been reset by intense deformation and secondary alteration.

In Chapter 4, the results for in situ LA-ICPMS U-Pb zircon geochronology and LA-MC-ICPMS Hf isotope compositions for zircon crystals separated from anorthosite and leucogabbro samples from Fiskenæsset and Nunataarsuk are also presented and used in conjunction with the lead isotope data to characterize the source of the two Archean anorthosites. In situ analysis of lead isotopes in plagioclase and Hf isotopes in zircon are powerful tools for the determination of initial isotope ratios and tracing the isotopic composition of the mantle through time because both minerals have extremely low

parent-daughter ratios for the respective isotope system of interest (plagioclase – low U/Pb; zircon – low Lu/Hf) and require, if necessary, only minimal correction for radiogenic in-growth. Lead isotopes are particularly sensitive indicators of heterogeneities due to crustal contamination, assimilation, magmatic recharge and secondary alteration within igneous systems (*e.g.* Oversby, 1975; Housh et al., 1989; McCulloch and Woodhead, 1993; Mathez and Waight, 2003; Waight and Lesher, 2010). Previous investigations employing Hf isotope measurements in zircon have demonstrated Hf systematics to be extremely robust through metamorphism and secondary alteration. Unless the zircon grain is completely recrystallized with open system exchange with other Hf-bearing minerals, zircons have been shown to retain their initial $^{176}Hf/^{177}Hf$, even when U-Th-Pb systematics within the zircon crystal have been reset: This makes Hf isotopes in zircon an ideal isotope tracer for the compositional evolution of the mantle and crustal growth processes (Patchett et al., 1981; Flowerdew et al., 2006; Gerdes and Zeh, 2009).

In situ LA-ICPMS U-Pb geochronology of zircon grains presented in Chapter 4 suggests that the crystallization age of the Fiskenæsset complex is 2936 ± 13 Ma (2σ, MSWD = 1.5) and the Nunataarsuk complex is 2914 ± 6.9 Ma (2σ, MSWD = 2.0). The range of Pb isotope compositions in plagioclase megacrysts and Hf isotopic compositions in zircon grains from both Fiskenæsset and Nunataarsuk extend beyond analytical uncertainty suggesting multiple sources contributed to the parent magma for both anorthosite complexes. The Pb isotope and Hf isotope data show that both anorthosite complexes share a depleted mantle end member yet the range of compositions suggests

the common depleted mantle end member interacted with ancient mafic crust prior to crystallization of both anorthosite complexes. At Fiskenæsset, Pb isotope models predict contamination by a high μ crust (μ ~ 12) with a mantle extraction age in the Eoarchean (between ~ 3600 and ~ 3800 Ma). For Nunataarsuk, the Pb isotope data suggest contamination of the depleted mantle end member by an ancient low μ crust (μ ~ 6) isolated in the Hadean (at ~ 4200 Ma).

Determining the nature of ancient crusts (mafic versus felsic) is of great interest for geologists today. The $^{176}Lu/^{177}Hf$ is characteristic of the nature of the source. The $^{176}Lu/^{177}Hf$ of the modern continental crust is 0.013 – 0.014 (Taylor and McLennan, 1995). Typical $^{176}Lu/^{177}Hf$ for felsic rocks range from ~ 0.05 to 0.015 (Pietranik et al., 2008). Mafic rocks and komatiites tend to have higher $^{176}Lu/^{177}Hf$ from ~ 0.02 to > 0.03 (Blichert-Toft and Albarade, 2008; Pietranik et al., 2008; Blichert-Toft and Putchel, 2010). The measured $^{176}Lu/^{177}Hf$ of an analyzed zircon is not representative of the parent magma because zircon strongly fractionates Lu (crystal/melt distribution coefficient or D << 1) from Hf (D > 1) during crystallization. In order to constrain the $^{176}Lu/^{177}Hf$ of the crustal end member for both anorthosite complexes, the timing of parent melt extraction from the depleted mantle (T_{DM}) must be known. Using the in situ Pb isotope compositions of plagioclase megacrysts from Nunataarsuk and Fiskenæsset in conjunction with the zircon Hf isotope compositions from both complexes, the nature of the ancient crustal contaminant can be determined. The in situ Pb isotope data are used to constrain the timing of crust (melt) extraction from the mantle, which is then used to calculate the $^{176}Lu/^{177}Hf$. For both Fiskenæsset and Nunataarsuk, the calculated

$^{176}Lu/^{177}Hf$ ratio is diagnostic of ancient mafic crust. The model presented is that the ancient mafic crusts have interacted with the depleted mantle melt prior to crystallization of each anorthosite complex.

Interpretation of the initial Pb and Hf isotope data provides evidence for the survival of Hadean and Eoarchean mafic crust until at least ~ 2900 Ma, suggesting the possibility that mafic crust was widespread very early (>3.7 Ga) in Earth history, and at least some of it was long-lived at the surface. There is great debate over the composition of the Earth's early crust (Armstrong 1981; Taylor and McLennan, 1995; Chase and Patchett, 1988; Bowring and Housh, 1995; Harrison et al., 2005, 2008; Blichert-Toft and Albarede, 2008; O'Neil et al., 2008). Much of our information comes from the zircon record. Unfortunately, this record is biased towards felsic rocks, which contain much greater proportions of zircon grains than mafic rocks. A large proportion of early mafic crust may be unrecognized because of the scarcity of zircon crystallizing from mafic magmas, which have extremely high zirconium solubilities (Watson and Harrison, 1983). Not only does the integration of in-situ Pb isotopes in plagioclase with Hf isotope compositions of zircons from the same rock provide a window into the isotope composition of the mantle through time, it also facilitates identification of ancient crusts.

1.4. References

Amelin Y., Lee D.-C. and Halliday A.N. (2000) Early-middle Archean crustal evolution deduced from Lu-Hf and U-Pb isotopic studies of single zircon grains. *Geochim. Cosmochim. Acta* **64**, 4205 – 4225.

Armstrong R.L. (1981) Radiogenic isotopes: the case for crustal recycling on a near-steady-state no-continental-growth. *Earth. Phil. Trans. Roy. Soc. London* **A301**, 443 – 472.

Ashwal L.D. (1993) Anorthosites. Springer-Verlag, New York, 422 p.

Ashwal L.D. (2010) The temporality of anorthosites. *Can. Min.* **48**, 711 – 728.

Ashwal L.D., Morrison D.A., Phinney W.C. and Wood J. (1983) Origin of Archean Anorthosites: Evidence from the Bad Vermilion Lake anorthosite complex, Ontario. *Contrib. Mineral. Petrol.* **82**, 259 – 272.

Ashwal L.D., Wooden J.L., Phinney W.C. and Morrison D.A. (1985) Sm-Nd and Rb-Sr isotope systematic of an Archean anorthosite and related rocks from the Superior Province of the Canadian Shield. *Earth Planet. Sci. Lett.* **74**, 338 – 346.

Ashwal L.D., Jacobsen S.B., Myers J.S., Kalsbeek F. and Goldstein S.J. (1989) Sm-Nd age of the Fiskenaesset Anorthosite Complex, West Greenland. *Earth Planet. Sci. Lett.* **91**, 261 – 270.

Barton J.M., Fripp R.E.P., Horrocks P. and McLean N. (1979) The geology, age and tectonic setting of the Messina layered intrusion, Limpopo Mobile Belt, Southern Africa. *Am. J. Sci.* **279**, 1108 – 1134.

Barton J.M., Ryan B. and Fripp R.E.P. (1983) Rb-Sr and U-Th-Pb isotopic studies of the Sand River Gneisses, Central Zone, Limpopo Mobile Belt. *Spec. Publ. Geol. Soc. S. Afr.* **8**, 9 – 18.

Barton Jr. J.M. (1996) The Messina layered intrusion, Limpopo belt, South Africa, an example on the in-situ contamination of an Archaean anorthosite complex by continental crust. *Precam. Res.* **78**, 139 – 150.

Bennett V.C. (2003) Compositional evolution of the mantle. In *The Mantle and Core Treatise on Geochemistry, v.2* (ed. R.W. Carlson). Elsevier, Amsterdam, pp. 493 - 515.

Bennett V.C., Nutman A.P. and McCulloch M.T. (1993) Nd isotopic evidence for transient, highly depleted mantle reservoirs in the early history of the Earth. *Earth Planet. Sci. Lett.* **119**, 299 – 317.

Bhaskar Rao Y.J., Chetty T.R.K., Janardhan A.S. and Gopalan K. (1996) Sm–Nd and Rb–Sr ages and P–T history of the Archean Sittampundi and Bhavani layered meta-anorthosite complexes in the Cauvery shear zone, South India: evidence for Neoproterozoic reworking of Archean crust. *Contrib. Mineral. Petrol.* **125**, 237-250.

Bhaskar Rao Y.J., Kumar A., Vrevsky A.B., Srinivasan R. and Anantha Iyer G.V. (2000): Sm–Nd ages of two meta-anorthosite complexes around Holenarsipur: constraints on the antiquity of Archean supracrustal rocks of the Dharwar Craton. *Proc. Indian Acad. Sci., Earth and Planetary Sci.* **109**, 57-65.

Black L.P., Moorbath S., Pankhurst R.J. and Windley B.F. (1973) $^{207}Pb/^{206}Pb$ whole rock age of the Archaean granulite facies metamorphic event in west Greenland. *Nature Phys. Sci.* **244**, 50 – 53.

Blichert-Toft J. and Albarede F. (2008) Hafnium isotopes in Jack Hills zircons and the formation of the Hadean crust. *Earth Planet. Sci. Lett.* **265**, 686 – 702.

Blichert-Toft J. and Puchtel I.S. (2010) Depleted mantle sources through time: Evidence from Lu-Hf and Sm-Nd isotope systematics of Archean Komatiites. *Earth Planet. Sci. Lett.* **297**, 598 – 606.

Blichert-Toft J., Arndt N.T. and Gruau G., (2004) Hf isotopic measurements on the Barberton komatiites: effects of incomplete sample dissolution and importance for primary and secondary magmatic signatures. *Chem. Geol.* **207**, 261 – 275.

Bowring S.A. and Housh T. (1995) The Earth's early evolution. *Science*. **269**, 1535 – 1540.

Burg J.P., Bodinier J.L., Chaudhry S., Hussain S., Dawood H. (1998) Infra-arc mantle-crust transition and intra-arc mantle diapers in the Kohistan complex (Pakistani Himalaya): petro-structural evidence. *Terra Nova* **10**, 74-80.

Chase C.G. and Patchett P.J. (1988) Stored mafic/ultramafic crust and early Archean mantle depletion. *Earth Planet. Sci. Lett.* **91**, 66 – 72.

Chauvel C. and Blichert-Toft J. (2001) A hafnium isotope and trace element perspective on melting of the depleted mantle. *Earth Planet. Sci. Lett.* **190**, 137 – 151.

Connelly J.N. and Thrane K. (2005) Rapid determination of Pb isotopes to define Precambrain allochthonous domains: and example from West Greenland. *Geology* **33**, 953 – 956.

Cottle J.M., Horstwood M.S.A. and Parrish R.R. (2009) A new approach to single shot laser ablation analysis and its application to in situ Pb-U geochronology. *J. Anal. At. Spectrom.* **24**, 1355 – 1363.

DePaolo D.J. and Wasserburg G.J. (1976) Inferences about magma sources and mantle structure from variations of $^{143}Nd/^{144}Nd$. *Geophys. Res. Lett.* **3**, 743-746.

Doe B.R. (1962) Relationships of lead isotopes among granites, pegmatites and sulfide ores near Balmat, New York. *J. Geophys. Res.* **67**, 2895 – 2906.

Escher J.C. and Myers J.S. (1975) New evidence concerning the original relationships of early Precambrian volcanics and anorthosites in the Fiskenæsset region, southern west Greenland. Rapp. *Gronl. Geol. Unders. Bull.* **75**, 72 – 76.

Fletcher I.R., Rosman K.J.R. and Libby W.G. (1988) Sm-Nd, Pb-Pb, and Rb-Sr geochronology of the Manfred Complex, Mount Narryer, Western Australia. *Precamb. Res.* **38**, 343 – 354.

Flowerdew M.J., Millar I.L., Vaughan A.P.M., Horstwood M.S.A. and Fanning C.M. (2006) The source of granitic gneisses and migmatites in the Antarctic Peninsula: a combined U-Pb SHRIMP and laser ablation Hf isotope study of complex zircons. *Contrib. Mineral Petrol.* **151**, 751 – 768.

Gagnevin D., Daly J.S., Waight T.E., Morgan D. and Poli G. (2005) Pb isotopic zoning of K-feldspar megacrysts determined by laser ablation multi-collector ICP-MS: insights into granite petrogenesis. *Geochim. Cosmochim. Acta* **69**, 1899 – 1915.

Gancarz A.J. (1976) Isotopic systematic in Archean rocks, west Greenland. PhD thesis, California Institute of Technology, Pasadena, 378p.

Gerdes A. and Zeh A. (2009) Zircon formation versus zircon alteration – new insights from combined U-Pb and Lu–Hf in-situ LA-ICP-MS analyses, and consequences for the interpretation of Archaean zircon from the Central Zone of the Limpopo Belt. *Chem. Geol.* **261**, 230 – 243.

Gibson G.M. and Ireland T.R. (1999) Black Giants anorthosite, New Zealand: a Paleozoic analogue of Archean stratiform anorthosites and implications for the formation of Archean high grade gneiss terranes. *Geology* **27**, 131 – 134.

Harrison T.M., Blichert-Toft J., Muller W., Albarede F., Holden P. and Mojzsis S.J. (2005) Heterogeneous Hadean Hafnium: evidence for continental crust at 4.4 to .5 Ga. *Science* **310**, 1947.

Harrison T.M., Schmitt A.K., McCulloch M.T. and Lovera O.M. (2008) Early (4.5 Ga) formation of terrestrial crust: Lu Hf, del ^{18}O, and Ti thermometry results for Hadean zircons. *Earth Planet. Sci. Lett.* **268**, 476 – 486.

Hawkesworth C.J., Dhuime B., Pietranik A.B., Cawood P.A., Kemp A.I.S. and Storey C.D. (2010) The generation and evolution of the continental crust. *J. Geol. Soc. Lon.* **167**, 229 – 248.

Henderson P., Fishlock S.J. Laul J.C., Cooper T.D., Conrad R.L., Boynton W.V. and Schmitt R.A. (1976) Rare earth element abundances in rocks and minerals from the Fiskenæsset complex, West Greenland. *Earth Planet. Sci. Lett.* **30**, 37 – 47.

Hiess J., Bennett V.C., Nutman A.P. and Williams I.S. (2009) In situ U-Pb, O and Hf isotopic compositions of zircon and olivine from Eoarchaean rocks, West Greenland: New insights to making old crust. *Geochim. Cosmochim. Acta* **73**, 4489-4516.

Hofmann A.W. (2004) Sampling mantle heterogeneity through oceanic basalts: isotopes and trace elements. In *The Mantle and Core Treatise on Geochemistry, v.2* (ed. R.W. Carlson). Elsevier, Amsterdam, pp. 493 - 515.

Hoffmann J.E., Munker C., Polat A., Konig S., Mezger K. and Rosing M.T. (2010) Highly depleted Hadean mantle reservoirs in the sources of early Archean arc-like rocks, Isua supracrustal belt, wouthern West Greenland. *Geochim Cosmochin Acta.* **74**, 7236 – 7260.

Horn I., Rudnick R.L., McDonough W.F. (2000) Precise elemental and isotope ratio determination by simultaneous solution nebulization and laser ablation ICP-MS: application to U-Pb geochronology. *Chem. Geol.* **164**, 281 – 301.

Horstwood M.S.A., Foster G.L., Parrish R.R., Noble S.R. and Nowell G.M. (2003) Common-Pb corrected in situ U-Pb accessory mineral geochronology by LA-MC-ICP-MS. *J. Anal. Atom. Spectrom.* **18**, 837 – 846.

Housh T. and Bowring S.A. (1991) Lead isotopic heterogeneities within alkali feldspars: Implications for the determination of initial lead isotopic compositions. *Geochim. Cosmochim. Acta* **55**, 2309 – 2316.

Housh T.B., Bowring S.A. and Villeneuve M. (1989) Lead isotopic study of arc magmatism within early Proterozoic Wopmay Orogen, NW Canada: Role of continental crust in arc magmatism. *J. Geol.* **97**, 735 – 747.

Jochum K.P., Dingwell D.B., Rocholl A., Stoll B., Hofmann A.W., Becker S., Besmehn A., Bessett D., Dietze H-J., Dulski P., Erzinger J., Hellebrand E., Hoppe P., Horn I., Janssens K., Jenner G.A., Klein M., McDonough W.F., Maetz M., Mezger K., Munker C., Nikogosian I.K., Pickhardt C., Raczek I., Rhede D., Seufert H.M., Simakin S.G., Sobolev A.V., Spettel B., Straub S., Vincze L., Wallianos A., Weckwerth G., Weyer S., Wolf D. and Zimmer M. (2000) The prepartion and preliminary characterization of eight geological MPI-DING reference glasses for in-situ microanalysis. *Geostandards Newsletter: The Journal of Geostandards and Geoanalysis*. **24**, 87 – 133.

Jochum K.P., Pfander J., Woodhead J.D., Willbold M., Stoll B., Herwig K., Amini M., Abouchami W. and Hofmann A.W. (2005) MPI-DING glasses: New geological reference materials for in situ Pb isotope analysis. *Geochem. Geophys. Geosys.* **6**, Q10008.

Kalsbeek F. and Pidgeon R.T. (1980) The geological significance of Rb-Sr whole-rock isochrons of polymetamorphic Archean gneisses, Fiskenæsset area, southern West Greenland. *Earth Planet. Sci. Lett.* **50**, 225 – 237.

Kamber B.S., Collerson K.D., Moorbath S. and Whitehouse M.J. (2003) Inheritance of early Archaean Pb-isotope variability from long-lived Hadean protocrust. *Contrib. Mineral Petrol.* **145**, 25 – 46.

Kemp A.I.S., Foster G.L., Schersten A. et al. (2009) Concurrent Pb-Hf isotope analysis of zircon by laser ablation multi-collector ICP-MS, with implications for the crustal evolution of Greenland and the Himalayas. *Chem. Geol.* **261**, 244 – 260.

Kemp A.I.S., Wilde S.A., Hawkesworth C.J., Coath C.D., Nemchin A., Pidgeon R.T., Vervoort J.D. and DuFrane S.A. (2010) Hadean crustal evolution revisited: New constraints from Pb-Hf isotope systematics of the Jack Hills zircons. *Earth Planet. Sci. Lett.* **296**, 45 - 56.

Kent A.J.R. (2008) In-situ analysis of Pb isotope ratios using laser ablation MC-ICP-MS: controls on precision and accuracy and comparison between Faraday cup and ion counting systems. *J. Anal. At. Spectrom.* **23**, 968 – 975.

Keulen N., Schersten A., Schumacher J.C., Næraa T. and Windley B.F. (2009) Geological observations in the southern West Greenland basement from Ameralik to Frederikshab Isblink in 2008. *Geo. Survey of Denmark and Greenland Bulletin* **17**, 49 – 52.

Keulen N., Næraa T., Kokfelt T., Schumacher J.C. and Schersten A. (2010) Zircon record of the igneous and metamorphic history of the Fiskenæsset anorthosite complex in southern West Greenland. *Geo. Survey of Denmark and Greenland Bulletin*. **20**, 67-70.

Kinney P.D., Williams I.S., Froude D.O., Ireland T.R. and Compston W. (1988) Early Archaean zircon ages from orthogneisses and anorthosites at Mount Narryer, Western Australia. *Precamb. Res.* **38**, 325 – 341.

Kosler J., Fonneland H., Sylvester P., Tubrett M. and Pederson R. (2002) U–Pb dating of detrital zircons for sediment provenance studies: a comparison of laser- ablation ICPMS and SIMS techniques. *ChemicalGeology*, **182**, 605–618.

Kramers J.D. and Tolstikhin I.N. (1997) Two terrestrial lead isotope paradoxes, forward transport modeling, core formation and the history of the continental crust. *Chem. Geol.* **139**, 75 – 110.

Lahaye Y., Arndt N., Byerly G., Chauvel C., Fourcade S. and Gruau G. (1995) The invluence of alteration of the trace-element and Nd isotopic compositions of komatiites. *Chem. Geol.* **126**, 43 – 64.

Longerich H. (2008) Laser ablation-inductively coupled plasma-mass spectrometry (LA-ICP-MS); an introduction. *In* Laser Ablation ICP-MS in the Earth Sciences: Current Practices and Outstanding Issues, v. 40 (ed. P.J. Sylvester). Mineralogical Association of Canada p. 1 - 18.

Ludwig K.R. and Silver L.T. (1977) Lead-isotope inhomogeneity in Precambrian igneous K-feldspars. *Geochim Cosmochim. Acta* **41**, 1457 – 1471.

Mason P.R.D., Kosler J., De Hoog J.C.M., Sylvester P.J., Meffan-Main S. (2006) In-situ determination of sulfur isotopes in sulfur-rich materials by laser ablation multiple-collector inductively coupled plasma mass spectrometry (LA-MC-ICP-MS). *J. Anal. Atom. Spectrom.* **21**, 177 – 186.

Mathez E.A. and Waight T.E. (2003) Lead isotopic disequilibrium between sulfide and plagioclase in the Bushveld complex and the chemical evolution of large layered intrusions. *Geochim Cosmochim Acta* **67**, 1875 – 1888.

Mathez E.A. and Kent A.J.R. (2007) Variable initial Pb isotopic compositions of rocks associated with the UG2 chromitite, eastern Bushveld Complex. *Geochim. Cosmochim. Acta* **71**, 5514 – 5527.

McCulloch M.T. and Woodhead J.D. (1993) Lead isotopic evidence for deep crustal-scale fluid transport during granite petrogenesis. *Geochim. Cosmochim. Acta* **57**, 659 – 674.

McGill R.A.R., Pearce J.M., Fortey N.J., Watt J., Ault L. and Parrish R.R. (2003) Contaminant source apportionment by PIMMS lead isotope analysis and SEM image analysis. *Environ. Geochem. Health* **25**, 25 – 32.

Moorbath S. and Pankhurst R.J. (1976) Further rubidium-strontium age and isotopic evidence for the nature of late Archean plutonic event in West Greenland. *Nature*. **262**, 124 – 126.

Morrison D.A., Haskin L.A., Qiu Y.Z., Phinney W.C. and Maczuga D.E. (1985) Alteration in Archean anorthosite complexes. *Lunar and Planetary Science XVI*. Lunar Planet Inst, Houston, p. 589 – 590.

Mouri H., Whitehouse M.J., Brandl G. and Rajesh H.M. (2009) A magmatic age and four successive metamorphic events recorded in zircons from a single metaanorthosite sample in the Central Zone of the Limpopo Belt, South Africa. *J. Geol. Soc. London* **166**, 827 – 830.

Myers J.S. (1976) Channel deposits of peridotite, gabbro and chromitite from turbidity currents in the stratiform Fiskenæsset anorthosite complex, southwest Greenland. *Lithos* **9**, 265 – 268.

Myers J.S. (1985) Stratigraphy and structure of the Fiskenaesset Complex, West Greenland. *Gronl. Geol. Unders. Bull.* **150**, 72p.

Myers J.S. (1988) Oldest known terrestrial anorthosites at Mount Narryer, Western Australia. *Precamb. Res.* **38**, 309 – 323.

Myers J.S. and Platt R.G. (1977) Mineral chemistry of layered Archean anorthosite at Majorqap qâva, near Fiskenaesset, southwest Greenland. *Lithos* **10**, 59 – 72.

Norman M., McCulloch M., O'Neill H. and Yaxley G. (2006) Manesium isotopic analysis of olivine by laser ablation multi-collector ICP-MS: Composition dependent matrix effects and a comparison of the Earth and Moon. *J. Anal. At. Spectrom.* **21**, 50 – 54.

Novak M., Mikova J., Krachler M., Kosler J., Erbanova L., Prechova E., Jackova I. and Fottova D. (2010) Radial distribution of lead and lead isotopes in stem wood of Norway spruce: A reliable archive of pollution trends in Central Europe. *Geochim. Cosmochim. Acta* **74**, 4207 – 4218.

O'Neil J., Carlson R.W., Francis D. and Stevenson R.K. (2008) Neodymium-142 evidence for Hadean mafic crust. *Science* **321**, 1828 – 1831.

Oversby V.M. (1975) Lead isotopic systematics and ages of Archean acid intrusives in the Kalgoorlie Norseman area, western Australia. *Geochim. Cosmochim. Acta* **39**, 1107 – 1125.

Owens B.E. and Dymek R.F. (1997) Comparative petrology of Archean anorthosites in amphibolite and granulite facies terranes, WE Greenland. *Contrib. Mineral. Petrol.* **128**, 371 – 384.

Patchett P.J., Kouvo O., Hedge C.E. and Tatsumoto M. (1981) Evolution of continental crust and mantle heterogeneity: evidence from Hf isotopes. *Contrib. Mineral. Petrol.* **78**, 279 – 297.

Paul B., Woodhead J.D. and Hergt J. (2005) Improved in situ isotope analysis of low Pb materials using LA-MC-ICP-MS with parallel ion counter and Faraday detection. *J. Analyt. Atom. Spectrom.* **20**, 1350 – 1357.

Peck W.H. and Valley J.W. (1996) The Fiskenæsset Anorthosite Complex: stable isotope evidence for shallow emplacement into Archean oceanic crust. *Geology*, **24**, 523 – 526.

Phinney W.C. (1982) Petrogenesis of Archean anorthosites. *In* Workshop on magmatic processes of early planetary crusts: magma oceans and stratiform layered intrusions. (eds. D. Walker, I.S. McCallum). Lunar Planet Inst Tech Rep 82 – 01, Lunar Planet Inst, Houston, p. 121 – 124.

Phinney W.C. and Morrison D.A. (1990) Partition coefficients for calcic plagioclase: implications for Archean anorthosites. *Geochim. Cosmochim. Acta.* **54**, 1639 – 1654.

Phinney W.C., Morrison D.A. and Maczuga D.E. (1988) Anorthosites and related megacrystic units in the evolution of Archean crust. *J. of Petrol.* **29**, 1283 – 1323.

Pidgeon R.T. and Kalsbeek, F. (1978) Dating of igneous and metamorphic events in the Fiskenaesset region of southern West Greenland. *Can. J. Earth Sci.* **15**, 2021 – 2025.

Pietranik A.B., Hawkesworth C.J., Storey C.D., Kemp A.I.S., Sircombe K.N., Whitehouse M.J. and Bleeker W. (2008) Episodic mafic crust formation from 4.5 to 2.8 Ga. New evidence from detrital zircons, Slave craton, Canada. *Geology*, **36**, 875 – 878.

Polat A., Hormann A.W., Munker C., Regelous M. and Appel P.W.U. (2003) Contrasting geochemical patterns in the 3.7 – 3.8 Ga pillow basalt cores and rims, Isua Greenstone Belt, southwest Greenland: Implications for postmagmatic alteration processes. *Geochim. Cosmochim. Acta.* **67**, 441 – 457.

Polat A., Appel P.W.U., Fryer B., Windley B., Frei R., Samson I.M. and Huang H. (2009) Trace element systematics of the Neoarchean Fiskenæsset anorthosite complex and associated met-volcanic rocks, SW Greenland: Evidenc for a magmatic arc origin. *Precamb. Res.* **175**, 87 – 115.

Polat A. Frei R. Schersten A. and Appel P.W.U. (2010) New age (ca. 2970 Ma), mantle source composition and geodynamic constraints on the Archean Fiskenæsset anorthosite complex, SW Greenland. *Chem. Geol.* **277**, 1 – 20.

Polat A., Fryer B.J., Appel P.W.U., Kalvig P., Kerrich R., Dilek Y., and Yang Z. (2011) Geochmistry of anorthositic differentiated sills in the Archean (~2970 Ma) Fiskenæsset Complex, SW Greenland: Implications for parental magma compositions, geodynamic setting, and secular heat flow in arcs. *Lithos* **123**, 50 – 72.

Rollinson H., Reid C. and Windley B. (2010) Chromitites from the Fiskenæsset anorthositic complex, West Greenland: clues to late Archaean mantle processes. In *The Evolving Continents: Understanding Processes of Continental Growth*, v. 338 (eds. T.M. Kusky, M.-G. Zhai, W. Xiao). Geological Society, London, pp. 197 – 212.

Rosholt J.N., Zartman R.E. and Nkomo I. T. (1973) Lead isotope systematics and uranium depletion in the Granite Mountains, Wyoming. *Geol. Soc. Amer. Bull.* **89**, 989 – 1002.

Rudnick R.L., McLennan S.M. and Taylor S.R. (1985) Large ion lithophile elements in rocks from high-pressure granulite facies terrains. *Geochim. Cosmochin. Acta* **49**, 645 – 655.

Simmons E.C., Hanson G.N. and Lumbers S.B. (1980) Geochemistry of the Shawmere anorthosite complex, Kapuskasing structural zone, Ontario. *Precam. Res.* **11**, 43 – 71.

Simonetti A., Heaman L.M., Hartlaub R.P., Creaser R.A., MacHattie T.G. and Bohm C. (2005) U-Pb zircon dating by laser ablation-MC-ICP-MS using a new multiple ion counting Faraday collector array. *J. Anal. At. Spectrom.* **20**, 677 – 686.

Sisson T.W. and Grove T.L. (1993) Temperatures and H_2O contents of low NgO high-alumina basalts. *Contrib. Mineral. Petrol.* **113**, 167 – 184.

Souders A.K. and Sylvester P.J. (2008a) Improved in situ measurements of lead isotopes in silicate glasses by LA-MC-ICPMS using multiple ion counters. *J. Anal. At. Spectrom.* **23**, 535 – 543. doi: 10.1039/b713934a

Souders A.K. and Sylvester P.J. (2008b) Use of multiple channeltron ion counters for LA-MC-ICPMS analysis of common lead isotopes in silicate glasses. *In* Laser Ablation ICP-MS in the Earth Sciences: Current Practices and Outstanding Issues, v. 40 (ed. P.J. Sylvester). Mineralogical Association of Canada p. 79 – 92.

Souders A.K. and Sylvester P.J. (2010) Accuracy and precision of non-matrix-matched calibration for lead isotope ratio measurements of lead-poor minerals by LA-MC-ICPMS. *J.Anal. At. Spectrom.* **25**, 975 – 988.

Souders A.K., Sylvester P.J., Myers J.S. (*in review*) Mantle and crustal sources of Archean anorthosite: a combined in-situ isotopic study of Pb-Pb in plagioclase and Lu-Hf in zircon. *Geochim. Cosmochim Acta.*

Stacey J.S. and Kramers J.D. (1975) Approximation of terrestrial lead isotope evolution by a two-stage model. *Earth Planet. Sci. Lett.* **26**, 207 – 221.

Streckeisen A. (1976) To each plutonic rock its proper name. *Earth Sci. Rev.* **12**, 1 – 33.

Stolper E. and Walker D. (1980) Melt density and the average composition of basalt. Ibid. **375**, 86 – 111.

Strom R.G. and Sprague A.L. (2003) Exploring Mercury: the iron planet. Springer-Verlag. 216p.

Sylvester P.J. (2008) Matrix effects in laser ablation ICP-MS. *In* Laser Ablation ICP-MS in the Earth Sciences: Current Practices and Outstanding Issues, v. 40 (ed. P.J. Sylvester). Mineralogical Association of Canada p. 79 – 92.

Takagi D., Sato H. and Nakagawa M. (2005) Experimental study of a low alkali tholeiite at 1-5 kbar: optimal condition for the crystallization of high-An plagioclase in hydrous arc tholeiite. *Contrib. Mineral. Petrol.* **149**, 527 – 540.

Taylor G.J. (2009) Ancient lunar crust: origin, composition and implications. *Elements* **5**, 17 – 22.

Taylor S.R. and McLennan S.M. (1995) The geochemical evolution of the continental crust. *Rev. Geophys.* **33**, 241 – 265.

Taylor P.N., Moorbath S., Goodwin R. and Petrykowski A.C. (1980) Crustal contamination as an indicator of the extent of early Archean continental crust: Pb isotopic evidence from the late Archean gneisses of West Greenland. *Geochim. Cosmochim. Acta.* **44**, 1437 – 1453.

Tyrrell S., Haughton P.D.W., Daly J.S., Kokfelt T.F. and Gagnevin D. (2006) The use of the common Pb isotope composition of detrital K-feldspar grains as a provenance tool and its application to Upper Carboniferous palaeodrainage, Northern England. *J. Sed. Res.* **76**, 324 – 345.

Vervoort J.D., Patchett P.J., Gehrels G.E. and Nutman A.P. (1996) Constraints on early Earth differentiation from hafnium and neodymium isotopes. *Nature* **379**, 624 – 627.

Vervoort, J.D. and Blichert-Toft J. (1999) Evolution of the depleted mantle: Hf isotope evidence from juvenile rocks through time. *Geochim. Cosmochim. Acta*, **63**, 533 – 556.

Vry J.K. and Baker J.A. (2006) LA-MC-ICPMS Pb–Pb dating of rutile from slowly cooled granulites: Confirmation of the high closure temperature for Pb diffusion in rutile. *Geochim. Cosmochim. Acta* **70**, 1807 – 1820.

Waight T.E. and Lesher C.E. (2010) Pb isotopes during crustal melting and magma mingling – a cautionary tale form Miki Fjord macrodike, central east Greenland. *Lithos* **118**, 191 – 201.

Watson E.B. and Harrison T.M. (1983) Zircon saturation revisited: temperature and composition effects in a variety of crustal magma types. *Earth Planet. Sci. Lett.* **64**, 295-304.

Weaver B.L., Tarney J. and Windley B. (1981) Geochemistry and petrogenesis of the Fiskenæsset anorthosite complex, southern West Greenland: nature of the parent magma. *Geochim. Cosmochim. Acta*. **45**, 711 – 725.

Weaver B.L., Tarney J., Windley B. and Leake B.E. (1982) Geochemistry and petrogenesis of Archean metavolcanic amphibolites from Fiskenæsset, S.W. Greenland. *Geochim. Cosmochim. Acta*, **46**, 2203 – 2215.

Willigers B.J.A., Baker J.A., Krogstad E.J. and Peate D.W. (2002) Precise and accurate in situ Pb-Pb dating of apatite, monazite, and sphene by laser ablation multiple-collector ICP-MS. *Geochim. Cosmochim. Acta*, **66**, 1051 – 1066.

Windley B.F., Herd R.K. and Bowden A.A. (1973) The Fiskenaesset complex, west Greenland. Part I: A preliminary study of the stratigraphy, petrology, and whole rock chemistry from Qeqertarssuatsiaq. *Gronl. Geol. Unders. Bull.*. No. 106, 54p.

Wood J., Dekker J., Jansen J.G., Keay J.P. and Panagapko D. (1980) Mine Centre area geological map with marginal notes. *Ontario Ministry of Natural Resources, Ontario Geol. Survey Preliminary maps* 2201 and 2202.

Zeh A., Gerdes A., Barton Jr J. and Klemd R. (2010) U-Th-Pb and Lu-Hf systematics of zircon from TTG's, leucosomes, meta-anorthosites and quartzites of the Limpopo Belt (South Africa): Constraints for the formation, recycling and metamorphism of Palaeoarchaean crust. *Precam. Res.* **179**, 50 – 68.

Table 1 - 1. Compilation of Sm - Nd, Pb - Pb, U - Pb and Lu - Hf data for Archean Anorthosites

Location	Isotope System	Samples[1]	Age Information	Source Information	Interpretation	Reference
Fiskenæsset Anorthosite complex, southwest Greenland						
	Pb - Pb	WR: anorthosite (5), gneiss (1)	2810 ± 70 Ma (2s)		regional granulite facies metamorphism	Black et al., 1973
	Pb - Pb	WR: leucogabbro (1) MS: plag, hbld	~2800 Ma	μ ~ 8	regional granulite facies metamorphism	Gancarz, 1976
	Pb - Pb	WR: anorthosite (20), leucogabbro (6) gabbro (4), ultramafic rock (6)	2945 ± 36 Ma (MSWD = 44)		crystallization age	Polat et al., 2010
	Sm - Nd	WR: leucogabbro (1), anorthosite (1), gabbro (1), ultramafic rock (1) MS: plag, mafic matrix	2.86 ± 0.05 Ga (MSWD = 2.5)	ε_{Nd}: + 2.9 ± 0.4	crystallization age; derived from depleted mantle reservoir	Ashwal et al., 1989
	Sm - Nd	WR: anorthosite (20), leucogabbro (6) gabbro (4), ultramafic rock (6)	2973 ± 2.8 Ma (MSWD = 33)	ε_{Nd}: + 3.3 ± 0.7	crystallization age; depleted mantle source	Polat et al., 2010
	U - Pb	zircon	2919 ± 7 Ma (2s) 2872 ± 5 Ma (2s) 2720 ± 28 Ma (2s)		crystallization age; metamorphic age; metamorphic age; max age ~ 2.95 (n = 2)	Keulen et al., 2010
Bad Vermillion Lake anorthosite complex, Superior Province, Canada						
	Sm - Nd	WR: anorthosite, gabbro, ultramafic rocks, associated mafic dikes MS	2747 ± 58 Ma	ε_{Nd}: + 2.0 ± 1.4	crystallization age; derived from depleted mantle reservoir	Ashwal et al., 1985
Sittampundi anorthosite complex, Dharwar craton, India						
	Sm - Nd	WR: anorthosite, gabbro MS: plag, hbld	2936 ± 60 Ma (2s) (MSWD = 5.5)	ε_{Nd}: + 1.85 ± 0.16	emplacement ~ 3000 Ma; derived from depleted mantle source	Bhaskar Rao et al., 1996
Bhavani anorthosite complex, Dharwar craton, India						
	Sm - Nd	WR: anorthosite, gabbro	2898 ± 52 Ma (2s) (MSWD = 0.18)	ε_{Nd}: + 2.18 ± 0.14	emplacement ~ 3000 Ma; derived from depleted mantle source	Bhaskar Rao et al., 1996
Holenarsipur anorthosite, Dharwar craton, India						
	Sm - Nd	WR: anorthsite, hornblendite, ultramafic rock	3285 ± 170 Ma (2s) (MSWD = 0.53)	ε_{Nd}: + 0.87 ± 0.78	crystallization age; derived derived from chondritic to marginally depleted source	Bhaskar Rao et al., 2000
Manfred Complex, Yilgarn craton, Western Australia						
	Pb - Pb	WR MS	3639 ± 146 Ma (2s)	μ = 10.2 ± 0.4	crystallization age, mantle source assimilated large amounts of old radiogenic crust	Fletcher et al., 1988
	Sm - Nd	WR MS	3680 + 70 Ma (2s) (MSWD = 2)	ε_{Nd}: − 0.2 ± 0.7	chondritic source contaminated with old evolved crust	Fletcher et al., 1988
	U - Pb	zircon	3730 + 6 Ma (2s)		crystallization age	Kinney et al., 1988
Messina Layered Intrusion, Limpopo Belt, South Africa						
	Pb - Pb	MS: plag		hi μ	assimilation of radiogenic crust prior to crystallization	Barton, 1996
	Sm - Nd	WR: anorthosite		ε_{Nd}: − 12 to + 1.98	depleted mantle and old crust mixing	Barton, 1996
	Pb - Pb	WR: ?	3270 +105/- 112 Ma		min. emplacement age	Barton, 1983
	U - Pb	zircon	3344 ± 3.6 Ma		crystallization age	Mouri et al., 2009

	(anorthosite)				
U - Pb	zircon (anorthosite)	3358 ± 14 Ma 3311 ± 24 Ma		crystallization age crystallization age	Zeh et al., 2010
Lu - Hf	zircon (anorthosite)		ε_{Hf}: + 1.4 ± 1.8 ε_{Hf}: + 0.1 ± 1.9	mantle-derived melt enriched by crustal contamination	Zeh et al., 2010

[1] WR - whole rock sample; MS - mineral separate; plag - plagioclase feldspar; hbld - hornblende; (n) - number of samples analyzed

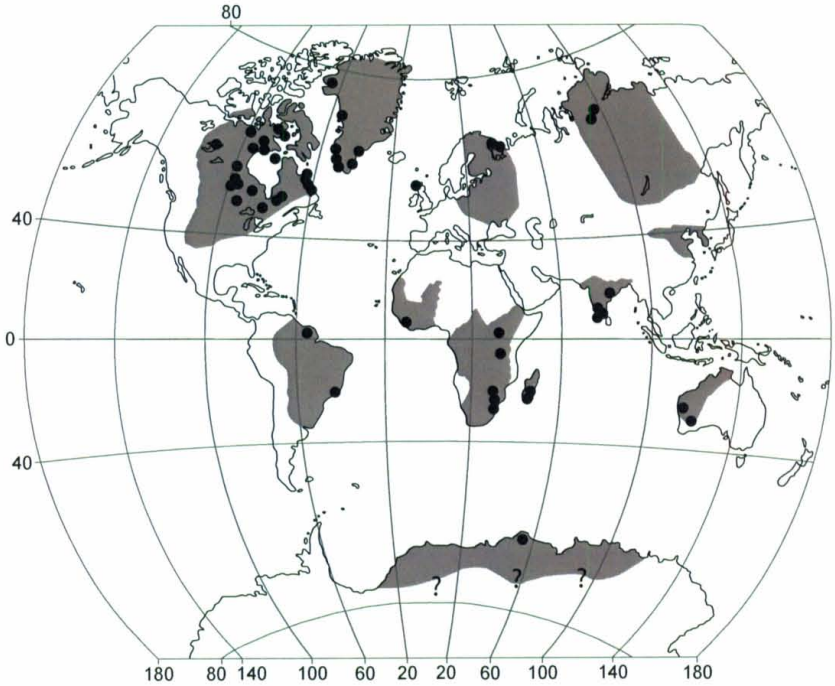

Figure 1-1: World map showing locations of Archean cratons (shaded regions) and the locations of documented Archean anorthosites (black dots). Modified from Ashwal and Myers (1994).

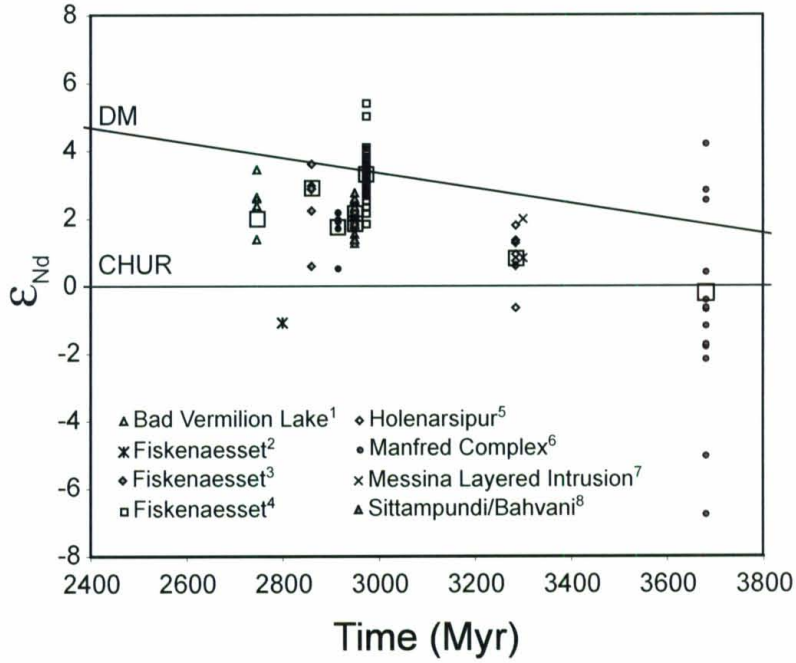

Figure 1-2: Compilation of Sm-Nd data from Archean anorthosite complexes. Large, open symbols represent the average Epsilon Nd for the respective anorthosite complex. ([1] Ashwal et al., 1985; [2] DePaolo and Wasserburg, 1979; [3] Ashwal et al., 1989; [4] Polat et al., 2010; [5] Bhaskar Rao et al., 2000; [6] Fletcher et al., 1988; [7] Barton, 1996; [8] Bhaskar Rao et al., 1996).

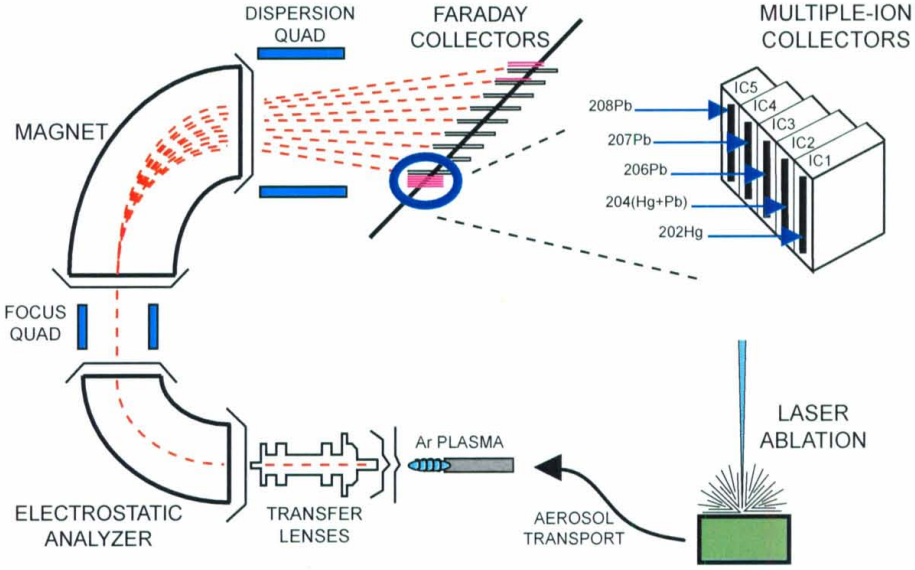

Figure 1-3: Generalized illustration of the Thermo Scientific NEPTUNE multi-collector inductively coupled plasma mass spectrometer with multiple ion counters installed within the cup configuration.

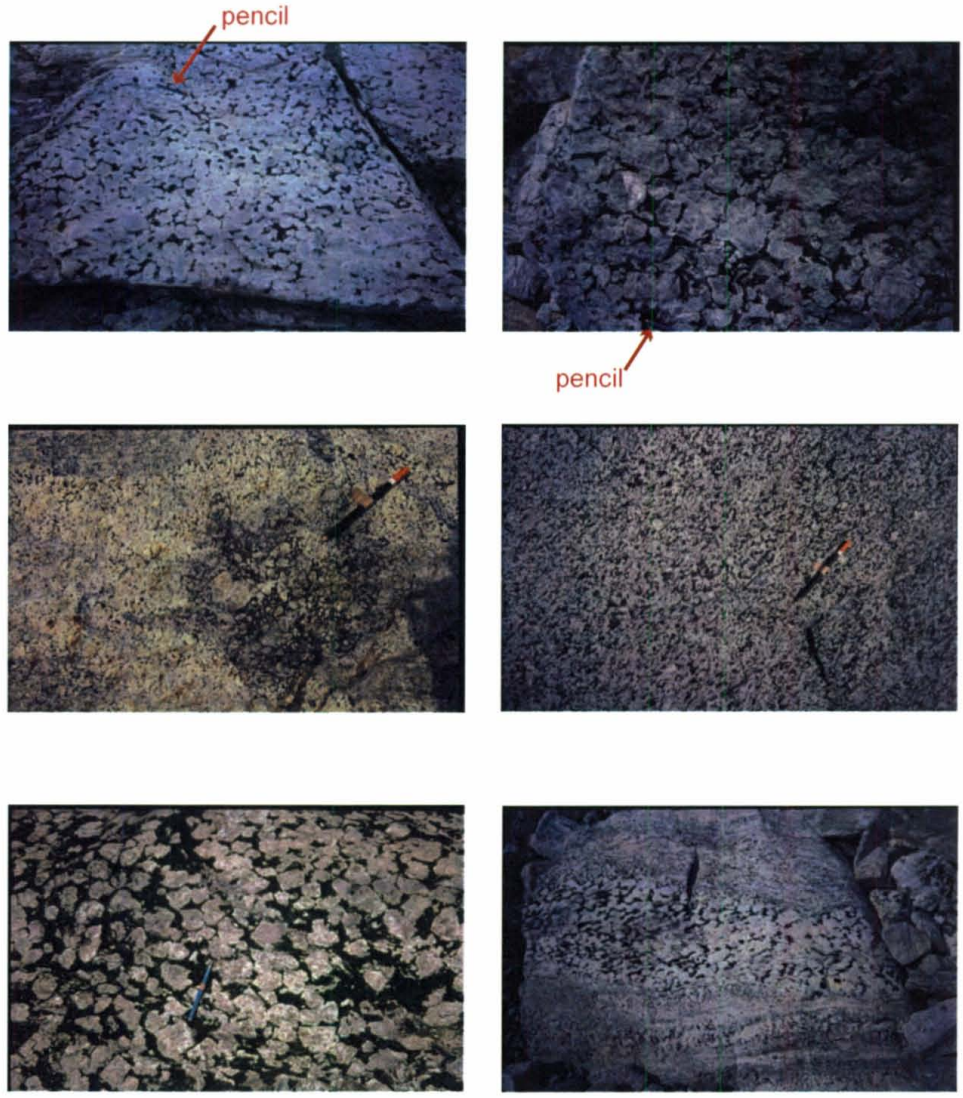

Figure 1-4: Examples of typical Archean megacrystic anorthosite from Fiskenæsset and Nunataarsuk consisting of euhedral to subhedral, calcic plagioclase crystals surrounded by a mafic matrix. Pencil for scale in all photos. (photos from J.S. Myers).

Figure 1-5: Rafts of dark-colored amphibolite country rock within the white-colored anorthosite unit at Fiskenæsset. Man in center of photo for scale (photo from J.S. Myers).

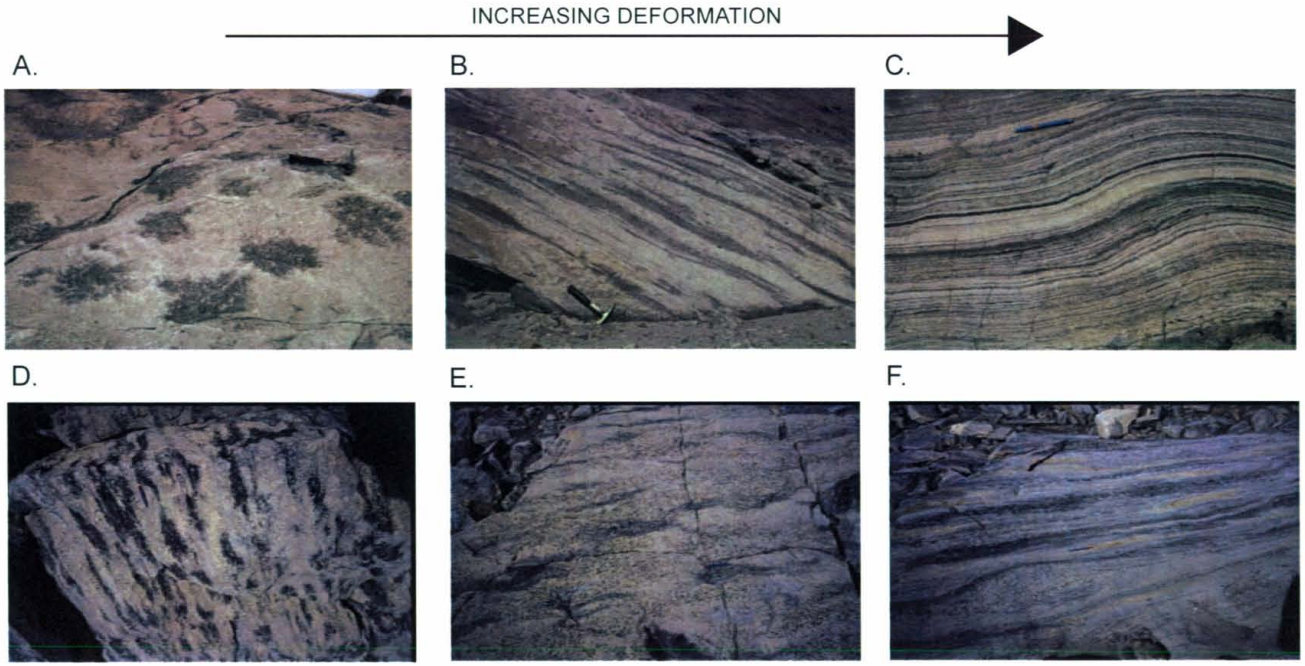

Figure 1-6 Examples of the range of deformation preserved within the anorthosite unit at Majorqap Qava, Fiskenæsset (A-C) and within the upper anorthosite-leucogabbro unit, Nunataarsuk (D-F). (A) Typical, best-preserved anorthosite unit containing undeformed, slightly-recrystallized patches of leucogabbro (dark patches). (B) Recrystallized, deformed anorthosite with schlieren of leucogabbro. (C) Recrystallized, deformed anorthosite with leucogabbro streaked out to form a tectonic banding. (D) Sheared pyroxene oikocryst and plagioclase chadacrysts. (E) Preserved, diffuse layering of mafic material to plagioclase dominated layers within leucocratic leucogabbro. (F) Extremely tectonized leucogabbro with flat, sheared layers of leucogabbro and mafic material. Hammer for scale in A and B. Pencil for scale in C, D, E and F (photos from John Myers).

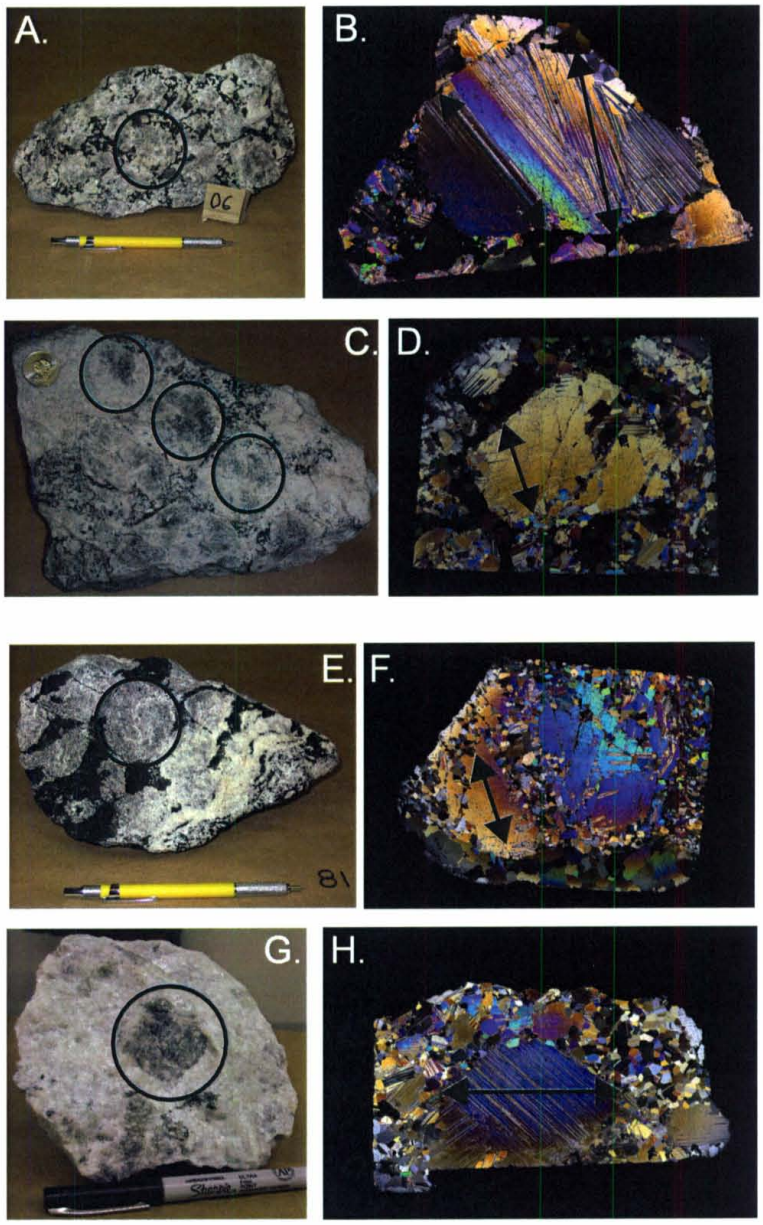

Figure 1-7: Representative leucogabbro (A-F) and anorthosite (G and **H**) samples from Fiskenæsset (C and D, G and **H**) and Nunataarsuk (A and B, E and F). B, D, F, and **H** are representative of the areas circled in A, C, E and G (images B, D, F, and **H** produced using a flat-bed scanner in 'film' mode and two pieces of polarizing film). Arrows in B, D, F, and **H** are typical transects across a single plagioclase megacryst used for in-situ analyses. The length of each transect in B and **H** is ~ 1 cm. The length of each transect in D and F is ~ 0.7 cm.

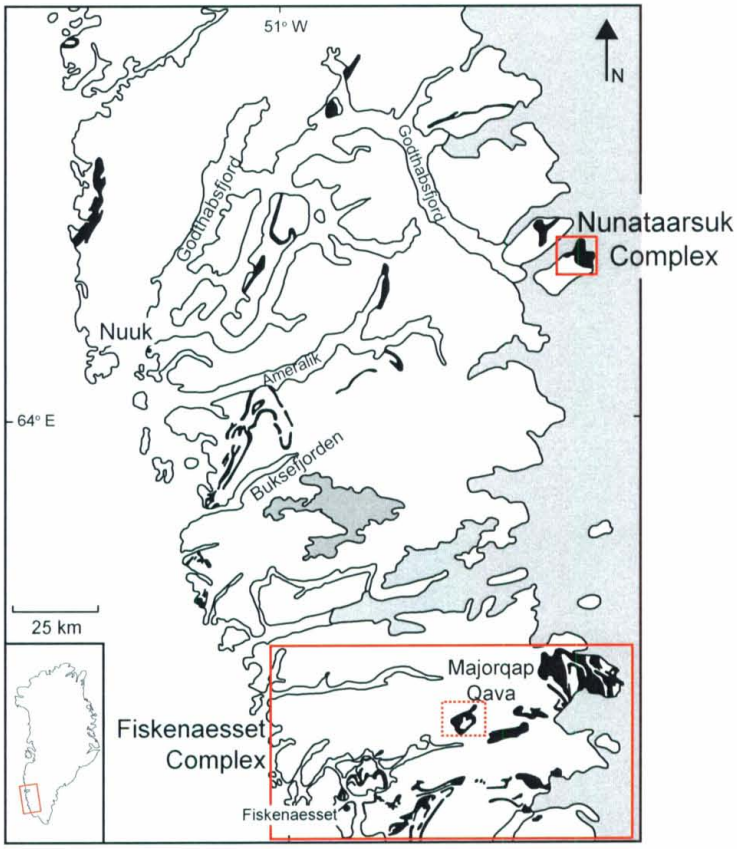

Figure 1-8: General map of southern West Greenland with Archean anorthosite complexes in black. Thick boxes surround the Fiskenæsset and Nunataarsuk regions. The Fiskenæset samples were all from the Majorqap Qava area, dashed box (Adapted from Owens and Dymek, 1997).

Chapter 2: Improved in situ measurements of lead isotopes in silicate glasses by LA-MC-ICPMS using multiple ion counters

Abstract

A new technique that improves the spatial resolution and quantification limits of the measurement of lead isotope ratios in silicate glasses with < 15 ppm total Pb by LA-MC-ICPMS is presented. The new method provides the capability of making quantitative, in-situ lead isotope measurements on tiny objects of geologic interest such as mineral growth bands, melt inclusions, and accessory minerals, even where they are lead poor. The method allows for the concurrent, static measurement of ^{204}Pb, ^{206}Pb, ^{207}Pb, ^{208}Pb along with ^{202}Hg in five Channeltron ion counters. Standard-sample-standard bracketing using USGS BCR2-G as the calibrant is used to correct for instrumental mass bias. Accuracy and precision of the method was evaluated by replicate analyses of various MPI-DING reference glasses with low lead concentrations (~1 – 11 ppm) and well-determined isotopic ratios. Spot sizes for in situ analyses were as small as 40 – 69 μm, providing better spatial resolution than previous LA-MC-ICPMS results reporting ^{204}Pb. Measured lead isotope ratios for the MPI-DING reference glasses T1-G (11.6 ppm total Pb) and ATHO-G (5.67 ppm total Pb) agree within 0.10% and 0.15% respectively of the preferred values using 40 μm spots. For MPI-DING KL2-G (2.07 ppm total Pb) and ML3B-G (1.38 ppm total Pb) measured ^{206}Pb/^{204}Pb, ^{207}Pb/^{204}Pb and ^{208}Pb/^{204}Pb agree within 0.75% of the accepted values with typical precisions of < 0.85% (RSD) using 69 μm spots; measured ^{207}Pb/^{206}Pb and ^{208}Pb/^{206}Pb are within 0.45% of preferred values with

precisions of < 0.25% (RSD). These results demonstrate improvement over previous LA-MC-ICPMS data in terms of both quantification limits and spatial resolution, while retaining similar levels of accuracy and precision.

2.1 INTRODUCTION

In situ lead isotopic measurements by laser-ablation multi-collector inductively coupled plasma mass spectrometry (LA-MC-ICPMS) have the potential to document isotopic variations in tiny objects of geologic interest such as mineral growth bands, melt inclusions, and accessory minerals (*e.g.* Mathez and Waight, 2003; Horstwood et al., 2003; Paul et al., 2005) on the scale of tens of microns. Lead isotope ratios are particularly useful for a variety of applications including Pb-Pb and U-Pb accessory mineral geochronology (*e.g.* Willigers et al., 2002; Simonetti et al., 2006), provenance investigations (*e.g.* Baker et al., 2006; Tyrrell et al., 2006), and petrogenetic interpretations of melt inclusions (*e.g.* Paul et al., 2005). A limiting factor for further development of in situ lead isotope analysis by LA-MC-ICPMS is sensitivity, both for reducing the sampling scale in lead "rich" (> 50 ppm) materials such as alkali feldspars and for extending the technique to lead-poor (< 50 ppm) materials such as plagioclase and melt inclusions, while retaining acceptable levels of analytical precision and accuracy. Another complication is proper procedures to correct for instrumental mass bias. Unlike other isotopic systems such as Hf and Sr, the Pb isotope system does not include an invariant isotope pair that can be used to make the mass bias correction internally for each sample analyzed. Alternative options such as aspirating a thallium tracer solution during laser analysis to monitor the lead fractionation (*e.g.* Horn et al.,

2000; Kosler et al., 2002) or external corrections based on the measured lead isotope ratios of silicate glass reference materials (*e.g.* Willigers et al., 2002; Paul et al., 2005) must be employed instead. With these latter approaches, however, the potential for mass bias variations as a function of matrix composition must be evaluated carefully.

In most previous LA-MC-ICPMS studies involving lead isotopes, the total lead concentration of the material of interest has been generally greater than ~80 ppm Pb (*e.g.* Horstwood et al., 2003; Mathez and Waight, 2003). As the total lead concentration of a material decreases, or as the radiogenic lead component increases, the ability to measure lead isotope ratios involving the minor ^{204}Pb isotope precisely becomes progressively more difficult due to its low relative abundance (~1.4 % of all common lead) and an isobaric interference from ^{204}Hg. The interference from ^{204}Hg is potentially very significant for laser analyses where target materials contain more than ~10 ppm Hg, and even for materials with less Hg where lead concentrations are very low (< 5 ppm total Pb). While not all applications involving lead isotopes require ^{204}Pb analysis, the accurate and precise measurement of radiogenic lead relative to ^{204}Pb can be especially important in investigations using lead isotopes as tracers for provenance or petrogenetic histories and for U-Pb geochronology, and is thus likely to be a focus of analytical development for some time to come. For instance, Paul et al., (2005) recently presented a LA-MC-ICPMS method for in situ lead isotope analysis by the simultaneous measurement of ^{204}Pb in an ion counter and the lead isotopes of greater abundance in Faraday cups. Simonetti et al., (2005) presented a LA-MC-ICPMS method for in situ U-

Pb geochronology, which measures ^{207}Pb, ^{206}Pb, $^{204}(Hg + Pb)$, and aspirated ^{205}Tl and ^{203}Tl in ion counters, while both ^{238}U and ^{235}U are measured in Faraday collectors.

We have developed an analytical protocol for LA-MC-ICPMS that allows us to measure lead isotope ratios, including ratios relative to ^{204}Pb, for silicate glasses with total lead concentrations between ~1 to 11 ppm. Lead isotope analyses are determined by static measurement of all lead isotopes and ^{202}Hg in Channeltron ion counters. The ^{202}Hg measurement is used to correct the isobaric interference from ^{204}Hg on ^{204}Pb. The new method retains similar levels of accuracy and precision for lead isotope ratios when compared to previous LA-MC-ICPMS measurements of silicate glasses but at total lead levels as low as ~ 1 ppm using 69 to 99 μm spots. This allows the use of smaller laser spot sizes for analysis or the measurement of materials with lower lead concentration than previously possible.

2.2 EXPERIMENTAL

2.2.1 Samples and Instrumentation

The samples used in this study are geologic reference material (GRM) glasses made from natural silicate rocks: USGS BCR2-G and MPI-DING T1-G, ATHO-G, KL2-G, and ML3B-G. Each glass has a well-defined lead isotopic ratio and chemical composition, with total lead concentrations ranging from ~1 to 11 ppm (Jochum et al., 2000, 2005a, 2006a). Small separates of each silicate glass were mounted in 10 or 25 mm diameter epoxy resin mounts. Once the epoxy had cured, the mount was ground to a flat surface and polished using diamond abrasive, exposing a cross-section of each glass.

Prior to in situ analysis great care was given to eliminate any potential surface contamination of the samples from lead in the ambient environment. Each epoxy mount was cleaned in an ultrasonic bath for approximately 15 minutes with double-distilled water, deionized and purified (to 18 mega-ohm cm^{-1}) by a Milli-Q water system. The surface of each mount was then scrubbed with double-distilled ~8N HNO_3 followed by a Milli-Q H_2O rinse. The mount was left to dry in a positive-pressure air box prior to loading into the laser ablation sample cell.

In the ICPMS, clean torch parts and cones resulted in lower instrumental backgrounds on all the lead masses of interest and enhanced signal stability; therefore, the torch, injector, quartz shield, glass T-piece used to mix the He and Ar gases, sampler and skimmer cones were all cleaned prior to each analytical session. Torch parts and glassware were soaked in a ~0.5N HNO_3 bath and subsequently rinsed with double-distilled ~8N HNO_3 followed by a Milli-Q H_2O rinse. Residue from prior ablations was removed from both the sample and skimmer cones with a cotton-tipped applicator and each cone was rinsed with deionized H_2O prior to installation on the instrument.

All analyses were performed on a Finnigan Neptune double-focusing MC-ICPMS equipped with 8 multiple (Channeltron) ion counter devices (MICs). In order to measure the low total lead concentrations of the glasses used in our experiments, concurrent, static measurements of ^{208}Pb, ^{207}Pb, ^{206}Pb, ^{204}Pb, and ^{202}Hg in the glass GRMs were made in 5 ion counters mounted onto the low mass (L4) Faraday cup. The ion counters are in fixed positions, spaced specifically to collect the four lead and ^{202}Hg isotopes of this study. The noise levels on plateaus of analyte signals measured by the

MICs are much improved when compared to Faraday detectors when dealing with materials with low lead concentrations (Figure 2-1). Typical instrument operating conditions and collector assignments for the analyses of materials with low lead concentrations are listed in Tables 2-1 and 2-2. ^{235}U is monitored in an ion counter attached to a high mass Faraday cup. These data are not relevant to the study of known reference materials and are not presented here, but would be important in the study of materials where lead isotope ratios of minerals may have been modified by in-growth of radiogenic lead by the decay of U after crystallization. Gas flow, torch position, and lens focus potentials were all adjusted to achieve a typical sensitivity of 23,000 cps/ppm ^{208}Pb for in situ analyses of BCR2-G with a 40 μm spot (~11 ppm total Pb) as well as optimal peak shape and peak overlap. Signal intensities during in situ analysis were typically less than ~5 mV, or ~312,500 cps, in all ion counters (for BCR2-G with a 40 μm spot, ~230,000 cps ^{208}Pb was typical). Argon gas was run through an activated charcoal filter made by Frontier GeoSciences Inc. placed in the gas line to the ICP torch, in order to reduce contaminant mercury levels in the gas. The dry sorbent in the trap collects all vapor phase Hg in both the elemental and oxidized forms.

The dark noise and operation voltage for each ion counter were determined twice over the time period of method development. The typical dark noise measurement for a single ion counter did not exceed 0.0060 cps. A plateau calibration curve (cps vs. voltage) was constructed to determine the operation voltage for each ion counter using a PCL script within the NEPTUNE operating software. This procedure was done to ensure that the relative yield values between ion counters remained within 20 %. To construct

the calibration curve for an individual ion counter, a signal was focused on the ion counter and the operation voltage of the ion counter was increased in 30 V steps. The output signal of the ion counter for each step was recorded in counts per second. The operation voltage for each ion counter was determined by observing the voltage representative of the point on a plateau calibration curve where the change in signal intensity (cps) no longer significantly increases with a corresponding increase in the detector voltage. The operation voltage can be different for each ion counter so a plateau calibration curve must be constructed for each individual ion counter. Operation voltages for the MICs during method development varied from 2000V to 2800V.

The MICs were cross-calibrated prior to each analytical period to determine the relative yield value for each ion counter referenced to IC1. The relative yield of each ion counter was determined in solution mode, using the ^{235}U signal from the NEPTUNE tune solution, in order to maximize signal stability and attain the best precision. A dynamic peak jumping method was used to determine the relative yield for the MICs. A reference signal of ~100,000 cps was sequentially placed in each of the 8 ion counters using an integration time of 4.194 seconds. This dynamic cycle was repeated 10 times. The relative yield value for each ion counter was then determined by normalizing the average of the measured signal intensities for each ion counter to the average response of IC1. If the relative yield values were not within 80% of IC1 the operation voltage on the ion counter was adjusted.

A GeoLas laser ablation system linked to the MC-ICPMS was used for the in situ analyses. This system includes a Lambda Physik ComPex Pro 110 ArF excimer laser

operating at a wavelength of 193nm and a pulse width of 20 ns. Typical operating conditions for the GeoLas system are included in Table 2-1. A laser fluence of approximately 5 J/cm^2 and a repetition rate of 10 Hz were used for all glass analyses. The spot size of the analyses ranged from 40 to 99 μm, depending on the total lead concentration. Samples were ablated in helium gas, which reduces sample re-deposition and elemental fractionation (Günther and Heinrich, 1999) while increasing sensitivity for 193 nm ablation (Eggins et al., 1998). Mercury was filtered from the helium using gold-coated glass wool placed on the helium gas line feeding the ablation cell.

2.2.2 Analytical Routine and Data Reduction

A standard – sample – standard bracketing approach was employed to correct for instrumental mass bias for two reasons: (1) the lead isotopic system does not have an invariant isotopic pair that can be used to monitor fractionation and (2) the configuration of ion counters on our instrument does not allow us to monitor mass bias relative to an aspirated thallium tracer solution of known isotopic composition using MICs in static mode. A Tl tracer solution collected in Faraday collectors could be employed but this produces additional errors associated with cross calibration of Faraday and ion counter cups. BCR2-G was chosen as the external calibrant because its lead concentration (~11 ppm total Pb) is sufficiently low to measure in the MICs without saturating the detectors, but high enough to provide good counting statistics on the lead analyte signals. Its concentration is also suitably matched to the lead concentrations of the MPI-DING glasses used in this study and the concentration range expected in plagioclase feldspars and melt inclusions. The following GeoREM preferred values (http://georem.mpch-

mainz.gwdg.de/; Jochum et al., 2000; Elburg et al., 2005; Paul et al., 2005) for BCR2-G were adopted: $^{206}Pb/^{204}Pb$ = 18.765 +/- 0.007 (1 SD); $^{207}Pb/^{204}Pb$ = 15.626 +/- 0.006(1 SD); $^{208}Pb/^{204}Pb$ = 38.73 +/- 0.02 (1 SD); $^{207}Pb/^{206}Pb$ = 0.833 +/- 0.001 (1 SD); $^{208}Pb/^{206}Pb$ = 2.066 +/- 0.001 (1 SD). The compositional homogeneity of the lead isotopic composition of BCR2-G is better than 0.1% for $^{206}Pb/^{204}Pb$, 0.02% for $^{207}Pb/^{204}Pb$, and 0.05% for $^{208}Pb/^{204}Pb$ based on bulk analyses of 100 milligram aliquots by solution-based MC-ICPMS (Elburg et al., 2005). These data do not prove that the lead isotopic composition of BCR2-G is homogeneous at the μg-scale sampled by the 40 – 99 μm spots used in this investigation but our in situ analyses of this glass suggest that this is the case to better than 1%: for 15 replicate analyses with a 49 μm spot, $^{207}Pb/^{206}Pb$, $^{206}Pb/^{204}Pb$, $^{207}Pb/^{204}Pb$, and $^{208}Pb/^{204}Pb$ vary by 0.075%, 0.47%, 0.45%, 0.36% (RSD), respectively.

The duration of each standard and sample analysis was ~ 90 seconds or 90 cycles using an integration time of ~1 sec/cycle. The first 40 seconds (cycles) were used to measure the background count rates with the laser off followed by 50 seconds of laser ablation monitoring the ^{202}Hg, ^{204}Pb, ^{206}Pb, ^{207}Pb, and ^{208}Pb isotopes. The lead isotope measurement of every three unknown samples were preceded and followed by three measurements of BCR2-G. On-line corrections for both yield and dark noise were performed using the NEPTUNE software prior to downloading the measured mass intensities into an Excel spreadsheet for off-line subtraction of mean gas background intensities from the time-resolved signal intensities for each isotope, ^{204}Hg interference

corrections on ^{204}Pb, lead isotope ratio calculations, and instrumental mass bias correction by standard – sample – standard bracketing.

Signal intensities were corrected for gas background and the ^{204}Hg interference on ^{204}Pb using two different off-line data reduction methods. For ^{206}Pb, ^{207}Pb, and ^{208}Pb, both methods subtract the average gas backgrounds, measured with the laser off, for each isotope from their respective measurements made in each cycle during laser ablation. The ^{204}Hg and ^{204}Pb background corrections are handled quite differently, however. In particular, in Method 1, ^{204}Hg/^{202}Hg is calculated from the relative natural abundances of the mercury isotopes and a mass bias factor determined from the observed ^{202}Hg/^{200}Hg, either (1) measured in the gas background at the start of a day's laser ablation session using a cup configuration in which ^{200}Hg is collected in IC1 and ^{202}Hg in IC2, or (2) ^{204}Hg/^{202}Hg is assumed to be the natural ratio recommended by IUPAC (Rosman and Taylor, 1997). In Method 2, the ^{204}Hg/^{202}Hg of the gas background is determined from measurements of ^{202}Hg, ^{204}(Hg+Pb) and ^{208}Pb made with the laser off prior to each analysis. The advantages and disadvantages of the two methods are compared in light of the results for the MPI-DING glasses below.

In detail, Method 1 is very similar to the off-line 204-correction procedure presented in Horstwood et al. (2003) and Paul et al. (2005). The mean gas background measured just prior to ablation is subtracted from each of ^{202}Hg, ^{204}(Hg + Pb), ^{206}Pb, ^{207}Pb, ^{208}Pb signals measured during ablation. As noted by Paul et al. (2005), this background correction removes the ^{204}Pb and ^{204}Hg in the gas from the ^{204}(Hg + Pb) measurement: any residual ^{204}Hg derived from the sample itself or due to variation in the

background is typically less than a few percent of the total measured 204-mass. To correct for this small, residual isobaric mercury interference on the measured 204-mass, and calculate the ^{204}Pb in the sample, the residual ^{204}Hg is calculated from the natural $^{204}Hg/^{202}Hg$ (~ 0.2301; IUPAC) and the background-corrected ^{202}Hg measurement in the sample. A mass bias correction may be applied to the natural $^{204}Hg/^{202}Hg$ using the exponential law and a mass bias factor (β; Albarede et al., 2004) derived from measurements of the $^{202}Hg/^{200}Hg$ in the gas background made prior to a day's session of analyses. The $^{206}Pb/^{204}Pb$, $^{207}Pb/^{204}Pb$, $^{208}Pb/^{204}Pb$, $^{207}Pb/^{206}Pb$, and $^{208}Pb/^{206}Pb$ are calculated for each measurement and a 2-sigma outlier rejection is performed prior to averaging the lead isotopic ratios.

Several attempts were made to measure the $^{202}Hg/^{200}Hg$ in the ion counters in order to use Method 1. However, the measured $^{202}Hg/^{200}Hg$ was unrealistically high compared to the natural $^{202}Hg/^{200}Hg$ for reasons that are not clear. Thus we could not calculate a mass bias factor for the $^{204}Hg/^{202}Hg$. Simonetti et al. (2005) noted that their measured $^{204}Hg/^{202}Hg$ in the gas background and during ablation was lower than the accepted, natural value. Combining these two observations suggests a possible isobaric interference on the ^{202}Hg that would lower the measured $^{204}Hg/^{202}Hg$ while increasing the measured $^{202}Hg/^{200}Hg$. Paul et al. (2005) noted that the correction of ^{204}Hg on ^{204}Pb, after gas background subtraction, is small for silicate materials, which have low Hg/Pb ratios, and so errors on the measurement of the mass bias factor for $^{204}Hg/^{202}Hg$ do not produce significant errors on the derived ^{204}Pb determinations. Therefore, our Method 1 results for lead isotope ratios measured on silicate glasses assume no mass bias on the calculated

$^{204}Hg/^{202}Hg$. In order to circumvent the problems associated with measuring the $^{202}Hg/^{200}Hg$ we developed a new data reduction procedure, Method 2, to correct for the isobaric interference of ^{204}Hg on ^{204}Pb.

Method 2 proceeds as follows: for each gas background measurement cycle, ^{204}Pb is calculated from the measured ^{208}Pb and $^{208}Pb/^{204}Pb$, assuming that the actual isotopic composition of lead in the gas is given by the $^{208}Pb/^{204}Pb$ for modern lead ($^{208}Pb/^{204}Pb$ = 38.63 +/- 0.98; Stacey and Kramers, 1975). The ^{204}Hg in the gas is then determined by subtraction of the calculated ^{204}Pb from the measured $^{204}(Hg + Pb)$, and a calculated $^{204}Hg/^{202}Hg$ in the gas is derived using the measured ^{202}Hg in the gas. With both ^{204}Pb and $^{204}Hg/^{202}Hg$ in the gas now established, the ^{204}Pb for each laser ablation measurement cycle is determined by subtracting ^{204}Hg from the measured $^{204}(Hg + Pb)$ using the measured ^{202}Hg during laser ablation and the average $^{204}Hg/^{202}Hg$ for the gas background. The resulting ^{204}Pb is then background corrected using the average ^{204}Pb calculated for the gas background. Lead isotope ratio calculations and outlier rejection procedures are performed as in Method 1.

The lead isotopic ratios calculated by both Methods 1 and 2 are corrected for instrumental mass bias and detector drift using a standard – sample – standard bracketing approach (Albarede et al.,2004). The lead isotope ratios determined for the set of three BCR2-G standards run before and after each set of 3 unknowns are averaged together. The lead isotope ratios for the unknowns are linearly interpolated, anchored by the average value of the three standards.

2.3 RESULTS AND DISCUSSION

Table 2-3 presents the mean lead isotope ratios for the MPI-DING reference glasses analyzed over five analytical sessions. Lead isotope ratios calculated by both Method 1 and Method 2 are listed separately. Results for every Pb isotope ratio measurement are listed in Tables S2-1, S2-2, S2-3 and S2-4 at the end of this chapter. Individual analyses are plotted in Figure 2-2.

In order to demonstrate the improved spatial resolution possible with the MIC collection procedure while maintaining similar levels of precision when compared to previous methods, spot sizes of only 40 and 49 μm were used for the two glasses with higher lead abundances, T1G and ATHO-G (11.6 ppm Pb, n = 11, and 5.67 ppm Pb, n = 16, respectively; Jochum et al., 2000; 2005a; 2006a). This is significantly smaller than the spot size of 200 μm used by Mathez and Waight (2003) with a Faraday-only collection procedure, and 93 μm used by Paul et al. (2005) with a combined Faraday-IC collection array. Even with the small spot, mean values for lead isotope ratios involving ^{204}Pb for T1G calculated by both Method 1 and Method 2 are all within 0.10% of the preferred values (Jochum et al., 2006a) with external precisions of less than 0.5% (RSD). The measured lead isotope ratios for ATHO-G are highly variable (+/- 2.4%), perhaps reflecting intrinsic heterogeneity in the glass at this sampling scale (49 μm) or possible matrix effects due to compositional differences between ATHO-G (rhyolitic bulk composition) and the calibration standard BCR2-G (basaltic bulk composition); yet the average values for all lead isotope ratios are all within 0.30% of the preferred values

(Jochum et al., 2006a) for Method 1, and within 0.15% of the preferred values (Jochum et al., 2006a) for Method 2.

Analyses of the two MPI-DING glasses with lower lead contents, KL2-G and ML3B-G (2.07 ppm Pb, n = 21, and 1.38 ppm Pb, n = 21, respectively; Jochum et al., 2000, 2005a, 2006a) were made with spots sizes of 69 and 99 μm in order to compare our results with previous LA-MC-ICPMS results at similar levels of spatial resolution. Using a 99 μm spot, lead isotope ratios involving ^{204}Pb for KL2-G calculated by both Method 1 and Method 2 are excellent, with all mean ratios within 0.20% of the preferred values (Jochum et al., 2006a) and external precisions of less than 0.5% (RSD). With the 69 μm spot, accuracy is still ~ 0.3% or better, although the precision degrades to almost 1.5% for Method 1 and almost 1% for Method 2. For 99-μm spot analyses of ML3B-G, lead isotope ratios involving ^{204}Pb give mean values that are within 0.7% and 0.4% of the preferred values (Jochum et al., 2006a) using Methods 1 and 2, respectively. Precisions are better than 1% (RSD) for both methods. Using a 69 μm spot, the accuracy of the mean ratios degrades to 1.6% for Method 1 and 0.7% for Method 2. Precision for Method 1 approaches 1.5% (RSD) but remains at ~1% (RSD) for Method 2.

For all spot sizes in all glasses, measurements of ^{207,208}Pb/^{206}Pb are as accurate and precise as the ^{206,207,208}Pb/^{204}Pb, and often much more so, attesting to the error associated with measurement of ^{204}Pb. The difference is most marked where the lead content of the glass is very low. For instance, in ML3B-G, using a 69 μm spot, ^{207,208}Pb/^{206}Pb measurements are accurate and precise to ~0.25% (RSD) or better.

2.3.1 Data Reduction Methods

Method 1 and Method 2 provide different approaches to correct for the isobaric interference of ^{204}Hg on ^{204}Pb. The fundamental difference between the two methods being Method 1 requires the $^{202}Hg/^{200}Hg$ to be independently measured and/or assumed constant throughout the analytical session. There is general agreement between the lead isotope ratios calculated by Method 1 and Method 2 (Fig. 2-2), especially between the two glasses with higher lead concentrations, yet we prefer to use Method 2 to calculate lead isotope ratios using the MICs because it eliminates the need to directly measure, or assume, the $^{202}Hg/^{200}Hg$. Also, Method 2 can be applied to materials with a range of Hg/Pb ratios as demonstrated below.

As previously stated, Paul et al. (2005) noted the ^{204}Hg derived from the silicate glass is generally only a very small percentage (~1 %) of the total 204 signal during ablation, making minor variations on the measurement of the $^{202}Hg/^{200}Hg$ and the mass bias factor calculated from this measurement insignificant in relation to the magnitude of the correction being made. The typical average measured $^{204}Hg/^{204}Pb$ intensities for all glasses analyzed in this study are less than 0.5. Figure 2-3 demonstrates that at $^{204}Hg/^{204}Pb$ intensities similar to those of the silicate glasses used in this study, variations in the mass bias factor (β) calculated from the $^{202}Hg/^{200}Hg$ have little effect on the accuracy of the final lead isotope ratio calculation. Method 1 begins to break down as the $^{204}Hg/^{204}Pb$ intensities from the sample increases and the ^{204}Hg interference correction on the 204-mass during ablation becomes significant. For matrices with $^{204}Hg/^{204}Pb$ intensities greater than ~2, variation of the $^{202}Hg/^{200}Hg$ mass bias factor can decrease the

accuracy of lead isotope ratios calculated using Method 1 beyond acceptable limits, particularly where the variation of the mass bias factor (β) exceeds +/- 0.5 units. In this study, for instance, the within run fluctuation of the mass bias factor calculated for the measured $^{208}Pb/^{206}Pb$ of BCR2-G is +/- 0.8 units. While the precise determination of the $^{202}Hg/^{200}Hg$ and the subsequent variation of the Hg-mass bias correction is not an issue for most silicates with typically low Hg/Pb ratios, this correction could become quite large for other geologic matrices such as sulfide minerals, which commonly have higher Hg/Pb ratios. For these reasons we favor using Method 2 for determining lead isotope ratios from LA-MC-ICPMS data.

2.3.2 Analytical Uncertainties

The analytical uncertainty of the all ion counter method to measure lead isotope ratios is dependant on many factors including the yield calibration of the MICs; detector linearity; the dark noise measurement for the MICs; the assumption that the lead isotope ratios in the gas are representative of the Stacey and Kramers (1975) estimate of modern lead; the homogeneity of the geologic reference material used for external normalization; and any within-run matrix effects or fluctuation of instrumental mass bias. The relative ion counter yield values varied from 0.1% to 0.5% over the duration of the ~10 minute yield calibration measurement. The uncertainty on the yield values for each ion counter can strongly influence the accuracy of the final lead isotope ratios, yet uncertainties associated with both the yield and the detector linearity are applied to all analysis, which are monitored by the bracketing process. Without an internal monitor, such as an aspirated Tl-tracer solution, any potential within-run matrix effects or instrumental mass

bias cannot be determined, emphasizing the importance of using a homogeneous, matrix-matched external calibrant.

The theoretical limits of precision are governed by Poisson counting statistics, detector dark noise and the uncertainty on the measurement of the blank. When determining the theoretical limits of precision for lead isotope measurements using MICs, the uncertainties associated with ion counter gain and the correction for the isobaric interference of ^{204}Hg on the 204-mass must also be considered. Figure 2-4 compares the calculated theoretical precision with the observed internal precision for the MPI-DING glasses analyzed in this study plotted as a function of total ^{208}Pb intensity. The theoretical precision will quickly degrade at total ^{208}Pb intensities of less than 0.001 volts. The minimum theoretical limits of precision for lead isotope ratios measured using MICs are approached at lower total ^{208}Pb count rates than for a Faraday-ion counter cup configurations (Paul et al., 2005) because the uncertainty budget of the MIC method is dominated by uncertainties in the ion counter gain, which are large only at very low ^{208}Pb count rates. Internal precision of measured lead isotope ratios for the MPI-DING glasses plot well above the theoretical curves. This reflects additional errors not included in the theoretical calculations, including matrix effects, spot-to-spot heterogeneity in the lead isotopic composition of the BCR2-G calibrant and fluctuations in mass bias factors over short time scales (*i.e.* between individual analyses).

2.3.3 Comparison With Other Investigations

It is difficult to compare the results of our lead isotope measurements of four MPI-DING reference glasses presented in this study to previous investigations due to

differences in instrumentation, analysis protocol, and ablation parameters. Using 5 MICs operating in static mode we were able to produce results with similar or improved precisions and accuracies to previous single-collector laser-ablation sector-field ICPMS (LA-SF-ICPMS; Jochum et al., 2005b; 2006b) and LA-MC-ICPMS (Paul et al., 2005) studies while improving the spatial resolution and quantification limits of these previous investigations. Smaller spot sizes (40 – 69 μm vs. 93 – 200 μm) than previously reported could be used for ATHO-G, KL2-G, and ML3B-G due to the high signal to noise ratio of the ion counters. The use of MICs to measure all lead isotopes allows us to measure both $^{206, 207, 208}Pb/^{204}Pb$ and $^{207,208}Pb/^{206}Pb$ for samples with low lead concentrations (< 10 ppm total Pb) or for samples where high spatial resolution is required. Using MICs to measure all lead isotopes allows us to use a reference material (BCR2-G), which has a lead concentration typical of the lead-poor materials being analyzed, to cross-calibrate detectors and as bracketing reference material to correct for instrumental mass bias. Standards with low lead concentrations can be used because it is not necessary to produce a signal of at least ~5mV (~310,000 cps) to be measured on a Faraday detector for Faraday-ion counter cross calibration, a common requirement of most MC-ICPMS lead isotope cup configurations used previously.

Figure 2-5 provides a comparison between the external precision of both $^{207}Pb/^{206}Pb$ and $^{208}Pb/^{204}Pb$ determined using Method 2 presented in the study with previous LA-MC-ICPMS and single-collector, LA-SF-ICPMS investigations. For each lead isotope ratio considered, the data are split into 2 categories: one for analysis using spot sizes between 40 and 50 μm, and the second for analysis using spot sizes between 90

and 120 μm. Measurements from studies using significantly larger spot sizes (>120 μm) are not considered in these comparison plots.

For lead isotope ratio measurements using spot sizes between 40 and 50 μm the external precision for our $^{207}Pb/^{206}Pb$ measurements for ATHO-G (5.67 ppm total Pb) T1G (11.6 ppm total Pb) is slightly higher, yet similar to, the single-collector LA-SF-ICPMS data of Jochum et al. (2005b) and Jochum et al. (2006b). However there is significant improvement in the reproducibility of the $^{208}Pb/^{204}Pb$ for ML3B-G and ATHO-G using the method presented in this study compared to previous single-collector LA-SF-ICPMS measurements for spot sizes between 40 and 50 μm. Our method also presents improvement in the external reproducibility of both $^{207}Pb/^{206}Pb$ and $^{208}Pb/^{204}Pb$ for both KL2-G (2.07 ppm total Pb) and ML3B-G (1.38 ppm Pb) for spot sizes ranging from 90 to 120 μm when compared to other LA-MC-ICPMS (Paul et al., 2005) and single-collector LA-SF-ICPMS (Jochum et al., 2005b, 2006b) methods.

2.4 CONCLUSION

The ability to measure in situ lead isotope ratios in materials with very low lead concentrations is a useful tool for accessory mineral geochronology, provenance investigations, and petrogenetic interpretations of melt inclusions. A new method to measure lead isotopes for materials of low lead concentrations (≤ 15 ppm) at the scale of tens of microns has been presented. In situ lead isotope measurements using an array of Channeltron ion counters produces results with similar or improved precisions and accuracies compared to mixed Faraday-ion counter multi-collector and single-collector, sector-field measurements of lead isotope ratios in silicate glasses from ~1 to ~11 ppm

total Pb using spot sizes from 40 to 69 μm. Because of the high signal to noise ratio of the Channeltrons compared to Faraday detectors, quantitative $^{20X}Pb/^{204}Pb$ and $^{20X}Pb/^{206}Pb$ can be measured in materials of very low lead concentrations (< 5 ppm) and at higher spatial resolution than previously presented while maintaining precisions and accuracies within acceptable limits. Precise and accurate lead isotope ratios can now be determined in situ for lead-poor minerals such as plagioclase, or for mineral growth bands or melt inclusions, which are more lead-rich but where higher spatial resolution is required.

2.5 REFERENCES

Albarede F., Telouk P., Blichert-Toft J., Boyet M., Agranier A. and Nelson B. (2004) Precise and accurate isotopic measurements using multiple-collector ICPMS. *Geochim. Cosmochim. Acta* **68**, 2725 – 2744.

Baker J., Stos S. and Waight T. (2006) Lead isotope analysis of archaeological metals by multiple-collector inductively coupled plasma mass spectrometry. *Archaeometry* **48**, 45 – 56.

Eggins S.M., Kinsley L.P.J. and Shelley J.M.G. (1998) Deposition and element fractionation processes during atmospheric pressure laser sampling for analysis by ICPMS. *Appl. Surf. Sci.* **129**, 278 – 286.

Elburg M., Vroon P., van der Wagt B. and Tchalikian A. (2005) Sr and Pb isotopic composition of five USGS glasses (BHVO-2G, BIR-1G, BCR-2G, TB-1G, NKT-1G) *Chem. Geol.* **223**, 196 – 207.

Gunther D. and Heinrich C.A. (1999) Enhanced sensitivity in laser ablation-ICP mass spectrometry using helium-argon mixtures as aerosol carrier. *J. Anal. At. Spectrom.* **14**, 1363 – 1368

Horn I., Rudnick R.L., McDonough W.F. (2000) Precise elemental and isotope ratio determination by simultaneous solution nebulization and laser ablation ICP-MS: application to U-Pb geochronology. *Chem. Geol.* **164**, 281 – 301.

Horstwood M.S.A., Foster G.L., Parrish R.R., Noble S.R. and Nowell G.M. (2003) Common-Pb corrected in situ U-Pb accessory mineral geochronology by LA-MC-ICP-MS. *J. Anal. Atom. Spectrom.* **18**, 837 – 846.

Jochum K.P., Dingwell D.B., Rocholl A., Stoll B., Hofmann A.W., Becker S., Besmehn A., Bessett D., Dietze H-J., Dulski P., Erzinger J., Hellebrand E., Hoppe P., Horn I., Janssens K., Jenner G.A., Klein M., McDonough W.F., Maetz M., Mezger K., Munker C., Nikogosian I.K., Pickhardt C., Raczek I., Rhede D., Seufert H.M., Simakin S.G., Sobolev A.V., Spettel B., Straub S., Vincze L., Wallianos A., Weckwerth G., Weyer S., Wolf D. and Zimmer M. (2000) The prepartion and preliminary characterization of eight geological MPI-DING reference glasses for in-situ microanalysis. *Geostand. Newsl.* **24**, 87 – 133.

Jochum K.P., Pfander J., Woodhead J.D., Willbold M., Stoll B., Herwig K., Amini M., Abouchami W. and Hofmann A.W. (2005a) MPI-DING glasses: New geological reference materials for in situ Pb isotope analysis. *Geochem. Geophys. Geosys.* **6**, Q10008.

Jochum K.P., Stoll B., Herwig K., Amini M., Abouchami W. and Hofmann A.W. (2005b) Lead isotope ratio measurements in geological glasses by laser ablation-sector field-ICP mass spectrometry (LA-SF-ICPMS). *Int. J. Mass Spectrom.* **242**, 281 – 289.

Jochum K.P, Stoll B., Herwig K., Willbold M., Hofmann A.W., Amini M., Aarburg S., Abouchami W., Hellerbrand E., Mocek B., Raczek I., Stracke A., Alard O., Bouman C., Becker S., Ducking M., Bratz H., Klemd R., deBruin D. Canil D., Cornell D., de Hoog C., Dalpe C., Danyushevsky L., Eisenhauer A., Gao Y., Snow J.E. Groschopf N., Gunther D., Latkoczy C., Gillong M., Hauri E.H., Hofer H.E., Lahaye Y., Horz K., Jacob D.E., Kasemann S.A., Kent A.J.R., Ludwig T., Zack T., Mason P.R.D., Meixner A., Rosner M., Misawa K., Nash B.P., Pfander J., Premo W.R., Sun W.D., Tiepolo M., Vannucci R., Vennemann T., Wayne D. and Woodhead J.D. (2006a) *Geochem. Geophys. Geosyst.*, 2006, **7**, DOI: 10.1029/2005GC001060.

Jochum K.P., Stoll B., Herwig K. and Willbold M. (2006b) Improvement of in situ Pb isotope analysis by LA-ICP-MS using a 193 nm Nd:YAG laser. *J. Anal. At. Spectrom.* **21**, 666 – 675.

Kosler J., Fonneland H., Sylvester P., Tubrett M. and Pederson R. (2002) U–Pb dating of detrital zircons for sediment provenance studies: a comparison of laser- ablation ICPMS and SIMS techniques. *ChemicalGeology*, **182**, 605–618.

Mathez E.A. and Waight T.E. (2003) Lead isotopic disequilibrium between sulfide and plagioclase in the Bushveld complex and the chemical evolution of large layered intrusions. *Geochim Cosmochim Acta* **67**, 1875 – 1888.

Paul B., Woodhead J.D. and Hergt J. (2005) Improved in situ isotope analysis of low Pb materials using LA-MC-ICP-MS with parallel ion counter and Faraday detection. *J. Analyt. Atom. Spectrom.* **20**, 1350 – 1357.

Rosman K.J.R. and Taylor P.D.P. (1997) Isotopic composition of the elements. *Pure Appl. Chem.* **70**, 217 – 236.

Simonetti A., Heaman L.M., Hartlaub R.P., Creaser R.A., MacHattie T.G. and Bohm C. (2005) U-Pb zircon dating by laser ablation-MC-ICP-MS using a new multiple ion counting Faraday collector array. *J. Anal. At. Spectrom.* **20**, 677 – 686.

Simonetti A., Heaman L.M., Chacko T. and Banerjee N.R. (2006) In situ petrographic thin section U-Pb dating of zircon, monazite, and titanite using laser ablation-MC-ICP-MS. *Int. J. Mass. Spectrom.* **253**, 87 – 97.

Stacey J.S. and Kramers J.D. (1975) Approximation of terrestrial lead isotope evolution by a two-stage model. *Earth Planet. Sci. Lett.* **26**, 207 – 221.

Tyrrell S., Haughton P.D.W., Daly J.S., Kokfelt T.F. and Gagnevin D. (2006) The use of the common Pb isotope composition of detrital K-feldspar grains as a provenance tool and its application to Upper Carboniferous palaeodrainage, Northern England. *J. Sed. Res.* **76**, 324 – 345.

Willigers B.J.A., Baker J.A., Krogstad E.J. and Peate D.W. (2002) Precise and accurate in situ Pb-Pb dating of apatite, monazite, and sphene by laser ablation multiple-collector ICP-MS. *Geochim. Cosmochim. Acta*, **66**, 1051 – 1066.

Table 2-1 Typical operating conditions for the Finnigan Neptune MC-ICP-MS and GeoLas laser ablation system

Finnigan Neptune MC-ICP-MS	
Operation power	1200 W
RF power	1200 W
HV	10 kV
Cool gas flow	16 l min^{-1}
Auxiliary gas flow	0.7 l min^{-1}
Ar make-up gas flow	0.9 l min^{-1}
Cones	Ni
GeoLas laser ablation system	
Lambda Physik Compex 110 Ar F excimer	193 nm
Laser fluence	~5 J cm^{-2}
Spot size	40 - 99 μm
Repetition rate	10 Hz
He carrier gas	1.2 l min^{-1}

Table 2-2 Finnigan Neptune collector assignments for Pb isotope analysis

Collector[a]	IC1	IC2	IC3	IC4	IC5	L4	L3	L2	L1	C	H1	H2	H3	IC6	H4	IC7	IC8
isotope	^{202}Hg	^{204}(Hg+Pb)	^{206}Pb	^{207}Pb	^{208}Pb					219.68				^{235}U			

[a] L4 to L1, C, and H1 to H4 are Faraday cups. IC1 to IC5 are ion counters fixed to Faraday cup L4. IC6 is an ion counter fixed to Faraday cup H3. IC7 and IC8 are ion counters fixed to Faraday cup H4.

Table 2-3 Lead isotope ratio values for samples measured in this study

		$^{206}Pb/^{204}Pb$	$^{207}Pb/^{204}Pb$	$^{208}Pb/^{204}Pb$	$^{207}Pb/^{206}Pb$	$^{208}Pb/^{206}Pb$
MP1-T1-G	**11.6 ± 1.5 µg g⁻¹ 1**	**18.728**	**15.679**	**38.973**	**0.83724**	**2.0810**
		+/- 0.004	**+/- 0.004**	**+/-0.008**	**+/- 0.00010**	**+/-0.0005**
Method 1	Mean	18.736	15.672	38.984	0.83668	2.08151
40 µm spot	S.D.	0.066	0.061	0.162	0.001	0.004
(*n* = 11)	Accuracy	0.04%	-0.04%	0.03%	-0.07%	0.02%
	2RSD	0.70%	0.78%	0.83%	0.22%	0.36%
Method 2	Mean	18.728	15.663	38.965	0.83661	2.08150
40 µm spot	S.D.	0.077	0.069	0.189	0.001	0.004
(*n* = 11)	Accuracy	0.00%	-0.10%	-0.02%	-0.08%	0.02%
	2RSD	0.82%	0.88%	0.97%	0.23%	0.37%
MP1-ATHO	**5.67 ± 0.62 µg g⁻¹**	**18.383**	**15.480**	**38.111**	**0.84204**	**2.0730**
		+/- 0.004	**+/- 0.004**	**+/- 0.003**	**+/- 0.00019**	**+/- 0.0006**
Method 1	Mean	18.367	15.444	38.058	0.84129	2.07833
40 µm spot	S.D.	0.193	0.153	0.363	0.001	0.003
(*n* = 16)	Accuracy	-0.09%	-0.23%	-0.14%	-0.09%	0.26%
	2RSD	2.10%	1.98%	1.91%	0.31%	0.31%
Method 2	Mean	18.409	15.482	38.148	0.84131	2.07345
40 µm spot	S.D.	0.218	0.175	0.417	0.002	0.007
(*n* = 16)	Accuracy	0.14%	0.01%	0.10%	-0.09%	0.02%
	2RSD	2.36%	2.27%	2.19%	0.44%	0.72%
MP1-KL2-G	**2.07 ± 0.10 µg g⁻¹**	**19.030**	**15.632**	**38.524**	**0.82146**	**2.0243**
		+/- 0.009	**+/- 0.004**	**+/- 0.015**	**+/- 0.00023**	**+/- 0.0004**
Method 1	Mean	19.053	15.633	38.581	0.82135	2.02745
69 µm spot	S.D.	0.269	0.196	0.500	0.001	0.004
(*n* = 21)	Accuracy	0.12%	0.01%	0.15%	-0.01%	0.16%
	2RSD	2.82%	2.51%	2.59%	0.34%	0.40%
Method 1	Mean	19.050	15.620	38.602	0.82037	2.02779
99 µm spot	S.D.	0.054	0.053	0.154	0.001	0.003
(n = 6)	Accuracy	0.10%	-0.08%	0.20%	-0.13%	0.17%
	2RSD	0.57%	0.68%	0.80%	0.18%	0.26%
Method 2	Mean	18.974	15.581	38.453	0.82136	2.02737
69 µm spot	S.D.	0.152	0.130	0.323	0.001	0.004
(*n* = 21)	Accuracy	-0.30%	-0.33%	-0.18%	-0.01%	0.15%
	2RSD	1.61%	1.67%	1.68%	0.35%	0.42%
Method 2	Mean	19.039	15.612	38.583	0.82038	2.02780
99 µm spot	S.D.	0.058	0.054	0.151	0.001	0.003
(n = 6)	Accuracy	0.05%	-0.13%	0.15%	-0.13%	0.17%
	2RSD	0.61%	0.69%	0.78%	0.17%	0.26%
MP1-ML3B-	**1.38 ± 0.07 µg g⁻¹**	**18.720**	**15.600**	**38.454**	**0.8334**	**2.0542**
		+/- 0.016	**+/- 0.014**	**+/- 0.043**	**+/- 0.0017**	**+/- 0.0006**
Method 1	Mean	18.521	15.368	37.934	0.82965	2.04804
69 µm spot	S.D.	0.253	0.210	0.514	0.001	0.005
(*n* = 21)	Accuracy	-1.07%	-1.49%	-1.59%	-0.45%	-0.30%
	2RSD	2.73%	2.73%	2.71%	0.34%	0.53%
Method 1	Mean	18.846	15.634	38.671	0.82981	2.05291
99 µm spot	S.D.	0.176	0.155	0.347	0.002	0.003
(*n* = 6)	Accuracy	0.67%	0.22%	0.33%	-0.43%	-0.06%
	2RSD	1.87%	1.99%	1.79%	0.42%	0.27%
Method 2	Mean	18.687	15.507	38.262	0.82966	2.04789
69 µm spot	S.D.	0.174	0.148	0.364	0.002	0.005
(*n* = 21)	Accuracy	-0.18%	-0.60%	-0.74%	-0.45%	-0.31%
	2RSD	1.86%	1.91%	1.90%	0.37%	0.53%
Method 2	Mean	18.788	15.591	38.559	0.82985	2.05273
99 µm spot	S.D.	0.165	0.159	0.362	0.002	0.003
(*n* = 6)	Accuracy	0.36%	-0.06%	0.04%	-0.43%	-0.07%
	2RSD	1.76%	2.04%	1.88%	0.45%	0.31%

[1] All values in bold are preferred reference values from Jochum et al. (2006a)

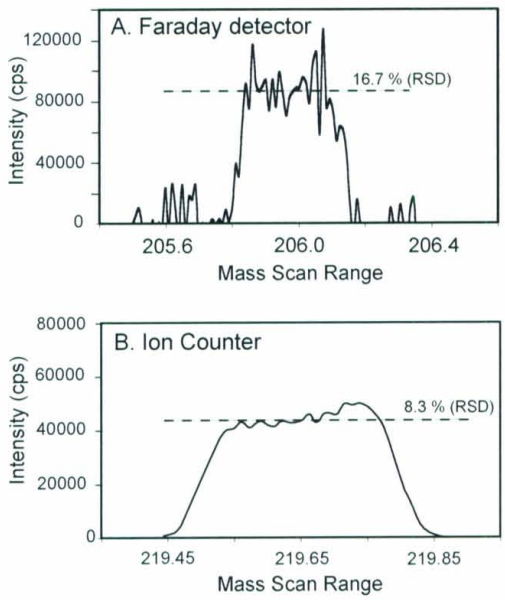

Figure 2 - 1: Peak shapes of ^{206}Pb from a SRM 981 standard solution of 0.5 ppm total Pb measured on a (A) Faraday detector and a (B) Channeltron ion counter. The x-axis corresponds to the mass range over which the peak was measured with the center value representing the axial mass of the collector array. The noise level for the plateau of the ^{206}Pb signal collected in the Faraday detector (16.7 % RSD, 1-sigma) is double that of the noise level for the plateau of the ^{206}Pb signal collected in the ion counter (8.3 % RSD, 1-sigma). A beam of equal intensity was measured in each detector, yet the scale is off-set by a factor of ~2 due to the detectors not being cross-calibrated prior to measurement.

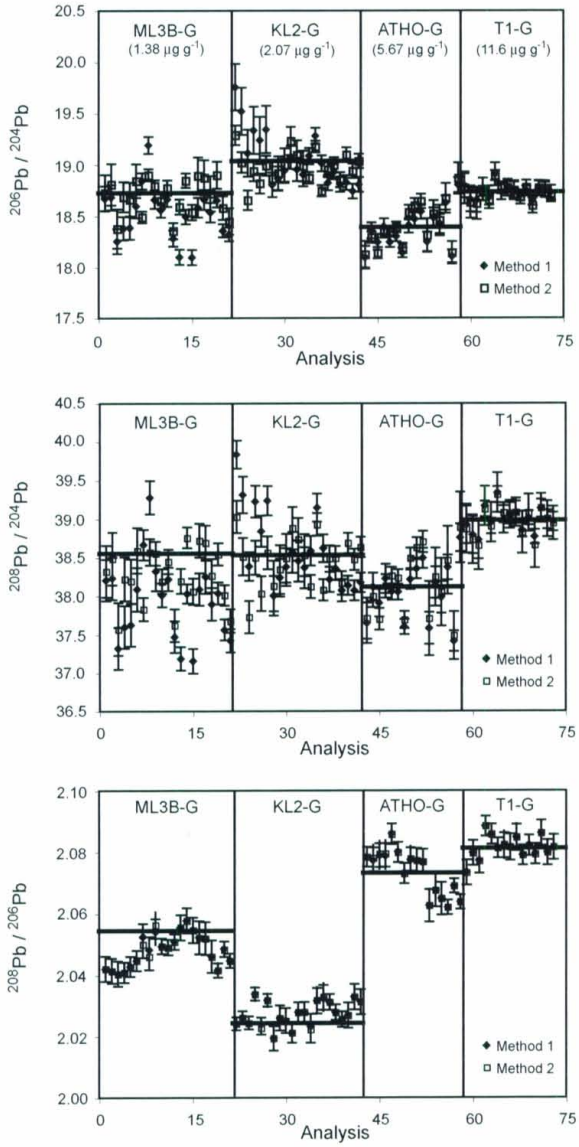

Figure 2-2: LA-MC-ICPMS analysis of lead isotope ratios in the four MPI-DING glasses used in the study, arranged from left to right in order of increasing lead concentration. Solid horizontal lines indicate the preferred lead isotope values (Jochum et al., 2006a) for each glass. Lead isotope ratios for each analysis are calculated using both Method 1 (filled diamonds) and Method 2 (open squares). There is general agreement between the Method 1 and 2 results and the preferred values for the glasses with higher lead concentrations (ATHO-G and T1-G) for the $^{206}Pb/^{204}Pb$, $^{208}Pb/^{204}Pb$, $^{208}Pb/^{206}Pb$. There is more scatter are larger discrepancies between the 2 methods for the 2 glasses with lower concentrations (ML3B-G and KL2-G) but, in general, Method 2 produces more accurate and precise results than Method 1.

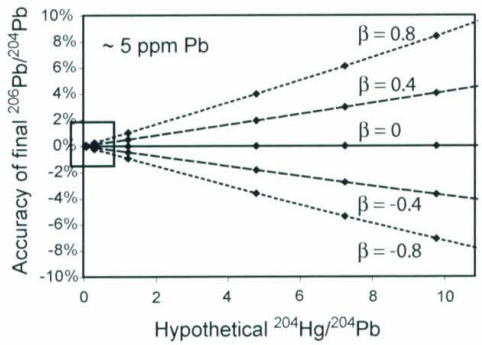

Figure 2-3: Plot of accuracy of the final $^{206}Pb/^{204}Pb$ as a function of hypothetical $^{204}Hg/^{204}Pb$ and various mass bias factors (B) for a material of approximately 5 ppm Pb. The box highlights the typical Hg/Pb ratios for silicate glasses used in our study, which is < 0.5.

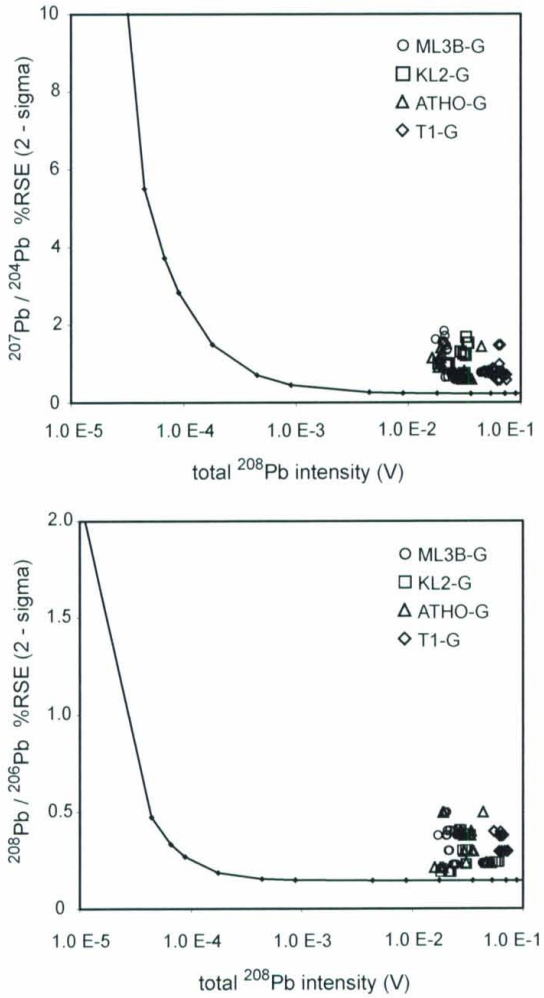

Figure 2-4: Theoretical limits of precision expressed as % RSE (2-sigma), for the measurement of lead isotope ratios using MICs are defined by the solid line. The observed internal precision of lead isotope ratio measurements for MPI-DING glasses of varying total lead concentrations presented in this study are also shown. Uncertainties due to counting statistics, dark noise, background subtraction, ion counter yield, and the ^{204}Hg correction on the 204-mass are all included in the calculation of the theoretical curves.

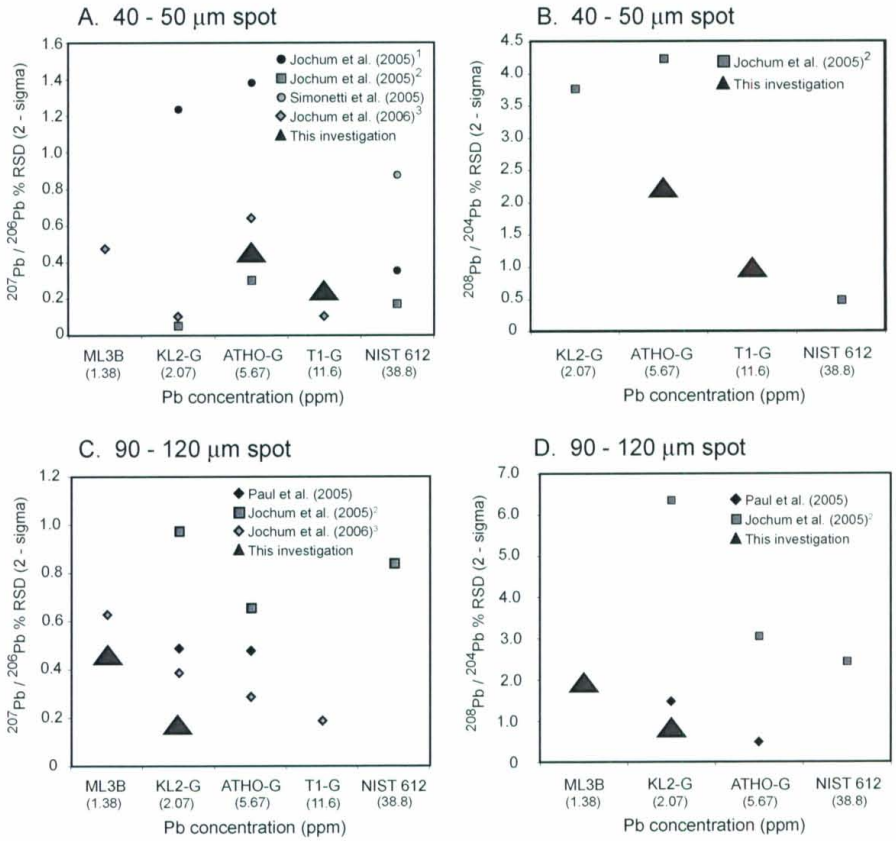

Figure 2-5: Comparison of the external precision of $^{207}Pb/^{206}Pb$ and $^{208}Pb/^{204}Pb$ as a function of spot size in this study and other LA-MC-ICPMS and single-collector LA-SF-ICPMS investigations. (A) and (B) compare analyses using spot sizes ranging from 40 to 50 μm, while (C) and (D) compare the reproducibility of measurements using spot sizes between 90 and 120 μm. [1]Measurements using Escan mode. [2]Measurements using combined Escan and Bscan modes. [3]Only 193nm data considered.

Table S2-1: Pb isotope ratio values[1] for T1-G

			$^{206}Pb/^{204}Pb$	SE (1σ)	$^{207}Pb/^{204}Pb$	SE (1σ)	$^{208}Pb/^{204}Pb$	SE (1σ)	$^{207}Pb/^{206}Pb$	SE (1σ)	$^{208}Pb/^{206}Pb$	SE (1σ)
Preferred Values[2]			**18.728**	**0.004**	**15.679**	**0.004**	**38.973**	**0.008**	**0.83724**	**0.00010**	**2.0810**	**0.0005**
Experiment		**Spot Size**										
de01a10	T1G-1	40	18.773	0.155	15.730	0.117	38.872	0.315	0.83870	0.001	2.07324	0.004
de01a11	T1G-2	40	18.634	0.158	15.576	0.120	38.734	0.316	0.83611	0.001	2.07967	0.004
de01a12	T1G-3	40	18.622	0.157	15.555	0.120	38.657	0.318	0.83584	0.001	2.07710	0.004
de01b16	T1G-4	40	18.739	0.050	15.658	0.050	39.126	0.102	0.83578	0.001	2.08842	0.003
de01b17	T1G-5	40	18.657	0.051	15.608	0.050	38.905	0.099	0.83663	0.001	2.08577	0.003
de01b18	T1G-6	40	18.894	0.051	15.821	0.050	39.313	0.106	0.83752	0.001	2.08135	0.003
de03a04	T1G-1	40	18.773	0.057	15.672	0.060	39.077	0.130	0.83540	0.001	2.08241	0.004
de03a05	T1G-2	40	18.774	0.081	15.686	0.074	39.068	0.137	0.83585	0.001	2.08164	0.004
de03a06	T1G-3	40	18.750	0.092	15.695	0.083	39.082	0.145	0.83718	0.001	2.08481	0.004
de03b04	T1G-4	40	18.683	0.068	15.635	0.058	38.826	0.270	0.83710	0.001	2.07897	0.003
de03b05	T1G-5	40	18.776	0.073	15.714	0.061	39.078	0.240	0.83710	0.001	2.08207	0.003
de03b06	T1G-6	40	18.600	0.074	15.579	0.060	38.662	0.301	0.83775	0.001	2.07932	0.003
de03d22	T1G-7	40	18.769	0.076	15.705	0.064	39.138	0.188	0.83693	0.001	2.08620	0.004
de03d23	T1G-8	40	18.760	0.081	15.678	0.067	39.000	0.233	0.83582	0.001	2.07986	0.004
de03d24	T1G-9	40	18.717	0.080	15.633	0.065	38.943	0.217	0.83540	0.001	2.08163	0.004

[1]calculated using Method 2

[2]preferred reference values from Jochum *et al.* (2006a)

Table S2-2: Pb isotope ratio values[1] for ATHO-G

			$^{206}Pb/^{204}Pb$	SE (1σ)	$^{207}Pb/^{204}Pb$	SE (1σ)	$^{208}Pb/^{204}Pb$	SE (1σ)	$^{207}Pb/^{206}Pb$	SE (1σ)	$^{208}Pb/^{206}Pb$	SE (1σ)
Preferred Values[2]			**18.383**	**0.004**	**15.480**	**0.004**	**38.111**	**0.003**	**0.84204**	**0.00019**	**2.0730**	**0.0006**
Experiment		**Spot Size**										
de01b06	ATHO-3	40	18.123	0.131	15.298	0.100	37.708	0.268	0.84327	0.001	2.07836	0.003
de03a22	ATHO-1	40	18.290	0.055	15.345	0.056	37.993	0.142	0.83920	0.001	2.07802	0.004
de03a23	ATHO-2	40	18.137	0.055	15.261	0.056	37.698	0.141	0.84173	0.001	2.07932	0.004
de03a24	ATHO-3	40	18.343	0.056	15.420	0.056	38.128	0.152	0.84121	0.001	2.07948	0.004
de03b10	ATHO-4	40	18.346	0.052	15.434	0.051	38.259	0.114	0.84136	0.001	2.08579	0.003
de03b11	ATHO-5	40	18.389	0.052	15.433	0.051	38.231	0.111	0.83938	0.001	2.07989	0.003
de03b12	ATHO-6	40	18.184	0.051	15.300	0.050	37.689	0.111	0.84137	0.001	2.07295	0.003
de03d10	ATHO-7	40	18.534	0.071	15.607	0.060	38.490	0.136	0.84283	0.001	2.07781	0.004
de03d11	ATHO-8	40	18.601	0.070	15.657	0.060	38.628	0.134	0.84185	0.001	2.07717	0.004
de03d12	ATHO-9	40	18.643	0.071	15.704	0.060	38.704	0.139	0.84250	0.001	2.07682	0.004
fe14a10	ATHO-01	40	18.310	0.165	15.336	0.115	37.707	0.484	0.83866	0.001	2.06260	0.005
fe14a11	ATHO-02	40	18.519	0.132	15.544	0.103	38.248	0.379	0.83963	0.001	2.06753	0.005
fe14a12	ATHO-03	40	18.456	0.151	15.495	0.114	38.052	0.440	0.84032	0.001	2.06484	0.005
fe14b10	ATHO-01	40	18.672	0.145	15.721	0.096	38.462	0.442	0.84234	0.001	2.06199	0.002
fe14b11	ATHO-02	40	18.139	0.111	15.332	0.075	37.484	0.312	0.84573	0.001	2.06895	0.002
fe14b12	ATHO-03	40	18.865	0.153	15.826	0.096	38.889	0.457	0.83964	0.001	2.06374	0.002

[1]calculated using Method 2

[2]preferred reference values from Jochum *et al.* (2006a)

Table S2-3: Pb isotope ratio values[1] for KL2-G

			$^{206}Pb/^{204}Pb$	SE (1σ)	$^{207}Pb/^{204}Pb$	SE (1σ)	$^{208}Pb/^{204}Pb$	SE (1σ)	$^{207}Pb/^{206}Pb$	SE (1σ)	$^{208}Pb/^{206}Pb$	SE (1σ)
Preferred Values[2]			**19.030**	**0.009**	**15.632**	**0.004**	**38.524**	**0.015**	**0.82146**	**0.00023**	**2.0243**	**0.0004**
Experiment		**Spot Size**										
no29b04	KL2G-1	69	19.286	0.095	15.804	0.082	39.026	0.207	0.81993	0.001	2.02424	0.002
no29b05	KL2G-2	69	19.022	0.101	15.615	0.085	38.511	0.244	0.82127	0.001	2.02616	0.002
no29b06	KL2G-3	69	18.653	0.096	15.307	0.082	37.726	0.210	0.82118	0.001	2.02449	0.002
no29b16	KL2G-4	69	18.937	0.097	15.519	0.083	38.499	0.221	0.81996	0.001	2.03387	0.002
no29b17	KL2G-5	69	18.817	0.097	15.414	0.083	38.030	0.227	0.81966	0.001	2.02279	0.002
no29b18	KL2G-6	69	18.990	0.096	15.616	0.082	38.561	0.213	0.82273	0.001	2.03189	0.002
de01a22	KL2G-1	69	18.865	0.183	15.466	0.136	38.129	0.327	0.81932	0.001	2.01946	0.004
de01a23	KL2G-2	69	18.917	0.165	15.534	0.125	38.343	0.318	0.82060	0.001	2.02609	0.004
de01a24	KL2G-3	69	18.996	0.164	15.630	0.126	38.491	0.317	0.82228	0.001	2.02521	0.004
de01b22	KL2G-4	69	19.229	0.136	15.795	0.102	38.878	0.273	0.82116	0.001	2.02121	0.003
de01b23	KL2G-5	69	19.093	0.142	15.667	0.104	38.734	0.274	0.82018	0.001	2.02797	0.003
de01b24	KL2G-6	69	18.985	0.148	15.605	0.108	38.529	0.275	0.82141	0.001	2.02802	0.003
de03a16	KL2G-1	69	18.872	0.056	15.476	0.057	38.121	0.150	0.82017	0.001	2.02229	0.004
de03a17	KL2G-2	69	19.176	0.056	15.758	0.056	38.927	0.145	0.82206	0.001	2.03184	0.004
de03a18	KL2G-3	69	18.744	0.055	15.392	0.056	38.076	0.139	0.82178	0.001	2.03302	0.004
de03c10	KL2G-4	69	18.953	0.075	15.557	0.065	38.484	0.171	0.82095	0.001	2.03130	0.003
de03c11	KL2G-5	69	18.996	0.075	15.581	0.064	38.491	0.159	0.82082	0.001	2.02797	0.003
de03c12	KL2G-6	69	18.853	0.073	15.498	0.064	38.167	0.151	0.82240	0.001	2.02567	0.003
de03d04	KL2G-7	69	19.096	0.070	15.680	0.060	38.688	0.133	0.82154	0.001	2.02699	0.004
de03d05	KL2G-8	69	18.938	0.071	15.589	0.060	38.475	0.138	0.82379	0.001	2.03295	0.004
de03d06	KL2G-9	69	19.033	0.070	15.697	0.060	38.634	0.134	0.82539	0.001	2.03134	0.004
de10b04	KL2G-7	99	19.071	0.075	15.662	0.067	38.723	0.179	0.82142	0.001	2.03149	0.003
de10b05	KL2G-8	99	18.965	0.075	15.534	0.067	38.406	0.179	0.81937	0.001	2.02613	0.003
de10b06	KL2G-9	99	19.003	0.075	15.594	0.066	38.527	0.175	0.82087	0.001	2.02830	0.003
de10b22	KL2G-10	99	19.131	0.075	15.685	0.067	38.809	0.184	0.82032	0.001	2.02994	0.003
de10b23	KL2G-11	99	19.049	0.075	15.609	0.067	38.531	0.179	0.81993	0.001	2.02443	0.003
de10b24	KL2G-12	99	19.014	0.075	15.590	0.067	38.501	0.176	0.82037	0.001	2.02650	0.003

[1]calculated using Method 2

[2]preferred reference values from Jochum *et al.* (2006b)

Table S2-4: Pb isotope ratio values[1] for ML3B-G

			$^{206}Pb/^{204}Pb$	SE (1σ)	$^{207}Pb/^{204}Pb$	SE (1σ)	$^{208}Pb/^{204}Pb$	SE (1σ)	$^{207}Pb/^{206}Pb$	SE (1σ)	$^{208}Pb/^{206}Pb$	SE (1σ)
Preferred Values[2]			**18.720**	**0.016**	**15.600**	**0.014**	**38.454**	**0.043**	**0.8334**	**0.0017**	**2.0542**	**0.0006**
Experiment		**Spot Size**										
de01a16	ML3B-1	69	18.726	0.176	15.588	0.133	38.321	0.337	0.83086	0.001	2.04202	0.004
de01a17	ML3B-2	69	18.807	0.203	15.635	0.151	38.484	0.344	0.82939	0.001	2.04136	0.004
de01a18	ML3B-3	69	18.376	0.191	15.267	0.137	37.568	0.342	0.82959	0.001	2.04041	0.004
de01b10	ML3B-4	69	18.686	0.148	15.503	0.110	38.222	0.285	0.82799	0.001	2.04083	0.003
de01b11	ML3B-5	69	18.662	0.164	15.472	0.113	38.192	0.288	0.82759	0.001	2.04275	0.003
de01b12	ML3B-6	69	18.841	0.165	15.641	0.121	38.589	0.294	0.82886	0.001	2.04468	0.003
de03a10	ML3B-1	69	18.488	0.056	15.332	0.056	37.829	0.151	0.82941	0.001	2.04991	0.004
de03a11	ML3B-2	69	18.900	0.059	15.654	0.058	38.571	0.171	0.82903	0.001	2.04596	0.004
de03a12	ML3B-3	69	18.793	0.058	15.619	0.058	38.552	0.155	0.83164	0.001	2.05622	0.004
de03c04	ML3B-4	69	18.647	0.075	15.479	0.064	38.190	0.160	0.83042	0.001	2.04938	0.003
de03c05	ML3B-5	69	18.773	0.074	15.572	0.064	38.446	0.158	0.82990	0.001	2.04899	0.003
de03c06	ML3B-6	69	18.353	0.080	15.190	0.067	37.617	0.212	0.82805	0.001	2.05084	0.003
de03d16	ML3B-7	69	18.590	0.073	15.429	0.062	38.193	0.163	0.83032	0.001	2.05544	0.004
de03d17	ML3B-8	69	18.846	0.070	15.649	0.060	38.757	0.133	0.83060	0.001	2.05767	0.004
de03d18	ML3B-9	69	18.535	0.075	15.404	0.062	38.059	0.171	0.83135	0.001	2.05459	0.004
fe14a04	ML3B-01	69	18.891	0.181	15.637	0.130	38.719	0.218	0.82863	0.001	2.05213	0.005
fe14a05	ML3B-02	69	18.876	0.170	15.694	0.128	38.692	0.223	0.83198	0.001	2.05194	0.005
fe14a06	ML3B-03	69	18.718	0.172	15.570	0.124	38.265	0.219	0.83179	0.001	2.04603	0.005
fe14b04	ML3B-01	69	18.899	0.132	15.636	0.089	38.543	0.145	0.82771	0.001	2.04154	0.002
fe14b05	ML3B-02	69	18.578	0.115	15.350	0.074	38.009	0.133	0.82676	0.001	2.04828	0.002
fe14b06	ML3B-03	69	18.444	0.130	15.319	0.081	37.675	0.154	0.83094	0.001	2.04466	0.002
de10b10	ML3B-7	99	18.781	0.076	15.541	0.068	38.452	0.185	0.82752	0.001	2.04827	0.003
de10b11	ML3B-8	99	18.798	0.082	15.552	0.070	38.499	0.215	0.82767	0.001	2.04924	0.003
de10b12	ML3B-9	99	18.619	0.076	15.458	0.067	38.239	0.186	0.83055	0.001	2.05468	0.003
de10b28	ML3B-10	99	18.702	0.076	15.547	0.067	38.430	0.181	0.83146	0.001	2.05568	0.003
de10b29	ML3B-11	99	18.728	0.075	15.539	0.067	38.456	0.176	0.82990	0.001	2.05435	0.003
de10b30	ML3B-12	99	19.099	0.079	15.908	0.069	39.274	0.205	0.83197	0.001	2.05418	0.003

[1]calculated using Method 2

[2]preferred reference values from Jochum *et al.* (2006a)

Chapter 3: Accuracy and precision of non-matrix-matched calibration for lead isotope ratio measurements of lead-poor minerals by LA-MC-ICPMS

Abstract

This study evaluates the necessity of matrix matching for laser ablation multi-collector inductively coupled plasma mass spectrometry (LA-MC-ICPMS) lead isotope ratio measurements of lead-poor (< 70 ppm total Pb) feldspar and sulfide using standard-sample-standard bracketing to correct for mass discrimination. Lead isotope ratios of three different feldspar minerals and three different sulfide matrices were measured by LA-MC-ICPMS to determine the quality of data possible when calibrating samples with standards having different physical characteristics and chemical compositions. Lead isotope ratios for the feldspars were calibrated against NIST 612 and BCR2-G. The average $^{206, 207, 208}Pb/^{204}Pb$ and $^{207, 208}Pb/^{206}Pb$ ratios determined by LA-MC-ICPMS on all three feldspars, independent of standard, are within 0.40% of the average TIMS measurements made in this study on the same grains. External precisions for the LA-MC-ICPMS measurements are better than 0.60% (RSD, 1-sigma). Lead isotope ratios for 3 sulfides were determined by LA-MC-ICPMS using either NIST 612 or PB-1, a synthetic sulfide glass, as the external calibration standard. For two sulfides that contain little to no mercury the mean $^{206, 207, 208}Pb/^{204}Pb$ and $^{207, 208}Pb/^{206}Pb$ ratios are accurate within 0.40% of the average TIMS measurements made in this study on the same grains, with only subtle differences in results between matrix-matched (PB-1) and non-matrix-matched (NIST 612) analyses. Lead isotope ratios determined for MASS-1, a pressed powder

sulfide containing high levels of mercury (~ 60 ppm), are highly variable. This is a result of intrinsic lead isotope heterogeneity in MASS-1 and errors in the isobaric overlap corrections for ^{204}Hg on ^{204}Pb caused by fractionation of Hg/Pb during spot analyses. Despite significant differences in the ablation behavior of silicate glass, feldspar and sulfide, the results demonstrate that precise and accurate lead isotope ratio data can be obtained by LA-MC-ICPMS for feldspar and sulfide containing little to no mercury, using commonly available silicate glasses as calibration standards.

3.1 INTRODUCTION

Lead isotope ratio measurements are used widely in the earth and environmental sciences, for instance as tracers of source and process in silicate and sulfide magmatic systems (Mathez and Waight, 2003; Gagnevin et al., 2005), in sedimentary provenance investigations (Tyrrell et al., 2006; Connelly and Thrane, 2005) and for contaminant source apportionment (McGill et al., 2003; Burnett et al., 2007). The incorporation of discrete-dynode and/or continuous dynode electron multipliers (ion counters) within multiple-collector inductively coupled plasma mass spectrometers (MC-ICPMS) coupled to a laser ablation system (LA-MC-ICPMS) has pushed limits of detection and spatial resolution for measurements of lead isotope ratios in minerals to remarkable levels in recent years (Simonetti et al., 2005; Souders and Sylvester, 2008). Yet an inherent limitation to the precision and accuracy of the technique for lead isotopes is the lack of an invariant isotope ratio of lead that can be used for internal mass bias corrections of measured lead isotope ratios. Unlike other radiogenic isotope systems of geologic

interest (e.g. Rb-Sr, Lu-Hf, Sm-Nd), the lead isotopic system has only one stable isotope (^{204}Pb), making internal mass bias corrections impossible. Methods of external normalization such as aspirating a thallium tracer solution during laser analysis to monitor lead isotope fractionation (e.g. Horn et al., 2000; Kosler et al., 2002), and standard-sample-standard bracketing with silicate glass reference materials of known lead isotope composition must be employed instead (e.g. Willigers et al., 2002; Simonetti et al., 2005; Paul et al., 2005; Souders and Sylvester 2008). With these external calibration approaches, the potential for mass bias variations as a function of matrix composition must be carefully evaluated.

An external calibration method such as standard-sample-standard bracketing can only be used to correct for mass bias if (1) drift of the measured isotopic ratios of the standards is linear over the course of an analytical session and (2) there is no difference in mass discrimination between isotopes of interest in the standard matrix relative to the sample matrix. Measured LA-MC-ICPMS isotope ratios generally differ from preferred isotope ratio values due to mass-dependant processes such as instrumental mass bias and isotopic fractionation produced by incomplete volatilization of ablated particles delivered to the ICP (Jackson and Günther, 2003). Mass discrimination is the main source of error affecting isotope ratio measurements and improper correction procedures limit the accuracy of these measurements (Pearson et al., 2008). Many factors have been shown to influence isotopic fractionation: instrument operating parameters such as extraction lens settings, RF power and gas flow (Pearson et al., 2008; Andren et al., 2004), laser ablation parameters such as wavelength and fluence (Jackson and Günther, 2003; Andren et al.,

2004; Kosler et al., 2005) as well as differences in chemical and physical properties between standards and samples, commonly referred to as matrix effects. Matrix effects can lead to variable ablation rates, particle size formation, particle composition, particle transport efficiency, ionization efficiency in the Ar-plasma and mass loading (Sylvester, 2008 and references therein).

Study of the influence of sample matrix on calibration of elemental analysis has been on-going (e.g. Halter et al., 2004; Jochum et al., 2007; Kroslakova and Günther, 2007; Sylvester, 2008) yet the extent to which matrix matching is necessary for external normalization of LA-MC-ICPMS isotope ratio measurements has just begun to be investigated. Several high-precision LA-MC-ICPMS isotope ratio investigations applying external correction procedures have identified significant biases directly related to differences in sample matrices (Mason et al., 2006; Norman et al., 2006). Lead isotope ratio measurements by solution-based MC-ICPMS have shown that varying concentrations of matrix elements such as Fe, Ca, Mg, and Al can enhance or suppress the sensitivity of measured lead isotopes (Barling and Weis, 2008). Yet it is unclear from existing work if these matrix effects are large enough to be detected at the levels of precision and accuracy possible for LA-MC-ICPMS measurements of lead isotope ratios.

Mathez and Waight (2003) found that ratios of $^{207}Pb/^{206}Pb$ and $^{208}Pb/^{206}Pb$ (referred hereafter as $^{207,\,208}Pb/^{206}Pb$) in individual plagioclase grains measured by LA-MC-ICPMS, with corrections for mass discrimination made using a silicate glass standard, agreed to better than ~0.8% and ~1.3% with analyses by TIMS and solution-based MC-ICPMS respectively of bulk separates of the plagioclase grains. Lead

concentrations of the plagioclase were only ~10 ppm or less so data for the minor ^{204}Pb isotope (only ~1.4% of all lead) could not be measured accurately using the Faraday collectors employed. The authors also compared silicate-glass-calibrated LA-MC-ICPMS measurements of various sulfides (discrete pyrrhotite and pentlandite grains, and sulfide intergrowth mixtures) with solution-based MC-ICPMS analyses of bulk sulfide separates from the same sample. For $^{207, 208}Pb/^{206}Pb$ ratios, the data agreed to within 1.9%. Some of the sulfides were sufficiently enriched in lead so that measurements of ^{204}Pb were possible with Faraday cups. For $^{206}Pb/^{204}Pb$, $^{207}Pb/^{204}Pb$ and $^{208}Pb/^{204}Pb$ (referred hereafter as $^{206, 207, 208}Pb/^{204}Pb$) ratios, the laser and solution data agreed to only within 5.8%.

Gagnevin et al. (2005) reported agreement to within ~0.3% between silicate-glass-calibrated, LA-MC-ICPMS analyses of K-feldspar (Or_{65-92}) megacrysts and solution-based, double-spike tracer, MC-ICPMS analyses of micro-samples drilled from the same megacrysts. The feldspar contained ~60 – 175 $\mu g\ g^{-1}$ total Pb so that both $^{206, 207, 208}Pb/^{204}Pb$ and $^{207, 208}Pb/^{206}Pb$ could be measured with Faraday cups. The laser analyses of the feldspars required corrections for small biases (up to 0.15%) seen between the LA-MC-ICPMS measurements of the NIST 610 glass standard and previous TIMS and solution-based, MC-ICPMS analyses of NIST 610.

Connelly and Thrane (2005) measured ratios of $^{206, 207, 208}Pb/^{204}Pb$ for K-feldspar in rock slabs and grain mounts by LA-MC-ICPMS with external calibration against a silicate glass. Compared to solution-based, double-spike, MC-ICPMS analyses of separates of the K-feldspar grains, most of the *in situ* laser analyses gave less radiogenic

$^{206, 207, 208}Pb/^{204}Pb$ ratios, by up to 1.25%. The authors ascribed the difference to the presence of unidentified, radiogenic micro-inclusions or domains in the K-feldspar, which were unavoidably included in the MC-ICPMS analyses of bulk separates but missed at the scale of the laser analyses.

Our investigation focuses on the extent to which matrix matching is necessary for LA-MC-ICPMS measurements of lead isotopes in lead-poor (< 70 ppm) feldspars and sulfides using standard-sample-standard bracketing to correct for mass bias. We present a much more detailed comparison of the quality of data that can be expected for non-matrix-matched and matrix-matched lead isotope ratio measurements of these minerals than has been reported before.

3.2 METHOD/ANALYTICAL SET-UP

We used a Thermo Scientific NEPTUNE double-focusing magnetic sector MC-ICPMS for in situ lead isotope ratio measurements following the analytical method of Souders and Sylvester (2008). The NEPTUNE is equipped with nine Faraday detectors and eight Channeltron ion counters. Static, concurrent measurement of ^{202}Hg, $^{204}(Hg + Pb)$, ^{206}Pb, ^{207}Pb and ^{208}Pb isotopes were made in 5 ion counters, set in fixed positions for the collection of the Hg and Pb isotopes of interest, attached to the low-mass side of Faraday detector L4. ^{235}U was monitored for all analyses in the ion counter mounted on the high mass side of Faraday cup H3. Typical operating conditions for the NEPTUNE and the multi-collector cup configuration are shown in Table 3-1. The isobaric

interference of ^{204}Hg on ^{204}Pb was corrected by the method described in detail by Souders and Sylvester (2008).

A GeoLas laser ablation system coupled to the NEPTUNE MC-ICPMS containing a Lambda Physik ComPex Pro 110 ArF excimer laser operating at a wavelength of 193 nm and a 20 ns pulse width was used for in situ analysis of silicates and sulfides. Samples were ablated in He gas atmosphere, which reduces sample re-deposition and elemental fractionation while increasing sensitivity for 193 nm ablation (Eggins et al., 1998; Günther and Heinrich,1999). Mercury was filtered from the He using Au-coated glass wool placed on the He gas line feeding into the ablation cell. The He gas is mixed with the Ar gas using a glass T-piece placed in the teflon tubing leading into the ICP torch. Typical laser ablation parameters for each matrix analyzed are described in Table 3-1. Identical ablation conditions were used for standard and sample pairs yet compromises between laser fluence, repetition rate and spot size were made based on the chemical and physical properties of the analyte in order to avoid count rates exceeding 300,000 counts per second (cps) where pulse pileup and dead time signal loss become significant and detector drift may be accelerated (Souders and Sylvester, 2008a, 2008b).

The duration of each standard and sample analysis was ~150 seconds using a 0.18 second or 1 second integration time, depending on the analytical session. The first 30 seconds were used to measure background count rates with the laser off, followed by 60 seconds of laser ablation, and 60 seconds of recorded wash out. On-line corrections for both ion counter yield and dark noise were performed using the NEPTUNE software

prior to downloading the measured mass intensities into "Pb-Tool", an Excel spreadsheet modified from "LAM-Tool" of Kosler et al. (2008) for off-line subtraction of mean gas background intensities from time-resolved signal intensities for each isotope, ^{204}Hg interference corrections on ^{204}Pb, ablation interval selection, lead isotope ratio calculations, and correction for instrumental mass bias. Spectroscopic interferences other than ^{204}Hg on ^{204}Pb were negligible for the matrices of this study. At the low oxide production rates (0.10 - 0.25%) in dry plasma mode, contributions from $^{186}W^{16}O$ on ^{202}Hg, $^{190}Pt^{16}O$ on ^{206}Pb, $^{191}Ir^{16}O$ on ^{207}Pb, and $^{192}Pt^{16}O$ on ^{208}Pb were each ~20 counts per second or less. The IrO interference was larger in MASS-1 (~70 cps) but, even in this case, the effect on final $^{207}Pb/^{206}Pb$ and $^{207}Pb/^{204}Pb$ ratios is just 0.1%. Only minimal counts (< 40 cps) were recorded for $^{166,167,168}Er^{40}Ar$ on $^{206,207,208}Pb$ respectively.

A standard-sample-standard bracketing approach was employed to correct for instrumental mass fractionation and detector drift (Albarede et al., 2008). Three standards followed by three unknowns followed by three standards were run sequentially. Calculated lead isotope ratios for every three standards are averaged and the lead isotope ratios for unknowns are determined by linear interpolation of the averaged standard ratios run before and after the unknowns. Reported uncertainties for each unknown analysis are based on the standard error of the mean of each lead isotope ratio for the selected ablation interval and the standard error of the y-estimate of the linear regression through the lead isotope ratios of the standards. Bulk compositions of silicate reference glasses used as external calibrants ranged from synthetic soda-lime aluminosilicate (NIST 612 and NIST

614) to natural basalt (BCR2-G). Lead isotope ratio reference values for each silicate glass are listed in Table S3-1 at the end of this chapter (Supplemental data).

Feldspar and sulfide materials analyzed by LA-MC-ICPMS for lead isotopes were also analyzed by thermal ionization mass spectrometry (TIMS) in order to provide baseline data to assess accuracy. Each aliquot of feldspar and sulfide analyzed by TIMS ranged from 3 to 15 mg. Detailed description of the TIMS procedure is given in Supplemental File S3-1 and the results are presented in Table S3-2 (Supplemental data).

3.3 FELDSPAR AND SULFIDE SAMPLES

Three different feldspars were analyzed as part of this study: an orthoclase megacryst from the Shap granite, northwest England; a bytownite crystal from the Fiskenæsset anorthosite complex, southwest Greenland; and a sanidine phenocryst from the Fish Canyon Tuff (FCT), Colorado, USA. The feldspars have different physical appearances, bulk compositions and total lead concentrations. Both Shap orthoclase and Fiskenæsset bytownite are translucent when cut into < 1 mm thick slices, the orthoclase is milky-white to pink in color whereas the bytownite is white. FCT sanidine is transparent. Both FCT sanidine and Shap orthoclase are potassic feldspars but the sanidine contains less lead than the orthoclase (~20 vs 35 ppm). The bytownite is a calcic feldspar with only 6.5 ppm total lead.

Three different synthetic sulfides, each spiked with lead, were investigated: PB-1, a synthetic Fe-sulfide glass, similar in physical character to a silicate glass; B41, a synthetic Fe-sulfide sinter, which has a subtle mottled appearance in high resolution

back-scattered electron (BSE) images, presumably reflecting areas between grains that almost reached their melting points; and MASS-1, a Fe-Cu-Zn-sulfide pressed powder pellet, which exhibits compositional heterogeneities on the micron scale. Both PB-1 and B41 were produced in the laboratory of C. Ballhaus (Universität Bonn). MASS-1 was made and distributed by the USGS (Wilson et al., 2002) as a standard reference material for in situ trace element measurements and is commonly available in many LA-ICPMS laboratories worldwide. PB-1 and B41 have similar lead concentrations (19 and 16 ppm total lead, respectively) whereas MASS-1 contains ~67 ppm total lead and significant amounts of total mercury (~57 ppm; Wilson et al., 2002; unpublished data, MUN LA-ICPMS lab).

Further information about the bulk composition and physical appearance of the feldspar and sulfide samples is given in Supplemental Figure S3.2.1 and Tables S3.2 – S3.4 at the end of this chapter.

3.4 RESULTS AND DISCUSSION

3.4.1 Isotopic Measurements of Feldspars

Mean values of lead isotope ratio measurements by LA-MC-ICPMS of the feldspars are presented in Table 3-2. The accuracy of each individual analysis and average %RSD (1-sigma) for each material are plotted in Figure 3-1. The results for each individual analysis are given in Table S3-5 (Supplemental data). In order to assess the effect of non-matrix-matched external standardization on the accuracy of lead isotope ratio analysis of several different feldspars, both USGS BCR2-G and NIST 612/NIST

614 silicate glasses were used as external calibrants. NIST 614 (~4 ppm total Pb) was used in place of NIST 612 (~38 ppm total Pb) as the external standard for analyses involving the Fiskenæsset bytownite because both NIST 614 and the bytownite have similar total lead concentrations, which allowed for the same laser ablation conditions to be used when analyzing both standards and samples producing similar count rates. Lead isotope ratios are calculated using method 2 described in Souders and Sylvester (2008).

There is general agreement between lead isotope ratios of the feldspars measured by TIMS and LA-MC-ICPMS despite significant differences in the volume of material analyzed between the two methods. In general, there is ~10^4 times greater mass of material analyzed by TIMS compared to a LA-MC-ICPMS analysis using a 69 μm spot and ~10^5 times greater than when using a 30 μm laser spot. Mean accuracies of all lead isotope ratios determined by LA-MC-ICPMS for all feldspars analyzed, independent of external calibration material, are within 0.40% of the average TIMS values. External precisions of lead isotope ratios determined by LA-MC-ICPMS for all feldspars are better than 0.60% (RSD, 1-sigma). Little difference is observed between the lead isotope ratio results produced using BCR2-G or NIST 612 or NIST 614 as the external calibrant to correct for instrumental mass bias.

3.4.2 Ablation Behavior of Feldspar vs. Silicate Glass

The results indicate that lead isotope ratios of the feldspars with less than ~ 40 ppm total lead are measured by LA-MC-ICPMS to within acceptable limits of precision and accuracy when calibrated externally against silicate glass standards. These results

are not unexpected based on the apparent success of previous LA-MC-ICPMS studies using various instrumentation, instrument parameters and laser ablation conditions to measure the lead isotope ratios of feldspars against a silicate glass standard reference material (*e.g.* Mathez and Waight, 2003; Gagnevin et al., 2005; Connelly and Thrane, 2005; Tyrrell et al., 2006; Mathez and Kent, 2007).

What comes as a surprise in our investigation is that acceptable results are produced despite large differences in the physical and chemical responses of the feldspar minerals and silicate glasses to the laser ablation conditions used in this study, which were evaluated by comparing pit morphology, apparent drill rate, sensitivity and fractionation indices of each matrix. Secondary electron (SE) images of craters after 30 seconds of laser ablation and representative time-resolved lead isotope spectra for the ablation interval for the glass standards and feldspar analyzed using a laser fluence of 3 J cm^{-2} and 10 Hz are shown in Figure 3-2 for a 69 μm laser spot and Figure 3-3 for a 30 μm laser spot. In both Figures 3-2 and 3-3, the apparent drill rate (μm sec^{-1}), ^{208}Pb sensitivity (cps of ^{208}Pb ppm^{-1}), and ^{208}Pb and $^{208}Pb/^{206}Pb$ fractionation indexes for each matrix at the specified laser ablation conditions are listed.

Craters formed with a 69-μm laser spot all appear morphologically similar with relatively smooth crater walls and flat crater floors. The walls of the pit created in NIST 614 appear to have a shallower slope, tapering towards the middle of the pit, than the crater walls in both BCR2-G and the bytownite. There is subdued development of a melt sheet on the crater floor and along the sidewalls of the pits with small melt-rims forming at the crater edges for all three materials. Very little splatter is noticeable on the sample

surfaces outside the crater rims at the magnification of the images shown in Figure 3-2. Apparent drill rates for BCR2-G, NIST 614 and the bytownite using a 69 μm laser spot are all above 1 μm sec^{-1}. We are unable to distinguish whether there are significant variations in ablation rates between the three matrices because of difficulties in determining the exact distance from the crater rim to crater floor in the presence of laser-produced melt. We estimate errors of ~20% on the calculated ablation rates. Procedures for determination of drill rates are described in Supplemental File S3-3.

In contrast to pits made with the 69-μm laser spots, those formed in silicate glasses and feldspars using a 30 μm spot have irregular melt surfaces along the crater walls and rims. Large piles of melt droplets have accumulated at the bottom of both the 30-μm craters in orthoclase and sanidine. Crater walls of NIST 612, orthoclase and sanidine all taper in towards the bottom of the pit, which differs from the (comparatively) vertical crater walls of the 30-μm crater in BCR2-G. A small volume of tiny melt droplets form a thin ejecta blanket covering the sample surface outside the crater rim, yet within the field of view of all images shown in Figure 3-3. Apparent drill rates for the 30 μm craters range between ~0.60 μm sec^{-1} and ~0.81 μm sec^{-1}, more than 20% lower than estimated errors on the drill rates calculated for the 69 μm craters. The slower ablation rates estimated for the 30 μm craters probably result in part from the difficulty in extracting melt droplets from them compared to the wider, 69 μm craters.

The fractionation index (f) is a measure of changes in analyte signals during laser ablation. It is calculated as the mean background corrected intensity of a measured isotope for the second half of the ablation interval divided by the mean background

corrected signal intensity of the same measured isotope for the first half of the ablation interval. The ^{208}Pb fractionation indices for BCR2-G, NIST 614 and the bytownite using a 69-μm laser spot range from 0.66 (NIST 614) to 0.95 (bytownite) yet all overlap within error (Figure 3-2). The fractionation indices for the silicate glasses and feldspars analyzed with a 30-μm spot are 0.62, 0.53, 0.68 and 0.67 for BCR2-G, NIST 612, orthoclase and sanidine, respectively (Figure 3-3). For each material, regardless of the laser spot size used, the fractionation index for each measured lead isotope (*e.g.* ^{206}Pb, ^{207}Pb, ^{208}Pb, etc.) is within 0.45% of the other measured lead isotopes such that when lead isotope ratios are calculated, the fractionation index is ~1 for all lead isotope ratios. This indicates that there is no measurable fractionation of lead isotope ratios during ablation, regardless of mass differences between the isotopes and differences in the chemical and physical properties of the studied matrices.

The ^{208}Pb sensitivity for BCR2-G is ~15% greater than that for NIST 614 and the bytownite using a 69 μm laser spot (Figure 3-2). For a 30 μm spot, BCR2-G has a sensitivity for ^{208}Pb of ~ 9600 cps ppm^{-1}), which is greater than the sensitivities for Shap orthoclase (^{208}Pb ~ 8800 cps ppm^{-1}), NIST 612 (^{208}Pb ~ 8100 cps ppm^{-1}) and FCT sanidine (^{208}Pb ~ 7800 cps ppm^{-1}) (Figure 3-3). Differences in lead sensitivities between matrices can be caused by several factors, in particular the degree to which materials of differing composition absorb laser energy and the resulting variations in total mass and size distribution of particles delivered to the ICP (Guillong and Günther, 2002; Kroslakova and Günther, 2007). Materials enriched in transition metals and darker in color tend to absorb laser energy more efficiently than transparent, transition metal-poor

materials. We suggest this is the cause of the greater sensitivity of ^{208}Pb recorded for Fe-rich BCR2-G when compared to that for Fe-poor, NIST 612, NIST 614 and feldspars. Sensitivity of ^{208}Pb of the orthoclase is somewhat higher than that of NIST 612, whereas that for the sanidine is somewhat lower. This is probably because the pinkish-white orthoclase absorbs somewhat more laser energy than the translucent NIST 612 whereas the clear, transparent sanidine absorbs much less.

3.4.3 Isotopic Measurements of Sulfides

LA-MC-ICPMS lead isotope ratio measurement of sulfide matrices using silicate glass as an external calibrant for mass discrimination represents an extreme case of non-matrix-matched analysis. In our experiments, NIST 612 was used as the external standard for LA-MC-ICPMS lead isotope analyses of three sulfides: PB-1, B41 and USGS MASS-1. To provide a comparison baseline for data quality by matrix matching, lead isotope ratios of the sulfides were also measured using PB-1 as the external calibrant. Results of the average LA-MC-ICPMS lead isotope ratio measurements are listed in Table 3-3 and accuracies relative to the adopted TIMS values are plotted in Figure 3-4. The results for each individual analysis are given in Table S3-6 (Supplemental data).

There is good agreement between lead isotope ratios measured by LA-MC-ICPMS using a 30 μm spot (2 J cm^{-2}, 10 Hz) and TIMS for both PB-1 and B41 despite the fact that greater than $\sim 10^5$ times more material was analyzed by TIMS. There is little difference between the matrix-matched (PB-1) and non-matrix-matched (NIST 612) lead

isotope ratio results for both PB-1 and B41, although there is a slight improvement in the accuracy of the mean $^{207,208}Pb/^{206}Pb$ ratios for B41 when PB-1 rather than NIST 612 is used as the external calibrant. In contrast, lead isotope analyses by both TIMS and LA-MC-ICPMS are highly variable for MASS-1, particularly for $^{206,207,208}Pb/^{204}Pb$ ratios.

We attribute the large discrepancies between the LA-MC-ICPMS and TIMS measurements and the variability of the individual LA-MC-ICPMS analyses to both (1) intrinsic heterogeneity in lead isotopes in the MASS-1 matrix, and (2) errors in the correction of ^{204}Hg on the LA-MC-ICPMS measurement on ^{204}Pb in this mercury-rich sulfide. Evidence for intrinsic lead isotopic heterogeneity in MASS-1 is the external precision of 1.4% for $^{206}Pb/^{204}Pb$ and 0.59% for $^{208}Pb/^{204}Pb$ determined by the TIMS measurements, which are much poorer than for all of the other feldspars and sulfides analyzed by TIMS in this study (Table S3-2, Supplemental data). The primary cause of the poor external precision however is error in the subtraction of ^{204}Hg from ^{204}Pb in MASS-1. Unlike all other materials in this investigation, MASS-1 contains a significant amount of total mercury (~57 ppm). After subtraction of ^{204}Hg from the gas background, only a small proportion (~1%) of the remaining $^{204}(Hg + Pb)$ signal is due to ^{204}Hg in the silicate glasses, feldspars, PB-1 or B41. For MASS-1, however, ~80% of the gas background subtracted $^{204}(Hg + Pb)$ signal is due to ^{204}Hg in the sulfide matrix. At these levels, differences in the fractionation behavior between Hg and Pb during laser ablation become important, leading to systematic errors in the ^{204}Hg correction. To illustrate, Figure 3-5 is an example of time-resolved-spectra of mercury and lead isotopes for a laser spot analysis in MASS-1 showing how the Pb signals decay somewhat faster than the Hg

signals. The fractionation index of ^{202}Hg is ~ 0.54, but for ^{208}Pb, it is only ~ 0.36. Thus the contribution of ^{204}Hg (as calculated from ^{202}Hg) to the total ^{204}(Hg + Pb) signal progressively increases with ablation time and the calculated ^{204}Pb (remaining after ^{204}Hg subtraction) progressively decreases. The result is that the corrected $^{206, 207, 208}$Pb /^{204}Pb ratios steadily increase during ablation. Unless the external calibration standard has a similar Hg/Pb ratio to the unknown, or an ablation method that minimizes element-element fractionation such as line rastering is employed, significant variability in the external precision of $^{206, 207, 208}$Pb /^{204}Pb ratios will be seen, as is the case here.

The $^{207, 208}$Pb/^{206}Pb ratios determined for MASS-1 suggest that MASS-1 has rather homogeneous $^{207, 208}$Pb/^{206}Pb ratios at the scale of the laser analyses, which is seemingly inconsistent with the rather poor external precision found in the TIMS analyses, 1.2% for ^{207}Pb/^{206}Pb and 0.78% for ^{208}Pb/^{206}Pb. The implication is that lead isotopic heterogeneities in MASS-1 are carried by sparsely distributed micronuggets that tend to be missed by the fine scale of the laser analyses but not by the larger aliquots analyzed by TIMS.

3.4.4 Ablation Behavior of Sulfide vs. Silicate Glass

As for feldspars, our results indicate that precise and accurate lead isotope data can be determined for sulfides by LA-MC-ICPMS with non-matrix matched calibration for mass discrimination using a silicate glass. This result is surprising in that laser ablation produced much more melt in the sulfides than in the silicate calibration standard. The concern is that lead isotopes may become fractionated in the melt droplets, either at

the ablation site or in the ICP. Figures 3-6 and 3-7 show images of craters produced by laser ablation in NIST 612 and the three sulfides after 30 seconds of ablation. Representative time-resolved lead isotope spectra, apparent drill rates, ^{208}Pb sensitivityand the fractionation indices for both ^{208}Pb and the $^{208}Pb/^{206}Pb$ ratio are also included.

Laser fluence was reduced from 3 J cm^{-2} used for the feldspar analyses to 2 J cm^{-2} for the sulfide experiments in an attempt to reduce melting of sulfide during ablation (Wohlgemuth-Ueberwasser et al., 2007; Woodhead et al., 2009). Sulfide minerals typically have lower melting points than silicates and absorb laser energy more efficiently due to their high concentrations of transition metals, leading to enhanced melting during laser ablation. Laser-produced sulfide melt may remain trapped in the ablation pit, rather than being transported to the ICP, thereby reducing analyte sensitivity (Sylvester, 2008). Significant melt production also increases the chance of delivery of melt particles to the ICP that are too large to be completely volatilized (Guillong and Günther, 2002), potentially inducing elemental or isotopic fractionations (Jackson and Günther, 2003). Despite the reduced fluence, however, SE images in Figures 3-6 and 3-7 show that considerable melt was still produced in and around the pits drilled in the sulfides. We attempted to reduce the laser fluence to less than 2 J cm^{-2} in order to limit melt production even further but found that this provided insufficient energy for consistent ablation of the NIST glass. Even at 2 J cm^{-2}, ablation pits in NIST 612 are poorly formed with shallow walls thinly lined with melt (Figures 3-6 and 3-7). This is reflected in the relative sensitivity of ^{208}Pb in NIST 612 (~6900 cps ppm^{-1}), which is only somewhat

more than half that found in PB-1 ($^{208}Pb \sim 11200$ cps ppm^{-1}) and B41 ($^{208}Pb \sim 10600$ cps ppm^{-1}) for the 30-μm spots (Figure 3-6).

The morphology and dispersion of laser-produced melt in ablation pits in PB-1 is similar to that in B41, despite their physical differences (glass *vs.* sinter), but melt features in MASS-1 are quite different from both PB-1 and B41. In particular, there is extensive build-up of melt along the crater rims creating wall-like structures (up to ~10 μm in height) for the 20 and 30 μm craters in PB-1 and the 30 μm crater in B41, but not for the 20 μm crater in MASS-1. Crater walls in PB-1 and B41 all taper inwards towards the center of the laser pit whereas the crater walls of MASS-1 are much steeper with finger-like melt structures present in vertical-layers. Numerous micron-sized melt droplets are visible on the sample surface outside of the 30 μm craters in PB-1 and B41 but there are few if any.droplets surrounding the 20 μm crater in MASS-1.

The implication of these observations is that ablation and removal of material from MASS-1 ablation pits was more efficient than from the pits in PB-1 and B41, leaving a crater in MASS-1 with nearly vertical walls and no significant melt rim and melt droplets in the ejecta blanket. Calculated drill rates and measured sensitivities for ^{208}Pb are consistent with this hypothesis (Figure 3-7). The apparent drill rate calculated for MASS-1 is ~0.71 μm sec^{-1}, significantly greater than that determined for PB-1 (~0.24 μm sec^{-1}) ablated under identical ablation conditions. During these ablations, the sensitivity for ^{208}Pb in MASS-1 was ~ 8700 cps ppm^{-1}, but much less, only ~ 5700 cps ppm^{-1}, for PB-1. We suggest that the granular nature of the pressed powder pellet of MASS-1 allowed more efficient drilling and removal of material by the laser than in the

case of the glassy matrix of PB-1. Evidently, however, the strikingly different ablation behavior for MASS-1 did not produce large errors in the $^{207,208}Pb/^{206}Pb$ ratios measured by LA-MC-ICPMS. The fractionation index for the $^{208}Pb/^{206}Pb$ ratio in MASS-1 is 0.99±0.03, indicating the lack of detectable time-dependent fractionation during ablation.

The ablation behavior for NIST 612 appears to be more similar to that for PB-1 and B41 than to MASS-1. In particular the ablation pits in NIST 612 taper downward in a cone shape as for the pits in PB-1 and B41. The most obvious difference is the smaller amounts of melt produced during ablation of NIST 612 compared to the sulfides. A melt wall did not form along the rim of the pits in NIST 612 unlike around the pits in PB-1 and B41. Nonetheless besides the differences in ^{208}Pb sensitivity described above, values for the various ablation parameters presented in Figures 3-6 and 3-7 for NIST 612 are similar to those for PB-1 and B41. For instance, apparent drill rates in the 30-μm pits for NIST 612 (~0.31 μm sec^{-1}) are similar to those for PB-1 (~0.41 μm sec^{-1}) and B41 (~0.37 μm sec^{-1}). Fractionation indices for ^{208}Pb in 30 μm pits are ~0.36 for NIST 612, ~0.41 for PB-1, and ~0.37 for B41. Fractionation indices for $^{208}Pb/^{206}Pb$ are ~1 for each of NIST 612, PB-1 and B41, demonstrating that there is little or no fractionation of lead isotopes during laser ablation of these silicate and sulfide matrices.

3.5 CONCLUSION

Mass bias is the largest source of error affecting isotope ratio measurements by LA-MC-ICPMS and if not properly corrected, the accuracy and precision of an isotope ratio analysis can be severely compromised. We have shown that a silicate glass

can be used effectively to make external corrections for mass discrimination of lead isotope ratios in both lead-poor feldspars (< 40 ppm total lead) and sulfides (< 20 ppm total lead) despite large differences in matrix composition, ablation behavior, apparent drill rates, and the sensitivities and fractionation indices of individual lead isotopes. For laser spot analyses, sample matrices containing significant amounts of Hg relative to Pb (Hg/Pb > 0.5) require external calibration standards that are matrix matched in terms of Hg/Pb ratios in order to properly correct for the isobaric interference of ^{204}Hg on ^{204}Pb. Accuracies and precisions of ~0.5% can be expected for in situ lead isotope ratio measurements of lead-poor feldspar and sulfide using 193 nm, nanosecond laser radiation and a MC-ICPMS instrument equipped with ion counters.

3.6 REFERENCES

Albarede F., Telouk P., Blichert-Toft J., Boyet M., Agranier A. and Nelson B. (2004) Precise and accurate isotopic measurements using multiple-collector ICPMS. *Geochim. Cosmochim. Acta* **68**, 2725 – 2744.

Andren H., Rodushkin I., Stenberg A., Malinovsky D. and Baxter D.C. (2004) Sources of mass bias and isotope ratio variation in multi-collector ICP-MS: optimization of instrumental parameters based on experimental observations. *J. Anal. At. Spectrom.* **19** 1217 – 1224.

Barling J. and Weis D. (2008) The influence of non-spectral matrix effects on the accuracy of Pb isotope ratio measurement by MC-ICP-MS. Implications for the external normalization method of instrumental mass bias correction. *J. Anal. At. Spectrom.* **23**, 1017-1025.

Burnett A., Kurtz A.C., Brabander D. and Shailer M. (2007) Dendrochemical Record of Historical Lead Contamination Sources, Wells G&H Superfund Site, Woburn, Massachusett. *J. of Environ. Qual.* **36**, 1488-1494.

Connelly J.N. and Thrane K. (2005) Rapid determination of Pb isotopes to define Precambrain allochthonous domains: and example from West Greenland. *Geology* **33**, 953 – 956.

Eggins S.M., Kinsley L.P.J. and Shelley J.M.G. (1998) Deposition and element fractionation processes during atmospheric pressure laser sampling for analysis by ICPMS. *Appl. Surf. Sci.* **129**, 278 – 286.

Gagnevin D., Daly J.S., Waight T.E., Morgan D. and Poli G. (2005) Pb isotopic zoning of K-feldspar megacrysts determined by laser ablation multi-collector ICP-MS: insights into granite petrogenesis. *Geochim. Cosmochim. Acta* **69**, 1899 – 1915.

Guillong M. and Günther D. (2002) Effect of particle size distribution on ICP-induced elemental fractionation in laser-ablation–inductively coupled plasma–mass spectrometry. *J. Anal. At. Spectrom.* **17**, 831 – 837.

Günther D. and Heinrich C.A. (1999) Enhanced sensitivity in laser ablation-ICP mass spectrometry using helium-argon mixtures as aerosol carrier. *J. Anal. At. Spectrom.* **14**, 1363 – 1368

Halter W.E., Pettke T. and Heinrich C.A. (2004) Laser–ablation ICP–MS analysis of silicate and sulfide melt inclusions in an andesitic complex I: analytical approach and data evaluation. *Contrib. Mineral. Petrol.* **147**, 385 – 396.

Hemming S.R. and Rasbury E.T. (2000) Pb isotope measurements of sanidine monitor standards: implications for provenance analysis and tephrochronology. *Chem. Geol.* **165**, 331 – 337.

Horn I., Rudnick R.L., McDonough W.F. (2000) Precise elemental and isotope ratio determination by simultaneous solution nebulization and laser ablation ICP-MS: application to U-Pb geochronology. *Chem. Geol.* **164**, 281 – 301.

Jackson S.E. and Günther D. (2003) The nature and source of laser induced isotopic fractionation in laser ablation -multicollector-inductively coupled plasma-mass spectrometry. *J. Anal. At. Spectrom.* **18** 205 – 212.

Jochum K.P., Stoll B. Herwig K. and Willbold M. (2007) Validation of LA–ICP–MS trace element analysis of geological glasses using a new solid-state 193 nm Nd:YAG laser and matrix-matched calibration. **22**, 112 – 122.

Kosler J., Fonneland H., Sylvester P., Tubrett M. and Pederson R. (2002) U–Pb dating of detrital zircons for sediment provenance studies: a comparison of laser- ablation ICPMS and SIMS techniques. *ChemicalGeology*, **182**, 605–618.

Kosler J., Pedersen R.B., Kruber C. and Sylvester P.J. (2005) Analysis of Fe isotopes in sulfides and iron meteorites by laser ablation high-mass resolution multi-collector-ICP mass spectrometry. *J.Anal. At. Spectrom.* **20**, 192 – 199.

Kosler J., Forst L. and Slama J. (2008) LAMDATE and LAMTOOL: Spreadsheet-based data reduction for laser ablation-ICPMS. *In* Laser Ablation ICP-MS in the Earth Sciences: Current Practices and Outstanding Issues, v. 40 (ed. P.J. Sylvester). Mineralogical Association of Canada pp. 315 - 317.

Kroslakova I. and Günther D. (2007) Elemental fractionation in laser ablation–inductively coupled plasma–mass spectrometry: evidence for mass load induced matrix effects in the ICP during ablation of a silicate glass. *J. Anal. Atom. Spectrom.* **22**, 51 – 62.

Mason P.R.D., Kosler J., De Hoog J.C.M., Sylvester P.J., Meffan-Main S. (2006) In-situ determination of sulfur isotopes in sulfur-rich materials by laser ablation multiple-collector inductively coupled plasma mass spectrometry (LA-MC-ICP-MS). *J. Anal. Atom. Spectrom.* **21**, 177 – 186.

Mathez E.A. and Waight T.E. (2003) Lead isotopic disequilibrium between sulfide and plagioclase in the Bushveld complex and the chemical evolution of large layered intrusions. *Geochim Cosmochim Acta* **67**, 1875 – 1888.

Mathez E.A. and Kent A.J.R. (2007) Variable initial Pb isotopic compositions of rocks associated with the UG2 chromitite, eastern Bushveld Complex. *Geochim. Cosmochim. Acta* **71**, 5514 – 5527.

McGill R.A.R., Pearce J.M., Fortey N.J., Watt J., Ault L. and Parrish R.R. (2003) Contaminant source apportionment by PIMMS lead isotope analysis and SEM image analysis. *Environ. Geochem. Health* **25**, 25 – 32.

Norman M., McCulloch M., O'Neill H. and Yaxley G. (2006) Manesium isotopic analysis of olivine by laser ablation multi-collector ICP-MS: Composition dependent matrix effects and a comparison of the Earth and Moon. *J. Analyt. Atom. Spectrom.* **21**, 50 – 54.

Paul B., Woodhead J.D. and Hergt J. (2005) Improved in situ isotope analysis of low Pb materials using LA-MC-ICP-MS with parallel ion counter and Faraday detection. *J. Analyt. Atom. Spectrom.* **20**, 1350 – 1357.

Pearson N.J., Griffin W.L. and O'Reilly S. Y. (2008) Mass fractionation correction in laser ablation multiple-collector ICP-MS: precise and accurate in-situ isotope ratio measurement. *In* Laser Ablation ICP-MS in the Earth Sciences: Current Practices and Outstanding Issues, v. 40 (ed. P.J. Sylvester). Mineralogical Association of Canada p. 93 – 116.

Simonetti A., Heaman L.M., Chacko T. and Banerjee, N.R. (2005) U-Pb zircon dating by laser ablation-MC-ICP-MS using a new multiple ion counting Faraday collector array. *J. Anal. At. Spectrom.* **20**, 677 – 686.

Souders A.K. and Sylvester P.J. (2008a) Improved in situ measurements of lead isotopes in silicate glasses by LA-MC-ICPMS using multiple ion counters. *J. Anal. At. Spectrom.* **23**, 535 – 543. doi: 10.1039/b713934a

Souders A.K. and Sylvester P.J. (2008b) Use of multiple channeltron ion counters for LA-MC-ICPMS analysis of common lead isotopes in silicate glasses. *In* Laser Ablation ICP-MS in the Earth Sciences: Current Practices and Outstanding Issues, v. 40 (ed. P.J. Sylvester). Mineralogical Association of Canada p. 79 – 92.

Sylvester P.J. (2008) Matrix effects in laser ablation ICP-MS. *In* Laser Ablation ICP-MS in the Earth Sciences: Current Practices and Outstanding Issues, v. 40 (ed. P.J. Sylvester). Mineralogical Association of Canada p. 79 – 92.

Tyrrell S., Haughton P.D.W., Daly J.S., Kokfelt T.F. and Gagnevin D. (2006) The use of the common Pb isotope composition of detrital K-feldspar grains as a provenance tool and its application to Upper Carboniferous palaeodrainage, Northern England. *J. Sed. Res.* **76**, 324 – 345.

Willigers B.J.A., Baker J.A., Krogstad E.J. and Peate D.W. (2002) Precise and accurate in situ Pb-Pb dating of apatite, monazite, and sphene by laser ablation multiple-collector ICP-MS. *Geochim. Cosmochim. Acta*, **66**, 1051 – 1066.

Wilson S.A., Ridley W.I. and Koenig A.E. (2002) Development of sulfide calibration standards for the laser ablation inductively-coupled plasma mass spectrometry technique. *J. Anal. At. Spectrom.* **17**, 4006 – 4009.

Wohlgemuth-Ueberwasser C.C., Ballhaus C., Berndt J., Stotter nee Paliulionyte V. and Meisel T. (2007) Synthesis of PGE sulfide standards for laser ablation inductively coupled plasma mass spectrometry (LA-ICP-MS). *Contrib. Mineral. Petrol.* **154**, 607 – 617.

Woodhead J., Hergt J., Meffre S., Large R.R. Danyushevsky L. and Gilber S. (2009) In situ Pb-isotope analysis of pyrite by laser ablation (multi-collector and quadrupole) ICPMS. *Chem. Geol.* **262**, 344 – 354.

Table 3-1 Summary of the operating conditions and cup configuration for LA-MC-ICPMS lead isotope measurements

Thermo-Finnigan Neptune MC-ICPMS		
RF power	1200 W	
HV	10 kV	
Carrier gas (He) flow	1.2 L min^{-1}	
Make-up gas (Ar) flow rate	0.7 L min^{-1}	
Auxiliary gas flow	0.7 L min^{-1}	
Cool gas flow	16 L min^{-1}	
Cones	Ni	
GeoLas Laser ablation system		
Lambda Physik Compex 110 Ar F excimer		
	silicate experiments	**sulfide experiments**
Wavelength	193 nm	193 nm
Pulsewidth	20 ns	20 ns
Laser fluence	3 J cm^{-2}	2 J cm^{-2}
Repetition rate	10 Hz	5 - 10 Hz
Ablation duration	60 sec	60 sec
Spot size	30 - 69 μm	20 - 30 μm
Ablation cell gas	He	He

Thermo-Finnigan Neptune collector assignments for lead isotope measurements

Collector[a]	IC1	IC2	IC3	IC4	IC5	L4	L3	L2	L1	C	H1	H2	H3	IC6	H4	IC7	IC8
isotope	^{202}Hg	$^{204}Hg+Pb$	^{206}Pb	^{207}Pb	^{208}Pb					219.68				^{235}U	^{238}U		

[a] L4 to L1, C, and H1 to H4 are Faraday cups. IC1 to IC5 are ion counters fixed to Faraday cup L4. IC6 is an ion counter fixed to Faraday cup H3. IC7 and IC8 are ion counters fixed to Faraday cup H4.

Table 3-2. Average LA-MC-ICPMS Lead isotope ratio values for feldspars[a]

		$^{206}Pb/^{204}Pb$	$^{207}Pb/^{204}Pb$	$^{208}Pb/^{204}Pb$	$^{207}Pb/^{206}Pb$	$^{208}Pb/^{206}Pb$
Shap orthoclase		**18.271 ± 0.0242**	**15.656 ± 0.0074**	**38.258 ± 0.0236**	**0.857 ± 0.0009**	**2.094 ± 0.0023**
BCR2-G standard	Mean	18.268	15.671	38.256	0.859	2.098
3 J cm^{-2}, 10 Hz	SD (1s)	0.0632	0.0742	0.1266	0.0018	0.0049
30 μm spot	% RSD (1s)	0.35%	0.47%	0.33%	0.21%	0.23%
(n = 15)	Accuracy (%)	-0.02%	0.10%	0.00%	0.19%	0.17%
612 standard	Mean	18.292	15.688	38.337	0.858	2.096
3 J cm^{-2}, 10 Hz	SD (1s)	0.0598	0.0630	0.1515	0.0013	0.0040
30 μm spot	% RSD (1s)	0.33%	0.40%	0.40%	0.15%	0.19%
(n = 15)	Accuracy (%)	0.12%	0.21%	0.21%	0.08%	0.09%
FCT sanidine[b]		**18.472 ± 0.016**	**15.604 ± 0.018**	**37.8025 ± 0.088**	**0.8447 ± 0.0003**	**2.0465 ± 0.003**
BCR2-G standard	Mean	18.471	15.609	37.902	0.846	2.050
3 J cm^{-2}, 10 Hz	SD (1s)	0.0225	0.0730	0.0658	0.0026	0.0029
30 μm spot	% RSD (1s)	0.12%	0.47%	0.17%	0.31%	0.14%
(n = 11)	Accuracy (%)	0.00%	0.03%	0.26%	0.12%	0.16%
612 standard	Mean	18.468	15.564	37.658	0.843	2.045
3 J cm^{-2}, 10 Hz	SD (1s)	0.0261	0.0418	0.0292	0.0015	0.0033
30 μm spot	% RSD (1s)	0.14%	0.27%	0.08%	0.18%	0.16%
(n = 3)	Accuracy (%)	-0.02%	-0.26%	-0.38%	-0.15%	-0.07%
Fiskenæsset bytownite		**13.275 ± 0.0308**	**14.457 ± 0.0281**	**33.103 ± 0.0612**	**1.089 ± 0.0035**	**2.494 ± 0.0075**
BCR2-G standard	Mean	13.265	14.476	33.077	1.091	2.500
3 J cm^{-2}, 10 Hz	SD (1s)	0.0391	0.0455	0.0925	0.0022	0.0089
69 μm spot	% RSD (1s)	0.30%	0.31%	0.28%	0.20%	0.36%
(n = 20)	Accuracy (%)	-0.07%	0.13%	-0.08%	0.21%	0.22%
614 standard	Mean	13.289	14.458	33.125	1.090	2.498
3 J cm^{-2}, 10 Hz	SD (1s)	0.0293	0.0795	0.1237	0.0036	0.0008
69 μm spot	% RSD (1s)	0.22%	0.55%	0.37%	0.33%	0.03%
(n = 3)	Accuracy (%)	0.11%	0.01%	0.07%	0.12%	0.17%

[a] all values in bold are the adopted average TIMS values for each matrix used in this investigation

[b] Hemming and Rasbury (2000)

Table 3-3. Average LA-MC-ICPMS lead isotope ratio values for sulfides matrices[a]

		$^{206}Pb/^{204}Pb$	$^{207}Pb/^{204}Pb$	$^{208}Pb/^{204}Pb$	$^{207}Pb/^{206}Pb$	$^{208}Pb/^{206}Pb$
PB-1		**20.586 ± 0.0346**	**15.834 ± 0.0052**	**39.559 ± 0.0419**	**0.7691 ± 0.0011**	**1.922 ± 0.0028**
612 standard	Mean	20.580	15.849	39.489	0.770	1.919
2 J cm^{-2}, 10 Hz	S.D.	0.038	0.058	0.127	0.002	0.005
30 μm spot	RSD (%)	0.19%	0.37%	0.32%	0.32%	0.26%
(n = 27)	Accuracy (%)	-0.03%	0.10%	-0.18%	0.06%	-0.16%
PB-1 standard	Mean	20.599	15.818	39.523	0.769	1.921
2 J cm^{-2}, 10 Hz	S.D.	0.040	0.051	0.108	0.002	0.005
30 μm spot	RSD (%)	0.19%	0.32%	0.27%	0.20%	0.25%
(n = 12)	Accuracy (%)	0.06%	-0.10%	-0.09%	-0.06%	-0.01%
B41		**18.566 ± 0.091**	**15.676 ± 0.004**	**38.168 ± 0.064**	**0.844 ± 0.004**	**2.056 ± 0.007**
612 standard	Mean	18.593	15.651	38.039	0.843	2.048
2 J cm^{-2}, 10 Hz	S.D.	0.049	0.057	0.141	0.003	0.005
30 μm spot	RSD (%)	0.26%	0.37%	0.37%	0.30%	0.25%
(n = 23)	Accuracy (%)	0.15%	-0.16%	-0.34%	-0.22%	-0.40%
PB-1 standard	Mean	18.596	15.701	38.152	0.844	2.053
2 J cm^{-2}, 10 Hz	S.D.	0.047	0.065	0.118	0.002	0.005
30 μm spot	RSD (%)	0.25%	0.42%	0.31%	0.27%	0.23%
(n = 12)	Accuracy (%)	0.17%	0.16%	-0.04%	-0.09%	-0.12%
MASS-1		**20.371 ± 0.277**	**15.802 ± 0.028**	**39.383 ± 0.232**	**0.778 ± 0.009**	**1.939 ± 0.0150**
612 standard	Mean	20.688	16.020	40.191	0.777	1.942
2 J cm^{-2}, 5 Hz	S.D.	0.373	0.284	0.463	0.000	0.010
20 μm spot	RSD (%)	1.80%	1.77%	1.15%	0.05%	0.52%
(n = 3)	Accuracy (%)	1.82%	1.38%	2.05%	-0.10%	0.17%
PB-1 standard	Mean	20.464	15.880	40.005	0.775	1.949
2 J cm^{-2}, 5 Hz	S.D.	0.977	0.775	1.964	0.001	0.001
20 μm spot	RSD (%)	4.77%	4.88%	4.91%	0.07%	0.03%
(n = 3)	Accuracy (%)	0.72%	0.49%	1.58%	-0.31%	0.55%

[a] all values in bold are the TIMS values for each matrix used in this investigation

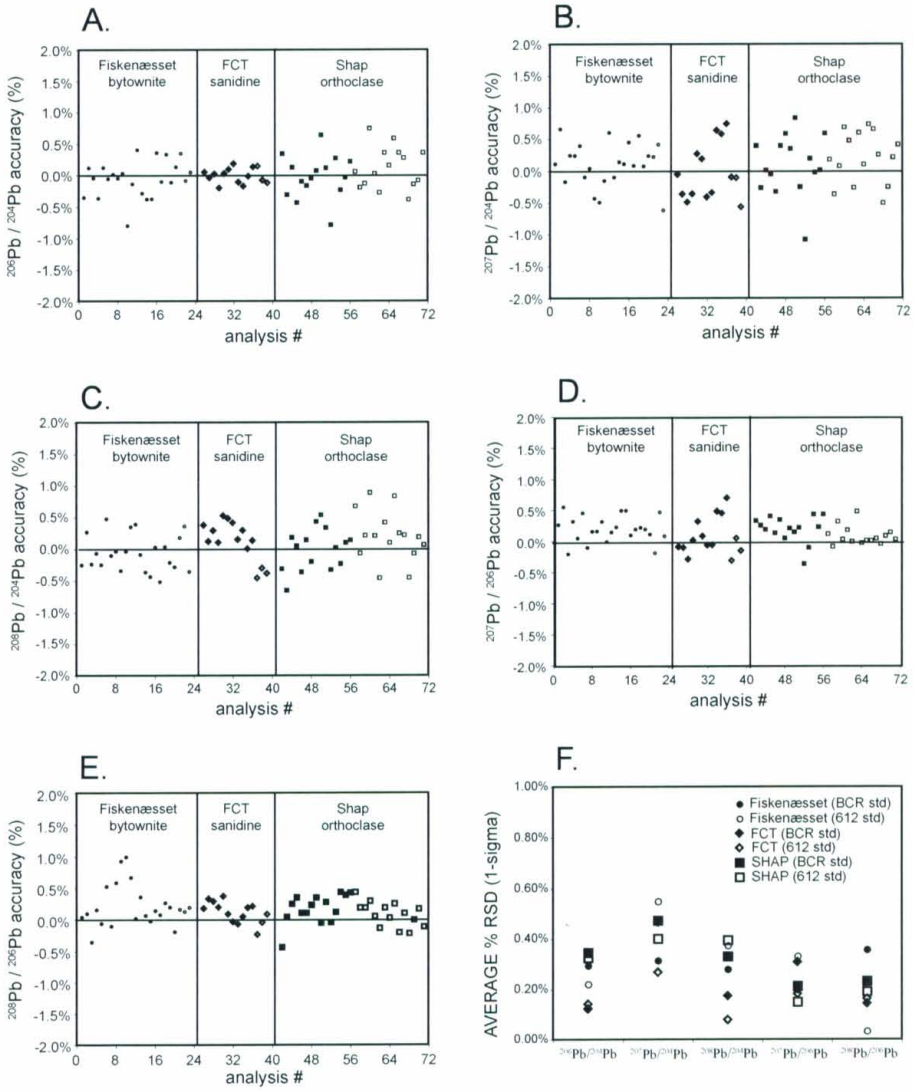

Figure 3-1: (A-E) Accuracy (%) of individual LA-MC-ICPMS lead isotope ratio measurements of the three feldspars used in this study, arranged from left to right in order of increasing lead concentration. Solid symbols indicate BCR2-G was used as the external calibrant. Open symbols indicate NIST 614 (Fiskenæsset bytownite) or NIST 612 (FCT sanidine and Shap orthoclase) was used as the reference standard. (F) Precision (% RSD, 1-sigma) of the average lead isotope ratio measurements for each of the feldspars analyzed is shown.

A. BCR2-G: 3 J cm^{-2}, 10 Hz, 69 μm spot

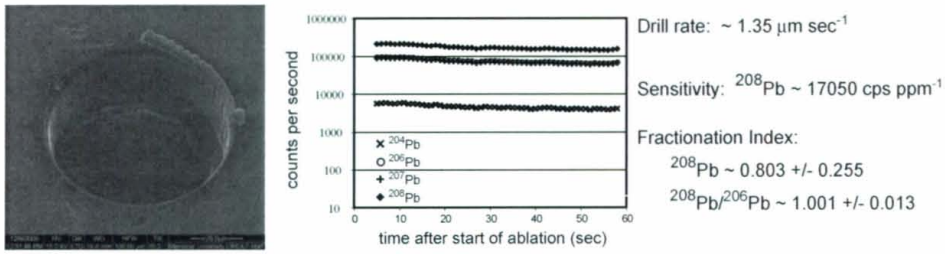

B. NIST 614: 3 J cm^{-2}, 10 Hz, 69 μm spot

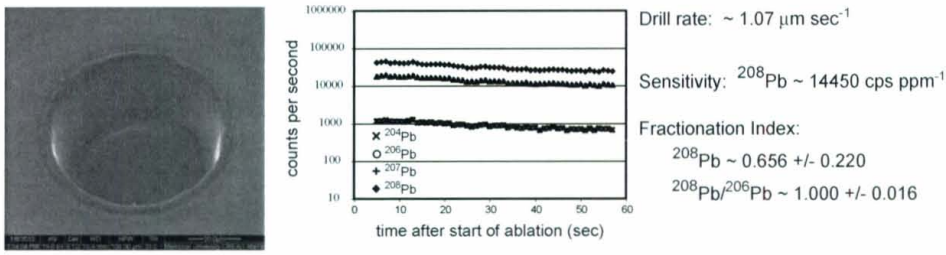

C. Fiskenæsset Bytownite: 3 J cm^{-2}, 10 Hz, 69 μm spot

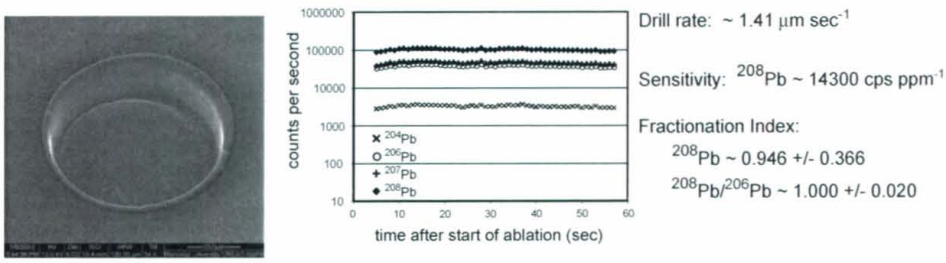

Figure 3-2: Representative examples of laser ablation craters and time-resolved Pb isotope spectra, apparent drill rates, sensitivity, and fractionation index for silicate glass standards and bytownite analyzed using laser ablation conditions of 3 J/cm^2, 10 Hz and a 69 μm laser spot. All secondary electron images included in this figure were taken after 30 seconds of ablation. The SEM stage is tilted at an angle of 35 degrees for each image. The first 4-5 sec of laser ablation are omitted from each time-resolved plot due to scatter. Drill rates were calculated by directly measuring the surface to depth distance of a representative crater for each matrix created under ablation conditions identical to those used for individual analyses, and then dividing this distance by the ablation time to produce the crater. Further details about the images, SEM parameters, and ablation rate calculations can be found in Supplemental file S3-3. Sensitivity is normalized to isotopic abundance for ^{208}Pb from the average TIMS values or the calibration values adopted for this study (Tables S3-1 and S3-2). Both the sensitivity and fractionation indices are calculated by taking the average of three representative analyses of the stated matrix.

A. BCR2-G: 3 J cm^{-2}, 10 Hz, 30 μm spot

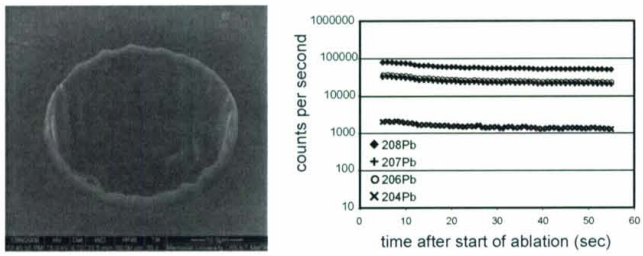

Drill rate: ~ 0.81 μm sec^{-1}

Sensitivity: ^{208}Pb ~ 9600 cps ppm^{-1}

Fractionation Index:

^{208}Pb ~ 0.822 +/- 0.002

^{208}Pb/^{206}Pb ~ 0.993 +/- 0.007

B. NIST 612: 3 J cm^{-2}, 10 Hz, 30 μm spot

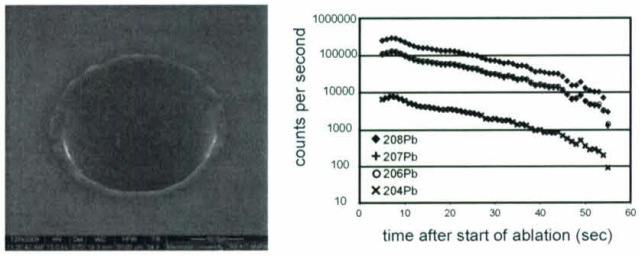

Drill rate: ~ 0.70 μm sec^{-1}

Sensitivity: ^{208}Pb ~ 8100 cps ppm^{-1}

Fractionation Index:

^{208}Pb ~ 0.583 +/- 0.166

^{208}Pb/^{206}Pb ~ 1.000 +/- 0.001

C. Shap orthoclase: 3 J cm^{-2}, 10 Hz, 30 μm spot

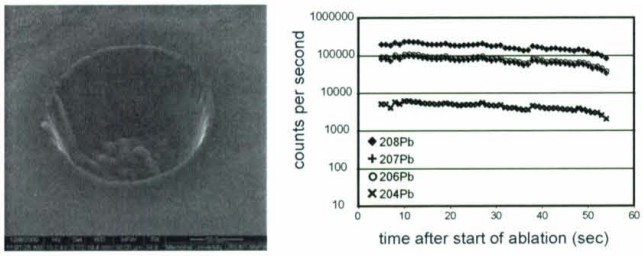

Drill rate: ~ 0.60 μm sec^{-1}

Sensitivity: ^{208}Pb ~ 8800 cps ppm^{-1}

Fractionation Index:

^{208}Pb ~ 0.973 +/- 0.053

^{208}Pb/^{206}Pb ~ 1.007+/- 0.015

D. FCT sanidine: 3 J cm^{-2}, 10 Hz, 30 μm spot

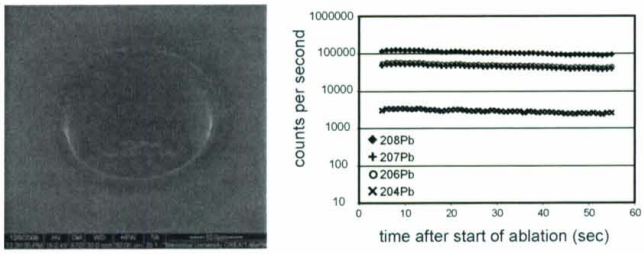

Drill rate: ~ 0.78 μm sec^{-1}

Sensitivity: ^{208}Pb ~ 7800 cps ppm^{-1}

Fractionation Index:

^{208}Pb ~ 0.891 +/- 0.046

^{208}Pb/^{206}Pb ~ 1.002 +/- 0.002

Figure 3-3: Representative laser ablation craters and time-resolved lead isotope spectra, apparent drill rates, sensitivity and fractionation index for silicate glass standards and two feldspars analyzed using laser ablation conditions of 3 J/cm^2, 10 Hz and a 30 μm laser spot. Details on the images and calculations are the same as those stated in Figure 3-2.

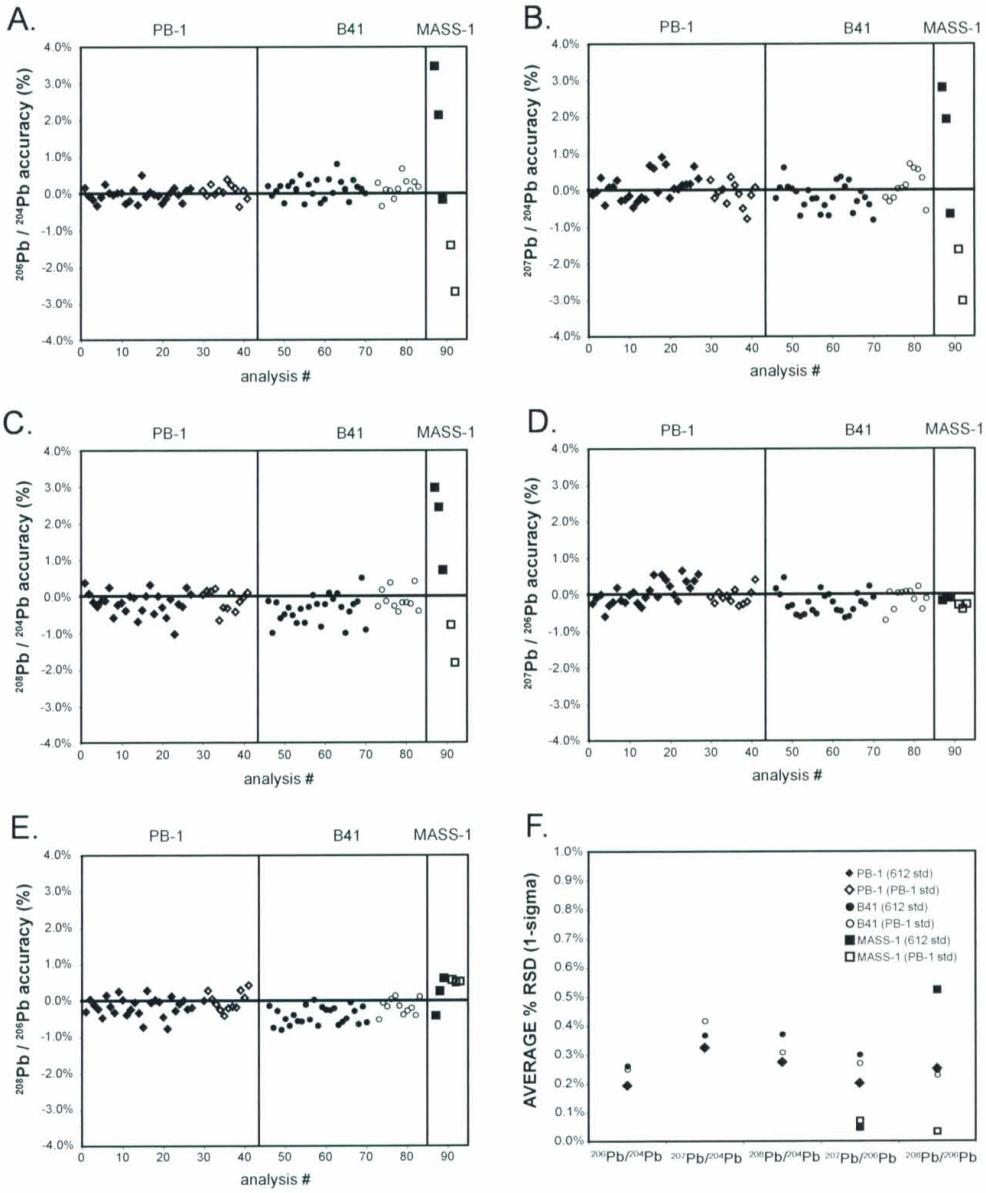

Figure 3-4: (A-E) Accuracy (%) of individual LA-MC-ICPMS lead isotope ratio measurements for the three sulfides analyzed in this study, arranged from left to right in order of increasing lead concentration. Solid symbols indicate NIST 612 was the external calibration material and open symbols indicate PB-1 was used as the standard. (F) Precision (% RSD, 1-sigma) of the average lead isotope ratio measurements for each of the sulfides analyzed in this study.

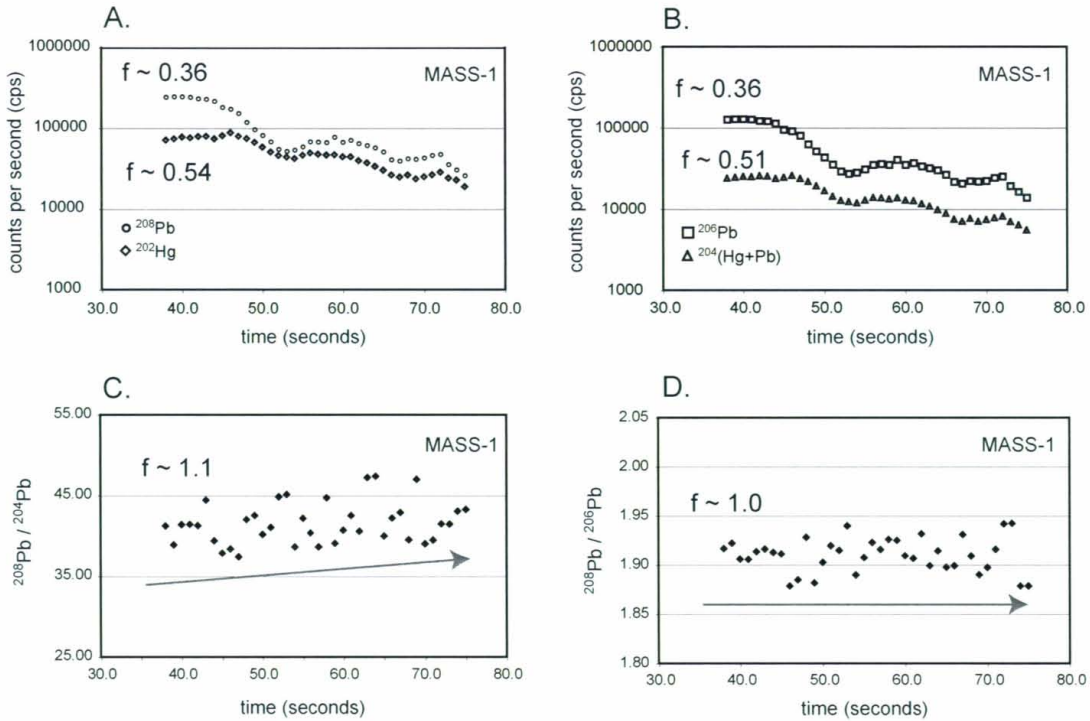

Figure 3-5: Representative MASS-1 (2 J/cm^2, 5 Hz, 20 μm laser spot) time-resolved spectra of individual lead and mercury isotopes (A and B) and corrected $^{208}Pb/^{204}Pb$ and $^{208}Pb/^{206}Pb$ (C and D) displaying different fractionation behavior. The fractionation index (f), a measure of changes in analyte signals during laser ablation, is listed for each isotope of isotope ratio. The fractionation index is calculated by dividing the mean background corrected intensity of a measured isotope or isotope ratio for the second half of the ablation interval by the mean background corrected intensity of the same measured isotope or isotope ratio for the first half of the ablation interval. In A and B, the intensity of the lead isotopes decreases somewhat faster than the mercury isotopes. The corrected $^{208}Pb/^{204}Pb$ in (C) progressively increases over the ablation interval due to systematic errors in the ^{204}Hg correction related to differences in the fractionation behavior between mercury and lead. This increase is not observed for lead isotope ratios normalized to ^{206}Pb (D).

A. NIST 612: 2 J cm^{-2}, 10 Hz, 30 μm spot

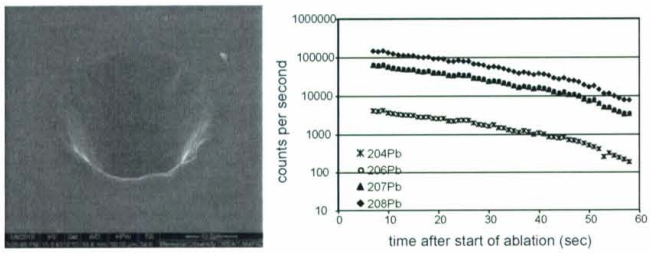

Drill rate: ~ 0.31 μm sec^{-1}

Sensitivity: ^{208}Pb ~ 6900 cps ppm^{-1}

Fractionation Index:

^{208}Pb ~ 0.363 +/- 0.165

^{208}Pb/^{206}Pb ~ 1.010 +/- 0.074

B. PB-1: 2 J cm^{-2}, 10 Hz, 30 μm spot

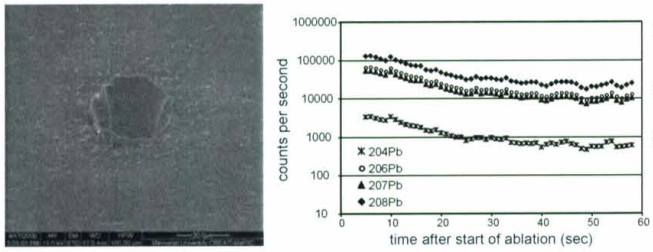

Drill rate: ~ 0.41 μm sec^{-1}

Sensitivity: ^{208}Pb ~ 11200 cps ppm^{-1}

Fractionation Index:

^{208}Pb ~ 0.362 +/- 0.195

^{208}Pb/^{206}Pb ~ 0.996 +/- 0.023

C. B41: 2 J cm^{-2}, 10 Hz, 30 μm spot

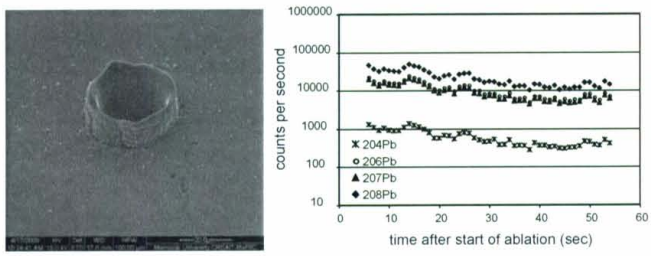

Drill rate: ~ 0.37 μm sec^{-1}

Sensitivity: ^{208}Pb ~ 10600 cps ppm^{-1}

Fractionation Index:

^{208}Pb ~ 0.391 +/- 0.169

^{208}Pb/^{206}Pb ~ 0.996 +/- 0.023

Figure 3-6: Representative laser ablation craters and time-resolved lead isotope spectra, apparent drill rates, sensitivity and fractionation index for NIST 612 and sulfides analyzed using laser ablation conditions of 2 J/cm^2, 10 Hz and a 30 μm laser spot. Imaging and calculation details are the same as those given for Figure 3-2.

A. NIST 612: 2 J cm^{-2}, 5 Hz, 20 μm spot

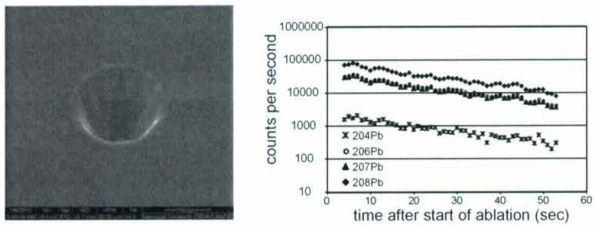

Drill rate: ~ 0.31 μm sec^{-1}

Sensitivity: ^{208}Pb ~ 2700 cps ppm^{-1}

Fractionation Index:

^{208}Pb ~ 0.342 +/- 0.182

^{208}Pb/^{206}Pb ~ 1.002 +/- 0.055

B. PB-1: 2 J cm^{-2}, 5 Hz, 20 μm spot

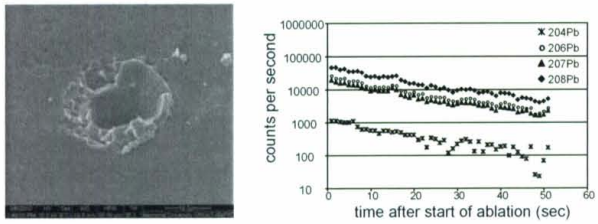

Drill rate: ~ 0.24 μm sec^{-1}

Sensitivity: ^{208}Pb ~ 5700 cps ppm^{-1}

Fractionation Index:

^{208}Pb ~ 0.264 +/- 0.148

^{208}Pb/^{206}Pb ~ 1.000 +/- 0.023

C. MASS-1: 2 J cm^{-2}, 5 Hz, 20 μm spot

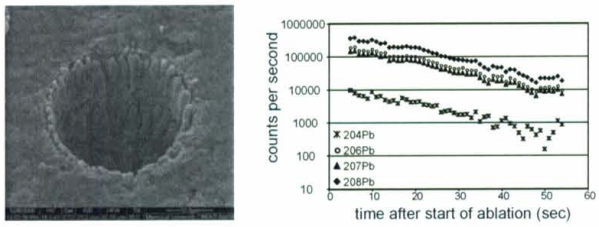

Drill rate: ~ 0.72 μm sec^{-1}

Sensitivity: ^{208}Pb ~ 8700 cps ppm^{-1}

Fractionation Index:

^{208}Pb ~ 0.189 +/- 0.127

^{208}Pb/^{206}Pb ~ 0.992 +/- 0.030

Figure 3-7: Representative laser ablation craters, time-resolved lead isotope spectra, drill rates, sensitivity and fractionation index for NIST 612 and sulfides analyzed using laser ablation conditions of 2 J/cm^2, 5 Hz and a 20 μm laser spot. Refer to Figure 3-2 for imaging and calculation details.

Supplemental File S3-1: Method – Thermal Ionization Mass Spectrometry (TIMS)

Feldspar minerals and sulfides chosen for thermal ionization mass spectrometry (TIMS) analysis were in the form of coarse solid fragments prior to dissolution with the exception of USGS MASS-1, which was a powder. All TIMS analytical work was performed in the Boise State University Isotope Geology Laboratory (IGL). For the feldspar minerals, each individual sample was between ~0.003 and 0.01g. Prior to dissolution, any potential surface contamination was removed from the feldspar separates through a series of steps. First, 1 mL of 3.5 N HNO_3 was added to each sample, the sample was capped and placed on a hot plate at 120 C for ~30 minutes. The HNO_3 was then removed with a pipette and each sample was rinsed three-times with milli-Q H_2O. 1 mL of 6M HCl was then added to each sample and again each sample was capped and placed on a hotplate set at 120 C. After ~30 minutes, the HCl was removed with a pipette and each feldspar separate was rinsed three-times with 0.5 mL milli-Q H_2O. Following the milli-Q H_2O rinse, a mixture of 1 mL concentrated (16M) HNO_3 and 3 mL concentrated (29M) HF was added to each sample. Each feldspar sample was then capped and placed on a hotplate set at ~150 C overnight. For the solid sulfide samples PB-1 and B41, 0.004 to 0.015 g chunks were dissolved in a mixture of 0.5 mL concentrated (16M) HNO_3 and 0.2 mL concentrated (16M) HCl mixture overnight on a hotplate set at ~150 C. Prior to dissolution, each sulfide solid was rinsed three-times with milli-Q H_2O and sonicated in milli-Q H_2O for 10 minutes to remove any surface contamination. For MASS-1, the sulfide powder, ~ 0.01 g of power was dissolved in a

mixture of 3 mL concentrated (16M) HNO_3 and 1 mL concentrated (16M) HCl and fluxed on a hotplate at ~150 C overnight.

After one night fluxing on a hotplate at ~150 C, all samples were fully dissolved in their respective acid mixtures. Each sample beaker was then uncapped and placed back on a hotplate under a heat lamp until dry. Once dry, 1 mL of concentrated (16M) HCl was added to each sample. Capped samples were then sonicated for ~1 hour. An additional 4 mL of 6M HCl (feldspar samples and MASS-1) or 1 mL of 6M HCl (PB-1 and B41) was added to each sample, the beakers capped and each sample was again placed back on a hotplate set at ~120 C to flux overnight. After ~24 hours on a hotplate, all samples were fully dissolved in 6M HCl. Each sample beaker was uncapped and the samples dried down to salts on a hotplate. Both feldspar and sulfide samples were and then converted to $PbBr_4^{2-}$ by adding 1 mL 0.5M HBr to each sample and placing on the hot plate until dry. Prior to ion exchange chromatography, each sample was redissolved in 1 mL of 0.5M HBr. Lead was separated from each matrix using ion-exchange columns filled with 100 μL (resin volume) AG1-X8, 200-400 mesh, and HCl-based anion exchange chromatography procedures.

Lead was analyzed on the Isoprobe-T thermal ionization mass spectrometer. Lead was loaded on single Re filaments with 1 – 2 μL of a dilute silica gel – 0.1M H_3PO_4 emitter solution. Lead was measured in static mode, maintaining a 3V ^{208}Pb beam for 200 cycles, or, for very small amounts of lead, dynamically peak-switching all ion beams into the Daly detector. TIMS lead isotope ratio results for the feldspars and sulfide minerals adopted for this study are listed in Table S3-2.

Supplemental File S3-2: Sample characterization/description

Prior to analysis, small separates (≤ 1 mm in thickness and no greater than 5 mm in any surface direction) of all silicate glasses, feldspars and sulfides were mounted in 10 mm or 25 mm diameter epoxy resin mounts and once cured, ground down to a flat surface and polished using diamond abrasive to expose a cross-sectional surface of each material. Sulfides and silicates were placed in separate epoxy mounts and the sulfides were polished on polishing cloths specifically designated for sulfide minerals.

The Shap orthoclase has been used in several other investigations (Clift et al., 2008; Tyrrell et al., 2009) as a secondary standard due to its homogeneous lead isotope composition on the μm-scale of a laser ablation analysis (Tyrrell et al., 2006). The Fish Canyon Tuff (FCT) sanidine has been analyzed for trace element concentrations, including lead, by Bachmann et al. (2005). TIMS lead isotope ratio values for the FCT sanidine adopted for this study are those determined by Hemming and Rasbury (2000). The bulk compositions of all three feldspars are given in Table S3-3.

Three different synthetic sulfides were analyzed as part of this investigation. Bulk analyses of the three sulfides are presented in Table S4-4. Surface images highlighting the differences in physical character of the 3 sulfides analyzed are presented in Figure S3-2.1.

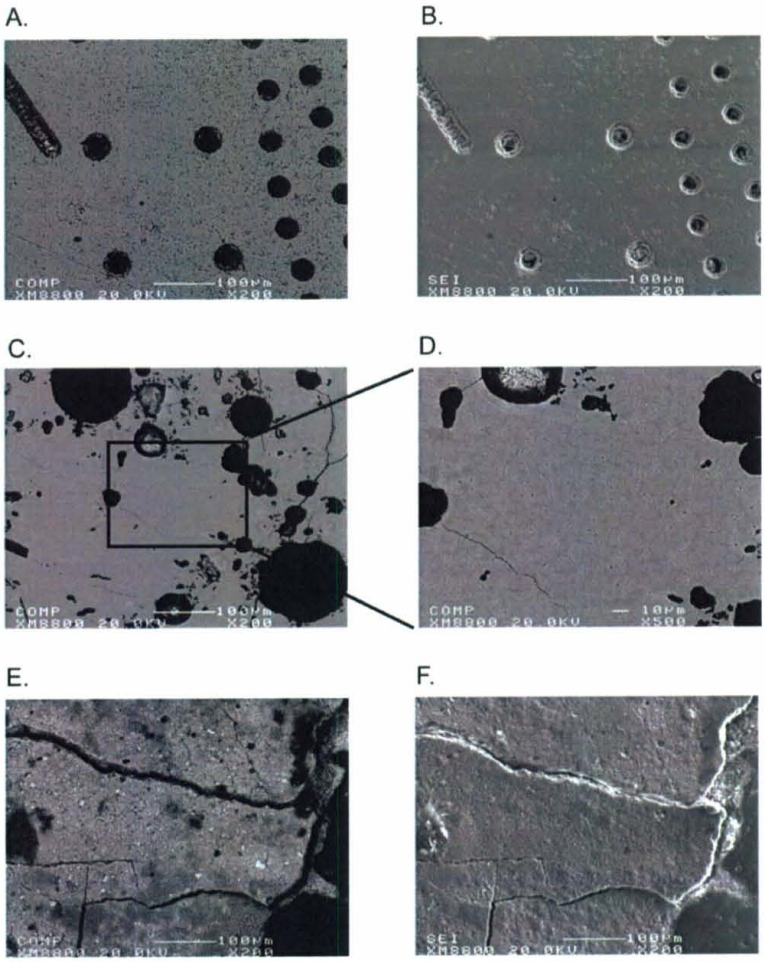

Figure S3-2.1: (A) Back-scattered electron (BSE) and (B) Secondary electron (SE) images of the same surface area of sulfide glass, PB-1. 30 – 40 μm diameter laser ablation pits and line scans mark the surface of the sulfide. (C and D) BSE images of sulfide sinter B-41 taken at two different magnifications. The area within the box in C is image D. The subtle changes in the gray-scale best seen in image D most likely are the result of individual grains approaching their melting points. (E) BSE and (F) SE images of the same surface area of pressed powder pellet MASS-1. Individual grains of different compositions can be readily identified in the BSE image by the varying levels of brightness. All images were collected on the JXA JEOL-8900L superprobe at McGill University.

Supplemental File S3-3: Ablation rate determination procedures

Ablation rates were calculated by dividing the surface to depth distance (μm) of a laser ablation crater by the ablation time to produce the crater (seconds). Representative craters for each matrix were drilled under ablation conditions identical to those used for each experiment. In order to monitor changes in pit morphology during the laser ablation interval, representative craters were produced for 10 seconds, 30 seconds and 60 seconds of laser ablation (3 different craters/matrix/set of ablation conditions). Secondary electron (SE) images of each crater were taken using a FEI Quanta 400 environmental secondary electron microscope (SEM) with an accelerating voltage of 15 kV and a beam diameter of 3.14 μm.

The surface to depth distance was determined in a series of steps (Figure A3.1). First, a SE image of the crater was taken to identify major physical features on the floor and walls of the pit. The SEM stage was then tilted to a 35 degree angle and a second SE image of the same crater was taken, making sure the SEM working distance (~20 mm) remained constant. Once distinguishing morphological features on the floor and walls of the crater had been identified, the tilt on the SEM stage was adjusted until the near-side crater rim was in line with the intersection of the crater floor and far-side crater wall (Figure S3-3.1). The tilt angle of the SEM stage was recorded and a third SE image was taken. After the proper tilt angle of the SEM stage was determined, the distance between the near-side crater rim and the crater wall/crater floor intersection point was measured directly from the 'in-line' tilted SE crater image. The surface to depth distance was calculated using the formula:

$$h = w * \tan(90 - \theta)$$

where:
h = surface to depth distance
w = crater width measured from 'in-line' tilted image
θ = tilt angle of the SEM stage for 'in-line' image

The apparent drill rates calculated are a function of how fast the laser is drilling down into a matrix over a given period of time and how much material is excavated from the crater within the same time interval. Our method also assumes both the sample surface and crater floor intersect the crater walls at right angles and the surface pit width equals the pit width on the crater floor. Determining the crater depth from sample surface to crater floor is critical when calculating drill rates, yet this quantitative measurement is obscured by melt deposition along the crater rim extending above the sample surface, and the build-up of melt droplet piles on the crater floor. The crater depth calculation assumes each crater is a cylinder, with a top and bottom of equal diameter and straight sides. This method does not account for tapering of the crater walls. Although variations exist between matrices, the estimate of the error on our apparent drill rate calculations does not exceed 20% of the calculated ablation rate. For example, if a 2 μm tall rim is associated with each ablation pit, the crater depth would decrease up to 11 % and there would be up to an 11% decrease in calculated drill rates. If we assume an ~8 μm high melt droplet pile on each crater floor, the crater depth would increase by up to 20 %. This translates to an ~20 % increase in the drill rates calculated. It is important to note when considering the potential errors on the apparent drill rate calculations that the

difference in drill rates between the ~30 μm diameter craters and the ~69 μm diameter craters are still distinct.

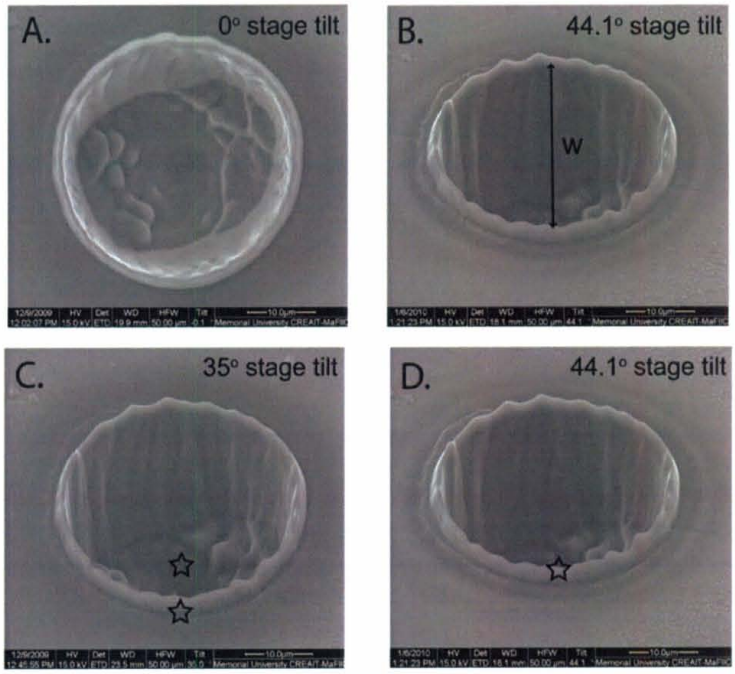

Figure S3-3.1: Secondary electron (SE) crater images. (A) Initial SE image taken to aid in the identification of major morphological features inside the crater. (B) Distance measured on 'in-line' tilt image to determine crater width (w). (C) Thirty-five degree stage-tilt SE image. The near-side crater rim and the intersection of the crater floor and far-side crater wall are marked with stars. (D) 'In-line' SE tilt image. The star marks where the near-side crater rim and the intersection of the crater floor and far-side crater wall are lined up.

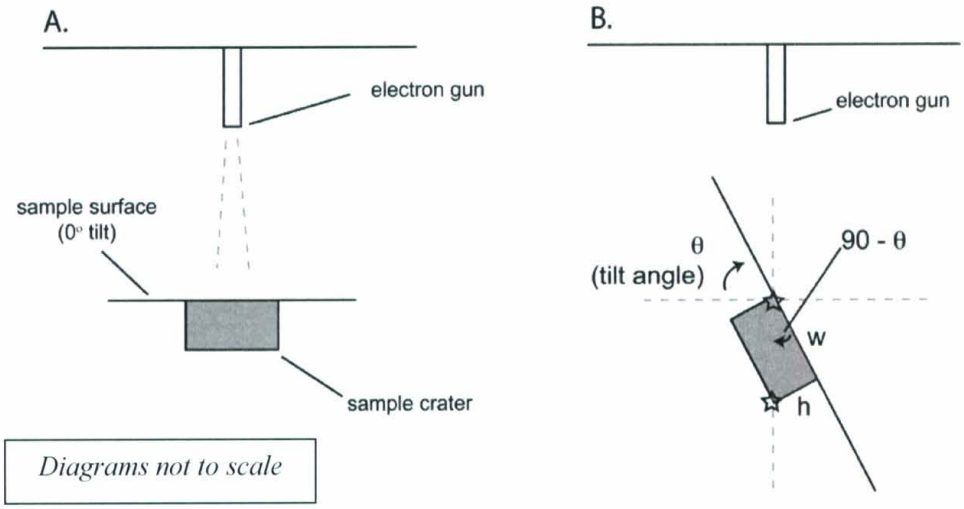

Figure S3-3.2: Schematic cross-section of the SEM chamber with (A) the stage at 0° tilt and (B) the stage tilted to an angle (θ) where the near-side crater rim and the intersection of the crater floor and far-side crater wall are in-line. Both the near-side crater rim and the intersection of the crater floor with the far-side crater wall are marked with stars. The crater width (w) and surface to depth distance (h) are also labeled. Both diagrams are not to scale.

Supplemental File S3-4: Supplemental File References

Bachmann O., Dungan M.A. and Bussy R. (2005) Insights into shallow magmatic processes in large silicic magma bodies: the trace element record in the Fish Canyon magma body, Colorado. *Contrib. Mineral. Petrol.* **149**, 338 – 349.

Baker J., Peate D., Waight T. and Meyzen C. (2004) Pb isotopic analysis of standards and samples using a $^{207}Pb - ^{204}Pb$ double spike and thallium to correct for mass bias with a double-focusing MC-ICP-MS. *Chemical Geology*, **211**, 275 – 303.

Clift P.D. Van Long H., Hinton R., Ellam R.M., Hannigan R., Tan M.T. Blusztajn J. and Duc N.A. (2008) Evolving east Asian river systems reconstructed by trace element and Pb and Nd isotope variations in modern and ancient Red River-Song Hong sediments. *Geochem. Geophys. Geosyst.* **9**, Q04039, DOI:10.1029/2007GC001867.

Hemming S.R. and Rasbury E.T. (2000) Pb isotope measurements of sanidine monitor standards: implications for provenance analysis and tephrochronology. *Chem. Geol.* **165**, 331 – 337.

Tyrrell S., Haughton P.D.W., Daly J.S., Kokfelt T.F. and Gagnevin D. (2006) The use of the common Pb isotope composition of detrital K-feldspar grains as a provenance tool and its application to Upper Carboniferous palaeodrainage, Northern England. *J. Sed. Res.* **76**, 324 – 345.

Tyrrell S., Leleu S., Souders A.K., Haughton P.D.W. and Daly J.S. (2009) K-feldspar sand-grain provenance in the Triassic, west of Shetland: distinguishing first-cycle and recycled sediment sources? **44**, 692 – 710.

Wilson S.A., Ridley W.I. and Koenig A.E. (2002) Development of sulfide calibration standards for the laser ablation inductively-coupled plasma mass spectrometry technique. *J. Anal. At. Spectrom.* **17**, 4006 – 40.

Table S3-1. Calibration values for silicate glasses used for LA-MC-ICPMS lead isotope analysis

Sample	$^{206}Pb / ^{204}Pb$	2SD	$^{207}Pb / ^{204}Pb$	2SD	$^{208}Pb / ^{204}Pb$	2SD	$^{207}Pb / ^{206}Pb$	2SD	$^{208}Pb / ^{206}Pb$	2SD	reference
BCR2-G	18.765	0.014	15.626	0.012	38.73	0.04	0.833	0.002	2.066	0.002	GeoREM preferred
NIST 612	17.099	0.003	15.516	0.002	37.02	0.007	0.90745	0.0017	2.1651	0.001	Baker et al. (2004)
NIST 614	17.842	0.01	15.541	0.001	37.499	0.009	0.87101	0.0004	2.1017	0.001	Baker et al. (2004)

Table S3-2. Thermal Ionization Mass Spectrometry (TIMS) Pb isotope ratios for the sulfide and feldspars analyzed and/or included in this investigation.

Sample		$^{206}Pb/^{204}Pb$ [1]	$\%s_m$ [2]	$^{207}Pb/^{204}Pb$ [1]	$\%s_m$ [2]	$^{208}Pb/^{204}Pb$ [1]	$\%s_m$ [2]	$^{207}Pb/^{206}Pb$ [1]	$\%s_m$ [2]	$^{208}Pb/^{206}Pb$ [1]	$\%s_m$ [2]
PB-1-1	sulfide glass	20.606	0.002	15.839	0.003	39.607	0.003	0.76869	0.0006	1.9221	0.0010
PB-1-2	sulfide glass	20.546	0.002	15.829	0.002	39.533	0.002	0.77043	0.0005	1.9241	0.0007
PB-1-3	sulfide glass	20.606	0.003	15.832	0.003	39.536	0.003	0.76831	0.0006	1.9186	0.0010
	AVERAGE	20.586		15.834		39.559		0.769		1.922	
	SD (1s)	0.0346		0.0052		0.0419		0.0011		0.0028	
	%RSD (1s)	0.17%		0.03%		0.11%		0.15%		0.14%	
Mass1-A	pressed powder	20.000	0.006	15.771	0.006	39.118	0.007	0.7887	0.0010	1.9561	0.0017
Mass1-B	pressed powder	20.443	0.005	15.810	0.005	39.477	0.005	0.7734	0.0007	1.9311	0.0012
Mass1-C	pressed powder	20.509	0.004	15.825	0.004	39.553	0.005	0.7716	0.0007	1.9286	0.0012
	AVERAGE	20.317		15.802		39.383		0.778		1.939	
	SD (1s)	0.2772		0.0278		0.2322		0.0094		0.0152	
	%RSD (1s)	1.36%		0.18%		0.59%		1.20%		0.78%	
B41 A	sulfide sinter	18.623	0.004	15.678	0.004	38.209	0.004	0.8419	0.0007	2.0518	0.0006
B41 B	sulfide sinter	18.461	0.010	15.672	0.011	38.094	0.011	0.8489	0.0013	2.0635	0.0022
B41 C	sulfide sinter	18.613	0.003	15.678	0.003	38.202	0.003	0.8423	0.0008	2.0524	0.0008
	AVERAGE	18.566		15.676		38.168		0.844		2.056	
	SD (1s)	0.0907		0.0035		0.0642		0.0040		0.0066	
	%RSD (1s)	0.02%		0.02%		0.17%		0.47%		0.32%	
SHAP A (lg)	orthoclase	18.267	0.001	15.662	0.001	38.281	0.001	0.8574	0.0003	2.0956	0.0005
SHAP B	orthoclase	18.272	0.002	15.649	0.002	38.236	0.002	0.8565	0.0004	2.0926	0.0005
SHAP C	orthoclase	18.243	0.002	15.649	0.002	38.240	0.002	0.8578	0.0004	2.0961	0.0005
SHAP D	orthoclase	18.302	0.002	15.662	0.002	38.276	0.002	0.8558	0.0004	2.0913	0.0004
	AVERAGE	18.271		15.656		38.258		0.857		2.094	
	SD (1s)	0.0242		0.0074		0.0236		0.0009		0.0023	
	%RSD (1s)	0.13%		0.05%		0.06%		0.11%		0.11%	
159430 (lg)	bytownite	13.308	0.001	14.442	0.001	33.074	0.001	1.0852	0.0003	2.4854	0.0003
159430 A	bytownite	13.246	0.015	14.441	0.015	33.060	0.015	1.0902	0.0018	2.4959	0.0018
159430B	bytownite	13.272	0.010	14.490	0.010	33.173	0.011	1.0919	0.0050	2.4999	0.0049
	AVERAGE	13.275		14.457		33.103		1.089		2.494	
	SD (1s)	0.0308		0.0281		0.0612		0.0035		0.0075	
	%RSD (1s)	0.23%		0.19%		0.19%		0.32%		0.30%	
Fish Canyon Sanidine(10 gr, 1.3 mg) [3]		18.483	0.043	15.617	0.051	37.865	0.066	0.8449	0.0007	2.0486	0.0008
Fish Canyon Sanidine(10 gr, 2.1 mg) [3]		18.461	0.010	15.591	0.016	37.74	0.018	0.8445	0.0002	2.0443	0.0002
	AVERAGE	18.472		15.604		37.8025		0.8447		2.0465	
	SD (1s)	0.016		0.018		0.088		0.000		0.003	
	%RSD (1s)	0.08%		0.12%		0.23%		0.03%		0.15%	

1 - ratios reported fractionation corrected 0.11%/amu based upon repeated measurements of NBS-981, NBS-982 and BCR-1

2 - $\%s_M$ is internal relative 1-sigma standard error; fractionation uncertainty imposes the following conservative absolute uncertainties (1-sigma): 208Pb/204Pb, 0.019; 207Pb/204Pb, 0.007; 206Pb/204Pb, 0.008; 208Pb/206Pb, 0.0009; 207Pb/206Pb, 0.0004

3 - Pb isotope ratios from Hemming and Rasbury (2000)

Table S3-3: Major element composition and lead concentration of feldspars analyzed.

SAMPLE	METHOD		SiO2 wt (%)	Al2O3 wt (%)	FeO wt (%)	MgO wt (%)	CaO wt (%)	Na2O wt (%)	K2O wt (%)	BaO wt (%)	Cl wt (%)	Total	Pb [2] ppm
Shap orthoclase	EMP[1]	Average (n=10)	64.82	18.56	0.08	0.01	0.05	1.61	14.24	0.34	< LD	99.70	~35
		Stdev	0.337	0.113	0.020	0.007	0.045	0.786	1.168	0.155			
Fiskenæsset bytownite	EMP[1]	Average (n=24)	46.74	33.81	0.11	N/A	17.27	1.82	0.04	< LD	0.08	99.88	~6.25
		Stdev	1.185	0.719	0.019		0.823	0.473	0.017		0.046		
FCT sanidine	EMP[1]	Average (n=12)	64.78	18.75	0.11	< LD	0.17	2.65	12.46	0.78	< LD	99.69	~20
			0.534	0.149	0.024		0.014	0.079	0.155	0.438			

< LD: below detection limits

[1] EMP data for feldspars collected on the JXA JEOL-8900L superprobe at McGill University with an accelerating voltage of 15 kV, beam current of 20 nA, using a 5 um beam and a 20 second counting time for each element of interest.

[2] Shap orthoclase total Pb concentration fromTyrrell et al. (2006) and average FCT sanidine total Pb concentration from Bachmann et al. (2005)

Table S3-4: Major element composition and Pb concentration of sulfides analyzed.

SAMPLE	METHOD		Zn wt (%)	Ni wt (%)	S wt (%)	Fe wt (%)	Co wt (%)	Cu wt (%)	Pb[1] (ppm)
PB-1	EMP[2]	Average (n=22)	-	4.897	37.475	57.046	-	-	19.417
		Stdev	-	0.0458	0.1788	0.2114	-	-	
B41	EMP[2]	Average (n=24)	-	6.894	36.870	51.094	-	4.706	15.788
		Stdev	-	0.8465	0.5881	1.9370	-	3.3423	
MASS-1	various[3]		21	-	27.6	15.6	67	13.4	
	solution - ICPMS[4]		18.74	-	-	11.799	-	13.636	67.273

[1] Pb concentration determined by solution ICP-MS at Memorial University

[2] EMP data for PB-1 and B41 collected on the JXA JEOL-8900L superprobe at McGill University with an accelerating voltage of 20 kV, beam current of 30 nA, using a3 um beam and a 20 second counting time for each element of interest.

[3] Zn, Fe, Cu determined by electron microprobe (EM), solution ICPMS, and ICP atomic emission spectrometry; Co analyzed by solution ICPMS and instrumental neutron activation analysis (INAA); S determined by cumbustion infared spectroscopy (CIS) (Wilson et al. 2002)

[4] average values determined by solution ICP-MS at Memorial University and Charles University

Table S3-5: LA-MC-ICPMS lead isotope ratios for three feldspar matrices (Souders and Sylvester, 2010)

Sample	Analysis ID	Std	$^{206}Pb/^{204}Pb$	std error (1-sigma)	$^{207}Pb/^{204}Pb$	std error (1-sigma)	$^{208}Pb/^{204}Pb$	std error (1-sigma)	$^{207}Pb/^{206}Pb$	std error (1-sigma)	$^{208}Pb/^{206}Pb$	std error (1-sigma)
Shap orthoclase	oc13b16	BCR2G	18.334	0.095	15.719	0.092	38.141	0.292	0.860	0.002	2.085	0.006
Shap orthoclase	oc13b17	BCR2G	18.215	0.102	15.615	0.096	38.010	0.300	0.859	0.002	2.095	0.005
Shap orthoclase	oc13b18	BCR2G	18.294	0.097	15.658	0.092	38.329	0.293	0.859	0.002	2.099	0.006
Shap orthoclase	my01b12	BCR2G	18.192	0.138	15.649	0.099	38.277	0.214	0.860	0.003	2.101	0.005
Shap orthoclase	my01b24	BCR2G	18.254	0.167	15.606	0.125	38.122	0.291	0.858	0.003	2.096	0.005
Shap orthoclase	my01c05	BCR2G	18.242	0.182	15.719	0.145	38.315	0.376	0.860	0.002	2.096	0.004
Shap orthoclase	my01c12	BCR2G	18.263	0.237	15.748	0.202	38.183	0.465	0.857	0.003	2.099	0.006
Shap orthoclase	my01d05	BCR2G	18.285	0.120	15.711	0.109	38.426	0.266	0.859	0.003	2.101	0.007
Shap orthoclase	my01d12	BCR2G	18.388	0.128	15.787	0.117	38.466	0.281	0.858	0.003	2.093	0.007
Shap orthoclase	my01e05	BCR2G	18.293	0.137	15.617	0.124	38.390	0.320	0.859	0.002	2.100	0.005
Shap orthoclase	my01e12	BCR2G	18.127	0.119	15.487	0.114	38.135	0.290	0.854	0.002	2.093	0.005
Shap orthoclase	my01f05	BCR2G	18.322	0.204	15.687	0.203	38.267	0.475	0.856	0.003	2.097	0.006
Shap orthoclase	my01g12	BCR2G	18.229	0.158	15.653	0.143	38.170	0.313	0.861	0.003	2.103	0.008
Shap orthoclase	my02b05	BCR2G	18.265	0.069	15.659	0.070	38.299	0.161	0.859	0.001	2.102	0.003
Shap orthoclase	my02b12	BCR2G	18.311	0.088	15.749	0.086	38.314	0.194	0.861	0.002	2.103	0.003
Shap orthoclase	oc13d19	612	18.282	0.051	15.685	0.047	38.519	0.140	0.858	0.001	2.103	0.004
Shap orthoclase	oc13d20	612	18.237	0.064	15.600	0.061	38.234	0.171	0.856	0.001	2.098	0.003
Shap orthoclase	oc13d21	612	18.247	0.069	15.669	0.069	38.342	0.167	0.860	0.001	2.098	0.003
Shap orthoclase	my01a04	612	18.407	0.110	15.764	0.082	38.601	0.248	0.857	0.002	2.100	0.005
Shap orthoclase	my02c12	612	18.276	0.071	15.731	0.064	38.340	0.143	0.859	0.002	2.095	0.003
Shap orthoclase	my02d04	612	18.221	0.074	15.616	0.073	38.086	0.166	0.857	0.002	2.091	0.003
Shap orthoclase	my02d12	612	18.337	0.068	15.751	0.064	38.421	0.121	0.861	0.002	2.098	0.002
Shap orthoclase	my02e04	612	18.300	0.079	15.672	0.064	38.297	0.155	0.857	0.002	2.095	0.003
Shap orthoclase	my02e12	612	18.379	0.068	15.771	0.060	38.581	0.144	0.857	0.002	2.099	0.003
Shap orthoclase	my02e24	612	18.338	0.077	15.760	0.076	38.355	0.181	0.857	0.002	2.090	0.004
Shap orthoclase	my02f04	612	18.322	0.082	15.697	0.070	38.343	0.173	0.857	0.001	2.096	0.003
Shap orthoclase	my02f12	612	18.201	0.094	15.578	0.071	38.088	0.202	0.857	0.001	2.089	0.003
Shap orthoclase	my02g04	612	18.246	0.085	15.618	0.090	38.231	0.216	0.858	0.001	2.094	0.004
Shap orthoclase	my02g12	612	18.257	0.061	15.690	0.065	38.332	0.178	0.858	0.001	2.098	0.004
Shap orthoclase	my02h04	612	18.337	0.095	15.722	0.070	38.284	0.204	0.857	0.002	2.092	0.004
FCT sanidine	oc05a10	BCR2G	18.481	0.145	15.595	0.144	37.945	0.319	0.844	0.002	2.050	0.005
FCT sanidine	oc05a11	BCR2G	18.464	0.138	15.547	0.139	37.847	0.306	0.844	0.002	2.053	0.005
FCT sanidine	oc05a12	BCR2G	18.476	0.134	15.527	0.138	37.913	0.303	0.842	0.002	2.052	0.005
FCT sanidine	oc05a16	BCR2G	18.434	0.139	15.548	0.140	37.842	0.304	0.845	0.002	2.051	0.004
FCT sanidine	oc05a17	BCR2G	18.477	0.137	15.646	0.142	38.003	0.307	0.847	0.002	2.054	0.004
FCT sanidine	oc05a18	BCR2G	18.489	0.140	15.633	0.142	37.987	0.311	0.845	0.002	2.048	0.004
FCT sanidine	oc05a23	BCR2G	18.506	0.142	15.540	0.143	37.960	0.310	0.844	0.002	2.046	0.005
FCT sanidine	oc05a24	BCR2G	18.452	0.146	15.550	0.144	37.860	0.318	0.844	0.002	2.045	0.005
FCT sanidine	oc13b10	BCR2G	18.440	0.109	15.703	0.116	37.915	0.312	0.849	0.003	2.047	0.007
FCT sanidine	oc13b11	BCR2G	18.469	0.176	15.695	0.166	37.804	0.436	0.848	0.003	2.050	0.006
FCT sanidine	oc13b12	BCR2G	18.497	0.126	15.720	0.118	37.853	0.336	0.851	0.002	2.051	0.006
FCT sanidine	oc13d13	612	18.498	0.098	15.589	0.118	37.629	0.285	0.842	0.003	2.042	0.007
FCT sanidine	oc13d14	612	18.457	0.139	15.587	0.089	37.687	0.320	0.845	0.002	2.046	0.004
FCT sanidine	oc13d15	612	18.450	0.200	15.515	0.166	37.656	0.402	0.843	0.003	2.048	0.007

Table S3-5 (continued): LA-MC-ICPMS lead isotope ratio values three feldspars from Souders and Sylvester (2010)

Sample	Analysis ID	Std	^{206}Pb / ^{204}Pb	std error (1-sigma)	^{207}Pb / ^{204}Pb	std error (1-sigma)	$^{208}Pb/^{204}Pb$	std error (1-sigma)	$^{207}Pb/^{206}Pb$	std error (1-sigma)	$^{208}Pb/^{206}Pb$	std error (1-sigma)
Fisk. Bytownite	no18b10	BCR2G	13.229	0.050	14.473	0.053	33.020	0.112	1.092	0.002	2.495	0.003
Fisk. Bytownite	no18b11	BCR2G	13.291	0.049	14.553	0.054	33.193	0.117	1.095	0.002	2.497	0.003
Fisk. Bytownite	no18b12	BCR2G	13.269	0.036	14.433	0.040	33.025	0.089	1.087	0.001	2.485	0.003
Fisk. Bytownite	oc04a10	BCR2G	13.227	0.172	14.493	0.152	33.082	0.361	1.092	0.002	2.498	0.005
Fisk. Bytownite	oc04a11	BCR2G	13.292	0.155	14.492	0.122	33.022	0.324	1.090	0.002	2.493	0.005
Fisk. Bytownite	oc04a12	BCR2G	13.268	0.149	14.515	0.113	33.263	0.302	1.094	0.002	2.507	0.004
Fisk. Bytownite	oc04a16	BCR2G	13.277	0.162	14.444	0.130	33.070	0.333	1.088	0.002	2.491	0.006
Fisk. Bytownite	oc04a17	BCR2G	13.269	0.146	14.464	0.110	33.093	0.291	1.091	0.002	2.509	0.004
Fisk. Bytownite	oc04b10	BCR2G	13.279	0.098	14.395	0.102	32.991	0.240	1.091	0.003	2.517	0.009
Fisk. Bytownite	oc04b11	BCR2G	13.169	0.081	14.386	0.080	33.092	0.204	1.092	0.003	2.519	0.008
Fisk. Bytownite	oc04b12	BCR2G	13.257	0.088	14.435	0.089	33.221	0.219	1.089	0.003	2.511	0.008
Fisk. Bytownite	oc04b16	BCR2G	13.329	0.095	14.544	0.094	33.234	0.230	1.091	0.004	2.495	0.010
Fisk. Bytownite	oc04b17	BCR2G	13.237	0.082	14.443	0.085	33.076	0.205	1.091	0.003	2.503	0.008
Fisk. Bytownite	oc12a04	BCR2G	13.225	0.082	14.478	0.075	32.983	0.166	1.094	0.002	2.496	0.004
Fisk. Bytownite	oc12a05	BCR2G	13.225	0.085	14.473	0.079	32.961	0.181	1.094	0.001	2.494	0.005
Fisk. Bytownite	oc12a06	BCR2G	13.323	0.080	14.523	0.072	33.114	0.171	1.090	0.001	2.498	0.005
Fisk. Bytownite	je29b06	BCR2G	13.262	0.116	14.470	0.100	32.933	0.230	1.091	0.002	2.496	0.006
Fisk. Bytownite	je29b10	BCR2G	13.319	0.109	14.538	0.100	33.116	0.220	1.091	0.002	2.501	0.006
Fisk. Bytownite	je29b11	BCR2G	13.260	0.101	14.468	0.102	33.033	0.221	1.091	0.003	2.499	0.006
Fisk. Bytownite	je29b12	BCR2G	13.293	0.115	14.492	0.131	33.010	0.267	1.090	0.002	2.489	0.006
Fisk. Bytownite	oc12b04	612	13.321	0.070	14.490	0.093	33.164	0.219	1.087	0.004	2.498	0.005
Fisk. Bytownite	oc12b05	612	13.264	0.066	14.517	0.091	33.224	0.212	1.094	0.004	2.497	0.005
Fisk. Bytownite	oc12b06	612	13.282	0.101	14.368	0.134	32.986	0.310	1.090	0.004	2.499	0.007

Table S3-6: LA-MC-ICPMS lead isotope ratios for three sulfide matrices (Souders and Sylvester, 2010)

Sample	Analysis ID	Std	^{206}Pb / ^{204}Pb	std error (1-sigma)	^{207}Pb / ^{204}Pb	std error (1-sigma)	$^{208}Pb/^{204}Pb$	std error (1-sigma)	$^{207}Pb/^{206}Pb$	std error (1-sigma)	$^{208}Pb/^{206}Pb$	std error (1-sigma)
PB-1	oc25d10	612	20.619	0.099	15.816	0.097	39.707	0.261	0.767	0.003	1.916	0.005
PB-1	oc25d11	612	20.573	0.123	15.828	0.114	39.589	0.256	0.769	0.003	1.923	0.006
PB-1	oc25d12	612	20.553	0.145	15.889	0.137	39.498	0.297	0.769	0.003	1.920	0.005
PB-1	ap06c04	612	20.519	0.173	15.770	0.140	39.451	0.351	0.765	0.003	1.917	0.005
PB-1	ap06c05	612	20.567	0.137	15.848	0.120	39.508	0.293	0.767	0.003	1.913	0.005
PB-1	ap06c06	612	20.639	0.122	15.850	0.094	39.511	0.246	0.768	0.003	1.925	0.005
PB-1	ap06c16	612	20.590	0.240	15.877	0.192	39.654	0.500	0.771	0.003	1.919	0.006
PB-1	ap06c17	612	20.579	0.164	15.789	0.137	39.329	0.328	0.768	0.003	1.916	0.006
PB-1	ap06c18	612	20.589	0.203	15.795	0.173	39.468	0.430	0.768	0.003	1.927	0.006
PB-1	ju06a10	612	20.591	0.160	15.810	0.131	39.491	0.362	0.769	0.003	1.922	0.006
PB-1	ju06a11	612	20.530	0.158	15.761	0.131	39.403	0.341	0.770	0.003	1.914	0.006
PB-1	ju06a12	612	20.546	0.212	15.786	0.173	39.561	0.412	0.767	0.003	1.917	0.006
PB-1	ju06a16	612	20.607	0.162	15.805	0.141	39.544	0.344	0.766	0.004	1.921	0.005
PB-1	ju06a17	612	20.523	0.133	15.796	0.124	39.286	0.294	0.769	0.003	1.915	0.005
PB-1	ju06a18	612	20.689	0.146	15.941	0.124	39.412	0.310	0.770	0.003	1.908	0.004
PB-1	ju06a22	612	20.571	0.206	15.929	0.172	39.564	0.410	0.773	0.003	1.927	0.006
PB-1	ju06a23	612	20.594	0.281	15.825	0.219	39.682	0.618	0.769	0.004	1.921	0.008
PB-1	ju06a24	612	20.581	0.188	15.978	0.143	39.372	0.361	0.773	0.003	1.922	0.006
PB-1	ju06a28	612	20.574	0.223	15.947	0.193	39.561	0.472	0.772	0.004	1.921	0.007
PB-1	ju06a29	612	20.530	0.198	15.801	0.171	39.442	0.408	0.771	0.003	1.913	0.006
PB-1	ju06a30	612	20.559	0.157	15.842	0.139	39.329	0.334	0.769	0.004	1.907	0.005
PB-1	ju10a10	612	20.591	0.175	15.839	0.137	39.529	0.363	0.768	0.003	1.924	0.007
PB-1	ju10a11	612	20.618	0.220	15.856	0.187	39.154	0.454	0.774	0.003	1.917	0.008
PB-1	ju10a12	612	20.580	0.168	15.860	0.129	39.477	0.356	0.772	0.003	1.920	0.008
PB-1	ju10a28	612	20.533	0.139	15.861	0.106	39.448	0.287	0.771	0.003	1.922	0.007
PB-1	ju10a29	612	20.603	0.160	15.937	0.133	39.654	0.357	0.772	0.003	1.917	0.008
PB-1	ju10a30	612	20.615	0.142	15.884	0.120	39.583	0.333	0.773	0.003	1.918	0.008
PB-1	oc25a04	PB-1	20.603	0.084	15.878	0.084	39.576	0.168	0.769	0.002	1.922	0.003
PB-1	oc25a05	PB-1	20.576	0.110	15.800	0.105	39.620	0.223	0.767	0.002	1.927	0.004
PB-1	oc25a06	PB-1	20.639	0.111	15.827	0.109	39.616	0.227	0.770	0.002	1.923	0.003
PB-1	ju06b04	PB-1	20.582	0.212	15.838	0.181	39.643	0.398	0.768	0.003	1.920	0.005
PB-1	ju06b05	PB-1	20.604	0.205	15.777	0.185	39.301	0.398	0.769	0.003	1.917	0.0051
PB-1	ju06b06	PB-1	20.594	0.230	15.891	0.196	39.440	0.423	0.768	0.003	1.914	0.0055
PB-1	ju06b10	PB-1	20.666	0.181	15.857	0.157	39.433	0.326	0.770	0.003	1.918	0.005
PB-1	ju06b11	PB-1	20.635	0.189	15.819	0.170	39.599	0.370	0.767	0.003	1.919	0.005
PB-1	ju06b12	PB-1	20.615	0.214	15.756	0.188	39.393	0.434	0.767	0.003	1.918	0.005
PB-1	ju06b13	PB-1	20.513	0.176	15.712	0.136	39.502	0.362	0.768	0.003	1.927	0.007
PB-1	ju06b14	PB-1	20.604	0.139	15.813	0.105	39.548	0.287	0.770	0.003	1.923	0.0064
PB-1	ju06b15	PB-1	20.558	0.117	15.847	0.107	39.601	0.273	0.772	0.003	1.930	0.007

Table S3-6 (continued): LA-MC-ICPMS lead isotope ratios for three sulfide matrices (Souders and Sylvester, 2010)

Sample	Analysis ID	Std	^{206}Pb / ^{204}Pb	std error (1-sigma)	^{207}Pb / ^{204}Pb	std error (1-sigma)	$^{208}Pb/^{204}Pb$	std error (1-sigma)	$^{207}Pb/^{206}Pb$	std error (1-sigma)	$^{208}Pb/^{206}Pb$	std error (1-sigma)
B41	oc11g04	612	18.658	0.415	15.582	0.357	38.242	0.918	0.844	0.005	2.049	0.010
B41	oc11g05	612	18.607	0.143	15.644	0.115	38.125	0.287	0.846	0.003	2.053	0.009
B41	oc11g06	612	18.558	0.205	15.690	0.168	37.795	0.395	0.844	0.004	2.041	0.008
B41	oc25d16	612	18.581	0.162	15.775	0.152	38.111	0.352	0.848	0.003	2.051	0.005
B41	oc25d17	612	18.607	0.225	15.692	0.178	37.948	0.457	0.842	0.004	2.040	0.007
B41	oc25d18	612	18.520	0.178	15.685	0.174	37.987	0.404	0.842	0.003	2.046	0.005
B41	ap06c10	612	18.606	0.131	15.673	0.131	38.057	0.277	0.840	0.003	2.042	0.005
B41	ap06c11	612	18.628	0.142	15.569	0.125	37.979	0.295	0.839	0.003	2.048	0.007
B41	ap06c12	612	18.591	0.251	15.617	0.216	37.897	0.522	0.840	0.004	2.045	0.008
B41	ju06a34	612	18.663	0.178	15.678	0.165	38.044	0.401	0.843	0.004	2.045	0.006
B41	ju06a35	612	18.514	0.201	15.642	0.216	37.901	0.474	0.841	0.004	2.054	0.007
B41	ju06a36	612	18.614	0.211	15.643	0.188	38.065	0.305	0.840	0.003	2.046	0.007
B41	ju06a40	612	18.568	0.243	15.573	0.211	38.186	0.530	0.846	0.004	2.057	0.007
B41	ju06a41	612	18.637	0.209	15.614	0.189	38.094	0.467	0.844	0.004	2.042	0.007
B41	ju06a42	612	18.520	0.281	15.570	0.231	37.858	0.579	0.844	0.005	2.053	0.009
B41	ju06a46	612	18.539	0.182	15.647	0.162	38.092	0.367	0.843	0.004	2.051	0.006
B41	ju06a47	612	18.639	0.178	15.724	0.149	38.210	0.391	0.841	0.004	2.051	0.006
B41	ju06a48	612	18.571	0.211	15.735	0.193	38.146	0.477	0.841	0.005	2.052	0.006
B41	ju06a52	612	18.717	0.235	15.693	0.205	38.203	0.511	0.839	0.004	2.042	0.007
B41	ju06a53	612	18.626	0.211	15.722	0.171	38.063	0.449	0.839	0.004	2.044	0.007
B41	ju06a54	612	18.591	0.234	15.580	0.196	37.793	0.496	0.841	0.004	2.046	0.008
B41	ju10a16	612	18.525	0.221	15.631	0.173	38.014	0.441	0.845	0.003	2.055	0.009
B41	ju10a17	612	18.635	0.159	15.673	0.130	38.092	0.347	0.843	0.003	2.050	0.008
B41	ju10a34	612	18.602	0.202	15.647	0.174	38.119	0.423	0.842	0.004	2.043	0.008
B41	ju10a35	612	18.592	0.250	15.617	0.210	38.367	0.550	0.846	0.003	2.053	0.009
B41	ju10a36	612	18.569	0.171	15.552	0.159	37.827	0.392	0.844	0.004	2.044	0.009
B41	oc11h04	PB-1	18.621	0.145	15.647	0.180	38.068	0.372	0.838	0.004	2.046	0.0060
B41	oc11h05	PB-1	18.504	0.163	15.630	0.170	38.241	0.340	0.845	0.003	2.055	0.0062
B41	oc11h06	PB-1	18.587	0.182	15.645	0.177	38.122	0.405	0.841	0.003	2.053	0.0073
B41	oc25a10	PB-1	18.582	0.159	15.684	0.143	38.316	0.336	0.845	0.002	2.057	0.005
B41	oc25a11	PB-1	18.540	0.171	15.686	0.173	38.073	0.459	0.845	0.002	2.059	0.005
B41	oc25a12	PB-1	18.591	0.235	15.700	0.224	38.012	0.478	0.845	0.003	2.053	0.007
B41	ap06c25	PB-1	18.693	0.163	15.790	0.172	38.108	0.345	0.845	0.003	2.048	0.006
B41	ap06c26	PB-1	18.628	0.161	15.772	0.179	38.111	0.356	0.843	0.003	2.051	0.007
B41	ap06c27	PB-1	18.583	0.208	15.766	0.202	38.095	0.438	0.846	0.004	2.052	0.008
B41	ju06b19	PB-1	18.626	0.190	15.730	0.188	38.331	0.445	0.841	0.004	2.048	0.010
B41	ju06b20	PB-1	18.601	0.219	15.591	0.175	38.022	0.462	0.843	0.004	2.059	0.009
B41	ju06b26	PB-1	18.599	0.188	15.772	0.159	38.321	0.388	0.844	0.004	2.060	0.009
MASS-1	fc25c10	612	21.024	0.556	16.248	0.415	40.557	1.031	0.777	0.003	1.931	0.008
MASS-1	fc25c11	612	20.753	0.256	16.110	0.203	40.346	0.458	0.777	0.003	1.944	0.007
MASS-1	fc25c12	612	20.286	0.262	15.702	0.207	39.670	0.507	0.777	0.003	1.951	0.007
MASS-1	fc25c25	PB-1	20.034	0.324	15.548	0.237	39.080	0.603	0.776	0.003	1.950	0.006
MASS-1	fc25c26	PB-1	19.775	0.353	15.327	0.250	38.675	0.656	0.775	0.003	1.949	0.006
MASS-1	fc25c27	PB-1	21.582	0.382	16.766	0.283	42.261	0.721	0.776	0.003	1.949	0.006

Chapter 4: Mantle and crustal sources of Archean anorthosite: a combined in-situ isotopic study of Pb-Pb in plagioclase and Lu-Hf in zircon

Abstract

Isotopic analyses of ancient mantle-derived magmatic rocks are used to trace the geochemical evolution of the Earth's mantle but it is often difficult to determine their primary, initial isotope ratios due to the detrimental effects of metamorphism and secondary alteration. We present in-situ analyses by LA-MC-ICPMS for the Pb isotope compositions of igneous plagioclase (An 75-89) megacrysts and the Hf isotope compositions of BSE-imaged domains of zircon grains from two mantle-derived anorthosite complexes from southwestern Greenland, Fiskenæsset and Nunataarsuk, which represent two of the best-preserved Archean anorthosites in the world. In situ LA-ICPMS U-Pb geochronology of the zircon grains suggests that the crystallization age of the Fiskenæsset complex is 2936 +/- 13 Ma (2σ, MSWD = 1.5) and the Nunataarsuk complex is 2914 +/- 6.9 Ma (2σ, MSWD = 2.0). Initial Hf isotope compositions of zircon grains from both anorthosite complexes fall between depleted mantle and a less radiogenic crustal source with a total range up to 5 ε_{Hf} units. In terms of Pb isotope compositions of plagioclase, both anorthosite complexes share a depleted mantle end member yet their Pb isotope compositions diverge in opposite directions from this point: Fiskenæsset toward a high-μ, more radiogenic Pb, crustal composition and Nunataarsuk toward low-μ, less radiogenic Pb, crustal composition. By using Hf isotopes in zircon in conjunction with Pb isotopes in plagioclase we are able to constrain both the timing of mantle extraction of the crustal end member and its composition. At Fiskenæsset, the

depleted mantle melt interacted with an Eoarchean (ca. 3600 - 3800 Ma) mafic crust with $^{176}Lu/^{177}Hf \sim 0.028$. At Nunataarsuk, the depleted mantle melt interacted with a Hadean (ca. 4100 - 4200 Ma) mafic crust with $^{176}Lu/^{177}Hf \sim 0.0315$. Evidence from both anorthosite complexes provides support for the long-term survival of ancient mafic crusts that, although unidentified at the surface to date, could still be present within the Fiskenæsset and Nunataarsuk regions.

4.1 INTRODUCTION

Long-lived radiogenic isotope systems (*e.g.* Sm-Nd, Lu-Hf, Pb-Pb) are powerful tracers of geochemical processes. They have been used extensively to track complementary processes such as the geochemical depletion of the mantle and the formation of the crust. Traditionally, for Archean-age rocks, initial Sm-Nd and Lu-Hf and Pb-Pb ratios determined by bulk rock and mineral separate analyses of mantle-derived mafic and ultramafic rocks and juvenile granites have been used to constrain the isotopic evolution of the depleted mantle and crust (*e.g.* Bennett et al., 1993; Lahaye et al., 1995; Bowring and Housh, 1995; Vervoort and Blichert-Toft, 1999; Kamber et al., 2003). The results depend on the assumption that the isotope systematics on the bulk rock scale are robust and parent-daughter ratios have been preserved through subsequent metamorphism or low-temperature alteration. For Archean rocks, accurate measurement of the parent-daughter ratio is essential for determining the initial isotope ratio where potentially large corrections for radiogenic in-growth must be made.

The advancement of laser ablation multi-collector magnetic sector inductively coupled plasma mass spectrometry (LA-MC-ICPMS) has produced new analytical

opportunities for in-situ analysis of individual minerals from mantle-derived rocks, such as Pb isotopes in feldspar and Hf isotopes in zircon. Low parent-daughter ratios (U/Pb in plagioclase and Lu/Hf in zircon) requiring minimal corrections for radiogenic in-growth, and the demonstrated ability to preserve initial isotope compositions through metamorphism and alteration make Pb isotopes in feldspar and Hf isotopes in zircon ideal tracers of mantle evolution and the timing of crust formation (*e.g.* Oversby, 1975; Patchett et al., 1981; Mathez and Waight, 2003; Kemp et al., 2009). The timing, volume and nature of the early crust is a fundamental issue of continuing debate (*e.g.* Stacey and Kramers, 1975; Armstrong 1981; Taylor and McLennan 1995; Chase and Patchett, 1988; Bowring and Housh 1995; Kramers and Tolstikhin 1997; Kamber et al., 2003, 2005; Harrison et al., 2005, 2008; Blichert-Toft and Albarede, 2008; O'Neil et al., 2008; Kemp et al., 2010). Hafnium model ages of zircon can be calculated to constrain the timing of crust extraction yet the results depend critically on the $^{176}Lu/^{177}Hf$ ratio of the crustal material separated from the mantle. The $^{176}Lu/^{177}Hf$ ratio of the extracted crust must be constrained, which is commonly done using either petrologic models for the origin of the crust and assuming a bulk crustal source Lu/Hf or by analysis of zircon grains of different ages crystallized from magmas assumed to have been produced by reworking of the same source over time (*e.g.* Amelin et al., 1999; Kemp et al., 2010; Pietranik et al., 2008). Alternatively, there is a general decrease in the Lu/Hf of igneous rocks with increasing silica (Hawkesworth et al., 2010). If the timing of source separation from the mantle (model age) is known, the calculated $^{176}Lu/^{177}Hf$ can be used to evaluate the nature of the crustal source.

To better understand late Archean crust – mantle evolution we will demonstrate

how the timing of source separation from the mantle determined from in-situ Pb isotope ratio measurements of feldspar can be combined with in-situ Hf isotope ratios of zircons from the same igneous rock to constrain the $^{176}Lu/^{177}Hf$, thereby characterizing the nature of the source. To demonstrate this approach, we have studied the Fiskenæsset and Nunataarsuk anorthosite complexes of south West Greenland (Myers, 1985). Both anorthosite complexes are located within high-grade gneiss terranes yet locally preserve primary igneous structures, textures and mineralogy and are two of the best-preserved Archean anorthosite complexes in the world. Petrologic data indicate that Archean anorthosites and related rocks are the products of mantle-derived magmas (Ashwal, 1993). Through careful selection of the best-preserved, least-deformed samples and in-situ isotopic analysis of igneous domains within minerals, we provide new insights into the source reservoirs of Archean anorthosites. We present data for in-situ U-Pb geochronology and Lu-Hf isotope geochemistry of zircon grains separated from anorthosites and leucogabbros, and in-situ Pb-Pb isotope analysis of plagioclase crystals from anorthosites, leucogabbros and gabbros. This is the first study of Archean anorthosites for in-situ Pb isotopes in plagioclase and only the second for in-situ Hf isotopes in zircon. The integration of the Pb isotope data from feldspars and Hf isotope data from zircons from the same igneous rock has potential applications for determining the timing and nature of ancient (Hadean) crusts.

4.2 ARCHEAN ANORTHOSITES

Anorthosites are enigmatic rocks restricted in time and space. They have been identified within many Archean cratons yet make up only a small proportion of Archean

greenstone belts where anorthosites form layered complexes with associated leucogabbros, gabbros and ultramafic rocks. Subsequent magmatism and tectonic activity has disrupted and deformed most Archean anorthosite complexes and today they outcrop as layers and lenses within Archean high-grade gneiss terranes. The metamorphic grade of Archean anorthosites ranges from greenschist through granulite facies, yet many still retain distinct, equidimensional, magmatic plagioclase megacrysts (up to 30 cm in diameter) with calcic compositions ($\sim An_{75-90}$) (Ashwal, 1993). The shape and composition of the igneous plagioclase crystals is what distinguishes Archean anorthosites from younger terrestrial anorthosites (Proterozoic massifs), which are characterized by sodic ($An_{50 \pm 10}$), lath-shaped plagioclase crystals (Ashwal, 1993). Similar calcic (An_{92-100}), primordial (> 4.4 Ga) anorthosites are the dominant lithology of the lunar crust, yet it is assumed these anorthosites formed by crystallization and floatation of plagioclase crystals from a magma ocean associated with lunar accretion (see Taylor, 2009, for a review). Archean anorthosites are thought to be the products of mantle-derived magmas that ponded at the base of the crust, crystallized mafic phases there, becoming enriched in aluminum, and then rose to higher levels in the crust where they crystallized calcic plagioclase (Phinney, 1982; Phinney et al., 1989). A recent alternative view proposes that the anorthosite parent magma is generated within a sub-arc mantle wedge where high-Al (Rollinson et al., 2010), LREE, Sr and Ca-enriched (Polat et al., 2009, 2011) partial melts of subducting ocean crust interact with depleted mantle.

4.2.1 Previous Isotopic Studies of Archean Anorthosites

Traditionally, isotopic studies of Archean anorthosites have focused on the Rb-Sr, Sm-Nd and Pb-Pb isotopic systems using whole rock powders and bulk mineral separates analyzed by thermal ionization mass spectrometry (TIMS). Both the Rb-Sr and Pb-Pb systems were typically used for age determination by the isochron method (*e.g.* Black et al., 1973; Gancarz, 1976; Moorbath and Pankhurst, 1976; Pidgeon and Kalsbeek, 1978; Kalsbeek and Pidgeon, 1980; Taylor et al., 1980; Basker Rao et al., 1996; Fletcher et al., 1988). Due to the high mobility of Rb-Sr during metamorphism and fluid alteration, much of these early data must be evaluated with caution. In recent years, particular emphasis has been placed on the Sm-Nd system to fingerprint the source(s) of Archean anorthosite complexes. The general conclusion of this approach is that Archean anorthosite complexes formed from chondritic or depleted mantle sources yet within each locality, there is a large range of ε_{Nd} (up to ~ 12 ε_{Nd} units; *e.g.* Ashwal et al., 1985, 1989; Barton, 1996; Basker Rao et al., 1996, 2000; Fletcher et al., 1988; Polat et al., 2010). It is ambiguous whether the observed isotopic variability reflects partial melting of heterogeneous mantle sources; mixing of mantle-derived magmas with crustal sources; or disturbance of primary isotopic ratios by secondary processes such as metamorphism and hydrous alteration.

Several recent studies have reported U-Pb and Pb-Pb zircon ages from Archean anorthosites and leucogabbros (*e.g.* Manfred Complex: Kinney et al., 1988; Messina Layered Intrusion: Mouri et al., 2009; Messina Layered Intrusion: Zeh et al., 2010; Fiskenæsset Complex: Keulen et al., 2010). Zeh et al. (2010) also analyzed ~3350 Ma

zircon grains from two anorthosite samples from the Messina Layered Intrusion, South Africa, for Hf isotopes by LA-MC-ICPMS. Initial ε_{Hf} (ca. 3350 Ma) for the anorthosites are + 1.4 ± 1.8 and + 0.1 ± 1.9, which was interpreted as reflecting slight enrichment of depleted mantle-derived melts by crustal contamination.

A number of the previous isotopic studies have been concerned with Fiskenæsset anorthosites (Black et al., 1973; Gancarz, 1976; Moorbath and Pankhurst, 1976; Pidgeon and Kalsbeek, 1978; Kalsbeek and Pidgeon, 1980; Taylor et al., 1980; Ashwal et al., 1989; Keulen et al., 2010; Polat et al., 2010) but none have dealt with Nunataarsuk anorthosites.

4.3 GEOLOGICAL SETTING OF THE FISKENÆSSET AND NUNATAARSUK ANORTHOSITE COMPLEXES

Several of the best-preserved Archean anorthosite complexes occur within the greenstone belts and high-grade gneiss terranes of southwestern Greenland (*e.g.* Windley et al., 1973; Myers, 1985; Ashwal, 1993; Owens and Dymek, 1997; Dymek and Owens, 2001; Windley and Garde, 2009). The anorthosite-leucogabbro-gabbro-ultramafic rock complexes typically form concordant, sheet-like bodies or trains of inclusions in amphibolite within the high-grade gneiss complexes. Contact relationships between the anorthosite complexes and mafic country rock are most often obscured by igneous intrusion, deformation and amphibolite to granulite facies metamorphism, yet these relationships are preserved within the Fiskenæsset anorthosite complex (Escher and Myers, 1975).

4.3.1 Fiskenæsset Complex, southwest Greenland

The Fiskenaesset anorthosite complex (Figure 4-1) is one of the most intensely studied Archean anorthosite complexes because it is so well preserved. It covers an area of ~ 2500 km^2 between the village of Fiskenæsset on the coast and the inland ice sheet, ~ 80 km to the east. The Fiskenæsset region consists of ~ 80% orthogneiss, ~ 10% amphibolite and ~ 5% anorthosite complex (Myers, 1985). The anorthosite complex is dominated by anorthosite and associated leucogabbro, along with less abundant gabbro and ultramafic rock. These rocks occur within the quartzofeldspathic gneisses as sheet-like layers and tectonic lenses (Windley et al., 1973; Myers, 1985). The sheets are generally less than 500 m thick but can extend up to ~ 25 km in length (Myers, 1985).

Preserved contact relationships suggest that the anorthosite complex was originally emplaced as a sill-like body into mafic volcanic rock containing pillow structures (Escher and Myers, 1975). Subsequently, the original sheet-like layers were fragmented by contemporaneous granitoid intrusion and thrusting at ~ 2800 Ma (Pidgeon and Kalsbeek, 1978; Myers, 1985). All the rocks in the Fiskenæsset complex have undergone three phases of intense folding, which has resulted in the formation of complex fold-interference structures with steeply dipping axial surfaces (Myers, 1985). The rocks were metamorphosed to upper-amphibolite or granulite facies and some areas have been retrogressed back to lower-amphibolite or greenschist facies (Windley et al., 1973; Myers, 1985). Metamorphism is thought to have taken place between 2900 and 2660 Ma (Black et al., 1973; Moorbath and Pankhurst, 1976; Pidgeon and Kalsbeek, 1978; Kalsbeek and Pidgeon, 1980; Taylor et al., 1980) with peak metamorphic conditions

estimated to have reached 780 ± 50 °C and 8.9 ± 1 kbar (~30 km depth) (Riciputi et al., 1990).

The Fiskenæsset region has experienced heterogeneous deformation and metamorphism and some areas, particularly those further inland towards the ice, underwent less-intense deformation and metamorphism no higher than amphibolite facies. Perhaps the best example is Majorqap qâva, an area located in the center of the Fiskenæsset complex, which has undergone intense folding yet has only experienced amphibolite facies metamorphism and minimal retrograde effects. This area is considered one of the best-preserved outcrops of the Fiskenæsset complex and provides a window into the primary igneous mineralogy and textures of Archean anorthosite complexes. It was the area sampled for this study (see below). Igneous features such as mineral and size-graded layering, slump structures, pipe-like bodies and channel-troughs are preserved within this region (Myers, 1976).

A generalized igneous stratigraphy for the Fiskenæsset complex can be reconstructed from observations of units across the region (Windley, 1971; Windley, 1973; Steele et al., 1977; Myers, 1975) but the outcrops at Majorqap qâva represent the most-complete stratigraphic section. Myers (1985) divided the anorthosite complex into seven lithostratigraphic units based on the well-preserved outcrops at Majorqap qâva and examination of all the anorthosite outcrops of the Fiskenæsset region. The seven defined lithostratigraphic units (from bottom to top) are: lower gabbro (LG, 50 m), ultramafic unit (UM, 40 m), lower leucogabbro (LLG, 50 m), middle gabbro (MG, 40 m), upper leucogabbro (60 m), anorthosite (AN, 250 m) and upper gabbro (UG, 50 m), for a total post-deformational thickness of 540 m (Figure 4-2).

Keulen et al. (2010) reported U-Pb LA-ICPMS zircon data for a mixed anorthosite-hornblende dike sample from the Majorqap qâva area. $^{207}Pb/^{206}Pb$ ages of zircon grains spanned from 2.95 ± 0.03 Ga to 2.70 ± 0.03 Ga with significant populations at 2919 ± 7 Ma (2σ), 2872 ± 5 Ma (2σ) and 2720 ± 28 Ma (2σ). They interpreted rare ~2.95 Ga grains (n = 2) to be representative of the intrusive age of the Fiskenæsset anorthosite complex. Similar emplacement ages also have been inferred from Sm-Nd isotopic data. Ashwal et al. (1989) reported a combined whole rock-mineral (plagioclase + hornblende) Sm-Nd isochron age of 2860 ± 50 Ma (MSWD 2.5) with a calculated initial ε_{Nd} of +2.9 ± 0.4 (total range: + 0.6 to + 3.0) for four samples from Majorqap qâva. Polat et al. (2010) determined a Sm-Nd isochron age of 2973 ± 28 Ma (MSWD 33) with an initial ε_{Nd} of + 3.3 ± 0.7 (total range: + 1.8 to + 5.4) for 46 whole rock samples from Qeqertarssuatsiaq Island, located some 35 km southwest of Majorqap qâva, where metamorphism reached granulite grade.

Most Pb-Pb isotope studies using whole rocks (Black et al., 1973; Pidgeon and Kalsbeek, 1978) and bulk mineral separates (Gancarz, 1976) have given younger ages of ~2850 – 2750 Ma, generally interpreted to represent the age of metamorphism in the complex. Polat et al. (2010), however, reported a Pb-Pb whole rock errorchron age of 2945 ± 36 Ma (MSWD=44), similar to the magmatic age inferred from the U-Pb zircon and Sm-Nd whole rock isotopic studies described above.

4.3.2 Nunataarsuk anorthosite complex

The Nunataarsuk anorthosite complex represents another very well preserved Archean anorthosite complex in south West Greenland yet very little is known about it

(Figure 4-1). The complex was mapped in detail by one of us (J.S. Myers) during the summer 2003 field season. The lithologies present in the Nunataarsuk complex are similar to those found in the Fiskenæsset complex, yet each complex has a distinct and different stratigraphy (Figure 4-2). This stratigraphy was distorted and disrupted by multiple tectonic events. However, the primary way-up of the igneous stratigraphy is known, but the original top and bottom contacts do not appear to be exposed and therefore the known stratigraphy may be incomplete.

Based on 1:10 000 scale mapping and field observations, the Nunataarsuk anorthosite complex is divided into four tectonic slices or thrust sheets. These rocks record several episodes of deformation that generated multiple superimposed fold and thrust structures. They were intruded by dioritic, tonalitic and granitic magmas during three major magmatic episodes. However, both the intensity of deformation and the volume of granitoid intrusions were heterogeneous. In the northern part of the nunatak of Nunataarsuk that was sampled, granitoid intrusions form less than 15% of the geology. Substantial portions of igneous stratigraphy and structure, including mineral- and size-graded layering, survive intact in the anorthosite complex, and igneous textures and minerals, including plagioclase megacrysts, are widely preserved.

A minimum crystallization age for the Nunataarsuk anorthosite complex has been inferred from a LA-ICPMS U-Pb $^{207}Pb/^{206}Pb$ age of 2852 ± 5 Ma for zircon grains separated from a granite that cross-cuts the anorthosite complex (Næraa and Schersten, 2008).

4.4 SAMPLING AND ANALYTICAL METHODS

Samples of both anorthosite complexes were selected from the best-preserved, least-recrystallized material available. All 16 samples of Fiskenæsset studied here are from Majorqap qava (Figures 4-1, 4-2). They represent the main part of the Fiskenæsset lithostratigraphic sequence and were selected from the Lower Leucogabbro Unit (LLG, 3 samples), the Middle Gabbro Unit (MG, 2 samples), the Upper Leucogabbro Unit (ULG, 7 samples) and the Anorthosite Unit (AN, 4 samples). The mineralogy of all of the anorthosite and leucogabbro samples is dominated by plagioclase megacrysts, ~ 3 mm up to 5 cm in diameter. Mafic minerals are mainly hornblende, with lesser amounts of mica and chromite, and comprise <5% of the anorthosites and 15-30% of the leucogabbros. The gabbros from the Middle Gabbro Unit contain subequal amounts of plagioclase (45-55%) and hornblende and mica.

Six samples were selected from the Nunataarsuk leucogabbro-anorthosite (LG-AN); all are leucogabbros containing 70-90% plagioclase megacrysts with the remainder being mostly amphibole. Three samples are from the lower LG-AN unit, dominated by plagioclase megacrysts, 2 – 5 cm in diameter, and three samples are from the upper LG-AN unit, made up of smaller plagioclase megacrysts, typically only 1 – 5 mm in diameter (Figures 4-1, 4-2).

4.4.1 Plagioclase petrography and sample preparation

Relict igneous plagioclase is present in all samples and was targeted for analysis in this study. It is typically present as darker, gray-colored crystals a few millimeters to several centimeters in diameter, surrounded by milky-white aggregates of smaller,

recrystallized plagioclase crystals, occasionally green or yellow in color (Figure 4-3). Grains that appeared to be strained or affected by secondary alteration were avoided.

Slices from the samples were cut with a saw, and relict igneous plagioclase in megacrysts (anorthosites, leucogabbros) and in the groundmass (gabbros) exposed in the slices were made into polished thin sections ~ 60 – 100 μm thick, suitable for thin section petrography and in-situ microanalysis. A polarized microscope was used to identify the most pristine areas of plagioclase within each thin section for analysis. The target-areas were photographed using plane-polarized light, cross-polarized light and in reflected light. A traverse across the best-preserved region of each plagioclase crystal was planned for in-situ electron probe microanalysis (EPMA) for An-content; LA-ICPMS analysis for Pb concentration; and LA-MC-ICPMS analysis for Pb isotope ratios. Measurement spots were spaced every ~750 – 1000 μm, depending on crystal-size and the inclusion-density. Amphibole inclusions are common within the preserved igneous plagioclase megacrysts (Figure 4-3) but were avoided during in-situ analysis of the feldspar. Laser analyses were excluded where spikes in radiogenic Pb were encountered as the beam drilled below the surface, on the assumption that hidden amphibole inclusions had been inadvertently intersected.

4.4.2 Plagioclase analyses

Details of the procedures used for the EPMA, LA-ICPMS and LA-MC-ICPMS measurements are given in Supplemental File S4-1. LA-ICPMS spots (49 μm) were placed directly on the sites of the EPMA analyses. A spot size ranging from 49 to 109 μm was used for the LA-MC-ICPMS measurements, depending on the lead concentration

of the plagioclase grain of interest and the mineral surface area available free of cracks or inclusions. Laser spots for lead isotope analysis were placed directly next to, or as close to, the EPMA and LA-ICPMS trace element analysis location as possible.

4.4.3 Zircon petrography and sample preparation

In situ LA-ICPMS U-Pb geochronology and LA-MC-ICPMS Lu-Hf isotope analyses were carried out on zircon grains separated from three of the samples analyzed for Pb isotopes in plagioclase in each of the Fiskenæsset and Nunataarsuk complexes. Heavy liquids were used to separate the zircon from bulk samples because searches of thin sections by optical microscopy did not reveal any zircon grains, suggesting that the phase is rare. Kilogram-sized samples were processed, where the material was available, because of the apparent scarcity of large quantities of zircon grains in the anorthositic rocks.

The three Fiskenæsset samples included one sample from the Lower Leucogabbro Unit (LLG, 159437), one sample from the Upper Leucogabbro Unit (ULG, 159394) and one sample from the Anorthosite Unit (AN, 159455) (Figure 4-2). An attempt was made to recover zircon from the Middle Gabbro unit (MG, 159448) of Fiskenæsset, but only a fist –sized sample was available and the zircon yield was minimal (less than 10 zircon grains total) with most grains too small (< 40 μm diameter) or the surface too damaged by cracks and secondary alteration for in situ analysis. For Nunataarsuk, zircon grains were separated and analyzed from leucogabbro samples, one from the Lower Leucogabbro-Anorthosite Unit (LLG-AN, N03-83) and two others from the Upper Leucogabbro-Anorthosite Unit (ULG-AN, N03-09 and N03-81) (Figure 4-2).

Heavy minerals ($\rho > 3.32$ g/cm^3) were isolated from rock samples by clean crushing techniques using a jaw crusher and disc mill and concentrated using methylene iodide heavy liquid and magnetic separation. Following magnetic separation, zircon grains from each sample were picked by hand using tweezers under a binocular microscope and transferred to double-sided tape. Picked zircon grains were mounted in 25 mm epoxy pucks and polished down to a flat surface exposing the center of each grain, removing the outer portion where Pb loss/gain typically occurs. Very few (< 25 grains) zircon grains large enough for laser ablation analysis (>40 μm) were identified by hand picking for most of the anorthosite and leucogabbro samples processed. In order to find more large grains, the entire heavy mineral fraction was also mounted in epoxy. The grains in the epoxy mounts were polished down to expose their centers and zircon grains were distinguished from other heavy minerals using back-scattered electron (BSE) imaging on the scanning electron microscope (SEM). The SEM used is an FEI Quanta 400 variable pressure ("environmental") microscope, operated under high vacuum conditions with an accelerating voltage of 25 keV, a beam current of 10 nA and at a 10 mm working distance. The SEM searches were done both manually and in automated mode using the Mineral Liberation Analysis (MLA) software (Fandrich et al. 2007). All zircon crystals identified by hand-picking or using the SEM were imaged at high resolution in BSE mode to further characterize grain size and shape, reveal any internal structures present and identify potential inclusions that would need to be avoided during laser analysis (Figure 4-4).

4.4.4 Zircon analyses

The methods used for analyses of the zircon for U-Pb geochronology by LA-ICPMS and Hf-isotopic composition by LA-MC-ICPMS are described in Supplemental File S4-2. U-Pb age measurements were made using a 40 μm x 40 μm box raster of the laser beam on discrete domains in the zircon grains identified from BSE images. For the in-situ Hf isotope analyses, a 49 μm laser spot was focused directly on top of, or next to, the U-Pb box raster made in each zircon grain (Figure 4-4).

4.5 RESULTS

4.5.1 U-Pb zircon geochronology

LA-ICPMS U-Pb zircon geochronology results for the Fiskenæsset samples are presented in Table 4-1 and Figure 4-5, and for the Nunataarsuk samples in Table 4-2 and Figure 4-6. A detailed summary of the method is included in Supplemental File S4-2. Age determinations were calculated using the decay constants of Jaffey et al., (1971) and the present day $^{238}U/^{235}U$ ratios of 137.88. Final ages and Concordia diagrams were produced using the Isoplot/Ex macro (Ludwig, 2003). $^{207}Pb/^{206}Pb$ ages are calculated using weighted mean diagrams in which the mean is weighted by data point errors only and the error is given as 2-sigma (2σ). For all unknown zircon grains, in order for the analyses to be included within the final data set the following quality-control criteria had to be met: (1) The average measured $^{207}Pb/^{206}Pb$ ratio must fall within 2-sigma uncertainty of the $^{207}Pb/^{206}Pb$ ratio calculated from the $^{206}Pb/^{238}U$ and $^{207}Pb/^{235}U$ ratios determined by the intercept method (Sylvester and Ghaderi, 1997), (2) the analysis cannot be more than 2% discordant and (3) no common Pb above background can be detected.

4.5.1.1 Fiskenæsset

Zircon grains from Fiskenæsset ULG 159394 have a significant range of size (< 40 μm – 500 μm) and shape. Zircon grains are both intact crystals, commonly with rounded edges, and crystal fragments with irregular, sometimes sub-rounded to rounded, grain boundaries. Using BSE imaging, most grains appear relatively homogeneous yet faint patchy or sector zoning is visible in some grains. Zones of secondary alteration, darker in BSE, occur along some grain boundaries and pathways within the crystal structure such as fractures or crystallographic discontinuities (Figure 4-4). Forty-nine U-Pb LA-ICPMS analyses of 38 zircon grains fit within the established quality-control criteria (listed above) and yield a range of $^{207}Pb/^{206}Pb$ ages from 2949 ± 10 Ma to 2690 ± 9 Ma (1σ) (Figure 4-5). Both U-concentration and Th/U ratio are correlated with $^{207}Pb/^{206}Pb$ age within this population of concordant analyses. Zircon grains with the oldest $^{207}Pb/^{206}Pb$ ages define a discrete age population and have the lowest U-concentrations (< 100 ppm U) and the highest Th/U ratios (> 0.375) (Figure 4-5). The weighted mean $^{207}Pb/^{206}Pb$ age of the two oldest grains (3 analyses) with the lowest U-contents and highest Th/U ratio is 2936 ± 13 Ma (2σ, MSWD = 1.5). We interpret this age to be the minimum crystallization age of the Fiskenæsset complex (discussed below). The age is within error of the oldest U-Pb zircon ages reported by Keulen et al. (2009) and both the whole rock Sm – Nd isochron age and Pb-Pb errorchron age of Polat et al. (2010).

U-Pb zircon ages were also determined for zircon grains from two other Fiskenæsset samples (LLG 159437 and AN 159455). Zircon crystals from both samples

were similar in size and morphology to zircon grains from sample ULG 159394. Both round crystals (up to ~ 400 μm diameter) and crystal fragments (< 40 μm to 400 μm) with sub-rounded to rounded grain boundaries occur in both samples (Figure 4-4). Ten analyses of ten zircon grains from LLG 159437 within the established quality-control criteria for U-Pb analyses have $^{207}Pb/^{206}Pb$ ages ranging from 2812 ± 11 Ma to 2774 ± 5 Ma (1σ) (Figure 4-5). Zircon grains from ULG 159394 show a trend to higher U-concentration and lower Th/U with decreasing $^{207}Pb/^{206}Pb$ age (Figure 4-5).

Twenty-one analyses from 19 zircon crystals and crystal fragments from anorthosite sample 159455 meet the U-Pb age quality-control criteria and have $^{207}Pb/^{206}Pb$ ages spanning from 2824 ± 11 Ma to 2661 ± 5 Ma (1σ) (Figure 4-5). No correlations between age and Th/U ratio or age and U-concentration are found for this sample.

4.5.1.2 Nunataarsuk

Zircon grains analyzed from Nunataarsuk leucogabbro N03-83 range in size from less than 40 μm to ~ 400 μm. All grains are crystal fragments with irregular grain boundaries and, in most cases, rounded corners. Faint growth zoning is observed within a few zircon grains yet most zircons lack any internal structure (Figure 4-4). Eighteen analyses from 13 zircon grains fit within the established U-Pb geochronology age criteria and yield a range of $^{207}Pb/^{206}Pb$ age from 2926 ± 9 Ma to 2730 ± 7 Ma (1σ) (Figure 4-6). All of the zircon grains analyzed from this sample have U concentrations less than 255 ppm (Figure 4-6). The weighted mean $^{207}Pb/^{206}Pb$ age of the six oldest dates (from 4 zircon grains) with some of the highest Th/U ratios (0.38 – 0.63), lowest U concentrations

(28 – 60 ppm U) and falling within 1σ error of each other is 2914 ± 6.9 Ma (2σ, MSWD = 2.0). We interpret 2914 ± 6.9 Ma to be the minimum magmatic age of the Nunataarsuk anorthosite complex and all younger ages recorded for this sample are the result of recrystallization or Pb loss due to subsequent tectonic and igneous activity. This age for leucogabbro N03-83 is some 60 Ma older than the $^{207}Pb/^{206}Pb$ age previously reported for a granite that cuts across the Nunataarsuk complex (Næraa and Schersten, 2008).

Like sample N03-83, zircon grains from leucogabbro N03-09 are all crystal fragments ranging in size from < 50 μm up to ~ 300 μm. Irregular grain boundaries are common with some rounded corners. Very faint sector and patchy zoning and/or trails of inclusions are observed within a few crystal fragments (Figure 4-4). Twenty-seven analyses of twenty-six zircon grains fit within the quality-control criteria for U-Pb zircon analyses and define a range of $^{207}Pb/^{206}Pb$ ages from 2901 ± 8 Ma to 2641 ± 12 Ma (1σ) (Figure 4-6). In contrast to other samples analyzed, a range of U concentrations is observed at a given $^{207}Pb/^{206}Pb$ age (e.g. at ~ 2875 Ma U ranges from 46 – 387 ppm) with a slight, but highly scattered ($r^2 = 0.1705$), trend of increasing U concentration with increasing age. A range of Th/U ratios for a given age is observed yet there is a general increase in the Th/U ratio with increasing age (Figure 4-6). It is difficult to assign a single age to this sample due to the spread, or smear, of ages along concordia and as seen on the $^{207}Pb/^{206}Pb$ weighted mean plot.

Eleven analyses from 11 different zircon grains from leucogabbro sample N03-81A fit within the acceptable criteria for U-Pb zircon analyses. The analyzed grains from sample N03-81A range in size from ~ 50 μm up to ~ 500 μm and represent a variety of

morphologies from subhedral to well-rounded crystals to crystal fragments with irregular grain boundaries. Internal structures, high-U inclusions and apatite inclusions are observed in a few of the larger, individual crystals while most of the rounded crystals lack any internal structure (Figure 4-4). The 11 analyses yielded a range of $^{207}Pb/^{206}Pb$ ages spanning from 2838 ± 7 Ma to 2556 ± 6 Ma (1σ) (Figure 4-6). As evident on both the concordia plot and the weighted mean plot, the spread of ages makes assigning a single age for sample N03-81A difficult. There are no significant correlations between U concentration or Th/U ratio and age (Figure 4-6).

4.5.2 In-situ Lu-Hf isotopes in zircon

Lu-Hf isotope results are given for the Fiskenæsset samples in Table 4-3, for the Nunataarsuk samples in Table 4-4, and for natural zircon standards in Supplemental Table S4-2.2 of Supplemental File S4-2. A detailed summary of the method is included in Supplemental File S4-2. The initial $^{176}Hf/^{177}Hf$ values are calculated for each *in situ* analysis of zircon using the measured $^{176}Hf/^{177}Hf$ and $^{176}Lu/^{177}Hf$ ratios, the ^{176}Lu decay constant of Söderlund et al. (2004) ($\lambda = 1.867 \times 10^{-11}$/ yr) and the $^{207}Pb/^{206}Pb$ ages interpreted here as the crystallization age for each anorthosite complex (Fiskenæsset = 2936 Ma; Nunataarsuk = 2914 Ma). The initial $^{176}Hf/^{177}Hf$ could also be calculated using the $^{207}Pb/^{206}Pb$ age measured at the laser spot corresponding to each pair of Lu-Hf and U-Pb analyses in zircon. There is little difference however in the calculated initial $^{176}Hf/^{177}Hf$ using the interpreted age of the complex *vs.* the measured $^{207}Pb/^{206}Pb$ age for each analytical spot (maximum net difference of ~ 0.005% and 0.004% for zircon grains from Fiskenæsset and Nunataarsuk, respectively), due to the low $^{176}Lu/^{177}Hf$ ratios of the

zircon analyzed. Epsilon Hf values are calculated using the present-day CHUR $^{176}Hf/^{177}Hf$ and $^{176}Lu/^{177}Hf$ values of 0.282785 and 0.0336, respectively (Bouvier et al., 2008). The depleted mantle model of Griffin et al. (2000) modified by Andersen et al. (2009) to the ^{176}Lu decay constant of Söderlund et al. (2004) and present-day CHUR Lu-Hf composition of Bouvier et al. (2008) was used as a reference. This model has a present-day $^{176}Hf/^{177}Hf$ value of 0.28325 ($\varepsilon Hf = +16.4$) at $^{176}Lu/^{177}Hf = 0.0388$, similar to modern-day MORB.

4.5.2.1 Fiskenæsset

Zircon grains from all three Fiskenæsset samples analyzed form horizontal arrays on the plots of initial $(^{176}Hf/^{177}Hf)_{2936\ Ma}$ vs. measured $^{207}Pb/^{206}Pb$ age for each laser spot (Figure 4-7). There are no distinct changes in initial $(^{176}Hf/^{177}Hf)_{2936\ Ma}$ with respect to measured $^{207}Pb/^{206}Pb$ zircon ages for zircons from Fiskenæsset. This suggests the zircon grain has retained its magmatic Hf isotope composition through recrystallization and Pb loss. Thirteen analyses of 11 zircon grains from ULG 159394 have an average $(^{176}Hf/^{177}Hf)_{2936\ Ma}$ of 0.280975 ± 55 (2σ) corresponding to $\varepsilon_{Hf(2936\ Ma)}$ of +3.1 ± 1.9 (2σ). The total range of $\varepsilon_{Hf\ (2936\ Ma)}$ for sample 159394 is 3.8 ε_{Hf} units, from + 1.2 to + 5.0 (Figures 4-8, 4-9). Three analyses from zircon grains retaining their magmatic $^{207}Pb/^{206}Pb$ age have $(^{176}Hf/^{177}Hf)_{2936\ Ma}$ from 0.280952 to 0.281008, or $\varepsilon_{Hf(2936\ Ma)}$ of +2.3 to +4.2, respectively. Ten analyses of ten grains from LLG 159437 have an average $(^{176}Hf/^{177}Hf)_{2936\ Ma}$ of 0.280936 ± 40 (2σ), which translates to an $\varepsilon_{Hf\ (2936\ Ma)}$ of +1.7 ± 1.4 (Figure 4-7). The total range in $\varepsilon_{Hf(2936\ Ma)}$ for this sample is 2.6 epsilon-units (Figure 4-8, 4-9). Seven analyses of 6 zircon grains from anorthosite sample 159455 have an

$(^{176}Hf/^{177}Hf)_{2936Ma}$ of 0.280965 ± 48 (2σ), corresponding to an average $\varepsilon_{Hf\,(2936\,Ma)}$ of +2.7 ± 1.7 (Figure 4-7). The range of $\varepsilon_{Hf(2936\,Ma)}$ for this sample is from + 1.6 to + 4.0, or 2.4 epsilon-units (Figures 4-8, 4-9).

There is very little observable difference in the total range of ε_{Hf} compositions from each of the three Fiskenæsset samples analyzed (Figures 4-7, 4-8, 4-9). The total range of ε_{Hf} values for each unit all overlap suggesting that zircons analyzed from all three samples could have crystallized from the same parent magma. The within sample heterogeneity of ε_{Hf} is greater than the analytical uncertainty (± 0.7 ε_{Hf} units (1.2 ε_{Hf} units total range), determined by the average external reproducibility of assumed homogeneous natural zircon reference materials, Supplemental Table S4-2.2, Supplemental File S4-2) for all three Fiskenæsset samples analyzed. The within sample ε_{Hf} heterogeneities implies multiple sources of distinct Hf isotopic composition contributed to the parent magma of the anorthosite complex.

4.5.2.2 Nunataarsuk

A majority of the zircon grains analyzed from the Nunataarsuk samples form a horizontal array with no obvious increase in initial $(^{176}Hf/^{177}Hf)_{2914\,Ma}$ with decrease $^{207}Pb/^{206}Pb$ age (Figure 4-7), suggesting that, like for Fiskenæsset, zircon recrystallization and Pb loss has not affected the magmatic Hf-isotope compositions significantly. An exception is the ~ 2600 Ma zircon population in ULG-AN N03-81A, which has a distinct Hf isotope composition, more radiogenic than the $^{176}Hf/^{177}Hf$ defined by the older magmatic population. Eight zircon grains analyzed from leucogabbro sample N03-83 have an average $(^{176}Hf/^{177}Hf)_{2914\,Ma}$ of 0.280977 ± 64 (2σ), which corresponds to an

average $\varepsilon_{Hf\,(2914\,Ma)}$ of +2.5 ± 2.3. The $\varepsilon_{Hf\,(2914\,Ma)}$ for all zircons analyzed from sample N03-83 ranges from + 0.6 to + 4.8 (Figures 4-8, 4-10). The four oldest grains (six analyses) comprising the 2914 Ma igneous age zircon population have $(^{176}Hf/^{177}Hf)_{2914\,Ma}$ from 0.280923 to 0.281042 and a range of $\varepsilon_{Hf(2914\,Ma)}$ from + 0.6 to + 4.8, defining the ε_{Hf} range for the sample. Eighteen analyses of 16 different zircon grains separated from leucogabbro N03-09 yielded an average $(^{176}Hf/^{177}Hf)_{2914\,Ma}$ of 0.280982 ± 64 (2σ) corresponding to an average $\varepsilon_{Hf\,(2914\,Ma)}$ of +2.7 ± 2.3 with a total $\varepsilon_{Hf(2914\,Ma)}$ range of 4.7 epsilon-units (- 0.1 to + 4.6; Figures 4-8, 4-10).

In contrast to all other samples analyzed, leucogabbro sample N03-81A contains two zircon populations with distinct $(^{176}Hf/^{177}Hf)_{2914\,Ma}$ values (Figure 4-7). Four of the nine zircon grains analyzed have $^{207}Pb/^{206}Pb$ ages from 2629 Ma to 2838 Ma and an average $(^{176}Hf/^{177}Hf)_{2914\,Ma}$ of 0.288970 ± 60 (2σ). This corresponds to an average $\varepsilon_{Hf\,(2914\,Ma)}$ of +2.4 ± 2.1 (total range + 2.3 ε-units) (Figure 4-10). The other 5 zircon grains analyzed have $^{207}Pb/^{206}Pb$ ages from 2566 to 2601 Ma and have an average $(^{176}Hf/^{177}Hf)_{2914\,Ma}$ of 0.281107 ± 44 (2σ), corresponding to an average $\varepsilon_{Hf\,(2914\,Ma)}$ of - 0.2 ± 1.6 and a total range of 2 ε_{Hf} units (Figures 4-7, 4-10).

With the exception of the young zircon population in ULG-AN N03-81A, there is little difference between the ranges in Hf isotope compositions of zircon grains from the three Nunataarsuk samples analyzed. Figure 4-10 shows the overlapping range of ε_{Hf} values for each sample suggesting that all Nunataarsuk zircon grains could be derived from the same parent magma. Also similar to Fiskenæsset, the total ε_{Hf} range for each sample is ~2 times greater than analytical uncertainty, suggesting the parent magma of the

Nunataarsuk anorthosite complex was derived from multiple sources with distinct Hf isotope compositions.

4.5.3 Pb isotopes in plagioclase

A summary of the measured Pb isotope data for plagioclase in Fiskenæsset and Nunataarsuk is provided in Table 4-5 and Figures 4-9 and 4-10. Results for each individual analysis are listed in Supplemental Tables S4-3.1 and S4-3.2 of Supplemental File S4-3. The addition of unsupported radiogenic lead in feldspars has plagued the determination of initial Pb isotope compositions. To ensure that the measured Pb isotope ratios represent the initial Pb isotope compositions for the plagioclase analyzed only the best-preserved plagioclase crystals were selected for Pb isotope analysis. Megacrysts range in size from ~0.5 cm to 3 cm in diameter and are typically surrounded by a recrystallized matrix dominated by plagioclase, amphibole and pyroxene. Analyses were made across the centers of the plagioclase megacrysts that had not been affected by recrystallization or fluid alteration (Figure 4-3). Traverses across megacrysts were planned to avoid analyses near cracks or mineral inclusions, typical sources of unsupported radiogenic Pb in feldspars. Two additional steps were taken to further ensure the measured Pb isotope ratios were not contaminated by radiogenic Pb: (1) if continuous U counts above background were recorded throughout Pb isotope measurements the analysis was discarded and (2) in-growth corrections were made for all analyses where U and Th were detected above background during trace element analysis by LA-ICPMS. Corrections for radiogenic Pb were made using the measured U and Th concentrations and the crystallization age of the respective anorthosite complex (Fiskenæsset = 2936 Ma,

Nunataarsuk = 2914 Ma). In-growth corrected Pb isotope ratios for Fiskenæsset samples were no more than 0.06 % different than the measured ratios and Nunataarsuk samples were all less than 0.065 % different. If the corrected Pb isotope ratios were outside of the 1-sigma internal error for each measured Pb isotope ratio the analysis was disgarded.

4.5.3.1 Fiskenæsset

The $^{206}Pb/^{204}Pb$ ratios measured for samples from the Fiskenæsset complex are plotted in Figure 4-9 along with plagioclase An number and Pb concentration as a function of stratigraphic position within the intrusion. Also shown are relative probability histograms for $^{206}Pb/^{204}Pb$ in each unit and for the complex as a whole. When all analyses for the Fiskenæsset complex are combined, each of the $^{206}Pb/^{204}Pb$, $^{207}Pb/^{204}Pb$ and $^{208}Pb/^{204}Pb$ ratios form a continuum on a relative probability histogram with large ranges of $^{206}Pb/^{204}Pb$ ratios from 12.81 to 13.47 (range = 5.1 %), $^{207}Pb/^{204}Pb$ from 14.04 to 14.66 (range = 4.3 %) and $^{208}Pb/^{204}Pb$ ratios between 31.97 and 33.38 (range = 4.3 %). The overall average $^{206}Pb/^{204}Pb$, $^{207}Pb/^{204}Pb$ and $^{208}Pb/^{204}Pb$ ratios for the Fiskenæsset complex are 13.21 ± 0.13 (1SD, 1.0 % RSD), 14.36 ± 0.16 (1SD, 0.8 % RSD) and 32.76 ± 0.26 (1SD, 0.8 % RSD), respectively. The extent of the Pb-isotope variability measured in the plagioclase from Fiskenæsset is far beyond that expected from analytical uncertainty from the LA-MC-ICPMS method. Repeated measurements of standard reference materials (MPI-ATHO-G and MPI-T1-G) at similar signal intensities as the unknown plagioclase measured over the course of all analytical sessions have uncertainties of 0.30 % RSD (1σ) for $^{206}Pb/^{204}Pb$, and 0.45 % RSD (1σ) for $^{207}Pb/^{204}Pb$ and $^{208}Pb/^{204}Pb$ (Supplemental Table S4-1.1, Supplemental File S4-1).

There is little discernable Pb isotope variation within individual units of the Fiskenæsset complex. All Pb isotope ratios measured for a unit define a unimodal population (Figure 4-9) and average Pb isotope ratios, maxima on the relative probability histograms, all fall within 1SD of the overall average for the Fiskenæsset complex (*e.g.* $^{206}Pb/^{204}Pb$: LLG = 13.07 ± 0.09 (0.75 % RSD, 1σ); MG = 13.18 ± 0.09 (0.72 % RSD, 1σ); ULG = 13.12 ± 0.13 (1.01 % RSD, 1σ); AN = 13.05 ± 0.11 (0.85 % RSD 1σ)) (Figure 4-9, Table 4-5, Supplemental Table S4-3.1, Supplemental File S4-3). The Pb isotope variability within a single unit can be evaluated using the average Pb isotope ratios for each sample/individual megacryst. The Pb isotope variability for each magmatic unit is similar to the variability for the entire Fiskenæsset complex. Within-unit variations in Pb isotope composition are greater than analytical uncertainties yet do not exceed 0.92 % RSD (1σ), 0.95 % RSD (1σ), 1.01 % RSD (1σ), and 0.85 % RSD (1σ) for the LLG, MG, ULG and AN units, respectively (Table 4-6). The Pb isotope ratios measured within a single sample/individual megacryst display the greatest heterogeneity with variations up to 1.28 % RSD (1σ) (Supplemental Table S4-3.1, Supplemental File S4-3). There is no correlation between Pb isotopic variability and Pb concentration.

4.5.3.2 Nunataarsuk

The $^{206}Pb/^{204}Pb$ ratios measured in plagioclase megacrysts from six Nunataarsuk leucogabbro-anorthosite samples are plotted in Figure 4-10, along with the An contents and Pb concentrations for each individual plagioclase megacryst analyzed. The average Nunataarsuk $^{206}Pb/^{204}Pb$, $^{207}Pb/^{204}Pb$ and $^{208}Pb/^{204}Pb$ are 12.66 ± 0.16 (1 SD, 1.3 % RSD), 13.96 ± 0.13 (1 SD, 0.9 % RSD) and 32.37 ± 0.30 (1 SD, 0.9 % RSD), respectively

(Table 4-5, Supplemental Table S4-3.2, Supplemental File S4-3). The total range of Nunataarsuk $^{206}Pb/^{204}Pb$ is 12.24 to 12.91 (range = 5.3 %), $^{207}Pb/^{204}Pb$ is 13.63 to 14.23 (range = 4.3 %) and $^{208}Pb/^{204}Pb$ is 31.54 to 32.93 (range = 4.3 %). The Pb isotope variability exceeds the analytical uncertainty of the LA-MC-ICPMS method indicating that natural Pb isotope variations exist within the Nunataarsuk complex.

Similar to Fiskenæsset, there is very little isotopic variability between the two Nunataarsuk units analyzed. On a relative probability histogram, compiled $^{206}Pb/^{204}Pb$, $^{207}Pb/^{204}Pb$ and $^{208}Pb/^{204}Pb$ from Nunataarsuk each define a unimodal peak skewed towards higher Pb-isotope ratios (Figure 4-10). The average $^{206}Pb/^{204}Pb$, $^{207}Pb/^{204}Pb$ and $^{208}Pb/^{204}Pb$ for each of the two units analyzed, defined by the histogram maxima, are within 1 SD of the average Pb ratios for Nunataarsuk as a whole (*e.g.* $^{206}Pb/^{204}Pb$: LLG-AN = 12.64 ± 0.17 (1.4 % RSD, 1σ); ULG-AN = 12.68 ± 0.17 (1.3 % RSD, 1σ)). Pb isotope variability for each unit, determined using the average Pb isotope ratios for each sample/individual megacryst does not exceed 1.4 % RSD (1σ) (Table 4-5). Variation within a Nunataarsuk sample/individual megacryst is greater than analytical error yet does not exceed 1.02 % RSD (1σ) (Supplemental Table S4-3.2, Supplemental File S4-3).

4.6 DISCUSSION

The Fiskenæsset and Nunataarsuk anorthosite complexes exhibit significant isotopic heterogeneity in Hf and Pb preserved, respectively, in zircon (magmatic domains and recrystallized domains retaining magmatic compositions, distinguished on the basis of U-Pb ages) and plagioclase (texturally distinct igneous megacrysts). The heterogeneity is most apparent on the scale of individual crystals in a sample, less so between the

averages of results from different hand samples, and not discernable between the averages of results from individual units of the magmatic stratigraphy. The implication is that significant isotopic heterogeneity existed in the parent magmas of both complexes but that the heterogeneities average out over the scale of the entire intrusion, though not at the scale of individual crystals, during crustal transport and/or emplacement. Models for the dynamics of modern basalt magmas suggest that they travel very quickly (~1-2.5 kyr) from their source regions in the asthenosphere (60-120 km depth) up to mid-ocean ridges at the surface, preserving isotopic heterogeneities inherited from the melting zone (Connolly et al., 2009). Similar models do not exist for Archean anorthosite complexes because insufficient detail is known about their magmatic histories. It is therefore important to constrain the nature of the magmatic sources of the isotopic heterogeneities in the Fiskenæsset and Nunataarsuk complexes not only to understand how their parent magmas were generated but also to provide information for the development of models for their transport and emplacement.

4.6.1 Hf isotope variability and potential end members

The range of zircon ε_{Hf} values from a single rock reflects the heterogeneity of the parent melt. The within sample ε_{Hf} variability of zircon grains from the three Fiskenæsset samples analyzed and the three Nunataarsuk samples analyzed exceeds analytical reproducibility suggesting measurable Hf isotope heterogeneity existed in the parent magma for each anorthosite complex. The range and average values of ε_{Hf} from individual samples overlap with one another within each of the Fiskenæsset and Nunataarsuk complexes. This suggests that the samples from each complex were derived

from a common (albeit heterogeneous) parent magma (Figures 4-8 to 4-10). The observed range of ε_{Hf} values (Fiskenæsset samples: 4.4 ε_{Hf} units; Nunataarsuk samples: 4.9 ε_{Hf} units) is most likely the result of open system behavior such as crustal contamination or magma mixing, between sources with distinct Hf isotope compositions, in each of the parent magmas of the 2 complexes.

The most straight-forward interpretation of the ε_{Hf} data for both Fiskenæsset and Nunataarsuk is that both anorthosite complexes were derived from a heterogeneous parent magma representing a mixture between ~ 2900 Ma depleted mantle (high ε_{Hf}) and either ~ 2900 Ma CHUR compositions or older crustal components (low ε_{Hf}, Figure 4-8). Zircon grains with higher ε_{Hf} values represent a greater depleted mantle component in their parent magma while zircon grains with lower ε_{Hf} values contain more of the CHUR-like, or crustal, end-member. Derivation from a depleted mantle source is consistent with the proposed model for Archean anorthosite petrogenesis (Phinney 1982; Phinney et al., 1989) and at Fiskenæsset is supported by previous whole rock Nd isotope investigations (Ashwal et al., 1989; Polat et al., 2010) but the significance of the lower ε_{Hf} end member is unclear. The low ε_{Hf} end member may be derived from CHUR or a crustal source, and if it does represent crust, it is desirable to constrain the age and composition (mafic vs. felsic) of the crust.

Assuming the upper ε_{Hf} end members for Fiskenæsset and Nunataarsuk are representative of ~ 2900 Ma depleted mantle, more complex multi-source histories can be considered by assuming a $^{176}Lu/^{177}Hf$ for the source of the lower ε_{Hf} end member and calculating a Hf depleted mantle model age ($T_{DM}(Hf)$). In Figure 4-8, Fiskenæsset and

Nunataarsuk Hf depleted mantle model ages are calculated for the lower ε_{Hf} end member composition using a range of $^{176}Lu/^{177}Hf$ values. The $^{176}Lu/^{177}Hf$ is characteristic of the nature of the source and generally decreases with increasing silica. Typical $^{176}Lu/^{177}Hf$ for felsic rocks range from ~ 0.05 to ~ 0.015, with Archean tonalites generally having a $^{176}Lu/^{177}Hf < 0.01$ (Blichert-Toft and Albarede, 2008; Martin, 1995; Pietranik et al., 2008). The $^{176}Lu/^{177}Hf$ of the modern continental crust is 0.013 – 0.014 (Taylor and McLennan, 1995). Mafic rocks and komatiites tend to have higher $^{176}Lu/^{177}Hf$, from ~ 0.02 to > 0.030 (Blichert-Toft and Albarede, 2008; Pietranik et al., 2008; Blichert-Toft and Putchel, 2010). Depleted mantle model ages for Fiskenæsset and Nunataarsuk increase with increasing $^{176}Lu/^{177}Hf$ (Figure 4-8) yet without additional constraints on the timing of source separation, a unique solution for the $^{176}Lu/^{177}Hf$ ratio of the low ε_{Hf} source cannot be made.

4.6.2 Pb isotope variations, end members and characterizing the nature of the source

Multiple isotope systems are often utilized in geological investigations to identify the effects of secondary alteration and metamorphic disturbance in magmatic systems and to determine the source and nature of multi-component magmatic systems involved in the origin and evolution of the continental crust. Measurements are made on the same material (*e.g.*, bulk rock powder or single zircon crystal) and the results often correlated on an analysis-by-analysis basis (*e.g.* $^{143}Nd/^{144}Nd$ vs. $^{206}Pb/^{204}Pb$ or $^{87}Sr/^{86}Sr$ vs. $^{206}Pb/^{204}Pb$ for whole rocks or $\delta^{18}O$ vs. ε_{Hf} for an individual zircon grains). The Lu-Hf isotope systematics of zircon grains from Fiskenæsset and Nunataarsuk fail to provide a unique solution for the source and nature for the low ε_{Hf} end members of both anorthosite

parent magmas. We can demonstrate however that by using Hf isotopes in zircon in conjunction with Pb isotopes in plagioclase, both the timing of source extraction and the nature of the end member sources can be constrained for both the Fiskenæsset and Nunataarsuk complexes. The results of each individual data set can be linked because the plagioclase and the zircon both crystallized from the same magma yet because the results consist of two separate isotopic measurements on two different minerals they cannot be correlated on an analysis-by-analysis basis.

Isotopic variations in Pb beyond analytical uncertainties are observed for the Fiskenæsset and Nunataarsuk complexes. The most radiogenic Nunataarsuk Pb isotope compositions and the least radiogenic Fiskenæsset Pb isotope compositions cluster around the ~2900 Ma depleted mantle model Pb isotope composition (Kramers and Tolstikihin, 1997), consistent with a proposed depleted mantle source for Archean anorthosites (Figure 4-11A). From this point, the Fiskenæsset and Nunataarsuk Pb isotope compositions diverge in opposite directions (Figure 4-11A). The divergent trends suggest the depleted mantle source interacted with two distinct end members with unique Pb isotope compositions: A more radiogenic Pb source at Fiskenæsset, not identified in the Nunataarsuk Pb isotope data, and a low-μ end member at Nunataarsuk, not observed at Fiskenæsset.

A number of possible scenarios provide potential solutions to constrain the Pb isotope end members at Fiskenæsset and Nunataarsuk yet only a few provide acceptable solutions to explain both the Hf and Pb isotope data collected in this investigation. For both Fiskenæsset and Nunataarsuk, the Pb data rule out mixing between depleted and primitive mantle sources – that is, one end member with an isotopic composition similar

to ~ 2900 Ma depleted mantle and a second end member with an isotopic composition similar to ~ 2900 Ma CHUR. While this scenario is a plausible solution for both the Fiskenæsset and Nunataarsuk Hf isotope data (Figure 4-8), it is inconsistent with the Pb isotope data because the estimated Pb isotope composition for the ~ 2900 Ma bulk silicate earth (BSE, Galer and Goldstein, 1996), analogous to CHUR, falls distinctly above and off of the trend of both Fiskenæsset and Nunataarsuk Pb isotope compositions (Figure 4-11A).

In contrast, if a crustal end member is considered, several solutions can be derived to describe the Fiskenæsset and Nunataarsuk Pb isotope data. Fiskenæsset Pb isotope compositions follow a trajectory from ca. 2900 Ma depleted mantle to higher μ-values (Figure 4-11A). Specifically, a high-μ source that separated from the mantle ca. 3700 Ma with a minimum μ ~ 12 provides a reasonable solution for these observations (Figure 4-11B). Source separation (model ages) between ca. 3600 Ma and ca. 3800 Ma with minimum μ ~12 would also be compatible with the Fiskenæsset Pb isotope data.

Nunataarsuk Pb isotope compositions project from ca. 2900 Ma depleted mantle to μ-values lower than the depleted mantle. A plausible end member scenario for the range of Pb isotope compositions is mixing between a ca. 2900 Ma depleted mantle and a low-μ source, isolated from the depleted mantle ca. 4200 Ma and evolving until ca. 2900 Ma with a maximum μ ~ 6 (Figure 4-11C). As the case with Fiskenæsset, this solution is non-unique and many end-member solutions could exist including solutions involving low-μ sources separated from the depleted mantle between ca. 4100 Ma and ca. 4300 Ma evolving until ca. 2900 Ma with a maximum μ ~ 6.

The timing of source separation, or model ages, provided by the Pb isotope models can be used in conjunction with the Hf isotope data to constrain the $^{176}Lu/^{177}Hf$ ratio for the low ε_{Hf} end member for Fiskenæsset and Nunataarsuk. This allows us to further characterize the nature of the crustal end member that interacted with ca. 2900 Ma depleted mantle to generate the observed range of isotope compositions at each anorthosite complex. For Fiskenæsset, a melt separated from the depleted mantle ca. 3700 Ma would evolve with a $^{176}Lu/^{177}Hf$ of ~ 0.028 to produce the lowest ε_{Hf} observed. Source separation ages from 3600 Ma to 3800 Ma result in variation in $^{176}Lu/^{177}Hf$ from ~ 0.026 to ~ 0.029. This range of $^{176}Lu/^{177}Hf$ is characteristic of mafic crust (Blichert-Toft and Albarede, 2008; Pietranik et al., 2008). A melt separated from depleted mantle ca. 4200 Ma would evolve over time at a $^{176}Lu/^{177}Hf$ of ~ 0.0315 to produce the low ε_{Hf} end member identified at Nunataarsuk. Variations in the model age of the low ε_{Hf} end member from ca. 4100 Ma to 4300 Ma result in a range of $^{176}Lu/^{177}Hf$ from ~ 0.031 to ~ 0.032. This range of $^{176}Lu/^{177}Hf$ is also characteristic of mafic crust (Blichert-Toft and Albarede, 2008; Pietranik et al., 2008).

It is most likely that the range of ε_{Hf} values for both Nunataarsuk and Fiskenæsset represent only a partial mixing array between depleted mantle and crustal components and the ε_{Hf} composition of the lower end member plots below that of the lowest measured zircon for each anorthosite complex. The calculated $^{176}Lu/^{177}Hf$ for the measured end members would represent a maximum value for the respective end member source. Lower ε_{Hf} values would result in lower derived $^{176}Lu/^{177}Hf$ for the end member source,

leading to source compositions with higher silica contents. The minimum ε_{Hf} values for each anorthosite complex cannot be determined from the available data.

The calculated $^{176}Lu/^{177}Hf$ of the crustal end member is also sensitive to the composition of the depleted mantle and, therefore, the depleted mantle model chosen. A depleted mantle model based on the Hf isotope composition of modern MORB (Griffin et al., 2000; recalculated by Andersen et al., 2009) was used in this study to provide a basis of comparison between the two anorthosite complexes. When compared with available Hf isotope data through time (dominantly zircon analyses), this model tends to overestimate the Hf isotope composition for the Archean depleted mantle (Hawkesworth et al., 2010). This is in contrast to other depleted mantle models, which suggest a more gradual increase in the Hf isotopic composition for the depleted mantle during the Archean (*e.g.* Pietranik et al., 2009; Tolstikhin et al., 2006). In general, there are large uncertainties regarding the Hf isotopic composition and evolution of the Archean mantle largely due to limited reliable Hf isotopic compositions of Archean mantle derived material. If a depleted mantle model suggesting a more retarded Hf isotope evolution was used in this study the Hf isotope compositions for the Archean depleted mantle would all be lower than those predicted by the Griffin et al. (2000) model, which in turn would bias the derived $^{176}Lu/^{177}Hf$ ratios for the end member source of the Fiskenæsset and Nunataarsuk anorthosite complexes to higher values.

4.6.3 Preservation of the crustal end members?

Mixing of depleted mantle and mafic crust sources can occur, in principle, within either the mantle (through subduction or delamination of the lithosphere) or crust

(through contamination of mantle-derived magmas by mafic crust). It is probable that the range of Hf and Pb isotope compositions observed at Fiskenæsset and Nunataarsuk were produced by crustal contamination for the following reasons.

The development of enriched and depleted compositional domains within the Archean mantle as the result of recycling mafic crust by subduction of oceanic lithosphere has been demonstrated by numerical models yet the "survival" time of these modeled heterogeneities in the upper mantle is limited by gravitational settling of the dense mafic components when converted to eclogite (Davies, 2006). The range of Nd, Hf and Pb isotope compositions of Archean mantle-derived rocks of a given age suggest that chemical heterogeneities existed within the Archean mantle at a given time (Bennett, 2003 and references therein; Kamber et al., 2003). Yet Sm-Nd isotope systematics indicate the lifespan of these heterogeneities within the hotter Archean mantle is ~ 100 million years, or ~ 1/10 the lifetime of chemical heterogeneities in the modern mantle (Blichert-Toft and Albarede, 1994). If the range of Hf and Pb isotope compositions at Fiskenæsset and Nunataarsuk were the result of the mixing between ~ 2900 Ma depleted mantle and recycled mafic crust, the crustal end member would have had to persist in the mantle sources region of the anorthosites for ≥ 1 billion years. The likely short lifespan of chemical heterogeneities in the Archean mantle makes this an unlikely scenario.

It has recently been suggested that the anorthositic parent magmas at Fiskenæsset were produced within a sub-arc mantle wedge, where harzburgitic, depleted mantle was metasomatized by high-Al (Rollinson et al., 2010), LREE, Sr and Ca-enriched (Polat et al., 2009, 2011) partial melts of subducting lithospheric crust. Slab melting in the Archean is thought to have produced tonalite-trondhjemite-granodiorite (TTG) magmas

(Defant and Drummond, 1990; Martin, 1993) with characteristically low $^{176}Lu/^{177}Hf$ ratios of < 0.01 (Vervoort and Blichert-Toft, 1999, Blichert-Toft and Albarede, 1998). The calculated mantle extraction age of a melt with a $^{176}Lu/^{177}Hf$ ratio of < 0.01 is < 3250 Ma for both Fiskenæsset and Nunataarsuk. Thus, neither the bulk composition (TTG) nor $^{176}Lu/^{177}Hf$ ratio of slab melts can represent the mafic crustal component required by the Pb and Hf isotope data for Fiskenæsset. The data do not preclude a subduction model for Fiskenæsset but do require that the parent magmas of the anorthosites were contaminated by mafic crust after extraction from their mantle source regions.

If the mantle-derived parent magmas of Fiskenæsset and Nunataarsuk were contaminated by long-lived Eoarchean and Hadean mafic crust at ~ 2900 Ma, is there any evidence that this ancient crust is still preserved today in south West Greenland? Three potential mafic end members have been identified: amphibolite country rock at Fiskenæsset; dioritic units of both the regional Eoarchean and Mesoarchean quartzo-feldspathic gneisses; and mafic metavolcanics from within the quartzo-feldspathic Eoarchean Itsaq Gneiss Complex (IGC). We show below that, based on current knowledge of the rocks of south West Greenland, the potential mafic crustal end members for Fiskenæsset and Nunataarsuk have yet to be identified.

The country rock into which the Nunataarsuk anorthosite was emplaced is unknown but evidence of an intrusive relationship between the Fiskenæsset anorthosite complex and amphibolite country rock has been documented at Fiskeaæsset; it has been interpreted to represent shallow-level emplacement of parent melt and crystal mush into oceanic crust (Escher and Myers, 1975; Myers, 1985). Geochemical investigations of the Fiskenæsset amphibolites have identified two distinct groups of basaltic magmas,

"MORB" (mid-ocean ridge basalt) and "tholeiitic" (Rivalenti, 1976; Weaver et al., 1982; Polat et al. 2009). Both types of basalts are thought to have been derived from a common parent magma and most workers have proposed petrogenetic links between the basalts and Fiskenæsset anorthosite complex through fractional crystallization. Specifically, the MORBs have been interpreted as ocean floor basalt into which the anorthosite complex intruded, whereas the tholeiite has been inferred to be the parent magma of the anorthosite complex (Weaver et al., 1982; Polat et al., 2009). More recently, Polat et al. (2011) suggested that the anorthosites and basalts formed in the same tectonic setting but had different petrogenetic origins. In either model, the close (genetic and/or tectonic) relationship between Fiskenæsset and both types of identified amphibolites suggests all units are similar in age, possibly within 20 Ma, which is thought to be the average age of Archean ocean crust (Hargraves, 1986). Therefore, the amphibolites identified at Fiskenæsset would be too young to be the mafic crust contaminant of the anorthosite magma, which is modeled here to have been extracted from the mantle some 700 – 900 million years earlier.

Eoarchean crust in south West Greenland is dominated by orthogneisses of the Itsaq Gneiss Complex (~ 3620 – 3880 Ma; Nutman et al., 1996) derived from granites, granodiorites, diorites and tonalites (Bridgwater et al., 1976). The calculated average $^{176}Lu/^{177}Hf$ of 141 diorite bulk rock analyses compiled in GEOROC (http://georoc.mpch-mainz.gwdg.de/georoc) is ~ 0.022, within the upper range of $^{176}Lu/^{177}Hf$ for dioritic to quartz-dioritic components of the Greenland Eaoarchean (Amitsoq) gneisses (Pettingill and Patchett, 1981; Vervoort and Blichert-Toft, 1999). Assuming the diorite component of the Itsaq Gneiss Complex had a $^{176}Lu/^{177}Hf$ of 0.022, a mantle extraction age of ~ 3500

Ma is calculated for the low ε_{Hf} Fiskenæsset end member and ~ 3400 Ma for the low ε_{Hf} Nunataarsuk end member. Both model ages are too young to consider the dioritic component of the Eoarchean gneisses as the potential crustal contaminant. Also, the probable Pb isotope compositions of the Eoarchean gneisses ca. 2900 Ma for a range of μ-values (μ = 0 - 50), based on an estimated initial Pb isotope composition of the least radiogenic feldspar separated from a quartz-diorite gneiss on Akilia Island (Kamber and Moorbath, 1998), fall above the Fiskenæsset Pb isotope compositions and cannot be considered as a crustal end member for Fiskenæsset. There are also dioritic gneisses associated with the quartzo-feldspathic (Nuk) gneisses of south West Greenland but these rocks are much too young to be considered as crustal end members for either anorthosite complex (~ 2900 - 3000 Ma, Bridgwater et al., 1976; Taylor et al., 1980; Baadsgaard and McGregor, 1981).

A third candidate for the crustal end member is mafic metavolcanic rocks found within the Eoarchean Itsaq Gneiss complex. Eoarchean mafic metavolcanics are not known to be present in the Fiskenæsset or Nunataarsuk region, yet are geographically related and could have been more widespread than is known currently. The age of the mafic metavolcanics present at Isua is >3700 Ma (Frei et al., 2004), consistent with the age of the crustal end member modeled for Fiskenæsset but too young for Nunataaruk. Predicted Pb isotope compositions of the Isua metavolcanics ca. 2900 Ma for a range of μ-values (μ = 0 – 50), based on the average initial Pb isotope compositions of the Isua metavolcanics (Frie et al., 2004) project well above the both the Fiskenæsset and

Nunataarsuk Pb isotope compositions and do not fit the Pb isotope characteristics of the crustal end member at either anorthosite complex.

4.6.4 Implications for Mantle-Crust Evolution

Many depleted mantle evolution models extrapolate present-day mantle isotopic compositions, assumed to be representative of modern MORB, back to the formation of the Earth at ~ 4.6 Ga. Ideally, pristine mantle-derived material with well-defined ages would be sampled to directly determine mantle compositions through time yet these samples are rare, especially for Archean-age material. Information about the isotopic composition of the Archean mantle is thus obtained from Archean mafic and ultramafic rocks instead. Unfortunately, primary compositions of these rocks are highly susceptible to metamorphism and secondary alteration and most lack well-defined ages.

The isotope composition of each anorthosite complex should reflect that of the mantle at the time of crystallization. Only one previous study has analyzed the Hf isotope compositions of zircon grains separated from an Archean anorthosite, the ~ 3350 Ma Messina layered intrusion (Zeh et al., 2010). While the total range of ε_{Hf} values (~ 5 ε_{Hf} units) in Messina is similar to that in Fiskenæsset and Nunataarsuk, the average Hf isotope composition of zircons from the Messina anorthosites is lower ($\varepsilon_{Hf\,(3350\,Ma)}$ = + 1.4 ± 1.8, and + 0.1 ± 1.9) than the ~ 3350 Ma depleted mantle (ε_{Hf} ~ 4.6, Griffin et al., 2000). The parent magma of the Messina anorthosite is thus interpreted to include a slightly enriched component, perhaps through contamination by (TTG) crustal melts (Zeh et al., 2010).

The Fiskenæsset and Nunataarsuk depleted mantle end members for Hf isotopes fall within error (dashed lines extrapolated from the range of modern MORB, Figure 4-8) of the model Hf-isotope composition of ~ 2900 Ma a depleted mantle (ε_{Hf} ~ 6.3) of Griffin et al. (2000). The Fiskenæsset and Nunataarsuk Pb depleted mantle end members also fall close to the ~ 2900 Ma depleted mantle model of Kramers and Tolstikhin (1997) for Pb isotopes. These observations indicate that current models for the Hf- and Pb-evolution of the depleted mantle provide a reasonable approximation of the ~ 2900 Ma depleted mantle source for Fiskenæsset and Nunataasuk. The Hf- and Pb-data also suggest that the depleted mantle source of Archean anorthosites is isotopically similar to the depleted mantle source of Archean tholeiites, requiring no special mantle source to explain the parental magmas of such plagioclase-rich rocks. The range of Fiskenæsset Pb isotope compositions extends slightly below the Kramers and Tolstikhin (1997) depleted mantle and is best-fit to a single-stage evolution line with a μ ~ 7.5 (Figure 4-11B). The difference between the Fiskenæsset and Nunataarsuk Pb depleted mantle end members is < 2%, much less than the total range of Pb isotope compositions observed in the modern mantle (Stracke et al., 2003).

The nature, origin and fate of Earth's Hadean crust is a topic of much interest: whether this early crust was felsic (Armstrong, 1981; Bowring and Housh, 1995; Harrison et al., 2005, 2008; Blichert-Toft and Albarede, 2008) or mafic (Chase and Patchett, 1988; Kamber et al., 2003, 2005; O'Neil et al., 2008; Kemp et al., 2010) in composition is debated, yet most models agree that most of the Hadean crust was destroyed by ~ 3800 Ma. Interpretation of the Nunataarsuk Hf and Pb isotope data provides evidence for the

persistence of Hadean mafic crust until at ~ 2900 Ma. Reworking of Hadean crust into Archean magmas, despite preservation difficulties due to the hotter Hadean Earth, has been suggested for both the Slave Craton, Canada (Amelin et al., 1999, 2000; Pietranik et al., 2008; Iizuka et al., 2009), the Superior Craton (O'Neil et al., 2008), the Pilbara Craton (Tessalina et al., 2010) and for ~ 2.65 Ga monzogranites in the Narryer Gneiss Complex of the Yilgarn craton (Kemp et al., 2010). The Nunataarsuk Hf and Pb isotope data provide additional evidence for the survival of Hadean mafic crust for more than a billion years and suggests that this crust could still be preserved in the Nunataarsuk region today.

4.7 CONCLUSION

Earth's rock record dates back only to ~ 4.0 Ga (Bowring and Williams, 1999) although older detrital zircon grains have been identified, dating back to perhaps ~ 4.4 Ga (Wilde et al., 2001). The age of identified crustal sections is biased towards felsic crust due to the scarcity of zircon grains in mafic rocks. The possibility exists that there is a significant abundance of unrecognized early mafic crust preserved today that has yet to be identified. The integration of in situ Pb isotopes in plagioclase with Hf isotopes in zircon from the same igneous rock facilitates the identification of ancient crust. Using our new in situ approach, contamination of mantle-derived magma by ancient mafic crust is suggested for both the Fiskenæsset and Nunataarsuk anorthosite complexes of Greenland. The isotope data presented here suggest the survival of Hadean and Eoarchean crust until ~ 2900 Ma. There is potential that this old mafic crustal could be preserved at the surface within the Nunataarsuk and Fiskenæsset regions today.

4.8 REFERENCES

Amelin Y., Lee D-C., Halliday A.N., and Pidgeon R.T. (1999) Nature of the Earth's earliest crust from hafnium sotopes in single detrital zircons. *Nature* **399**, 252 – 255.

Amelin Y., Lee D.-C. and Halliday A.N. (2000) Early-middle Archean crustal evolution deduced from Lu-Hf and U-Pb isotopic studies of single zircon grains. *Geochiim. Cosmochim. Acta* **64**, 4205 – 4225.

Andersen T., Andersson U.B., Graham S., Aberg G., and Simonsen S.L. (2009) Granitic magmatism by melting of juvenile continental crust: new constraints on the source of Palaeoproterozoic granitoids in Fennoscandia from Hf isotopes in zircon. *J. Geol. Soc. London* **166**, 233 – 247.

Armstrong R.L. (1981) Radiogenic isotopes: the case for crustal recycling on a near-steady-state no-continental-growth Earth. *Phil. Trans. Roy. Soc. London* **A301**, 443 – 472.

Ashwal L.D. (1993) Anorthosites. Springer-Verlag, New York, 422 p.

Ashwal L.D., Wooden J.L., Phinney W.C. and Morrison D.A. (1985) Sm-Nd and Rb-Sr isotope systematic of an Archean anorthosite and related rocks from the Superior Province of the Canadian Shield. *Earth Planet. Sci. Lett.* **74**, 338 – 346.

Ashwal L.D., Jacobsen S.B., Myers J.S., Kalsbeek F. and Goldstein S.J. (1989) Sm-Nd age of the Fiskenaesset Anorthosite Complex, West Greenland. *Earth Planet. Sci. Lett.* **91**, 261 – 270.

Baadsgaard H. and McGregor V.R. (1981) The U-Th-Pb systematics of zircons from the type Nuk Gneisses, Godthabsfjord, West Greenland. *Geochim. Cosmochim. Acta* **45**, 1099 – 1109.

Barton Jr. J.M. (1996) The Messina layered intrusion, Limpopo belt, South Africa, an example on the in-situ contamination of an Archaean anorthosite complex by continental crust. *Precam. Res.* **78**, 139 – 150.

Bennett V.C., Nutman A.P. and McCulloch M.T. (1993) Nd isotopic evidence for transient, highly depleted mantle reservoirs in the early history of the Earth. *Earth Planet. Sci. Lett.* **119**, 299 – 317.

Bennett V.C. (2003) Compositional evolution of the mantle. In *The Mantle and Core Treatise on Geochemistry, v.2* (ed. R.W. Carlson). Elsevier, Amsterdam, pp. 493 - 515.

Bhaskar Rao Y.J., Chetty T.R.K., Janardhan A.S. and Gopalan K. (1996) Sm–Nd and Rb–Sr ages and P–T history of the Archean Sittampundi and Bhavani layered meta-anorthosite complexes in the Cauvery shear zone, South India: evidence for Neoproterozoic reworking of Archean crust. *Contrib. Mineral. Petrol.* **125**, 237-250.

Bhaskar Rao Y.J., Kumar A., Vrevsky A.B., Srinivasan R. and Anantha Iyer G.V. (2000): Sm–Nd ages of two meta-anorthosite complexes around Holenarsipur: constraints on the antiquity of Archean supracrustal rocks of the Dharwar Craton. *Proc. Indian Acad. Sci., Earth and Planetary Sci.* **109**, 57-65.

Black L.P., Moorbath S., Pankhurst R.J. and Windley B.F. (1973) $^{207}Pb/^{206}Pb$ whole rock age of the Archaean granulite facies metamorphic event in west Greenland. *Nature Phys. Sci.* **244**, 50 – 53.

Blichert-Toft J. and Albarede F. (1994) Short-lived chemical heterogeneities in the Archean mantle with implications for mantle convection. *Science* **263**, 1593 – 1596.

Blichert-Toft J. and Albarede F. (2008) Hafnium isotopes in Jack Hills zircons and the formation of the Hadean crust. *Earth Planet. Sci. Lett.* **265**, 686 – 702.

Blichert-Toft J. and Puchtel I.S. (2010) Depleted mantle sources through time: Evidence from Lu-Hf and Sm-Nd isotope systematics of Archean komatiites. *Earth Planet. Sci. Lett.* **297**, 598 – 606.

Bouvier A., Vervoort J.D. and Patchett P.J. (2008) The Lu-Hf and Sm-Nd isotopic composition of CHUR: constraints from unequilibrated chondrites and implications for the bulk composition of terrestrial planets. *Earth Planet. Sci. Lett.* **273**, 48 – 57.

Bowring S.A. and Housh T. (1995) The Earth's early evolution. *Science* **269**, 1535 – 1540.

Bridgwater D., Keto L., McGregor V.R. and Myers J.S. (1976) Archaean geniss complex of Greenland. *In* Geology of Greenland (eds. A. Escher and W.S. Watt), Grønlands geol. Unders. p. 18 – 75.

Chase C.G. and Patchett P.J. (1988) Stored mafic/ultramafic crust and early Archean mantle depletion. *Earth Planet. Sci. Lett.* **91**, 66 – 72.

Chauvel C. and Blichert-Toft J. (2001) A hafnium isotope and trace element perspective on melting of the depleted mantle. *Earth Planet. Sci. Lett.* **190**, 137 – 151.

Connolly J.A.D., Schmidt M.W., Solferino G. and Bagdassarov N. (2009) Permeability of asthenospheric mantle and melt extraction rates at mid-ocean ridges. *Nature* **462**, 209 – 212.

Davies G.F. (2006) Gravitational depletion of the early Earth's upper mantle and the viability of early plate tectonics. *Earth Planet. Sci. Lett.* **243**, 376 – 382.

Defant M.J., and Drummond M.S. (1990) Derivation of some modern arcs by melting of young subducted lithosphere. *Nature* **347**, 662 – 665.

Dymek R.F. and Owens B.R. (2001) Chemical assembly of Archean anorthosites from amphibolite-and granulite-facies terranes, SW Greenland. *Contrib. Mineral Petrol.* **141**, 513 – 528.

Escher J.C. and Myers J.S. (1975) New evidence concerning the original relationships of early Precambrian volcanics and anorthosites in the Fiskenæsset region, southern west Greenland. Rapp. *Gronl. Geol. Unders.* 75, 72 – 76.

Fandrich R., Gu Y., Burrows D. and Moeller K. (2007) Modern SEM-based mineral liberation analysis. *International Journal of Mineral Processing* **84 (1-4)**, 310 – 320.

Fletcher I.R., Rosman K.J.R. and Libby W.G. (1988) Sm-Nd, Pb-Pb, and Rb-Sr geochronology of the Manfred Complex, Mount Narryer, Western Australia. *Precamb. Res.* **38**, 343 – 354.

Frei R., Polat A. and Meibom A (2004) The Hadean upper mantle conundrum: Evidence for source depletion and enrichment from Sm-Nd, Re-Os, and Pb isotopic compositions in 3.71 Gy boninite-like metabaslts from the Isua Supracrustal Belt, Greenland. *Geochim. Cosmochim. Acta* **68**, 1645 – 1660.

Galer S.J.G. and Goldstein S.L. (1996) Influence of accretion on lead in the Earth. *In* Earth processes: reading the isotopic code. (eds. A. Basu, S. Hart). American Geophysical Union, Washington, DC, pp 75 – 98.

Gancarz A.J. (1976) Isotopic systematics in Archean rocks, west Greenland. PhD thesis, California Institute of Technology, Pasadena, 378p.

Griffin W.L. Pearson N.J. Belousova E. Jackson S.E. van Achterbergh E. O'Reilly S.Y. Shee S.R. (2000) The Hf isotope composition of cratonic mantle; LAM-MC-ICPMS analysis of zircon megacrysts in kimberlites. *Geochim. Cosmochim Acta.* **64**, 133 – 147.

Hargraves R.B. (1986) Faster spreading or greater ridge length in the Archean? *Geology* **14**, 750 – 752.

Harrison T.M., Blichert-Toft J., Muller W., Albarede F., Holden P. and Mojzsis S.J. (2005) Heterogeneous Hadean Hafnium: evidence for continental crust at 4.4 to 4.5 Ga. *Science* **310**, 1947.

Harrison T.M., Schmitt A.K., McCulloch M.T. and Lovera O.M. (2008) Early (4.5 Ga) formation of terrestrial crust: Lu Hf, del ^{18}O, and Ti thermometry results for Hadean zircons. *Earth Planet. Sci. Lett.* **268**, 476 – 486.

Hawkesworth C.J., Dhuime B., Pietranik A.B., Cawood P.A., Kemp A.I.S., and Storey C.D. (2010) The generation and evolution of the continental crust. *J. Geol. Soc. London* **167**, 229 – 248.

Iizuka T., Komiya T., Johnson S.P., Kon Y., Maruyama S. and Hirata T. (2009) Reworking of Hadean crust in the Acasta gneisses, northwestern Canada: evidence from in situ Lu-Hf isotope analysis of zircon. *Chem. Geol.* **259,** 230 – 239.

Jaffey A.H., Flynn K.F., Glendenin L.E., Bentley W.C. and Essling A.M. (1971) Precision measurement of half-lives and specific activities of ^{235}U and ^{238}U. *Phys. Rev. C.* **4**, 1889 – 1906.

Kamber B.S. and Moorbath S (1998) Initial Pb of the Amitsoq gneiss revisited: implication for the timing of early Archaean crustal evolution in West Greenland. *Chem. Geol.* **150**, 19 – 41.

Kamber B.S., Collerson K.D., Moorbath S. and Whitehouse M.J. (2003) Inheritance of early Archaean Pb-isotope variability from long-lived Hadean protocrust. *Contrib. Mineral Petrol.* **145**, 25 – 46.

Kamber B.S., Whitehouse M.J., Bolhar R. and Moorbath S. (2005) Volcanic resurfacing and the early terrestrial crust: zircon U-Pb and REE constraints from the Isua Greenstone Belt, southern West Greenland. *Earth Planet. Sci. Lett.* **240**, 276 – 290.

Kalsbeek F. and Pidgeon R.T. (1980) The geological significance of Rb-Sr whole-rock isochrons of polymetamorphic Archean gneisses, Fiskenæsset area, southern West Greenland. *Earth Planet. Sci. Lett.* **50**, 225 – 237.

Kemp A.I.S., Foster G.L., Schersten A., Whitehouse M.J., Darling J. and Storey C. (2009) Concurrent Pb-Hf isotope analysis of zircon by laser ablation multi-collector ICP-MS, with implications for the crustal evolution of Greenland and the Himalayas. *Chem. Geol.* **261**, 244 – 260.

Kemp A.I.S., Wilde S.A., Hawkesworth C.J., Coath C.D., Nemchin A., Pidgeon R.T., Vervoort J.D. and DuFrane S.A. (2010) Hadean crustal evolution revisited: New constraints from Pb-Hf isotope systematics of the Jack Hills zircons. *Earth Planet. Sci. Lett.* **296**, 45 – 56.

Keulen N., Næraa T., Kokfelt T., Schumacher J.C. and Schersten A. (2010) Zircon record of the igneous and metamorphic history of the Fiskenæsset anorthosite complex in southern West Greenland. *Geol. Surv. Den. Greenland Bull.* **20**, 67-70.

Kinny P.D., Williams I.S., Froude D.O., Ireland T.R. and Compston W. (1988) Early Archean zircon ages from orthogneisses and anorthosites at Mount Narryer, Western Australia. *Precambrian Res.* **38**, 325 – 341.

Kosler J., Forst L. and Slama J. (2008) LAMDATE and LAMTOOL: Spreadsheet-based data reduction for laser ablation-ICPMS. *In* Laser Ablation ICP-MS in the Earth Sciences: Current Practices and Outstanding Issues, v. 40 (ed. P.J. Sylvester). Mineralogical Association of Canada pp. 315 - 317.

Kramers J.D. and Tolstikhin I.N. (1997) Two terrestrial lead isotope paradoxes, forward transport modeling, core formation and the history of the continental crust. *Chem. Geol.* **139**, 75 – 110.

Lahaye Y., Arndt N., Byerly G., Chauvel C., Fourcade S. and Gruau G. (1995) The influence of alteration of the trace-element and Nd isotopic compositions of komatiites. *Chem. Geol.* **126**, 43 – 64.

Ludwig K. (2008) Isoplot 3, A Geochronological Toolkit for Microsoft Excel. Special Publication 1a. Berkeley Geochronology Center.

Martin H. (1993) The mechanisms of petrogenesis of the Archean continental crust – comparison with modern processes. *Lithos* **30**, 373 – 388.

Martin H., (1995) Archaean grey gneisses and the generation of the continental crust. *In* Archaean Crustal Evolution, (ed. K.C. Condie). Elsevier pp. 205 – 260.

Mathez E.A. and Waight T.E. (2003) Lead isotopic disequilibrium between sulfide and plagioclase in the Bushveld complex and the chemical evolution of large layered intrusions. *Geochim. Cosmochim. Acta* **67**, 1875 – 1888.

Moorbath S. and Pankhurst R.J. (1976) Further rubidium-strontium age and isotopic evidence for the nature of late Archean plutonic event in West Greenland. *Nature* **262**, 124 – 126.

Mouri H., Whitehouse M.J., Brandl G. and Rajesh H.M. (2009) A magmatic age and four successive metamorphic events recorded in zircons from a single metaanorthosite sample in the Central Zone of the Limpopo Belt, South Africa. *J. Geol. Soc. London* **166**, 827 – 830.

Myers J.S. (1975) Igneous stratigraphy of Archaean anorthosite at Majorqap qava, near Fiskenæsset, South-West Greenland. *Rapp. Grønlands Geol. Unders.* **74**, 27p.

Myers J.S. (1976) Channel deposits of peridotite, gabbro and chromitite from turbidity currents in the stratiform Fiskenæsset anorthosite complex, southwest Greenland. *Lithos* **9**, 265 – 268.

Myers J.S. (1985) Stratigraphy and structure of the Fiskenæsset Complex, West Greenland. *Grønl. Geol. Unders. Bull.* **150**, 72p.

Myers J.S. and Platt R.G. (1977) Mineral chemistry of layered Archean anorthosite at Majorqap qâva, near Fiskenaesset, southwest Greenland. *Lithos* **10**, 59 – 72.

Næraa T. and Schersten A. (2008) New zircon ages from the Tasiusarsuaq terrane, southern West Greenland. *Geol. Surv. Den. Greenland Bull.* **15**, 73 – 76.

Nutman A.P., McGregor V.R., Friend C.R.L., Bennett V.C. and Kinny P.D. (1996) The Itsaq Gneiss Complex of southern West Greenland; the world's most extensive record of early crustal evolution (3900 – 3600 Ma). *Precambrian Res.* **78**, 1 – 39.

O'Neil J., Carlson R.W., Francis D. and Stevenson R.K. (2008) Neodymium-142 evidence for Hadean mafic crust. *Science* **321**, 1828 – 1831.

Oversby V.M. (1975) Lead isotopic systematics and ages of Archean acid intrusives in the Kalgoorlie Norseman area, western Australia. *Geochim. Cosmochim. Acta* **39**, 1107 – 1125.

Owens B.E. and Dymek R.F. (1997) Comparative petrology of Archean anorthosites in amphibolite and granulite facies terranes, WE Greenland. *Contrib. Mineral. Petrol.* **128**, 371 – 384.

Patchett P.J., Kouvo O., Hedge C.E. and Tatsumoto M. (1981) Evolution of continental crust and mantle heterogeneity: evidence from Hf isotopes. *Contrib. Mineral. Petrol.* **78**, 279 – 297.

Pettingill H.S. and Patchett P.J. (1981) Lu-Hf total-rock age for the Amitsoq gneisses, West Greenland. *Earth Planet. Sci. Let.* **55**, 150 – 156.

Phinney W.C. (1982) Petrogenesis of Archean anorthosites. *In* Workshop on magmatic processes of early planetary crusts: magma oceans and stratiform layered intrusions. *In* Lunar Planet Inst Tech Rep 82 – 01 (eds. D. Walker, I.S. McCallum). Lunar Planet Inst, Houston, pp. 121 – 124.

Phinney W.C., Morrison D.A. and Maczuga D.E. (1989) Anorthosites and related megacrystic units in the evolution of Archean crust. *J. Petrol.* **29**, 1283 – 1323.

Pidgeon R.T. and Kalsbeek, F. (1978) Dating of igneous and metamorphic events in the Fiskenaesset region of southern West Greenland. *Can. J. Earth Sci.* **15**, 2021 – 2025.

Pietranik A.B., Hawkesworth C.J., Storey C.D., Kemp A.I.S., Sircombe K.N., Whitehouse M.J. and Bleeker W. (2008) Episodic mafic crust formation from 4.5 to 2.8 Ga. New evidence from detrital zircons, Slave craton, Canada. *Geology* **36**, 875 – 878.

Pietranik A.B., Hawkesworth C.J., Storey C., and Kemp T. (2009) Depleted mantle evolution and how it is recorded in zircon. *Geochim. Cosmochim. Acta* **73**, A1028.

Polat A., Appel P.W.U., Fryer B., Windley B., Frei R., Samson I.M. and Huang H. (2009) Trace element systematics of the Neoarchean Fiskenæsset anorthosite complex and associated meta-volcanic rocks, SW Greenland: Evidence for a magmatic arc origin. *Precambrian Res.* **175**, 87 – 115.

Polat A., Frei R., Schersten A. and Appel P.W.U. (2010) New age (ca. 2970 Ma), mantle source composition and geodynamic constraints on the Archean Fiskenæsset anorthosite complex, SW Greenland. *Chem. Geol.* **277**, 1 – 20.

Polat A., Fryer B.J., Appel P.W.U., Kalvig P., Kerrich R., Dilek Y., and Yang Z. (2011) Geochmistry of anorthositic differentiated sills in the Archean (~2970 Ma) Fiskenæsset Complex, SW Greenland: Implications for parental magma compositions, geodynamic setting, and secular heat flow in arcs. *Lithos* **123**, 50 – 72.

Riciputi L.R., Valley J.W. and McGregor V.R. (1990) Conditions of Archean granulite metamorphism in the Gadthab-Fiskenaesset region, southern West Greenland. *J. Meta. Geol.* **8**, 171 – 190.

Rivalenti G. (1976) Geochemistry of metavolcanic amphibolites from south-west Greenland. In *The Early History of the Earth* (ed. B.F. Windley). Wiley, London, pp. 213 – 223.

Rollinson H., Reid C. and Windley B. (2010) Chromitites from the Fiskenæsset anorthositic complex, West Greenland: clues to late Archaean mantle processes. In *The Evolving Continents: Understanding Processes of Continental Growth*, v. 338 (eds. T.M. Kusky, M.-G. Zhai, W. Xiao). Geological Society, London, pp. 197 – 212.

Slama J., Kosler J., Condon D.J., Crowley J.L., Gerdes A., Hanchar J.M., Horstwood M.S.A., Morris G.A., Nasdala L., Norberg N., Schaltegger U., Schoene B., Tubrett M.N. and Whitehouse M.J. (2008) Plesovice zircon – a new natural reference material for U-Pb and Hf isotopic microanalysis. *Chem. Geol.* **249**, 1 – 35.

Soderlund U., Patchett P.J., Vervoort J.D. and Isachsen C.E. (2004) The ^{176}Lu decay constant determined by Lu-Hf and U-Pb isotope systematics of Precambrian mafic intrusions. *Earth Planet. Sci. Lett.* **219**, 311 – 324.

Stacey J.S. and Kramers J.D. (1975) Approximation of terrestrial lead isotope evolution by a two-stage model. *Earth Planet. Sci. Lett.* **26**, 207 – 221.

Steele I.M., Bishop F.C., Smith J.V. and Windley B.F. (1977) The Fiskenæsset complex, West Greenland, Part III. Chemistry of silicates and oxide minerals from oxide bearing rocks, mostly from Qeqertarssuatsiaq. *Grønl. Geol. Unders Bull.*. **124**, 38p.

Stracke A.M., Bizimis M. and Salters V.J.M. (2003) Recycling oceanic crust: Quantitative constraints. *Geochem. Geophys. Geosyst.* **4**, doi: 10.1020/2001GC000223.

Sylvester P.J. and Ghaderi M. (1997) Trace element analysis of scheelite by excimer laser ablation–inductively coupled plasma–mass spectrometry (ELA–ICP–MS) using a synthetic silicate glass standard. *Chem. Geol.* **141**, 49–65.

Taylor D.J., McKeegan K.D. and Harrison T.M. (2009) Lu-Hf zircon evidence for rapid lunar differentiation. *Earth Planet. Sci. Lett.* **279**, 157 – 164.

Taylor S.R. and McLennan S.M. (1995) The geochemical evolution of the continental crust. *Rev. Geophys.* **33**, 241 – 265.

Taylor P.N., Moorbath S., Goodwin R. and Petrykowski A.C. (1980) Crustal contamination as an indicator of the extent of early Archean continental crust: Pb isotopic evidence from the late Archean gneisses of West Greenland. *Geochim. Cosmochim. Acta* **44**, 1437 – 1453.

Tessalina S.G., Bourdon B., Van Kranendonk M., Birck J-L. and Philippot P. (2010) Influence of Hadean crust evident in basalts and cherts from the Pilbara Craton. *Nature Geosci.* **3**, 214 – 217.

Tolstikhin I.N., Kramers J.D., and Hofmann A.W. (2006) A chemical Earth model with whole mantle convection: the importance of a core-mantle boundary layer (D") and its early formation. *Chem. Geol.* **226**, 79 – 99.

Vervoort J.D. (2010) Hf Analysis in zircon by LA-MC-ICPMS: promise and pitfalls. *Geol. Soc. Amer. Abstracts with Program*. Paper No. 286-9.

Vervoort, J.D. and Blichert-Toft J. (1999) Evolution of the depleted mantle: Hf isotope evidence from juvenile rocks through time. *Geochim. Cosmochim. Acta* **63**, 533 – 556.

Weaver B.L., Tarney J., Windley B. and Leake B.E. (1982) Geochemistry and petrogenesis of Archean metavolcanic amphibolites from Fiskenæsset, S.W. Greenland. *Geochim. Cosmochim. Acta* **46**, 2203 – 2215.

Wiedenbeck M., Alle P., Corfu F. et al. (1995) Three natural zircon standards for U–Th–Pb, Lu–Hf, trace element and REE analyses. *Geostandards Newsletter* **19**, 1–23.

Wilde S.A., Valley J.W. Peck W.H. and Graham C.M. (2001) Evidence from detrital zircons for the existence of continental crust and oceans on the Earth 4.4 Ga ago. *Nature* **409**, 175 – 178.

Windley B.F. (1971) The stratigraphy of the Fiskenæsset anorthosite complex. *Gronl. Geol. Unders. Rapport* **35**, 19 – 21.

Windley B.F. and Garde A.A. (2009) Arc-generated blocks with crustal sections in the North Atlantic craton of West Greenland; new mechanism of crustal growh in the Archean with modern analogues. *Earth Sci. Rev.* **93**, 1 – 30.

Windley B.F., Herd R.K. and Bowden A.A. (1973) The Fiskenæsset complex, west Greenland. Part I: A preliminary study of the stratigraphy, petrology, and whole rock chemistry from Qeqertarssuatsiaq. *Gronl. Geol. Unders. Bull.* No. 106, 54p.

Zeh A., Gerdes A., Barton Jr. J. and Klemd R. (2010) U-Th-Pb and Lu-Hf systematics of zircon from TTG's, leucosomes, meta-anorthosites and quartzites of the Limpopo Belt (South Africa): Constraints for the formation, recycling and metamorphism of Palaeoarchaean crust. *Precambrian Res.* **179**, 50 – 68.

Table 4-1. LA-ICPMS U-Pb isotopic analyses of zircons from the Fiskenaesset Anorthosite Complex

						Measured Isotopic Ratios[4]							Calculated Ages						
file name[1]	sample	mount[2]	^{232}Th ppm[3]	^{238}U ppm[3]	Th/U Ratio	^{207}Pb/^{235}U	1s error	^{206}Pb/^{238}U	1s error	Rho[5]	^{207}Pb/^{206}Pb	1s error	^{207}Pb/^{235}U Ma	1s error	^{206}Pb/^{238}U Ma	1s error	^{207}Pb/^{206}Pb Ma	1s error	U-Pb/Pb-Pb concordancy (%)[6]
Fiskenaesset leucogabbro 159394 (Upper leucogabbro unit, section A)																			
au29b22	159394-053	picked	51	575	0.09	14.9945	0.5127	0.5470	0.0194	0.52	0.1956	0.0007	2815	33	2813	81	2790	6	101
au29b23	159394-051	picked	101	792	0.13	14.7668	0.2569	0.5431	0.0092	0.49	0.1943	0.0005	2800	17	2796	38	2779	4	101
au29b24	159394-049	picked	75	853	0.09	14.9332	0.2240	0.5445	0.0087	0.53	0.1943	0.0005	2811	14	2802	36	2779	4	101
au29b28	159394-044	picked	68	1998	0.03	13.7260	0.3574	0.5261	0.0131	0.48	0.1880	0.0004	2731	25	2725	55	2725	4	100
au29b29	159394-043	picked	163	1672	0.10	14.5935	0.2151	0.5413	0.0081	0.51	0.1929	0.0005	2789	14	2789	34	2767	4	101
au29b33	159394-042b	picked	134	2345	0.06	14.3479	0.1912	0.5355	0.0072	0.50	0.1920	0.0006	2773	13	2765	30	2759	5	100
au29b34	159394-041a	picked	77	698	0.11	14.3721	0.2074	0.5297	0.0079	0.52	0.1945	0.0005	2775	14	2740	33	2780	4	99
au29b36	159394-039b	picked	266	2330	0.11	14.5713	0.2302	0.5385	0.0088	0.52	0.1924	0.0005	2788	15	2777	37	2763	4	101
au29b42	159394-032	picked	65	726	0.09	15.1027	0.3182	0.5481	0.0124	0.54	0.1949	0.0006	2822	20	2817	52	2784	5	101
ap11A59	159394-01-007	MLA	105	999	0.11	15.0293	0.2457	0.5398	0.0091	0.5	0.1995	0.0008	2817	16	2782	38	2822	6	99
ap11A60	159394-01-007	MLA	104	1034	0.10	15.0888	0.3111	0.5462	0.0118	0.5	0.1987	0.0008	2821	20	2809	49	2816	6	100
ap11A61	159394-07-001	MLA	61	775	0.08	14.8751	0.2200	0.5425	0.0073	0.5	0.1987	0.0006	2807	14	2794	31	2816	5	99
ap11A62	159394-07-001b	MLA	80	707	0.11	14.9587	0.2124	0.5394	0.0077	0.5	0.1993	0.0006	2813	14	2781	32	2821	5	99
ap11A63	159394-08-001	MLA	92	1000	0.09	14.8588	0.2594	0.5393	0.0094	0.5	0.1987	0.0008	2806	17	2780	39	2816	6	99
ap11A64	159394-08-001b	MLA	103	917	0.11	15.1086	0.2167	0.5450	0.0083	0.5	0.1997	0.0008	2822	14	2804	35	2824	6	99
ap11A65	159394-26-001	MLA	136	1751	0.08	15.1914	0.4511	0.5447	0.0186	0.6	0.1992	0.0009	2827	28	2803	78	2820	7	99
ap11A70	159394-35-006	MLA	109	1078	0.10	14.9658	0.2858	0.5372	0.0102	0.5	0.1999	0.0008	2813	18	2772	43	2825	7	98
ap11A71	159394-35-006b	MLA	99	1061	0.09	15.0870	0.2193	0.5447	0.0080	0.5	0.1996	0.0008	2821	14	2803	33	2823	6	99
ap11A72	159394-35-006	MLA	76	796	0.10	14.6389	0.2136	0.5338	0.0083	0.5	0.1983	0.0008	2792	14	2757	35	2812	6	98
ap11A73	159394-36-007a	MLA	62	654	0.09	14.9317	0.2300	0.5386	0.0085	0.5	0.1995	0.0008	2811	15	2778	35	2822	7	98
ap11A74	159394-36-007b	MLA	43	546	0.08	14.7835	0.2348	0.5377	0.0089	0.5	0.1986	0.0009	2801	15	2774	37	2815	7	99
ap11A75	159394-36-007c	MLA	57	566	0.10	14.8796	0.3603	0.5437	0.0133	0.5	0.1972	0.0008	2808	23	2799	56	2803	7	100
ap11A82	159394-76-004a	MLA	44	492	0.09	14.9231	0.2563	0.5424	0.0088	0.5	0.1986	0.0008	2810	16	2794	37	2815	6	99
ap11A83	159394-76-004b	MLA	55	503	0.11	15.0482	0.2182	0.5466	0.0091	0.6	0.1972	0.0007	2818	14	2811	38	2803	6	100
ap11A84	159394-76-004c	MLA	61	566	0.11	15.1414	0.2501	0.5493	0.0088	0.5	0.1994	0.0007	2824	16	2822	37	2822	6	100
au23A39	159394-f001	picked	26	130	0.20	17.2544	0.5230	0.5799	0.0125	0.36	0.2121	0.0020	2949	29	2948	51	2922	15	101
au23A40	159394-f003a	picked	14	21	0.66	17.1909	0.2735	0.5786	0.0098	0.53	0.2157	0.0013	2946	15	2943	40	2949	10	100
au23A41	159394-f003b	picked	20	70	0.29	16.6904	0.4969	0.5697	0.0151	0.44	0.2132	0.0013	2917	29	2907	62	2930	10	99
mr01A07	159394-086B	MLA	145	1526	0.10	15.4022	0.2966	0.5521	0.0110	0.52	0.1936	0.0011	2840	18	2834	46	2773	9	102
mr01A11	159394-073	MLA	86	760	0.11	15.6133	0.2499	0.5566	0.0088	0.49	0.1947	0.0010	2853	15	2852	36	2783	8	103
mr01A12	159394-078	MLA	56	928	0.06	15.0934	0.2745	0.5480	0.0109	0.55	0.1914	0.0010	2821	17	2817	46	2755	9	102
mr01A17	159394-055	MLA	93	992	0.09	14.9644	0.3261	0.5372	0.0126	0.54	0.1936	0.0010	2813	21	2772	53	2773	8	100
mr01A19	159394-061	MLA	89	919	0.10	15.5923	0.2957	0.5564	0.0116	0.55	0.1929	0.0010	2852	18	2852	48	2767	9	103
mr01A22	159394-080	MLA	58	762	0.08	14.9071	0.3439	0.5395	0.0129	0.52	0.1914	0.0009	2809	22	2781	54	2754	8	101
mr01A23	159394-008A	MLA	71	788	0.09	15.0660	0.3748	0.5329	0.0162	0.61	0.1939	0.0010	2819	24	2754	68	2776	9	99
mr01A24	159394-008B	MLA	92	710	0.13	15.3962	0.2523	0.5497	0.0094	0.52	0.1945	0.0010	2840	16	2824	39	2781	8	102
mr01A28	159394-066	MLA	65	813	0.08	15.1627	0.3666	0.5427	0.0139	0.53	0.1944	0.0010	2826	23	2795	58	2780	9	101
mr01A31	159394-046	MLA	66	1516	0.04	13.9041	0.3687	0.5292	0.0140	0.50	0.1841	0.0010	2743	25	2738	59	2690	9	102
mr01A32	159394-070B	MLA	76	925	0.08	15.5705	0.4416	0.5555	0.0174	0.55	0.1951	0.0010	2851	27	2848	72	2785	8	102
mr01A33	159394-075	MLA	106	1044	0.10	15.0331	0.2859	0.5428	0.0104	0.51	0.1944	0.0008	2817	18	2795	44	2780	7	101
mr01A35	159394-026 SE	MLA	89	1024	0.09	15.1185	0.5299	0.5483	0.0195	0.51	0.1927	0.0011	2823	33	2818	81	2766	9	102
mr01A41	159394-037	MLA	48	444	0.11	15.6470	0.2755	0.5560	0.0107	0.55	0.1947	0.0009	2855	17	2850	44	2783	8	102
mr01A43	159394-004	MLA	75	783	0.10	14.7533	0.3404	0.5429	0.0125	0.50	0.1936	0.0009	2799	22	2796	52	2773	8	101
mr01A44	159394-023 top	MLA	92	851	0.11	15.2384	0.3153	0.5506	0.0128	0.56	0.1943	0.0010	2830	20	2828	53	2779	9	102

mr01A45	159394-023 bottom	MLA	59	678	0.09	14.6768	0.4409	0.5424	0.0153	0.47	0.1932	0.0010	2795	29	2793	64	2769	9	101
mr01A47	159394-054	MLA	135	1319	0.10	15.6091	0.3959	0.5556	0.0148	0.53	0.1940	0.0011	2853	24	2849	61	2777	9	103
mr01A52	159394-084	MLA	89	809	0.11	15.2930	0.6162	0.5514	0.0244	0.55	0.1935	0.0011	2834	38	2831	101	2772	10	102
mr01A53	159394-002 center	MLA	164	1676	0.10	15.8936	0.2773	0.5539	0.0121	0.63	0.1933	0.0009	2870	17	2841	50	2770	8	103
mr01A57	159394-089 center	MLA	181	1429	0.13	15.2938	0.6281	0.5509	0.0261	0.58	0.1921	0.0013	2834	39	2829	109	2760	11	102
Fiskenaesset leucogabbro 159437 (Lower leucogabbro unit, section A)																			
au29b03	159437-081a	picked	93	286	0.33	14.9802	0.2491	0.5472	0.0087	0.48	0.1971	0.0007	2814	16	2814	36	2803	6	100
au29b06	159437-078	picked	109	866	0.13	14.7112	0.5224	0.5426	0.0186	0.48	0.1941	0.0006	2797	34	2794	78	2777	5	101
au29b07	159437-077	picked	212	1044	0.20	14.8718	0.1981	0.5413	0.0074	0.51	0.1947	0.0005	2807	13	2789	31	2783	4	100
au29b08	159437-076	picked	314	1344	0.23	14.6941	0.3476	0.5417	0.0125	0.49	0.1943	0.0005	2796	22	2791	52	2779	4	100
au29b09	159437-074	picked	80	81	0.99	15.0069	0.2464	0.5445	0.0090	0.50	0.1978	0.0012	2816	16	2802	38	2808	10	100
au29b10	159437-068	picked	112	90	1.25	15.3632	0.3086	0.5513	0.0105	0.47	0.1983	0.0013	2838	19	2830	43	2812	11	101
au29b13	159437-066	picked	79	156	0.50	15.0526	0.5595	0.5443	0.0194	0.48	0.1977	0.0008	2819	35	2801	81	2807	7	100
au29b15	159437-062	picked	154	946	0.16	14.9682	0.2587	0.5446	0.0107	0.57	0.1937	0.0005	2813	16	2803	45	2774	5	101
au29b16	159437-059	picked	107	298	0.36	14.8573	0.2263	0.5345	0.0088	0.54	0.1960	0.0007	2806	14	2760	37	2793	6	99
au29b18	159437-056	picked	149	1199	0.12	14.8846	0.3556	0.5454	0.0129	0.50	0.1954	0.0005	2808	23	2806	54	2788	4	101
Fiskenaesset anorthosite 159455 (Anorthosite unit, section A)																			
au29b49	159455-019	picked	83	691	0.12	15.0061	0.1949	0.5459	0.0078	0.55	0.1946	0.0005	2816	12	2808	33	2781	4	101
au29b52	159455-018	picked	66	448	0.15	15.1505	0.1637	0.5462	0.0066	0.56	0.1955	0.0006	2825	10	2809	28	2789	5	101
au29b53	159455-016	picked	71	685	0.10	14.9374	0.5432	0.5462	0.0204	0.51	0.1947	0.0006	2811	35	2809	85	2782	5	101
au29b57	159455-004b	picked	49	1977	0.02	13.9279	0.2175	0.5293	0.0079	0.48	0.1873	0.0004	2745	15	2739	33	2719	4	101
au29b58	159455-003	picked	73	474	0.15	15.2087	0.2095	0.5485	0.0081	0.54	0.1946	0.0007	2828	13	2819	34	2781	6	101
au29b59	159455-001a	picked	61	650	0.09	13.5175	0.1706	0.5217	0.0067	0.51	0.1847	0.0008	2717	12	2706	28	2695	7	100
au29b60	159455-001b	picked	116	1190	0.10	14.6544	0.2380	0.5407	0.0091	0.52	0.1925	0.0005	2793	15	2786	38	2764	4	101
ap11A17	159455-97-008	MLA	116	950	0.12	14.1179	0.4062	0.5197	0.0178	0.60	0.1894	0.0009	2758	27	2698	76	2737	8	99
ap11A14	159455-55-006	MLA	123	805	0.15	15.6867	0.3612	0.5567	0.0124	0.48	0.1984	0.0009	2858	22	2853	51	2813	7	101
ap11A15	159455-69-001	MLA	38	411	0.09	15.2772	0.3738	0.5430	0.0159	0.60	0.1980	0.0009	2833	23	2796	66	2810	8	100
ap11A16	159455-69-001b	MLA	62	353	0.18	15.2526	0.3177	0.5422	0.0118	0.52	0.1997	0.0014	2831	20	2793	49	2824	11	99
ap11A20	159455-135-002	MLA	93	744	0.12	15.6203	0.2996	0.5474	0.0118	0.56	0.1991	0.0007	2854	18	2814	49	2819	6	100
ap11A21	159455-154-011	MLA	164	1233	0.13	15.4804	0.3805	0.5492	0.0143	0.53	0.1986	0.0010	2845	23	2822	59	2815	8	100
ap11A26	159455-176-006	MLA	170	1217	0.14	14.2932	0.3211	0.5286	0.0127	0.53	0.1901	0.0008	2769	21	2736	54	2743	7	100
jl31a06	159455-007	MLA	127	1121	0.11	13.6371	0.1729	0.5261	0.0072	0.54	0.1839	0.0008	2725	12	2725	30	2689	7	101
jl31a08	159455-013	MLA	121	1043	0.12	13.3427	0.1773	0.5202	0.0068	0.49	0.1831	0.0006	2704	13	2700	29	2681	5	101
jl31a12	159455-020	MLA	152	1175	0.13	14.6382	0.1809	0.5407	0.0070	0.53	0.1900	0.0006	2792	12	2786	29	2742	5	102
jl31a13	159455-015	MLA	75	750	0.10	13.9125	0.1413	0.5286	0.0058	0.54	0.1827	0.0005	2744	10	2736	25	2677	5	102
jl31a16	159455-009	MLA	157	1531	0.10	13.5481	0.3875	0.5240	0.0166	0.56	0.1814	0.0006	2719	27	2716	70	2666	5	102
jl31a17	159455-008	MLA	99	609	0.16	14.8106	0.3063	0.5448	0.0123	0.55	0.1912	0.0006	2803	20	2804	51	2752	6	102
jl31a24	159455-002	MLA	347	1828	0.19	13.0998	0.1590	0.5109	0.0064	0.52	0.1809	0.0005	2687	11	2661	27	2661	5	100

Notes:

[1] 'File name' is the lab ID of the raw data file for each individual analysis.

[2] 'Mount' identifies whether the zircon grain was hand picked or located within an epoxy grain mount by MLA/SEM software after being processed by traditional mineral separation techniques.

[3] interpolated using the within run average count rates of 91500 zircon and the Th and U concentrations (Wiedenbeck et al., 1995)

[4] Measured isotopic ratios determined using the LAMDATE data reduction program for LA-ICPMS (Kosler et al. 2008)

[5] 'Rho' is the correlation coefficient between the two U/Pb isotope ratios, calculated as the ratio of the covariance to the product of the standard deviations for each ratio.

[6] 'U-Pb/Pb-Pb concordancy (%) is a measure of U-Pb discordancy

Table 4- 2. LA-ICPMS U-Pb isotopic analyses of zircons from the Nunataarsuk Anorthosite Complex

						Measured Isotopic Ratios[4]							Calculated Ages						
file name[1]	sample	mount[2]	^{232}Th ppm[3]	^{238}U ppm[3]	Th/U Ratio	^{207}Pb/^{235}U	1s error	^{206}Pb/^{238}U	1s error	Rho[5]	^{207}Pb/^{206}Pb	1s error	^{207}Pb/^{235}U Ma	1s error Ma	^{206}Pb/^{238}U Ma	1s error Ma	^{207}Pb/^{206}Pb Ma	1s error Ma	U-Pb/Pb-Pb concordancy (%)[6]
Nunataarsuk leucogabbro N03-09																			
ap11A86	N03-09-17-001	MLA	28	48	0.58	14.7816	0.4702	0.5429	0.0149	0.43	0.1974	0.0018	2801	30	2795	62	2805	15	100
ap11A87	N03-09-22-002	MLA	145	273	0.53	15.1783	0.4231	0.5438	0.0139	0.46	0.2021	0.0009	2826	27	2799	58	2843	8	98
ap11A88	N03-09-26-001	MLA	40	72	0.55	15.8762	0.4129	0.5590	0.0141	0.49	0.2023	0.0016	2869	25	2862	58	2845	13	101
ap11A93	N03-09-27-001	MLA	513	381	1.35	15.3646	0.2648	0.5491	0.0096	0.51	0.2026	0.0010	2838	16	2821	40	2847	8	99
ap11A94	N03-09-29-001	MLA	29	46	0.63	15.6981	0.3595	0.5475	0.0110	0.44	0.2065	0.0016	2859	22	2815	46	2878	13	98
ap11A95	N03-09-60-001	MLA	137	302	0.46	16.4336	0.2887	0.5631	0.0105	0.53	0.2066	0.0010	2902	17	2879	43	2879	8	100
ap11A96	N03-09-64-001	MLA	39	78	0.50	15.4213	0.3380	0.5465	0.0120	0.50	0.2024	0.0013	2842	21	2811	50	2845	10	99
ap11A97	N03-09-65-001a	MLA	61	100	0.61	16.0359	0.3324	0.5573	0.0101	0.44	0.2047	0.0014	2879	20	2856	42	2864	11	100
ap11A98	N03-09-65-001b	MLA	164	199	0.82	16.6324	0.2447	0.5584	0.0097	0.59	0.2094	0.0011	2914	14	2860	40	2901	8	99
ap11A99	N03-09-91-001	MLA	113	162	0.70	15.1508	0.2697	0.5461	0.0106	0.55	0.1991	0.0009	2825	17	2809	44	2819	7	100
fe29A06	N03-09-20	MLA	50	103	0.48	14.7075	0.3277	0.5319	0.0135	0.57	0.1949	0.0013	2797	21	2749	57	2784	11	99
fe29A09	N03-09-09	MLA	105	183	0.57	14.9307	0.2869	0.5433	0.0108	0.52	0.1927	0.0012	2811	18	2797	45	2765	10	101
fe29A10	N03-09-16	MLA	110	169	0.65	13.7323	0.3078	0.5143	0.0119	0.52	0.1898	0.0010	2731	21	2675	51	2740	9	98
fe29A14	N03-09-13	MLA	166	363	0.46	15.7729	0.3125	0.5591	0.0141	0.64	0.1996	0.0010	2863	19	2863	58	2823	8	101
fe29A16	N03-09-06	MLA	145	190	0.76	14.8547	0.3324	0.5406	0.0122	0.51	0.1990	0.0011	2806	21	2786	51	2818	9	99
fe29A18	N03-09-12	MLA	160	387	0.41	15.9874	0.3979	0.5539	0.0139	0.50	0.2065	0.0010	2876	24	2841	58	2879	8	99
fe29A20	N03-09-24	MLA	19	36	0.54	14.9450	0.3492	0.5465	0.0129	0.50	0.1967	0.0012	2812	22	2811	54	2799	10	100
fe29A24	N03-09-25	MLA	7	24	0.29	13.5868	0.3760	0.5226	0.0135	0.47	0.1830	0.0018	2721	26	2710	57	2681	16	101
fe29A25	N03-09-31	MLA	27	77	0.35	14.4423	0.3943	0.5387	0.0151	0.51	0.1913	0.0013	2779	26	2778	63	2753	11	101
fe29A26	N03-09-03	MLA	76	113	0.67	15.5969	0.3229	0.5545	0.0120	0.52	0.2004	0.0012	2852	20	2844	50	2829	10	101
fe29A27	N03-09-04	MLA	7	25	0.29	12.8962	0.3500	0.5096	0.0149	0.54	0.1787	0.0013	2672	26	2655	64	2641	12	101
fe29A30	N03-09-14	MLA	29	60	0.49	13.3623	0.3056	0.5120	0.0107	0.46	0.1863	0.0013	2706	22	2665	46	2710	11	98
fe29A31	N03-09-33	MLA	230	285	0.81	15.7103	0.2685	0.5516	0.0102	0.54	0.2015	0.0010	2859	16	2832	42	2838	8	100
fe29A35	N03-09-28	MLA	91	291	0.31	14.6268	0.2088	0.5379	0.0098	0.64	0.1914	0.0009	2791	14	2775	41	2754	7	101
fe29A36	N03-09-21	MLA	38	95	0.40	16.1319	0.2534	0.5642	0.0093	0.52	0.2044	0.0009	2885	15	2884	38	2862	7	101
fe29A37	N03-09-17	MLA	95	135	0.70	13.6275	0.1946	0.5237	0.0076	0.51	0.1864	0.0009	2724	14	2715	32	2711	8	100
fe29A38	N03-09-32	MLA	37	72	0.51	14.4851	0.4528	0.5378	0.0162	0.48	0.1933	0.0011	2782	30	2774	68	2771	10	100
Nunataarsuk leucogabbro N03-81A																			
jl31a29	N03-81A-001	picked	298	760	0.39	15.3578	0.1617	0.5517	0.0068	0.58	0.1952	0.0007	2838	10	2832	28	2786	6	102
jl31a30	N03-81A-002	picked	72	463	0.16	12.2796	0.1482	0.4982	0.0063	0.53	0.1740	0.0006	2626	11	2606	27	2597	5	100
jl31a31	N03-81A-003	picked	52	336	0.16	12.5863	0.1525	0.5049	0.0070	0.57	0.1745	0.0006	2649	11	2635	30	2601	6	101
jl31a33	N03-81A-006	picked	47	373	0.13	12.4056	0.1908	0.5050	0.0079	0.51	0.1744	0.0006	2636	14	2635	34	2601	6	101
jl31a34	N03-81A-008	picked	95	185	0.51	14.4081	0.1640	0.5357	0.0069	0.57	0.1881	0.0008	2777	11	2765	29	2726	7	101
jl31a37	N03-81A-009	picked	69	983	0.07	11.4356	0.1694	0.4847	0.0068	0.48	0.1696	0.0007	2559	14	2548	30	2553	7	100
jl31a39	N03-81A-010	picked	895	1133	0.79	15.4096	0.1822	0.5517	0.0066	0.50	0.1963	0.0006	2841	11	2832	27	2795	5	101
jl31a40	N03-81A-011	picked	172	224	0.77	15.8631	0.2265	0.5522	0.0075	0.48	0.2015	0.0009	2869	14	2834	31	2838	7	100
jl31a41	N03-81A-012	picked	140	1830	0.08	11.9296	0.1857	0.4928	0.0080	0.52	0.1708	0.0005	2599	15	2583	34	2566	5	101
jl31a42	N03-81A-013	picked	57	350	0.16	12.2792	0.1401	0.4993	0.0057	0.50	0.1738	0.0006	2626	11	2611	24	2595	6	101
jl31a47	N03-81A-014	picked	41	89	0.46	13.0161	0.1691	0.5152	0.0059	0.44	0.1774	0.0009	2681	12	2679	25	2629	9	102
Nunataarsuk leucogabbro N03-83																			

ap12A06	N03-83-24-003	MLA	12	23	0.51	14.8028	0.5286	0.5366	0.0170	0.44	0.2007	0.0021	2803	34	2769	71	2832	17	98
ap12A07	N03-83-32-001	MLA	16	91	0.17	14.0981	0.4712	0.5333	0.0175	0.49	0.1913	0.0017	2756	32	2755	74	2754	15	100
ap12A08	N03-83-65-004	MLA	26	49	0.54	13.7349	0.3952	0.5274	0.0132	0.43	0.1949	0.0018	2732	27	2730	56	2784	15	98
ap12A09	N03-83-106-002	MLA	13	23	0.55	14.8732	0.4627	0.5438	0.0139	0.41	0.1995	0.0021	2807	30	2799	58	2822	17	99
ap12A10	N03-83-106-002b	MLA	14	25	0.56	14.4407	0.4297	0.5354	0.0181	0.57	0.1949	0.0021	2779	28	2764	76	2784	18	99
ap12A11	N03-83-42-002	MLA	55	163	0.34	14.6419	0.3685	0.5334	0.0110	0.41	0.1998	0.0015	2792	24	2756	46	2824	12	98
au23A11	N03-83-12a	picked	12	28	0.42	16.1758	0.2585	0.5625	0.0089	0.49	0.2127	0.0012	2887	15	2877	37	2926	9	98
au23A12	N03-83-12b	picked	14	34	0.42	16.2588	0.2192	0.5655	0.0074	0.49	0.2114	0.0023	2892	13	2889	31	2916	18	99
au23A13	N03-83-09a	picked	12	26	0.45	16.1265	0.2235	0.5544	0.0076	0.50	0.2074	0.0012	2884	13	2843	32	2886	10	99
au23A19	N03-83-02a	picked	25	51	0.49	14.4693	0.2153	0.5390	0.0079	0.49	0.1954	0.0010	2781	14	2779	33	2788	8	100
au23A20	N03-83-01a	picked	50	129	0.39	13.8041	0.1464	0.5243	0.0064	0.58	0.1886	0.0007	2736	10	2717	27	2730	7	100
au23A26	N03-83-04c	picked	16	40	0.41	15.8987	0.2538	0.5571	0.0087	0.49	0.2106	0.0011	2871	15	2855	36	2911	8	98
au23A27	N03-83-04d	picked	23	59	0.38	16.2596	0.1892	0.5646	0.0075	0.57	0.2111	0.0012	2892	11	2886	31	2914	9	99
au23A28	N03-83-13a	picked	20	37	0.55	14.6609	0.1898	0.5400	0.0065	0.46	0.2001	0.0009	2793	12	2783	27	2827	8	98
au23A29	N03-83-13b	picked	56	255	0.22	14.6694	0.1908	0.5405	0.0064	0.45	0.2012	0.0007	2794	12	2786	27	2836	6	98
au23A31	N03-83-16	picked	13	28	0.47	15.7262	0.2373	0.5547	0.0080	0.48	0.2105	0.0011	2860	14	2845	33	2909	8	98
au23A35	N03-83-19a	picked	44	71	0.62	15.8333	0.1885	0.5574	0.0069	0.52	0.2068	0.0009	2867	11	2856	29	2881	7	99
au23A36	N03-83-19b	picked	38	60	0.63	16.2952	0.1974	0.5660	0.0077	0.56	0.2106	0.0013	2894	12	2891	32	2911	10	99

Notes:

[1] 'File name' is the lab ID of the raw data file for each individual analysis

[2] 'Mount' identifies whether the zircon grain was hand picked or located within an epoxy grain mount by MLA/SEM software after being processed by traditional mineral separation techniques

[3] interpolated using the within run average count rates of 91500 zircon and the Th and U concentrations (Wiedenbeck et al., 1995)

[4] Measured isotopic ratios determined using the LAMDATE data reduction program for LA-ICPMS (Kosler et al. 2008).

[5] 'Rho' is the correlation coefficient between the two U/Pb isotope ratios, calculated as the ratio of the covariance to the product of the standard deviations for each ratio.

[6] 'U-Pb/Pb-Pb concordancy (%) is a measure of U-Pb discordancy

Table 4-3. LA-MC-ICPMS Lu-Hf isotopic analyses of zircons from the Fiskenaesset Anorthosite Complex

file name[1]	sample	mount[2]	age[3]	178Hf (V)	$^{176}Lu/^{177}Hf$	2SE	$^{176}Yb/^{177}Hf$	2SE	$^{178}Hf/^{177}Hf$	2SE	$^{176}Hf/^{177}Hf$	2SE	$^{176}Hf/^{177}Hf$ (2936 Ma)[4]	ε_{Hf} (2936 Ma)[5]	±2SE
Fiskenaesset leucogabbro 159394 (Upper leucogabbro unit, section A)															
11oc04e17	159394-053	picked	2790	2.53	0.000207	0.000007	0.004191	0.000169	1.467245	0.000039	0.280985	0.000025	0.280974	3.0	0.9
11oc04e18	159394-051	picked	2779	2.74	0.000129	0.000008	0.002639	0.000184	1.467245	0.000044	0.280973	0.000024	0.280966	2.8	0.9
11oc04e19	159394-049	picked	2779	2.73	0.000191	0.000003	0.004242	0.000099	1.467249	0.000045	0.280966	0.000033	0.280955	2.4	1.2
11oc04e20	159394-044	picked	2725	5.55	0.000171	0.000009	0.003168	0.000166	1.467203	0.000059	0.280933	0.000021	0.280924	1.2	0.7
11oc04e21	159394-043	picked	2767	4.22	0.000243	0.000010	0.004960	0.000220	1.467255	0.000058	0.281015	0.000027	0.281002	4.0	1.0
11oc04e22	159394-043	picked	2767	3.13	0.000186	0.000007	0.003702	0.000129	1.467276	0.000060	0.280973	0.000032	0.280962	2.6	1.1
11oc04e23	159394-042b	picked	2759	3.61	0.000248	0.000002	0.005133	0.000070	1.467245	0.000044	0.280993	0.000026	0.280979	3.2	0.9
11oc04e24	159394-041a	picked	2780	4.57	0.000143	0.000002	0.002810	0.000053	1.467301	0.000042	0.281036	0.000026	0.281028	5.0	0.9
11oc04e25	159394-039b	picked	2763	3.16	0.000226	0.000007	0.004387	0.000147	1.467243	0.000040	0.280968	0.000021	0.280955	2.4	0.7
11oc04e26	159394-032	picked	2784	3.25	0.000182	0.000003	0.003611	0.000047	1.467253	0.000040	0.280991	0.000027	0.280981	3.3	0.9
11oc04e36	159394-f03a	picked	2949	3.84	0.001743	0.000016	0.041065	0.000375	1.467262	0.000051	0.281085	0.000034	0.280987	3.5	1.2
11oc04e37	159394-f03b	picked	2930	3.79	0.001456	0.000018	0.035376	0.000332	1.467250	0.000039	0.281090	0.000035	0.281008	4.2	1.3
11oc04e35	159394-f01	picked	2922	2.96	0.001873	0.000010	0.061098	0.000300	1.467105	0.000057	0.281058	0.000037	0.280952	2.3	1.3
Fiskenaesset leucogabbro 159437 (Lower leucogabbro unit, section A)															
11oc04e08	159437-081a	picked	2803	3.46	0.000100	0.000002	0.001974	0.000042	1.467224	0.000042	0.280941	0.000023	0.280935	1.6	0.8
11oc04e07	159437-078	picked	2777	4.44	0.000188	0.000001	0.003734	0.000025	1.467234	0.000035	0.280959	0.000019	0.280949	2.1	0.7
11oc04e06	159437-077	picked	2783	3.49	0.000148	0.000004	0.003255	0.000073	1.467185	0.000040	0.280915	0.000024	0.280907	0.6	0.8
11oc04e05	159437-076	picked	2779	4.20	0.000231	0.000001	0.004898	0.000035	1.467224	0.000034	0.280963	0.000023	0.280950	2.2	0.8
11oc04e04	159437-074	picked	2808	2.98	0.000141	0.000002	0.002805	0.000057	1.467214	0.000040	0.280935	0.000025	0.280927	1.4	0.9
11oc04e13	159437-068	picked	2812	3.12	0.000104	0.000003	0.002108	0.000057	1.467250	0.000039	0.280937	0.000024	0.280931	1.5	0.9
11oc04e11	159437-066	picked	2807	3.27	0.000241	0.000014	0.005022	0.000352	1.467184	0.000043	0.280945	0.000028	0.280932	1.5	1.0
11oc04e09	159437-062	picked	2774	4.24	0.000124	0.000007	0.002553	0.000151	1.467206	0.000038	0.280945	0.000022	0.280938	1.7	0.8
11oc04e10	159437-059	picked	2793	3.48	0.000212	0.000003	0.004331	0.000078	1.467226	0.000042	0.280928	0.000027	0.280916	1.0	1.0
11oc04e12	159437-056	picked	2788	3.79	0.000315	0.000004	0.006328	0.000180	1.467255	0.000051	0.280997	0.000021	0.280980	3.2	0.7
Fiskenaesset anorthosite 159455 (Anorthosite unit, section A)															
11oc04e36	159455-019	picked	2781	3.56	0.000394	0.000028	0.008229	0.000555	1.467217	0.000033	0.280958	0.000027	0.280936	1.7	1.0
11oc04e35	159455-018	picked	2789	3.09	0.000375	0.000002	0.007982	0.000045	1.467169	0.000047	0.280954	0.000037	0.280933	1.6	1.3
11oc04e34	159455-016	picked	2782	3.80	0.000081	0.000001	0.001618	0.000024	1.467206	0.000036	0.281006	0.000025	0.281001	4.0	0.9
11oc04e30	159455-004b	picked	2719	3.29	0.000185	0.000003	0.003789	0.000081	1.467208	0.000044	0.280985	0.000025	0.280975	3.1	0.9
11oc04e31	159455-003	picked	2781	3.16	0.000390	0.000003	0.008025	0.000072	1.467225	0.000046	0.280988	0.000021	0.280966	2.7	0.8
11oc04e32	159455-001a	picked	2695	3.78	0.000548	0.000025	0.011513	0.000586	1.467231	0.000049	0.281009	0.000025	0.280978	3.2	0.9
11oc04e33	159455-001b	picked	2764	3.58	0.000604	0.000002	0.012361	0.000034	1.467239	0.000044	0.281002	0.000033	0.280968	2.8	1.2

Notes:

[1] 'File name' is the lab ID of the raw data file for each individual analysis

[2] 'Mount' identifies whether the zircon grain was hand picked or located within an epoxy grain mount by MLA/SEM software after being processed by traditional mineral separation techniques

[3] 207Pb/206Pb age in millions of years (this study).

[4] The 176Hf/177Hf (t) values are calculated using a Lu decay constant of 1.867 x 10-11 (Soderlund et al. 2004)

[5] Epsilon Hf values are calculated with 176Hf/177Hf and 176Lu/177Hf (CHUR) values of 0.282785 and 0.0336, respectively (Bouvier et al. (2008)).

Table 4-4. LA-MC-ICPMS Lu-Hf isotopic analyses of zircons from the Nunataarsuk Anorthosite Complex

file name[1]	sample	mount[2]	age[3]	178Hf (V)	$^{176}Lu/^{177}Hf$	2SE	$^{176}Yb/^{177}Hf$	2SE	$^{178}Hf/^{177}Hf$	2SE	$^{176}Hf/^{177}Hf$	2SE	$^{176}Hf/^{177}Hf$ (2936 Ma)[4]	ε_{Hf} (2936 Ma)[5]	±2SE
Nunataarsuk leucogabbro N03-09															
11oc04b14	N03-09-22-002	MLA	2843	3.06	0.001267	0.000238	0.031769	0.006333	1.467291	0.000050	0.281067	0.000033	0.280996	3.2	1.2
11oc04b19	N03-09-26-001	MLA	2845	2.63	0.002056	0.000055	0.046360	0.001440	1.467243	0.000071	0.281148	0.000040	0.281033	4.5	1.4
11oc04b11	N03-09-29-001	MLA	2878	3.44	0.000903	0.000045	0.022522	0.001138	1.467193	0.000047	0.281002	0.000027	0.280952	1.6	0.9
11oc04b08	N03-09-60-001	MLA	2879	3.40	0.000637	0.000014	0.013863	0.000336	1.467160	0.000061	0.281014	0.000041	0.280978	2.6	1.5
11oc04b22	N03-09-64-001	MLA	2845	2.19	0.001390	0.000054	0.032572	0.001214	1.467208	0.000049	0.281061	0.000037	0.280983	2.7	1.3
11oc04b23	N03-09-64-001	MLA	2845	2.53	0.001632	0.000023	0.038638	0.000523	1.467279	0.000046	0.281081	0.000030	0.280990	3.0	1.1
11oc04b25	N03-09-65-001a	MLA	2864	3.58	0.000771	0.000020	0.019172	0.000576	1.467250	0.000037	0.281019	0.000019	0.280976	2.5	0.7
11oc04b26	N03-09-65-001b	MLA	2901	2.85	0.002075	0.000031	0.053256	0.000904	1.467223	0.000058	0.281018	0.000028	0.280902	-0.1	1.0
11oc04b24	N03-09-20	MLA	2784	2.39	0.000794	0.000043	0.020192	0.001124	1.467245	0.000061	0.281081	0.000035	0.281036	4.6	1.3
11oc04b21	N03-09-09	MLA	2765	2.42	0.002991	0.000046	0.069476	0.000876	1.467267	0.000070	0.281153	0.000050	0.280985	2.8	1.8
11oc04b20	N03-09-16	MLA	2740	3.26	0.001866	0.000018	0.045670	0.000516	1.467245	0.000045	0.281070	0.000032	0.280966	2.1	1.1
11oc04b18	N03-09-13	MLA	2823	3.54	0.000809	0.000044	0.018409	0.001106	1.467236	0.000046	0.281032	0.000035	0.280986	2.8	1.2
11oc04b15	N03-09-06	MLA	2818	3.64	0.000726	0.000059	0.018174	0.001613	1.467284	0.000053	0.281063	0.000040	0.281022	4.1	1.4
11oc04b13	N03-09-12	MLA	2879	3.96	0.000467	0.000016	0.009887	0.000385	1.467228	0.000043	0.281023	0.000027	0.280997	3.2	1.0
11oc04b12	N03-09-24	MLA	2799	2.18	0.001393	0.000037	0.034013	0.000767	1.467259	0.000042	0.281028	0.000034	0.280950	1.6	1.2
11oc04b27	N03-09-03	MLA	2829	3.52	0.000773	0.000028	0.019667	0.000688	1.467259	0.000048	0.281016	0.000022	0.280973	2.4	0.8
11oc04b10	N03-09-04	MLA	2641	3.72	0.000061	0.000001	0.001093	0.000024	1.467228	0.000051	0.280998	0.000039	0.280995	3.1	1.4
11oc04b09	N03-09-21	MLA	2862	3.38	0.000283	0.000002	0.007123	0.000090	1.467266	0.000056	0.280968	0.000035	0.280952	1.6	1.3
Nunataarsuk leucogabbro N03-81A															
11oc04d14	N03-81A-001	picked	2786	4.77	0.001226	0.000048	0.025433	0.001178	1.467234	0.000038	0.281018	0.000019	0.280949	1.5	0.7
11oc04d15	N03-81A-001	picked	2786	4.24	0.001094	0.000035	0.022071	0.000665	1.467208	0.000033	0.281020	0.000027	0.280959	1.9	1.0
11oc04d06	N03-81A-002	picked	2597	2.94	0.000407	0.000003	0.007726	0.000062	1.467175	0.000046	0.281117	0.000021	0.281097	-0.5	0.8
11oc04d07	N03-81A-003	picked	2601	2.89	0.000266	0.000015	0.005233	0.000311	1.467261	0.000052	0.281158	0.000027	0.281145	1.2	1.0
11oc04d08	N03-81A-006	picked	2601	2.79	0.000205	0.000017	0.003871	0.000320	1.467244	0.000049	0.281099	0.000029	0.281089	-0.8	1.0
11oc04d09	N03-81A-008	picked	2726	2.89	0.000943	0.000004	0.022155	0.000115	1.467217	0.000061	0.281003	0.000040	0.280950	1.6	1.4
11oc04d11	N03-81A-012	picked	2566	2.97	0.000536	0.000039	0.009740	0.000655	1.467240	0.000054	0.281134	0.000024	0.281107	-0.1	0.9
11oc04d12	N03-81A-013	picked	2595	3.18	0.000386	0.000014	0.008220	0.000342	1.467250	0.000038	0.281114	0.000025	0.281095	-0.6	0.9
11oc04d13	N03-81A-014	picked	2629	3.30	0.000061	0.000001	0.001177	0.000025	1.467240	0.000036	0.281002	0.000021	0.280999	3.3	0.8
Nunataarsuk leucogabbro N03-83															
11oc04c15	N03-83-n012a	picked	2926	2.43	0.001022	0.000001	0.024054	0.000031	1.467258	0.000046	0.281071	0.000031	0.281014	3.8	1.1
11oc04c16	N03-83-n012b	picked	2916	2.46	0.000976	0.000002	0.023368	0.000060	1.467197	0.000066	0.280977	0.000029	0.280923	0.6	1.0
11oc04c31	N03-83-n009a	picked	2886	2.56	0.000781	0.000051	0.018229	0.001283	1.467189	0.000090	0.281035	0.000030	0.280991	3.0	1.1
11oc04c12	N03-83-n002a	picked	2788	2.79	0.001678	0.000012	0.041305	0.000307	1.467204	0.000050	0.281052	0.000030	0.280959	1.9	1.1
11oc04c14	N03-83-n001a	picked	2730	3.17	0.000980	0.000095	0.020008	0.002278	1.467220	0.000033	0.281063	0.000022	0.281009	3.6	0.8
11oc04c10	N03-83-n004c	picked	2911	4.00	0.001047	0.000005	0.024431	0.000127	1.467215	0.000038	0.281031	0.000021	0.280972	2.3	0.8
11oc04c11	N03-83-n004d	picked	2914	4.03	0.001051	0.000001	0.024759	0.000030	1.467213	0.000038	0.281019	0.000024	0.280960	1.9	0.9
11oc04c29	N03-83-n013a	picked	2827	4.08	0.000778	0.000056	0.018012	0.001447	1.467237	0.000039	0.281018	0.000021	0.280975	2.4	0.8
11oc04c30	N03-83-n013b	picked	2836	3.28	0.000552	0.000023	0.013039	0.000568	1.467260	0.000059	0.281001	0.000027	0.280970	2.3	1.0
11oc04c34	N03-83-n016	picked	2909	4.67	0.000650	0.000018	0.014995	0.000439	1.467251	0.000051	0.281078	0.000028	0.281042	4.8	1.0
11oc04c32	N03-83-n019a	picked	2881	4.32	0.002562	0.000055	0.062273	0.001438	1.467259	0.000062	0.281100	0.000027	0.280956	1.8	1.0
11oc04c33	N03-83-n019b	picked	2911	3.80	0.001691	0.000148	0.038474	0.003567	1.467200	0.000047	0.281054	0.000024	0.280959	1.9	0.9

Notes:

[1] 'File name' is the lab ID of the raw data file for each individual analysis

[2] 'Mount' identifies whether the zircon grain was hand picked or located within an epoxy grain mount by MLA/SEM software after being processed by traditional mineral separation techniques

[3] 207Pb/206Pb age in millions of years (this study).

[4] The 176Hf/177Hf (t) values are calculated using a Lu decay constant of 1.867 x 10-11 (Soderlund et al. 2004)

[5] Epsilon Hf values are calculated with 176Hf/177Hf and 176Lu/177Hf (CHUR) values of 0.282785 and 0.0336, respectively (Bouvier et al. (2008)).

Table 4-5. Summary of An-contents, Pb concentration and LA-MC-ICPMS Pb isotope compositions for the Fiskenæsset anorthosite complex and Nunataarsuk anorthosite complex

	AVG An-contents[2]	AVG Pb (ppm)[3]	$^{206}Pb/^{204}Pb$	1SD	$^{207}Pb/^{204}Pb$	1SD	$^{208}Pb/^{204}Pb$	1SD	$^{207}Pb/^{206}Pb$	1SD	$^{208}Pb/^{206}Pb$	1SD	no. analyses
Fiskenæsset Anorthosite Complex[1]													
Fiskenæsset AVG	86.1	5.2	13.121	0.134	14.368	0.116	32.767	0.268	1.095	0.006	2.500	0.020	209
% RSD (1s)	2.4%	53.2%	1.0%		0.81%		0.82%		0.54%		0.82%		
Lower Leucogabbro	86.7	6.2	13.075	0.093	14.363	0.095	32.827	0.287	1.098	0.004	2.512	0.013	38
% RSD (1s)	1.4%	48.8%	0.71%		0.66%		0.87%		0.36%		0.51%		
159430a	86.7	9.0	13.144	0.058	14.393	0.070	32.875	0.174	1.094	0.003	2.502	0.009	11
159430b	86.1	8.4	13.098	0.046	14.403	0.039	33.085	0.129	1.099	0.002	2.527	0.006	12
159437	87.0	2.8	13.006	0.097	14.309	0.118	32.584	0.246	1.101	0.003	2.508	0.006	15
Middle Gabbro	89.3	2.8	13.236	0.156	14.410	0.141	32.607	0.299	1.084	0.007	2.458	0.015	12
% RSD (1s)	0.90%	33.9%	1.17%		0.98%		0.92%		0.62%		0.60%		
159444	88.1	1.4	13.073	0.020	14.226	0.089	32.334	0.186	1.088	0.006	2.475	0.006	3
159448	89.8	3.5	13.291	0.058	14.442	0.110	32.622	0.257	1.085	0.004	2.457	0.011	9
Upper Leucobaggro	86.1	4.6	13.166	0.131	14.377	0.133	32.753	0.284	1.092	0.005	2.491	0.017	99
% RSD (1s)	3.2%	60.3%	0.99%		0.92%		0.87%		0.46%		0.67%		
124613	86.1	1.8	13.143	0.063	14.328	0.061	32.589	0.130	1.092	0.006	2.485	0.013	13
124665	88.1	0.9	13.198	0.152	14.375	0.183	32.722	0.396	1.089	0.004	2.481	0.007	12
125765	85.3	3.4	13.179	0.088	14.399	0.085	32.817	0.153	1.092	0.003	2.492	0.006	8
125767	87.2	4.4	13.092	0.096	14.338	0.119	32.814	0.236	1.095	0.002	2.508	0.007	22
125469	86.5	6.2	13.075	0.099	14.330	0.114	32.629	0.243	1.098	0.002	2.501	0.003	14
159394	83.2	8.8	13.238	0.082	14.460	0.097	32.955	0.222	1.091	0.003	2.491	0.008	20
159452	85.0	3.2	13.333	0.096	14.458	0.112	32.684	0.229	1.084	0.003	2.456	0.008	10
Anorthosite	84.7	6.1	13.039	0.112	14.340	0.105	32.781	0.241	1.099	0.003	2.515	0.007	60
% RSD (1s)	2.6%	35.9%	0.86%		0.73%		0.74%		0.25%		0.26%		
124652	84.6	3.6	12.933	0.047	14.247	0.055	32.642	0.183	1.100	0.002	2.522	0.005	15
125760	84.3	8.0	13.048	0.167	14.355	0.134	32.749	0.337	1.098	0.005	2.508	0.007	9
125763	86.1	4.6	13.062	0.095	14.344	0.100	32.800	0.229	1.100	0.002	2.516	0.005	18
159455	83.6	8.4	13.105	0.068	14.410	0.066	32.909	0.179	1.099	0.002	2.513	0.002	18
Nunataarsuk Anorthosite Complex[1]													
Nunataarsuk AVG	81.4	3.5	12.663	0.167	13.968	0.131	32.378	0.301	1.102	0.009	2.556	0.022	61
% RSD (1s)	5.9%	62.9%	1.3%		0.9%		0.9%		0.8%		0.9%		
Lower Leucogabbro-Anorthosite	80.2	3.2	12.681	0.164	13.979	0.128	32.464	0.238	1.101	0.010	2.558	0.023	35
% RSD (1s)	6.9%	24.0%	1.3%		0.9%		0.7%		0.9%		0.9%		
N03-06	77.7	4.0	12.847	0.065	14.083	0.075	32.629	0.157	1.097	0.004	2.543	0.009	12
N03-10	76.6	2.5	12.699	0.090	13.935	0.125	32.389	0.281	1.095	0.005	2.547	0.009	13
N03-83c	88.0	2.7	12.471	0.059	13.902	0.101	32.348	0.143	1.115	0.006	2.592	0.010	10
Upper Leucogabbro-Anorthosite	82.5	3.8	12.716	0.265	14.003	0.197	32.356	0.449	1.100	0.010	2.545	0.025	26
% RSD (1s)	4.6%	79.0%	2.1%		1.4%		1.4%		0.9%		1.0%		
N03-09	82.8	1.4	12.463	0.145	13.854	0.174	32.012	0.379	1.110	0.004	2.568	0.008	12
N03-72	79.3	6.7	12.779	0.050	14.052	0.048	32.545	0.108	1.100	0.003	2.546	0.005	11
N03-81A	86.0	2.0	12.736	0.047	13.903	0.078	32.013	0.386	1.090	0.005	2.511	0.013	3

[1] Results for each individual analysis provided in Tables EA-3-1 and EA-3-2 in Electronic Annex EA-3

[2] determined by EPMA, method details given in Electronic Annex EA-1

[3] determined by LA-ICPMS, full method details given in Electronic Annex EA-1

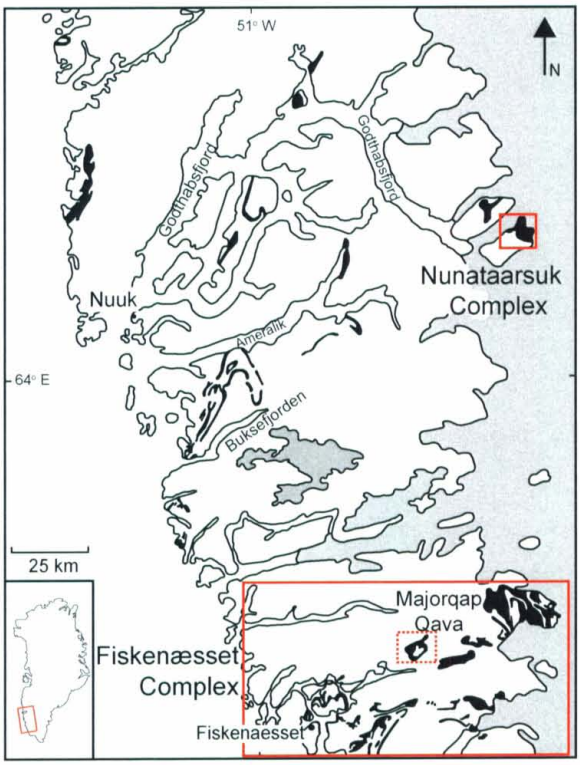

Figure 4.1: General map of south West Greenland with Archean anorthosite complexes in black. Thick boxes surround the Fiskenæsset and Nunataarsuk regions. The Fiskenæsset samples were all from the Majorqap qava area, dashed box (modified from Owens and Dymek, 1997).

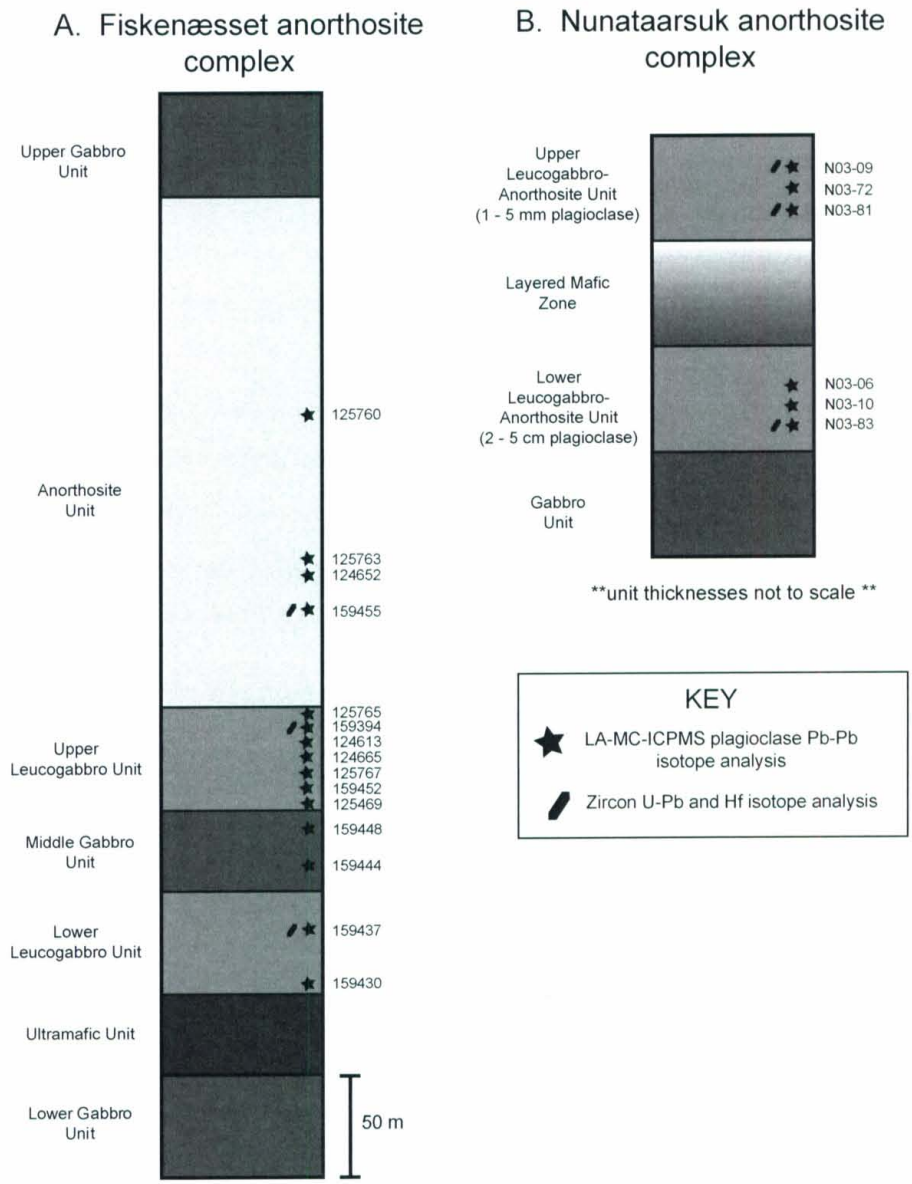

Figure 4-2: Simplified stratigraphy of the Fiskenæsset (after Myers, 1985) and Nunataarsuk anorthosite complexes with relative stratigraphic positions of samples discussed.

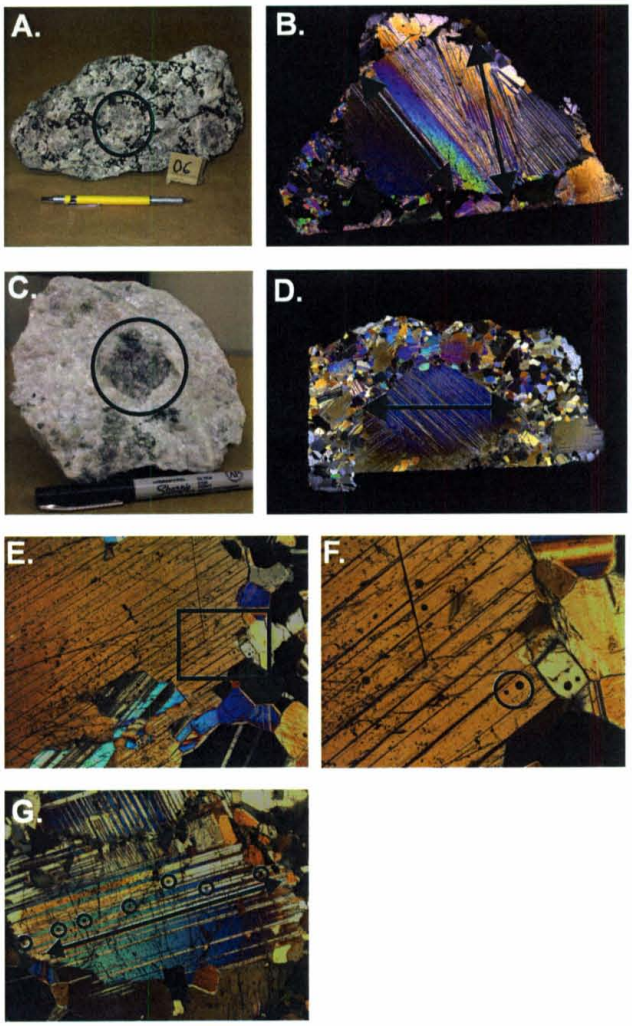

Figure 4-3: Representative leucogabbro (A, B) and anorthosite (C,D) samples. B and D are representative of the areas circled in A and C (images B and D produced using a flat-bed scanner in 'film' mode and two pieces of polarizing film). Arrows in B and D are typical transects across a single plagioclase megacryst used for in-situ analyses. The length of each transect shown is ~ 1 cm. E, F and G are transmitted optical microscope images (cross-polarized light) of plagioclase megacrysts and the surrounding recrystallized matrix dominated by plagioclase. F is an enlargement of the area within the box in E. Within the circled area in F, the larger laser ablation pites are 99 µm (LA-MC-ICPMS Pb isotope analysis) and adjacent smaller laser ablation pits are 49 µm (LA-ICPMS trace element analysis). Trails of tiny amphibole inclusions are visible on the left-hand side of F (center of image). G is representative of a typical transect (shown by the arrow, ~ 0.7 cm) across a plagioclase megacryst. Each laser ablation pit is cirlced (99 µm diameter).

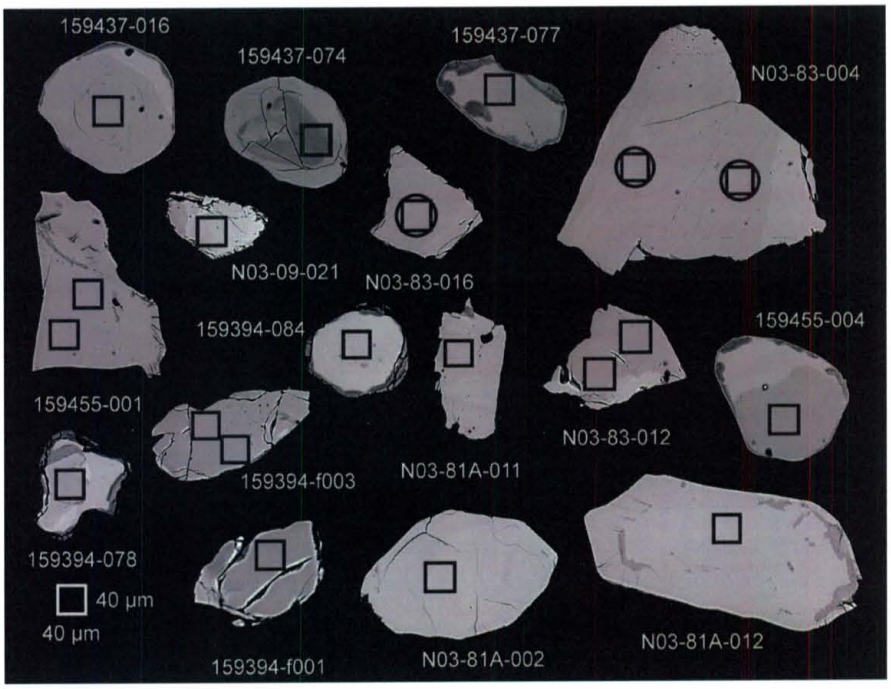

Figure 4-4: Back-scattered electron images of representative zircon crystals from Fiskenæsset (grains labeled 159xxx-xxx) and Nunataarsuk (grains labeled N03-xx-xxx) leucogabbro and anorthosite samples analyzed. Squares mark the U-Pb analysis locations. A Hf isotope analysis was made directly over each of the U-Pb square rasters using a circular laser beam. To illustrate, this is shown schematically for grains N03-83-004 and N03-83-016. The two zircon grains that give the oldest U-Pb ages (2936 +/- 13 Ma) for Fiskenæsset are 159394-f001 and 159394-f003. Three (N03-83-004, N03-012, N03-83-016) of the four oldest grains (2914 +/- 6.9 Ma from Nunataarsuk are also shown.

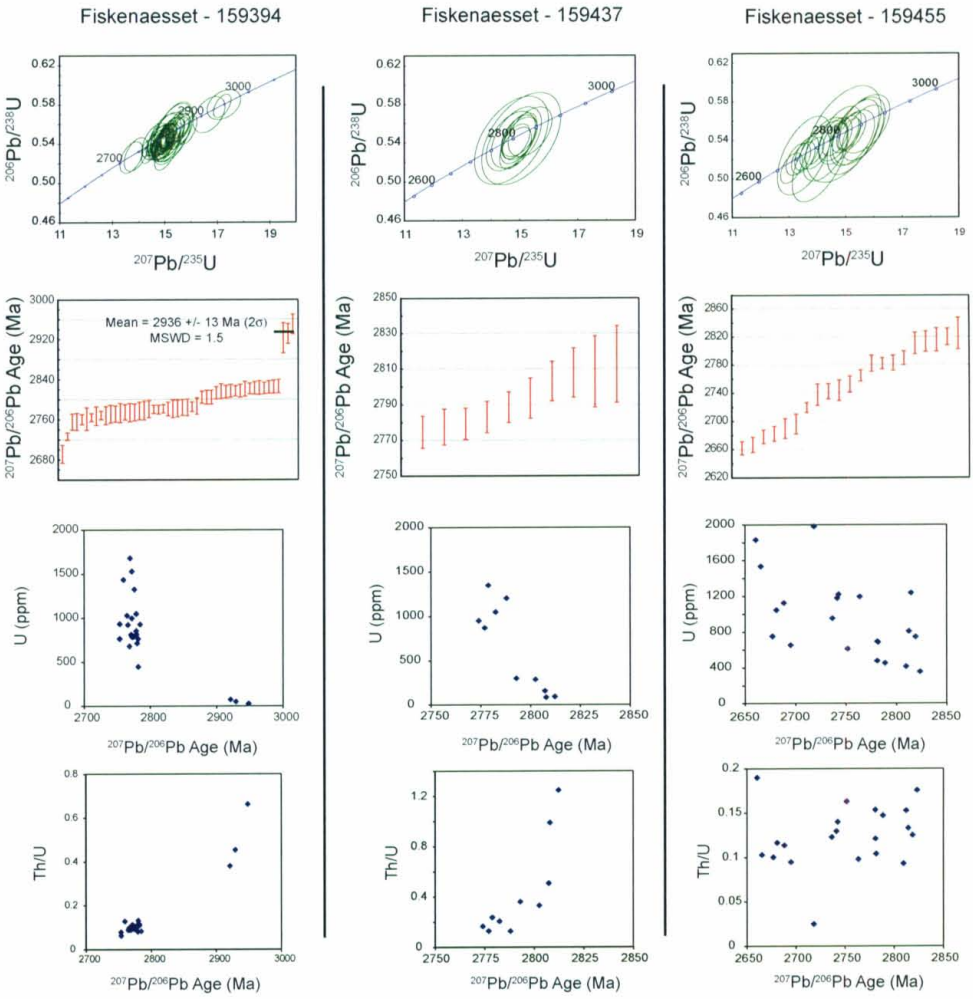

Figure 4-5: Results of in-situ LA-ICPMS U-Pb zircon analysis from Fiskenæsset anorthosite complex. Error ellipses on the concordia diagrams are 1-sigma. Error bars on the $^{207}Pb/^{206}Pb$ weighted mean plots are 2-sigma.

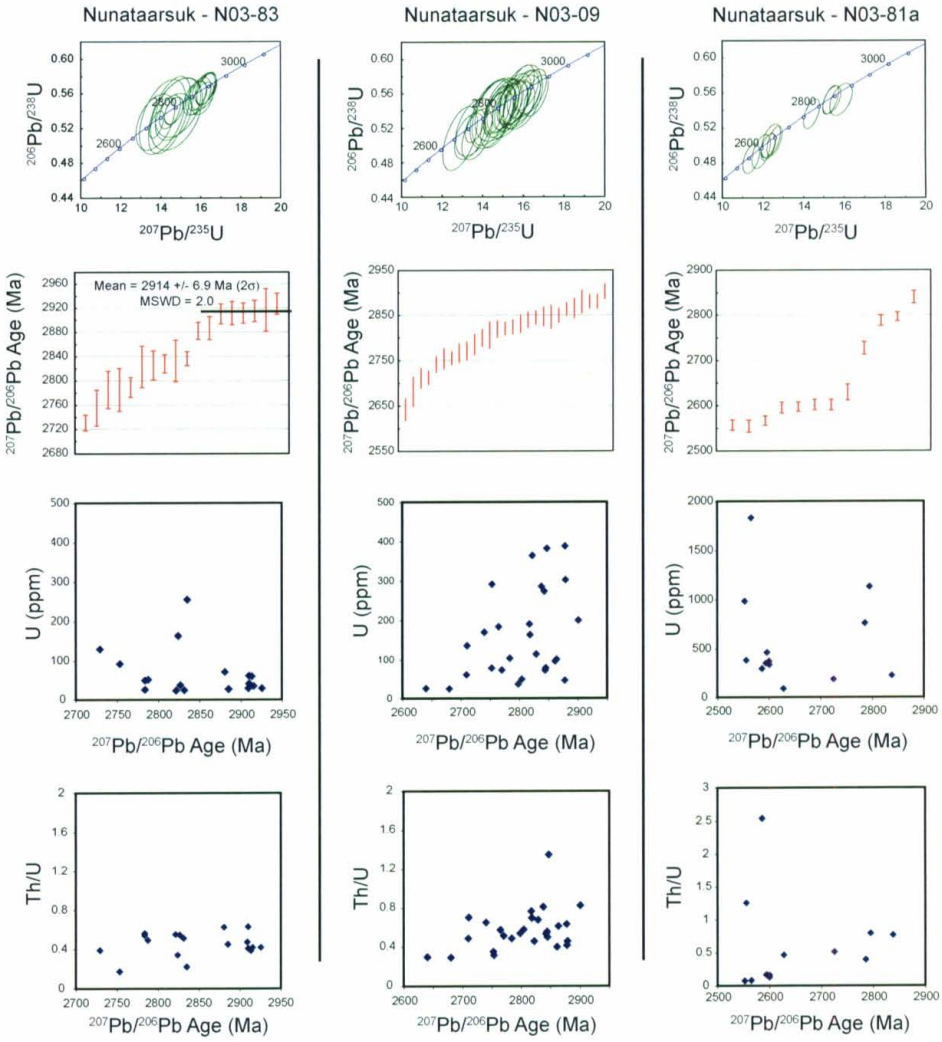

Figure 4-6: Results of in-situ LA-ICPMS U-Pb zircon analysis from Nunataarsuk anorthosite complex. Error ellipses on the concordia diagrams are 1-sigma. Error bars on the $^{207}Pb/^{206}Pb$ weighted mean plots are 2-sigma.

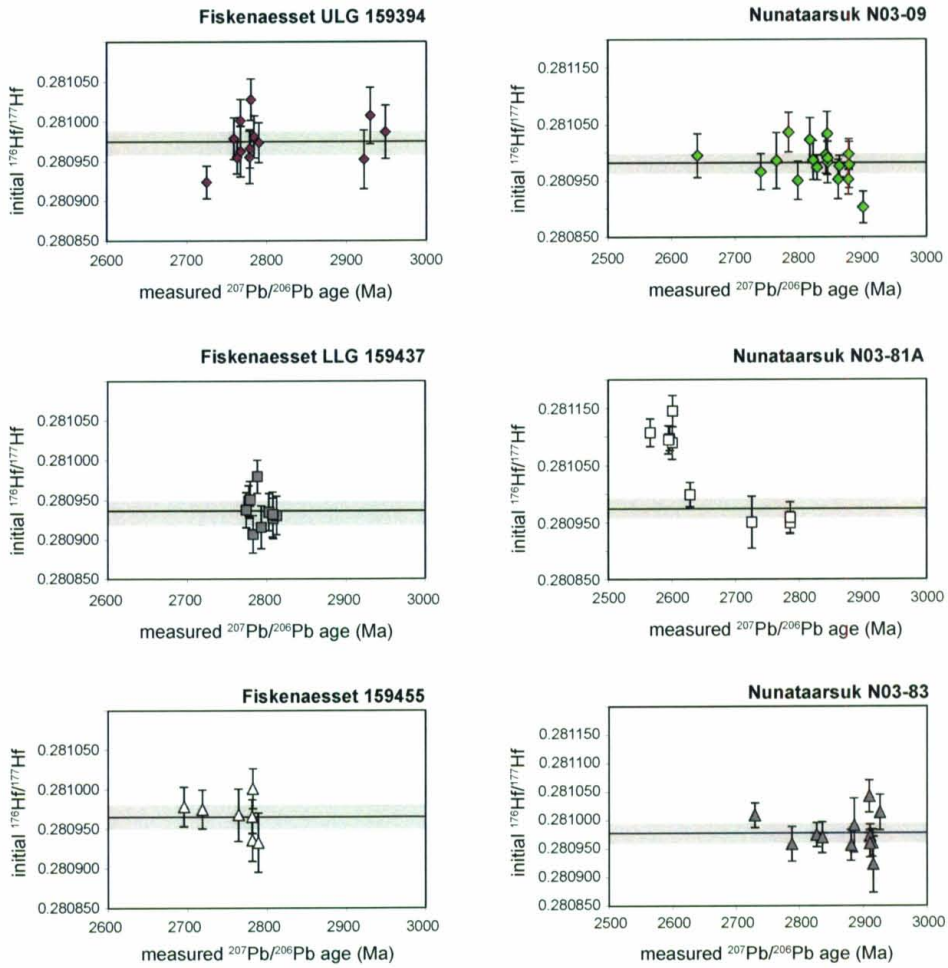

Figure 4-7: Initial $^{176}Hf/^{177}Hf$ vs. measured $^{207}Pb/^{206}Pb$ age from Fiskenæsset and Nunataarsuk zircon grains analyzed. Five analyses of four zircon grains from sample N03-81A have distinctly higher initial $^{176}Hf/^{177}Hf$ than other grains analyzed. These grains also have younger $^{207}Pb/^{206}Pb$ ages (2566 Ma to 2601 Ma) than other zircons found within this sample and represent new zircon growth, rather than zircon dissolution - homgenization- re-precipitation within the Nunataarsuk system. The solid black horizontal line in eachplot is the average initial $^{176}Hf/^{177}Hf$ for the represented sample. The gray shaded region within each plot represents the total range of initial $^{176}Hf/^{177}Hf$ for the three natural zircon standards analyzed during this study (total range = 0.000036).

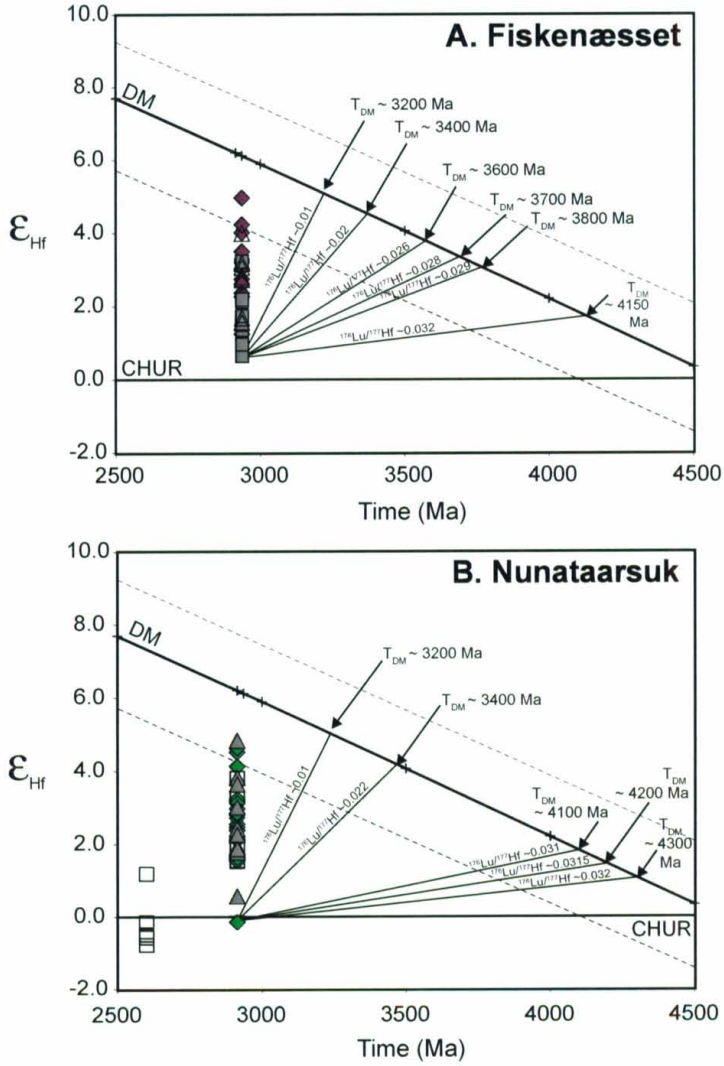

Figure 4-8: Hf isotope evolution plots for all Fiskenæsset and Nunataarsuk zircon grains analyzed. Hf depleted mantle model ages (T_{DM}) are calculated for the lower ε_{Hf} end member for both Fiskenæsset and Nunataarsuk using a range of $^{176}Lu/^{177}Hf$ ratios representative of mafic and felsic crust. The depleted mantle evolution curve (solid line) was calculated using the modern MORB values of Griffin et al. (2000) recalculated by Andersen et al. (2009), the decay constant of Soderlund et al. (2004) and the CHUR parameters of Bouvier et al. (2008). Dashed lines represent most of the range of Hf isotope compositions of modern MORB extrapolated back to the Archean (Chauvel and Blichert-Toft, 2001 and references therein).

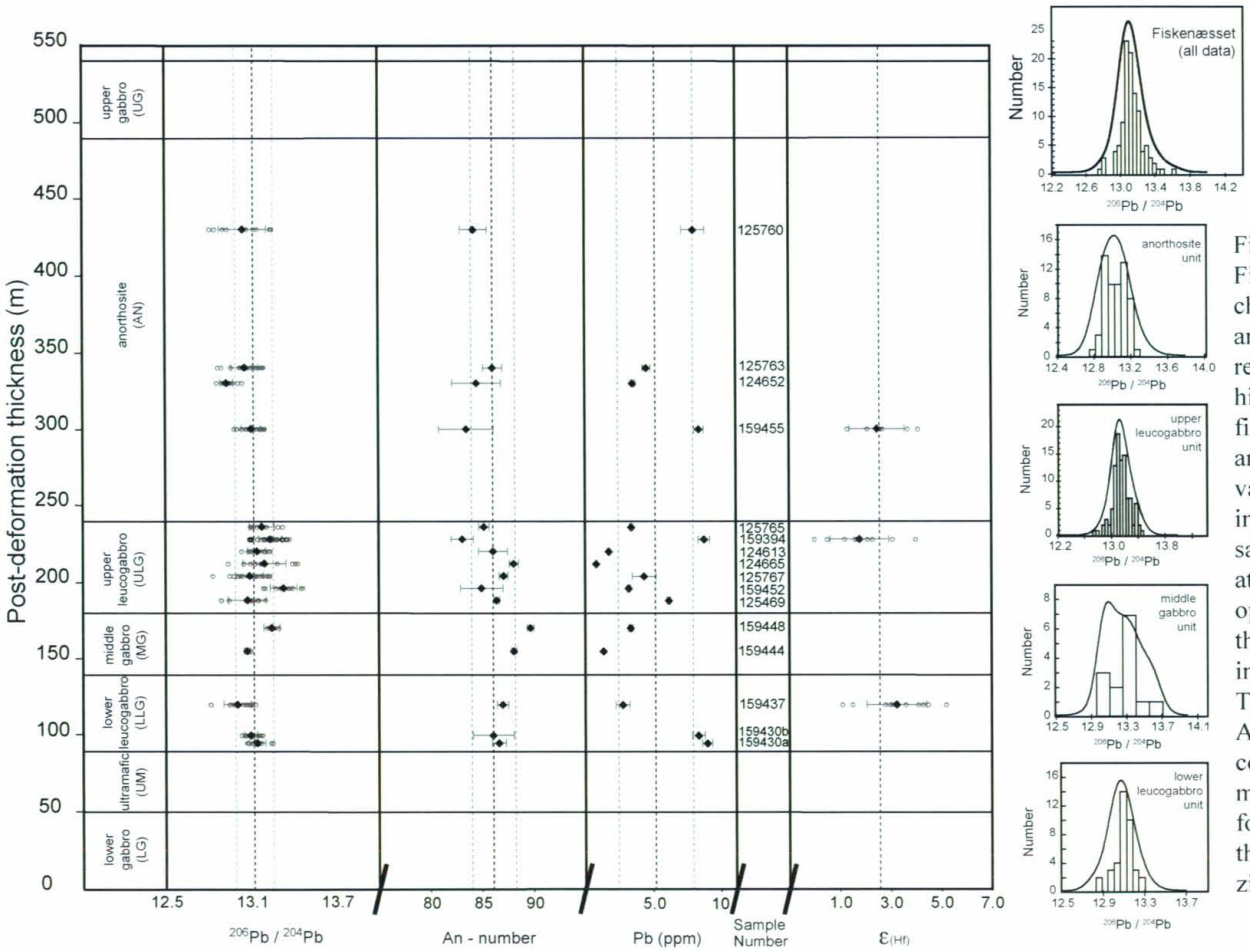

Figure 4-9: Fiskenæsset chemostratigraphy and $^{206}Pb/^{204}Pb$ relative probability histograms. Black, filled symbols are the average value for an individual sample (error bars at 1-sigma). Grey, open symbols are the value for each individual analysis. The $^{206}Pb/^{204}Pb$, An-content and Pb concentration measurements are for plagioclase and the ε_{Hf} are for zircon.

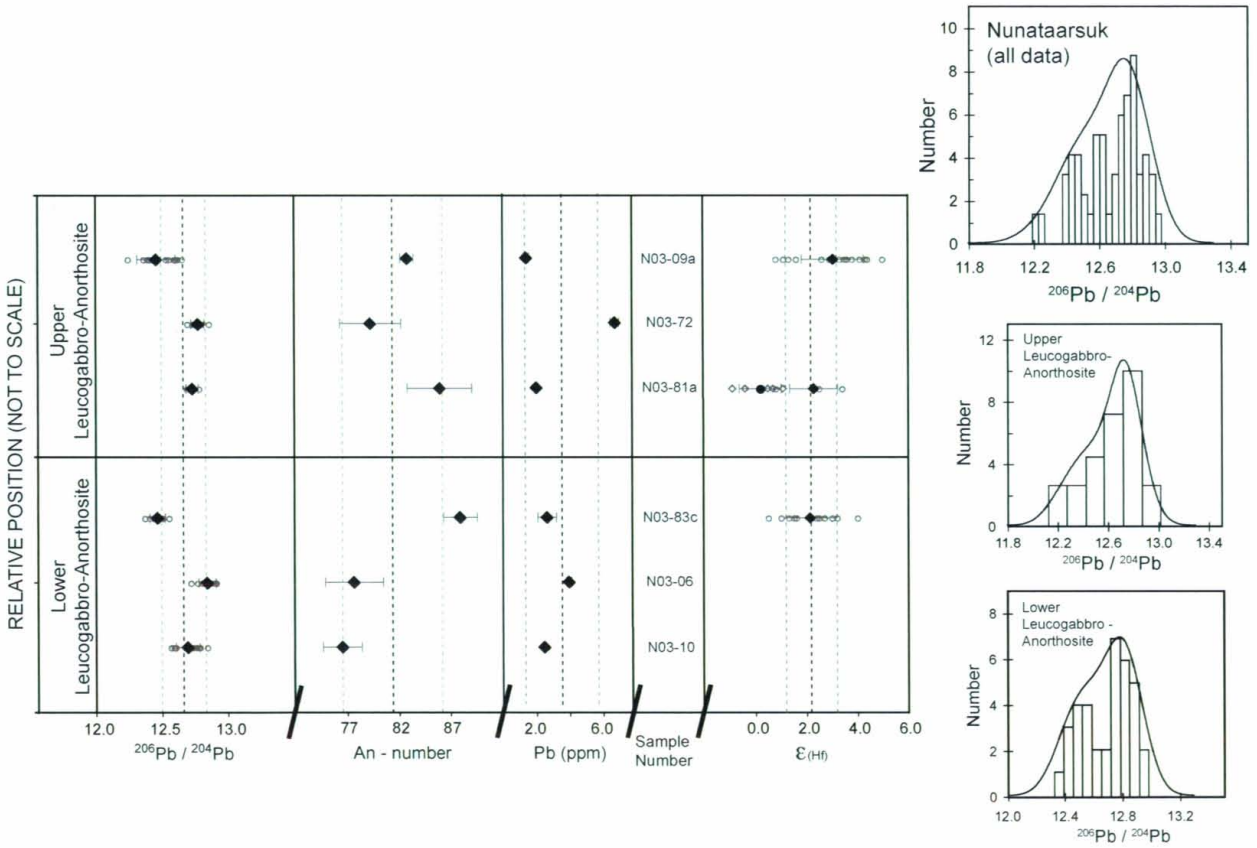

Figure 4-10: Nunataarsuk chemostratigraphy and $^{206}Pb/^{204}Pb$ relative probability histograms. Black, filled symbols are the average value for an individual sample (error bars at 1-sigma). Grey, open symbols are the value for each individual analysis. The $^{206}Pb/^{204}Pb$, An-content and Pb concentration measurements are for plagioclase and the ε_{Hf} are for zircon.

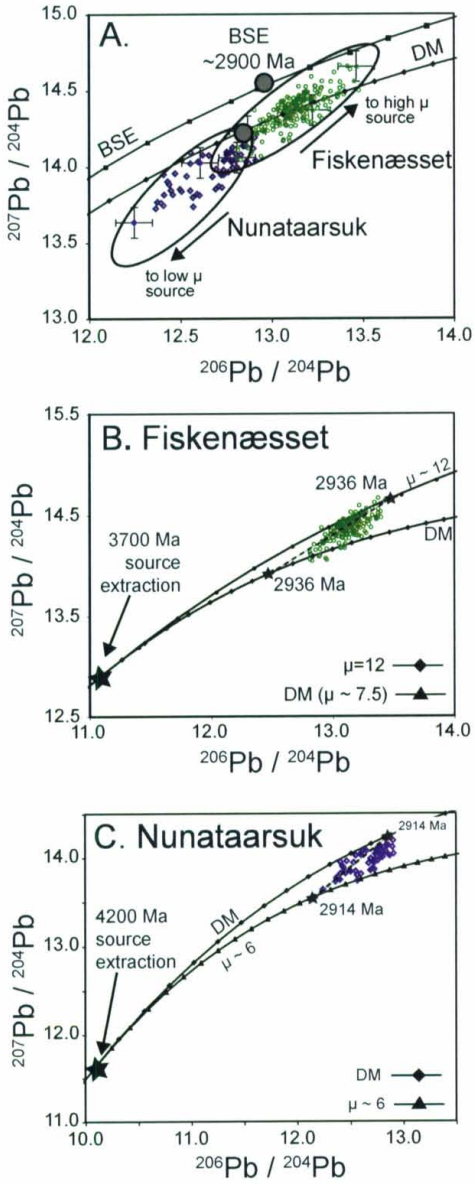

Figure 4-11: (A) $^{206}Pb/^{204}Pb$ vs. $^{207}Pb/^{204}Pb$ for Fiskenæsset (circles) and Nunataarsuk (diamonds). Representative error bars are shown, and are applicable to all of the LA-MC-ICPMS Pb isotope analyses. Also shown are the model depleted mantle (DM; Kramers and Tolstikhin, 1997) and model bulk silicate Earth (BSE; Galer and Goldstein, 1996) evolution lines. The DM and BSE Pb isotope compositions at 2900 Ma are marked with silled grey circles. (B) Fiskenæsset Pb isotope evolution model. Pb isotope compositions range between depleted mantle and a high μ source, extracted from the depleted mantle at 3700 Ma. (C) Nunataarsuk Pb isotope evolution model. Pb isotope compositions range from depleted mantle (~ 2900 Ma) and a low μ source, extracted from the depleted mantle at ~ 4200Ma.

Supplemental File S4-1: Analytical Methods for Plagioclase Analysis

S4-1.1 Major and Trace Element Analysis

The chemical composition of each plagioclase megacryst was analyzed for major elements by electron probe microanalysis (EPMA) and for trace elements by laser ablation-inductively coupled plasma mass spectrometry (LA-ICPMS). The EPMA was carried out using the JEOL JXA-733 microprobe at the University of New Brunswick with a 5 μm electron beam, an accelerating voltage of 15 kV and beam current of 30 nA. The Na_2O, MgO, Al_2O_3, SiO_2, K_2O, CaO, Fe_2O_3, BaO and Cl composition were determined for multiple analysis points along a traverse across each plagioclase megacryst (~ 750 – 1000 μm spacing between points).

LA-ICPMS trace element analysis (to determine total Pb concentration) was done at Memorial University of Newfoundland using a Thermo-Scientific ELEMENT XR magnetic sector, single-collector ICPMS coupled to a Lambda Physik ComPex Pro 110 ArF excimer GeoLas laser ablation system operating at a wavelength of 193nm and a pulse width of 20 ns. A 40-μm laser beam was focused as closely as possible to the EPMA analysis site making sure to avoid any cracks or inclusions visible on the surface of the plagioclase crystal. The laser beam operated at an energy density of 3 $J/cm^2$and a repetition rate of 10 Hz. Measurements were performed on the ELEMENT-XR using a combination of electrical and magnetic scan modes. Each pass was ~ 1.5 sec for the measurement of 27 major and trace elements with 60 passes per individual analysis. Each analysis consisted of ~ 30 seconds of gas background measurement followed by ~ 90 sec of laser ablation. Raw data was converted to concentrations with LAMTRACE (Jackson,

2008) using NIST 612 as the external calibration material. Ca-concentration determined by EPMA was used as the internal standard to correct for differences in ablation yield and potential matrix effects between the plagioclase unknowns and NIST 612.

S4.1.2 LA-MC-ICPMS Pb Isotopes

The analytical method followed that described in detail by Souders and Sylvester (2008a, b). All data were acquired using a Thermo Scientific NEPTUNE multi-collector inductively coupled plasma mass spectrometer (MC-ICPMS). The NEPTUNE at MUN is also equipped with 9 Faraday cups and 8 multiple ion counter (Channeltron) devices. Concurrent, static measurements of ^{208}Pb, ^{207}Pb, ^{206}Pb, ^{204}Pb and ^{202}Hg were made in 5 ion counters mounted onto the low mass (L4) Faraday cup. ^{235}U was measured in an ion counter attached to a high mass (L6) Faraday cup, to monitor for lead isotope ratios that may have been modified by in-growth of radiogenic lead in the samples by the decay of U after crystallization. The ion counters attached to L4 are in fixed positions, spaced to collect the four lead and ^{202}Hg isotopes. ^{202}Hg was measured in order to correct for the isobaric interference of ^{204}Hg on ^{204}Pb. The mercury is almost exclusively derived from the carrier gases rather than from the samples themselves. The ^{204}Hg/^{202}Hg of the gas background was determined from measurements of ^{202}Hg, ^{204}(Hg + Pb) and ^{208}Pb made with the laser off prior to each analysis, assuming that the isotopic composition of lead in the gas is given by the ^{208}Pb/^{204}Pb for modern lead (^{208}Pb/^{204}Pb = 38.63 ± 0.98, Stacey and Kramers, 1975). Many analyses over more than 2 years in our laboratory suggests that this method gives superior results compared to trying to determine the mass bias on the ^{204}Hg/^{202}Hg ratio through measurements of Hg isotopic ratios directly (Souders and

Sylvester 2008a, 2008b, 2010).

The same GeoLas laser ablation system previously described was linked to the NEPTUNE MC-ICPMS for in situ analyses. Ablation conditions were 3 J/cm^2 and 10 Hz with a spot size ranging from 49 to 109 μm depending on the lead concentration of the megacryst of interest and the mineral surface area available free of cracks or inclusions. Laser spots for lead isotope analysis were placed directly next to, as close to the EPMA and LA-ICPMS trace element analysis location as possible. Count rates never exceeded ~300,000 cps to limit potential analytical difficulties related to pulse pile-up, dead-time signal loss and accelerated detector drift. Samples were ablated in helium gas, which reduces sample re-deposition while increasing sensitivity for 193 nm laser ablation. Mercury was filtered from the He and Ar gases using gold-coated glass wool placed on the helium gas line feeding the ablation cell, and by an activated charcoal filter in the argon gas line.

The duration of each standard and unknown analysis was ~ 150 sec using a 0.18 sec or 1 sec integration time, depending on the analytical session. The first 30 seconds of the measurement were with the laser off, measuring the background count rates followed by 60 seconds of laser ablation, and then 60 seconds of recorded wash out. The NEPTUNE software was used for both ion counter yield and dark noise corrections prior to downloading the measured mass intensities into 'Pb-Tool', an in-house macro-based excel spreadsheet modified from 'LAM-Tool' (Kosler et al., 2008). Gas background subtraction, ^{204}Hg interference correction on ^{204}Pb, ablation interval

selection and lead isotope ratio calculations are all performed within Pb-Tool.

Unlike other radiogenic isotope systems of geologic interest (*e.g.* Sm-Nd, Lu-Hf, Rb-Sr), the lead isotope system lacks an invariant ratio to use for internal mass bias corrections. Instead, a standard – sample – standard bracketing approach was used to correct for instrumental mass bias and detector drift (Albarede et al., 2004). Three standards followed by three unknowns, followed by three standards are run sequentially. USGS BCR2-G, a natural reference glass of basalt composition, was used as the external calibration standard for all analyses because of its well-defined lead isotope ratio and chemical composition (GeoREM: http://georem.mpch-mainz.gwdg.de/), a lead concentration low enough to measure with the ion counters without saturating the detectors yet high enough for good counting statistics on isotopes of interest and it has a similar lead concentration to unknowns. It has been demonstrated that matrix matching is not a necessity for lead isotope ratio measurements of lead-poor (< 40 ppm total Pb) feldspars, and accuracies within 0.4 % of preferred values and external precisions of better than 0.6 % (RSD, 1 σ) can be attained using BCR2-G as an external calibration material (Souders and Sylvester, 2010). The calculated lead isotope ratios for every three standards are averaged together and the lead isotope ratios of each unknown analysis are determined by linear interpolation of the average standard ratios run before and after every group of three unknowns. Reported uncertainties for each unknown is based on the standard error of the mean of each unknown isotope ratio from the selected ablation interval and the standard error of the y-estimate of the linear regression line through the lead isotope ratios of the standards. MPI-DING T1-G (11.6 ± 1.6 ppm total Pb) and MPI-

DING ATHO-G (5.67 ± 0.62 ppm total Pb), standard reference materials of natural quartz diorite (T1-G) and rhyolite (ATHO-G) compositions, with well-characterized lead isotope ratios and chemical compositions (Jochum et al., 2000; Jochum et al., 2005) and similar lead concentrations to unknowns were run as unknowns for quality control purposes. The results of these analyses are listed in Table S4-1.1.

S4-1.3 References

Albarède F., Telouk P., Blichert-Toft J., Boyet M., Agranier A. and Nelson B. (2004) Precise and accurate isotopic measurements using multiple-collector ICPMS. *Geochim. Cosmochim. Acta* **68**, 2725–2744.

Jackson S.E. (2008) Calibration strategies for elemental analysis by LA-ICP-MS. *In* Laser Ablation ICP-MS in the Earth Sciences: Current Practices and Outstanding Issues, v. 40 (ed. P.J. Sylvester). Mineralogical Association of Canada pp.

Jochum K.P., Dingwell D.B., Rocholl A., Stoll B., Hofmann A.W., Becker S., Besmehn A., Bessett D., Dietze H-J., Dulski P., Erzinger J., Hellebrand E., Hoppe P., Horn I., Janssens K., Jenner G.A., Klein M., McDonough W.F., Maetz M., Mezger K., Munker C., Nikogosian I.K., Pickhardt C., Raczek I., Rhede D., Seufert H.M., Simakin S.G., Sobolev A.V., Spettel B., Straub S., Vincze L., Wallianos A., Weckwerth G., Weyer S., Wolf D. and Zimmer M. (2000) The prepartion and preliminary characterization of eight geological MPI-DING reference glasses for in-situ microanalysis. *Geostandards Newsletter: The Journal of Geostandards and Geoanalysis* **24**, 87 – 133.

Jochum K.P., Pfander J., Woodhead J.D., Willbold M., Stoll B., Herwig K., Amini M., Abouchami W. and Hofmann A.W. (2005) MPI-DING glasses: New geological reference materials for in situ Pb isotope analysis. *Geochem. Geophys. Geosys.* **6**, Q10008.

Kosler J., Forst L. and Slama J. (2008) LAMDATE and LAMTOOL: Spreadsheet-based data reduction for laser ablation-ICPMS. *In* Laser Ablation ICP-MS in the Earth Sciences: Current Practices and Outstanding Issues, v. 40 (ed. P.J. Sylvester). Mineralogical Association of Canada pp. 315 - 317.

Souders A.K. and Sylvester P.J. (2008a) Improved in situ measurements of lead isotopes in silicate glasses by LA-MC-ICPMS using multiple ion counters. *J. Anal. At. Spectrom.* **23**, 535 – 543.

Souders A.K. and Sylvester P.J. (2008b) The use of multiple Channeltron ion counters for LA-MC-ICP-MS analysis of common lead isotopes in silicate glasses. *In* Laser Ablation ICP-MS in the Earth Sciences: Current Practices and Outstanding Issues, v. 40 (ed. P.J. Sylvester). Mineralogical Association of Canada. pp. 265 – 281.

Souders A.K. and Sylvester P.J. (2010) Accuracy and precision of non-matrix-matched calibration for lead isotope ratio measurements of lead-poor minerals by LA-MC-ICPMS. *J. Anal. At. Spectrom.* **25**, 975 – 988.

Stacey J.S. and Kramers J.D. (1975) Approximation of terrestrial lead isotope evolution by a two-stage model. *Earth Planet. Sci. Lett.* **26**, 207 – 221.

Table S4-1.1: LA-MC-ICPMS Pb isotope ratios for MPI-DING-ATHO-G and MPI-DING-T1-G

File	STD	Spot size (µm)	$^{206}Pb/^{204}Pb$	SE (1s)	$^{207}Pb/^{204}Pb$	SE (1s)	$^{208}Pb/^{204}Pb$	SE (1s)	$^{207}Pb/^{206}Pb$	SE (1s)	$^{208}Pb/^{206}Pb$	SE (1s)
ju18a04	ATHO-G	49	18.360	0.150	15.431	0.143	37.865	0.333	0.841	0.003	2.063	0.005
ju18a05	ATHO-G	49	18.402	0.139	15.553	0.132	37.999	0.310	0.842	0.002	2.067	0.004
ju18a18	ATHO-G	59	18.366	0.137	15.384	0.127	37.964	0.303	0.842	0.002	2.076	0.004
ju18a30	ATHO-G	59	18.413	0.124	15.514	0.121	38.173	0.278	0.844	0.002	2.076	0.004
ju18a42	ATHO-G	59	18.442	0.129	15.553	0.128	38.110	0.296	0.844	0.002	2.070	0.004
ju18a54	ATHO-G	59	18.326	0.128	15.352	0.122	37.702	0.285	0.839	0.002	2.069	0.004
ju18a66	ATHO-G	59	18.387	0.156	15.347	0.144	37.951	0.347	0.843	0.003	2.073	0.005
ju19b04	ATHO-G	69	18.289	0.148	15.523	0.129	37.831	0.322	0.845	0.003	2.067	0.005
ju19b05	ATHO-G	69	18.367	0.103	15.353	0.098	37.886	0.239	0.840	0.002	2.069	0.004
ju19b22	ATHO-G	69	18.395	0.112	15.546	0.100	38.259	0.252	0.842	0.002	2.072	0.005
ju19b84	ATHO-G	69	18.425	0.110	15.483	0.102	38.105	0.250	0.843	0.002	2.066	0.004
ju19a04	ATHO-G	59	18.448	0.120	15.549	0.101	38.214	0.267	0.841	0.002	2.070	0.004
ju19a05	ATHO-G	59	18.487	0.119	15.605	0.095	38.213	0.265	0.842	0.002	2.071	0.005
ju19a22	ATHO-G	59	18.337	0.134	15.447	0.109	37.841	0.296	0.843	0.002	2.066	0.005
ju19a40	ATHO-G	59	18.349	0.132	15.450	0.107	38.014	0.291	0.842	0.002	2.071	0.005
ju19a58	ATHO-G	59	18.329	0.148	15.400	0.116	37.674	0.300	0.838	0.002	2.060	0.005
ju19a76	ATHO-G	59	18.446	0.131	15.463	0.111	38.019	0.294	0.841	0.002	2.069	0.005
ju20a04	ATHO-G	69	18.426	0.113	15.542	0.096	38.275	0.258	0.844	0.002	2.071	0.004
ju20a05	ATHO-G	69	18.325	0.116	15.432	0.099	37.942	0.263	0.842	0.002	2.071	0.003
ju20a22	ATHO-G	69	18.331	0.118	15.386	0.103	37.966	0.279	0.841	0.002	2.068	0.004
ju20a40	ATHO-G	69	18.348	0.130	15.428	0.113	37.762	0.290	0.843	0.002	2.066	0.004
ju20a54	ATHO-G	69	18.248	0.118	15.406	0.102	37.889	0.268	0.843	0.002	2.071	0.004
ju22a04	ATHO-G	59	18.387	0.095	15.414	0.084	37.986	0.198	0.840	0.002	2.071	0.004
ju22a05	ATHO-G	59	18.240	0.093	15.300	0.082	37.754	0.189	0.844	0.002	2.076	0.004
ju22a22	ATHOG	59	18.374	0.102	15.410	0.090	38.002	0.207	0.842	0.002	2.070	0.004
ju22a36	ATHO-G	59	18.369	0.102	15.479	0.090	37.925	0.203	0.840	0.002	2.067	0.004
ju25a04	ATHO-G	69	18.365	0.128	15.531	0.101	38.028	0.275	0.844	0.002	2.073	0.003
ju25a05	ATHO-G	69	18.446	0.131	15.528	0.102	38.284	0.281	0.844	0.002	2.078	0.003
ju25a22	ATHO-G	69	18.465	0.130	15.559	0.103	38.404	0.280	0.843	0.002	2.074	0.003
ju25a40	ATHO-G	69	18.387	0.155	15.411	0.118	38.097	0.333	0.840	0.002	2.076	0.004
ju25a48	ATHO-G	69	18.359	0.141	15.557	0.113	38.114	0.299	0.845	0.002	2.074	0.004
je27a05	ATHO-G	49	18.348	0.165	15.478	0.131	37.981	0.344	0.844	0.004	2.068	0.011
je27a40	ATHO-G	49	18.324	0.239	15.536	0.192	37.794	0.469	0.842	0.005	2.061	0.011
no10a10	AHTO-G	49	18.401	0.075	15.498	0.087	37.898	0.203	0.844	0.003	2.065	0.004
no10a11	ATHO-G	49	18.368	0.063	15.364	0.071	37.906	0.173	0.838	0.003	2.063	0.003
no10a28	ATHO-G	49	18.303	0.071	15.482	0.080	37.931	0.182	0.846	0.003	2.074	0.003
no10b04	ATHO-G	49	18.384	0.111	15.487	0.110	37.923	0.287	0.843	0.002	2.069	0.004
no10b05	ATHO-G	49	18.373	0.111	15.447	0.111	37.796	0.285	0.843	0.002	2.060	0.004
no10b18	ATHO-G	49	18.432	0.114	15.571	0.113	37.941	0.276	0.845	0.002	2.066	0.004
no10b24	ATHO-G	49	18.374	0.114	15.475	0.110	37.963	0.294	0.841	0.001	2.064	0.004
no10b28	ATHO-G	49	18.445	0.116	15.546	0.110	38.213	0.289	0.841	0.002	2.073	0.004
no11a04	ATHO-G	69	18.387	0.085	15.485	0.072	38.108	0.196	0.844	0.002	2.076	0.004
no11a05	ATHO-G	69	18.378	0.086	15.565	0.071	38.194	0.201	0.845	0.001	2.080	0.004
no11a22	ATHO-G	69	18.356	0.091	15.500	0.074	38.170	0.203	0.842	0.001	2.077	0.004
no11a60	ATHO-G	69	18.416	0.089	15.491	0.074	38.169	0.203	0.842	0.002	2.075	0.005
no15b06	ATHO-G	69	18.398	0.083	15.442	0.066	37.909	0.154	0.841	0.002	2.065	0.003
no15b22	ATHO-G	69	18.283	0.089	15.388	0.075	37.726	0.174	0.842	0.002	2.066	0.003
no15b40	ATHO-G	69	18.450	0.085	15.500	0.070	38.110	0.182	0.843	0.002	2.068	0.003
no15b58	ATHO-G	69	18.406	0.102	15.464	0.081	37.916	0.187	0.840	0.002	2.065	0.004
no15c04	ATHO-G	69	18.412	0.083	15.457	0.061	37.968	0.149	0.841	0.001	2.064	0.003
no15c22	ATHO-G	69	18.293	0.084	15.433	0.062	37.691	0.140	0.842	0.001	2.065	0.003

no15c40	ATHO-G	69	18.375	0.080	15.455	0.058	37.958	0.142	0.842	0.001	2.070	0.002
no15c52	ATHO-G	69	18.330	0.078	15.467	0.055	37.916	0.142	0.842	0.001	2.065	0.003
no15c60	ATHO-G	69	18.358	0.089	15.467	0.069	37.876	0.144	0.841	0.001	2.067	0.003
		mean	18.375		15.469		37.987		0.842		2.069	
		SD (1s)	0.053		0.068		0.166		0.002		0.005	
		% RSD (1s)	0.29%		0.44%		0.44%		0.20%		0.23%	
		preferred[1]	**18.383**	**0.004**	**15.480**	**0.004**	**38.111**	**0.003**	**0.84204**	**0.0002**	**2.073**	**0.0006**
ju06d04	T1G	40	18.725	0.119	15.676	0.111	38.876	0.255	0.837	0.002	2.077	0.004
ju06d22	T1G	40	18.693	0.115	15.684	0.110	38.930	0.249	0.841	0.001	2.082	0.004
ju06c04	T1G	40	18.762	0.139	15.724	0.110	39.066	0.256	0.838	0.002	2.082	0.003
ju06b04	T1G	40	18.702	0.103	15.615	0.107	38.835	0.331	0.835	0.002	2.080	0.004
ju06b22	T1G	40	18.652	0.118	15.609	0.120	38.897	0.343	0.842	0.002	2.083	0.004
ju06b36	T1G	40	18.675	0.124	15.671	0.115	38.823	0.345	0.839	0.002	2.088	0.004
ju06b46	T1G	40	18.689	0.124	15.685	0.124	39.083	0.363	0.838	0.002	2.085	0.004
ju06a04	T1G	40	18.720	0.079	15.688	0.108	38.823	0.293	0.838	0.003	2.076	0.011
ju06a22	T1G	69	18.759	0.084	15.723	0.104	39.128	0.288	0.837	0.003	2.084	0.011
ju06a34	T1G	69	18.634	0.079	15.627	0.106	38.795	0.286	0.840	0.003	2.084	0.011
ju03b04	T1G	40	18.772	0.121	15.762	0.089	39.077	0.252	0.837	0.001	2.078	0.003
ju03b22	T1G	40	18.701	0.153	15.647	0.106	39.099	0.289	0.837	0.001	2.080	0.003
ju03b40	T1G	40	18.743	0.136	15.712	0.101	39.036	0.265	0.839	0.001	2.084	0.003
ju03c04	T1G	40	18.776	0.181	15.687	0.106	38.845	0.310	0.839	0.001	2.089	0.003
ju03c18	T1G	40	18.727	0.155	15.621	0.097	39.043	0.299	0.833	0.001	2.079	0.003
je28a04	T1G	40	18.710	0.111	15.514	0.089	38.507	0.249	0.833	0.004	2.067	0.008
je28a22	T1G	40	18.670	0.128	15.508	0.099	38.752	0.261	0.836	0.004	2.084	0.008
je28a36	T1G	40	18.734	0.131	15.745	0.111	38.959	0.289	0.839	0.004	2.074	0.008
ju04d04	T1G	40	18.720	0.059	15.568	0.072	38.680	0.172	0.835	0.001	2.075	0.003
		mean	18.714		15.656		38.908		0.837		2.081	
		SD (1s)	0.040		0.071		0.163		0.002		0.005	
		% RSD (1s)	0.21%		0.45%		0.42%		0.28%		0.25%	
		preferred[1]	**18.728**	**0.004**	**15.679**	**0.004**	**38.973**	**0.008**	**0.83724**	**0.0001**	**2.081**	**0.0005**

[1] preferred values from Jochum et al. (2005)

Supplemental File S4-2: Analytical Methods for Zircon Analysis

S4-2.1 U-Pb Zircon Geochronology by LA-ICPMS

U-Pb isotopic data were acquired using the same Thermo-Scientific ELEMENT XR magnetic sector, single-collector ICPMS and Lambda Physik ComPex Pro 110 ArF GeoLas laser ablation system described in Supplemental File S4-1. During laser ablation, a stationary 10 um laser beam with an energy density of ~ 5 J/cm^2 at a repetition rate of 10 Hz is scanned across the sample surface by moving the sample stage at a velocity of 10 μm/sec creating a 40 x 40 μm box. A scanning method is employed to reduce the depth of ablation and supply a more constant mass-load to the ICP, reducing U-Pb fractionation while providing stable signals at high spatial resolution long enough to produce precise and accurate U-Pb zircon ages (Kosler, 2008a and references therein). The sample aerosol is transported from the sample cell to the ICP using a He-carrier gas to reduce sample redeposition within the ablation cell, improving sample transport efficiency and resulting in more stable time-resolved signals.

During data acquisition, ^{202,204}Hg, ^{206,207}Pb, ^{232}Th and ^{238}U isotopes from the zircon and gas are measured along with a mixed ^{203}Tl, ^{205}Tl, ^{209}Bi, ^{233}U, ^{237}Np internal standard tracer solution, simultaneously nebulized throughout each analysis. Aspiration of the tracer solution allow for matrix-independent, real-time instrumental mass bias correction of the U/Pb and Pb/Pb ratios using the known isotopic composition of the tracer solution (Kosler and Sylvester, 2003). Data acquisition for each analysis is 3 minutes, with the first ~30 seconds used to measure the gas background and tracer solution followed by ~150 sec of laser ablation. Measurements are carried out in peak-

jumping mode with one point measured per peak.

Raw data are dead-time corrected and reduced off-line using the LAMDATE macro-based spreadsheet program (Kosler et al., 2008b). The $^{207}Pb/^{206}Pb$, $^{207}Pb/^{235}U$ and $^{206}Pb/^{238}U$ ratios were calculated and background corrected for each analysis. An instrumental mass bias correction was made using the measured ratios of the tracer solution (Kosler et al. 2002; Kosler and Sylvester, 2003). Laser-induced U-Pb fractionation was corrected using the intercept method of Sylvester and Ghaderi (1997). Measured $^{207}Pb/^{206}Pb$ ratios were not intercept corrected because Pb/Pb isotope ratios are not fractionated by laser ablation. Instead the average ratio for the ablation interval selected was used for age calculation. An analysis was rejected from the final data set if the $^{207}Pb/^{206}Pb$ ratio calculated from the intercept method $^{206}Pb/^{238}U$ and $^{207}Pb/^{235}U$ ratios did not fall within 1-sigma uncertainty of the average measured $^{207}Pb/^{206}Pb$ ratio. Analyses more than 2% discordant were also rejected. These conservative filters were used to eliminate any analyses that may not have been properly corrected for U-Pb fractionation and to determine the best possible age. No common Pb correction was applied to any data. An analysis was rejected when ^{204}Pb was detected above background.

In order to monitor the efficiency of the instrumental mass bias correction and the laser-induced fractionation correction, standard reference materials 91500 zircon (1065 ± 3 Ma; Wiedenback et al., 1995) and Plesovice zircon (337 ± 0.37 Ma; Slama et al., 2008) were each analyzed between every ~ 8 unknowns during the analytical session. These standard measurements also monitor the accuracy and reproducibility of U-Pb analyses. Age determinations were calculated using the decay constants of Jaffey et al., (1971) and

the present day $^{238}U/^{235}U$ ratios of 137.88. Final ages and Concordia diagrams were produced using the Isoplot/Ex macro (Ludwig, 2003). The weighted mean $^{207}Pb/^{206}Pb$ age for all analyses of 91500 is 1068 ± 8 Ma (2σ, MSWD = 0.94; n = 32) and for Plesovice is 337 ± 9 Ma (2σ, MSWD = 0.37; n = 19) over the course of all the U-Pb analytical sessions (Table S4-2.1).

S4-2.2 Zircon Lu-Hf analysis by LA-MC-ICPMS

Hf isotopic compositions of zircon grains were determined by LA-MC-ICPMS using the same Thermo-Scientific NEPTUNE MC-ICPMS coupled to the same laser system described in Supplemental Files S4-1 and S4-2. A 49 μm laser spot was focused on each zircon grain directly on top of the U-Pb box raster, firing at a frequency of 10 Hz with an energy density of 5 J/cm^2 for 600 pulses. ^{171}Yb, ^{173}Yb, $^{174}(Hf + Yb)$, ^{175}Lu, $^{176}(Hf + Yb + Lu)$, ^{177}Lu, ^{178}Hf and ^{179}Hf were all measured simultaneously in 8 Faraday collectors. Each analysis consists of 30 seconds of gas background measurement, followed by 60 seconds of laser ablation and ending with 30 seconds of monitoring wash out. Isotope measurements were acquired using a 1 second on-peak integration time. Raw data are processed off-line using Hf-Tool, an in-house macro-based spreadsheet modified from LAMTOOL (Kosler et al., 2008b). The spreadsheet allows the user to select background and ablation intervals to be used in the final ratio calculations based on plots of both signal intensity vs. time and isotope ratio vs. time.

Mass bias factors (ß) for Yb and Hf were calculated using the exponential law and the invariant $^{173}Yb/^{171}Yb$ ratio of 1.13014 (Segal et al., 2003) and the $^{179}Hf/^{177}Hf$ ratio of 0.732500 (Patchett et al., 1981). The ß(Yb) is used as an approximation for ß(Lu) since

the 2 isotopes are chemically similar and only 2 Lu isotopes are found in nature. In order to determine the ^{176}Hf signal intensity the ^{176}Yb and ^{176}Lu interferences on the 176-mass must be removed. Interference-free ^{173}Yb and ^{175}Lu were measured and the ^{176}Yb and ^{176}Lu contributions to the 176-mass were calculated using the ^{176}Yb/^{173}Yb ratio of 0.7938 (Segal et al., 2003) and the ^{176}Lu/^{175}Lu ratio of 0.2656 (Chu et al., 2002). The ^{176}Hf/^{177}Hf, ^{176}Hf/^{177}Hf, ^{176}Yb/^{177}Hf, ^{176}Lu/^{177}Hf and ^{178}Hf/^{177}Hf ratios are calculated and corrected for instrumental mass bias using ß(Hf). No normalization correction to a solution value was applied to the data. The invariant ^{178}Hf/^{177}Hf ratio provides a quality-control monitor for the accuracy of the Hf mass bias correction. The mean ^{178}Hf/^{177}Hf ratio for all 91500 and PL reference zircons analyzed during the course of this study is 1.467245 ± 0.000052 (2SD, n = 60), which is within the uncertainty of the ^{178}Hf/^{177}Hf ratios reported by Thirlwall and Anczhiewicz (2004).

Reference zircons PL and 91500 were analyzed after every eight unknowns to evaluate the accuracy and reproducibility of our LA-MC-ICPMS Lu-Hf isotope analyses. Identical laser ablation conditions were used for both unknown zircon grains and reference zircon crystals. The average ^{176}Hf/^{177}Hf for Plesovice zircon analyzed during this study is 0.282480 ± 19 (2SD, n = 24) compared to the reference value of 0.282482 ± 0.000013 (2SD) (Slama et al., 2008). The average ^{176}Hf/^{177}Hf ratio for R33 zircon is 0.282761 ± 15 (2SD, n = 14) compared to the literature value of 0.282767 ± 18 (Vervoort, 2010). The average ^{176}Hf/^{177}Hf ratio for the 91500 zircon is 0.282306 ± 0.000015 (2SD, n = 16) compared to the literature value of 0.282308 ± 0.000006 (2SD; Blichert-Toft, 2008) (Table S4-2.2).

For unknown zircon grains, the initial ^{176}Hf/^{177}Hf ratios were calculated using the

measured $^{176}Lu/^{177}Hf$, the ^{176}Lu decay constant, $\lambda = 1.867 \times 10^{-11}$/ yr, of Söderlund et al. (2004) and the LA-ICPMS $^{207}Pb/^{206}Pb$ zircon age for each individual grain. Epsilon Hf values are calculated using the present-day CHUR $^{176}Hf/^{177}Hf$ and $^{176}Lu/^{177}Hf$ values of 0.282785 and 0.0336, respectively (Bouvier et al., 2008). The depleted mantle model of Griffin et al. (2000), modified to the ^{176}Lu decay constant of Söderlund et al. (2004) and present-day CHUR Lu-Hf composition of Bouvier et al. (2008) by Andersen et al. (2009) was used as a reference. This model has a present-day $^{176}Hf/^{177}Hf$ value of 0.28325 (εHf = +16.4) at $^{176}Lu/^{177}Hf = 0.0388$, similar to modern-day MORB (Andersen et al., 2009).

S4-3 References

Andersen T., Andersson U.B., Graham S., Aberg G., and Simonsen S.L. (2009) Granitic magmatism by melting of juvenile continental crust: new constraints on the source of Palaeoproterozoic granitoids in Fennoscandia from Hf isotopes in zircon. *J. Geol. Soc. London* **166**, 233 – 247.

Blichert-Toft J. (2008) The Hf isotopic composition of zircon reference material 91500. *Chem. Geol.* **253**, 252 – 257.

Bouvier A., Vervoort J.D. and Patchett P.J. (2008) The Lu-Hf and Sm-Nd isotopic composition of CHUR: constraints from unequilibrated chondrites and implications for the bulk composition of terrestrial planets. *Earth Planet. Sci. Lett.* **273**, 48 – 57.

Chu N.C., Taylor R.N., Chavagnac V., Nesbitt R.W., Boella R.M., Milton J.A., German C.R., Bayon G. and Burton K. (2002) Hf isotope ratio analysis using multi-collector inductibely coupled plasma mass spectrometry: an evaluation of isobaric interference corrections. *J. Anal. At. Spectrom.* **17**, 1567 – 1574.

Griffin W.L. Pearson N.J. Belousova E. Jackson S.E. van Achterbergh E. O'Reilly S.Y. Shee S.R. (2000) The Hf isotope composition of cratonic mantle; LAM-MC-ICPMS analysis of zircon megacrysts in kimberlites. *Geochim. Cosmochim Acta.* **64**, 133 – 147.

Jaffey A.H., Flynn K.F., Glendenin L.E., Bentley W.C. and Essling A.M. (1971) Precision measurement of half-lives and specific activities of ^{235}U and ^{238}U. *Phys. Rev. C.* **4**, 1889 – 1906.

Kosler J. and Sylvester P.J. (2003) Present trends and the future of zircon in geochronology: laser ablation ICPMS. *In* Zircon, Vol. 53, Reviews in Mineralogy and

Geochemistry (eds. J.M. Hanchar, P.W.O. Hoskin). Mineralogical Society of America. pp. 243 – 275.

Kosler J., Fonneland H., Sylvester P., Tubrett M. and Pederson R. (2002) U–Pb dating of detrital zircons for sediment provenance studies: a comparison of laser- ablation ICPMS and SIMS techniques. *Chem. Geol.* **182**, 605–618.

Kosler J. (2008a) Laser ablation sampling strategies for concentration and isotope ratio analyses by ICP-MS. *In* Laser Ablation ICP-MS in the Earth Sciences: Current Practices and Outstanding Issues, v. 40 (ed. P.J. Sylvester). Mineralogical Association of Canada pp. 79 – 92.

Kosler J., Forst L. and Slama J. (2008b) LAMDATE and LAMTOOL: Spreadsheet-based data reduction for laser ablation-ICPMS. *In* Laser Ablation ICP-MS in the Earth Sciences: Current Practices and Outstanding Issues, v. 40 (ed. P.J. Sylvester). Mineralogical Association of Canada pp. 315 - 317.

Ludwig K. (2008) Isoplot 3, A Geochronological Toolkit for Microsoft Excel. Special Publication 1a. Berkeley Geochronology Center.

Patchett P.J., Kouvo O., Hedge C.E. and Tatsumoto M. (1981) Evolution of continental crust and mantle heterogeneity: evidence from Hf isotopes. *Contrib. Mineral. Petrol.* **78**, 279 – 297.

Segal I., Halicz L. and Platzner I.T. (2003) Accurate isotope ratio measurements of ytterbium by multiple collection inductively coupled plasma mass spectrometry applying erbium and hafnium in an improved double external normalization procedure. *J. Anal. Atom. Spec.* **18**, 1217 – 1223.

Slama J., Kosler J., Condon D.J., Crowley J.L., Gerdes A., Hanchar J.M., Horstwood M.S.A., Morris G.A., Nasdala L., Norberg N., Schaltegger U., Schoene B., Tubrett M.N. and Whitehouse M.J. (2008) Plesovice zircon – a new natural reference material for U-Pb and Hf isotopic microanalysis. *Chem. Geol.* **249**, 1 – 35.

Soderlund U., Patchett P.J., Vervoort J.D. and Isachsen C.E. (2004) the ^{176}Lu decay constant determined by Lu-Hf and U-Pb isotope systematics of Precambrian mafic intrusions. *Earth Planet. Sci. Lett.* **219**, 311 – 324.

Sylvester P.J. and Ghaderi M. (1997) Trace element analysis of scheelite by excimer laser ablation–inductively coupled plasma–mass spectrometry (ELA–ICP–MS) using a synthetic silicate glass standard. *Chem. Geol.* **141**, 49–65.

Thirlwall M.F. and Anczkiewicz R. (2004) Multidynamic isotope ratio analysis using MC-ICP-MS and the causes of secular drift in Hf, Nd, and Pb isotope ratios. *Int. J. Mass Spec.* 235, 59.

Wiedenbeck M., Alle P., Corfu F. et al. (1995) Three natural zircon standards for U–Th–Pb, Lu–Hf, trace element and REE analyses. *Geostandards Newsletter* **19**, 1–23.

Table S4-2.1: U - Pb zircon LA-ICPMS analyses of reference zircons

					Measured Isotopic Ratios[3]							Calculated Ages						
file name[1]	sample	^{232}Th ppm[2]	^{238}U ppm[2]	Th/U Ratio	^{207}Pb/^{235}U	1s error	^{206}Pb/^{238}U	1s error	Rho[4]	^{207}Pb/^{206}Pb	1s error	^{207}Pb/^{235}U Ma	1s error Ma	^{206}Pb/^{238}U Ma	1s error Ma	^{207}Pb/^{206}Pb Ma	1s error Ma	U-Pb/Pb-Pb concordancy (%)[5]
ap11A03	91500	31	86	0.37	1.8144	0.0747	0.1745	0.0042	0.30	0.0754	0.0009	1051	27	1037	23	1080	25	96
ap11A25	91500	29	77	0.38	1.9051	0.0919	0.1823	0.0047	0.27	0.0772	0.0010	1083	32	1079	26	1127	27	96
ap11A24	91500	24	63	0.38	1.8693	0.1098	0.1799	0.0072	0.34	0.0751	0.0012	1070	39	1066	39	1070	32	100
ap11A45	91500	33	94	0.35	1.8607	0.0700	0.1797	0.0037	0.27	0.0761	0.0012	1067	25	1065	20	1097	31	97
ap11A53	91500	30	80	0.38	1.8532	0.0588	0.1792	0.0031	0.28	0.0750	0.0009	1065	21	1062	17	1068	25	99
ap11A81	91500	28	76	0.36	1.8314	0.0530	0.1777	0.0033	0.3	0.0755	0.0009	1057	19	1054	18	1081	23	98
ap11A55	91500	26	71	0.36	1.8230	0.0690	0.1764	0.0045	0.3	0.0746	0.0009	1054	25	1047	25	1057	24	99
ap11A56	91500	29	81	0.36	1.8418	0.0985	0.1796	0.0067	0.3	0.0757	0.0010	1061	35	1065	36	1087	27	98
ap11A69	91500	33	95	0.35	1.8495	0.0415	0.1774	0.0034	0.4	0.0737	0.0008	1063	15	1053	19	1032	21	102
ap11A80	91500	27	77	0.36	1.8846	0.0660	0.1808	0.0036	0.3	0.0763	0.0010	1076	23	1071	20	1103	27	97
ap11A80	91500	28	79	0.35	1.9008	0.0671	0.1803	0.0038	0.3	0.0759	0.0010	1081	23	1069	21	1092	27	98
ap11A81	91500	28	79	0.36	1.8616	0.0511	0.1781	0.0027	0.3	0.0757	0.0009	1068	18	1057	15	1087	23	97
ap11A89	91500	29	83	0.35	1.8608	0.0561	0.1794	0.0040	0.4	0.0773	0.0009	1067	20	1063	22	1129	23	94
ap11A90	91500	29	82	0.35	1.8737	0.0641	0.1761	0.0030	0.2	0.0800	0.0011	1072	23	1045	16	1197	28	87
ap12A02	91500	24	69	0.35	1.9206	0.0836	0.1830	0.0043	0.3	0.0761	0.0012	1088	29	1084	24	1097	32	99
ap12A12	91500	30	85	0.36	1.9407	0.0655	0.1830	0.0038	0.3	0.0773	0.0009	1095	23	1083	21	1130	24	96
ap12A13	91500	32	91	0.35	1.8140	0.0591	0.1750	0.0033	0.3	0.0750	0.0011	1051	21	1040	18	1068	28	97
mr01A01	91500	30	82	0.36	1.8353	0.0859	0.1735	0.0061	0.38	0.0746	0.0009	1058	31	1031	34	1059	25	97
mr01A02	91500	32	88	0.36	1.8545	0.0709	0.1752	0.0056	0.42	0.0741	0.0009	1065	25	1041	31	1044	24	100
mr01A03	91500	23	66	0.34	1.8983	0.0741	0.1802	0.0051	0.37	0.0758	0.0008	1080	26	1068	28	1089	22	98
mr01A13	91500	32	90	0.35	1.8297	0.0586	0.1776	0.0040	0.35	0.0740	0.0008	1056	21	1054	22	1042	21	101
mr01A25	91500	26	72	0.36	1.9143	0.0778	0.1780	0.0054	0.37	0.0760	0.0008	1086	27	1056	30	1095	20	96
mr01A37	91500	32	91	0.35	1.8564	0.0481	0.1774	0.0032	0.35	0.0736	0.0007	1066	17	1053	18	1030	19	102
mr01A48	91500	25	75	0.34	1.8791	0.0862	0.1768	0.0069	0.43	0.0748	0.0007	1074	30	1050	38	1063	19	99
mr01A59	91500	32	88	0.37	1.8368	0.0609	0.1755	0.0035	0.30	0.0742	0.0008	1059	22	1043	19	1046	22	100
jl31a01	91500	28	77	0.36	1.8818	0.0726	0.1814	0.0049	0.35	0.0757	0.0009	1075	26	1074	27	1088	23	99
jl31a02	91500	27	77	0.35	1.8666	0.0571	0.1787	0.0036	0.33	0.0756	0.0007	1069	20	1060	20	1086	18	98
jl31a05	91500	32	91	0.36	1.8853	0.0723	0.1813	0.0054	0.38	0.0737	0.0009	1076	25	1074	29	1033	24	104
jl31a10	91500	32	88	0.36	1.8924	0.0530	0.1817	0.0033	0.33	0.0739	0.0007	1078	19	1076	18	1038	20	104
jl31a19	91500	29	82	0.35	1.9539	0.0598	0.1824	0.0034	0.30	0.0758	0.0009	1100	21	1080	19	1091	23	99
jl31a20	91500	29	81	0.36	1.8213	0.0675	0.1765	0.0041	0.32	0.0743	0.0009	1053	24	1048	23	1050	24	100
jl31a27	91500	26	75	0.35	1.8266	0.0574	0.1779	0.0037	0.33	0.0743	0.0008	1055	21	1056	20	1050	22	101
jl31a50	91500	30	83	0.36	1.8572	0.0643	0.1786	0.0039	0.31	0.0739	0.0008	1066	23	1059	21	1040	23	102
fc29A21	91500	29	82	0.36	1.7411	0.0488	0.1730	0.0037	0.38	0.0746	0.0006	1024	18	1028	20	1059	17	97
au29b11	91500	29	81	0.35	1.8751	0.0682	0.1804	0.0045	0.34	0.0740	0.0009	1072	24	1069	25	1041	25	103
au29b20	91500	25	71	0.35	1.8708	0.0559	0.1805	0.0036	0.33	0.0763	0.0010	1071	20	1069	20	1102	26	97
au29b39	91500	29	82	0.36	1.8649	0.0585	0.1800	0.0034	0.30	0.0757	0.0009	1069	21	1067	19	1088	23	98
au29b50	91500	32	90	0.36	1.8656	0.0611	0.1792	0.0043	0.36	0.0754	0.0009	1069	22	1062	23	1078	23	99
au23A34	91500		70		1.8292	0.0524	0.1799	0.0034	0.33	0.0762	0.0008	1056	19	1067	19	1100	21	97
au23A37	91500		80		1.8042	0.0430	0.1797	0.0032	0.37	0.0751	0.0007	1047	16	1065	17	1071	18	99
au23A42	91500		73		1.9130	0.0526	0.1772	0.0028	0.28	0.0797	0.0007	1086	18	1051	15	1190	18	88
au23A43	91500		75		1.8842	0.0511	0.1825	0.0034	0.35	0.0770	0.0007	1076	18	1081	19	1120	18	96
mr01A04	PL	45	562	0.08	0.4309	0.0200	0.0566	0.0025	0.48	0.0533	0.0006	364	14	355	15	343	24	104
mr01A14	PL	55	636	0.09	0.4362	0.0196	0.0581	0.0021	0.40	0.0535	0.0005	368	14	364	13	350	19	104
mr01A38	PL	54	651	0.08	0.4310	0.0145	0.0574	0.0016	0.41	0.0536	0.0004	364	10	360	10	356	17	101
mr01A49	PL	76	837	0.09	0.3985	0.0113	0.0524	0.0014	0.48	0.0528	0.0003	341	8	329	9	318	14	103
mr01A60	PL	52	632	0.08	0.3966	0.0164	0.0525	0.0019	0.44	0.0534	0.0004	339	12	330	12	346	18	95
jl31a04	PL	90	900	0.10	0.3979	0.0134	0.0527	0.0018	0.49	0.0533	0.0004	340	10	331	11	342	18	97

jl31a21	PL	81	852	0.10	0.3899	0.0126	0.0524	0.0011	0.32	0.0530	0.0004	334	9	329	7	330	19	100
jl31a51	PL	96	906	0.11	0.3964	0.0086	0.0527	0.0008	0.35	0.0532	0.0004	339	6	331	5	339	16	98
jl31a44	PL	85	884	0.10	0.4011	0.0087	0.0538	0.0007	0.30	0.0531	0.0004	342	6	338	4	331	16	102
fe29A02	PL	57	497	0.12	0.3836	0.0104	0.0518	0.0012	0.44	0.0528	0.0005	330	8	326	8	322	20	101
fe29A12	PL	65	637	0.10	0.3880	0.0157	0.0533	0.0015	0.35	0.0538	0.0004	333	11	335	9	362	18	93
au29b12	PL	32	408	0.08	0.3976	0.0104	0.0534	0.0009	0.32	0.0531	0.0005	340	8	336	5	332	20	101
au29b21	PL	33	411	0.08	0.3852	0.0154	0.0520	0.0015	0.36	0.0528	0.0005	331	11	327	9	322	23	102
ap11A05	PL	56	630	0.09	0.3869	0.0103	0.0534	0.0010	0.35	0.0532	0.0005	332	8	335	6	339	23	99
ap11A12	PL	59	632	0.09	0.3964	0.0191	0.0536	0.0014	0.27	0.0535	0.0009	339	14	336	9	349	36	96
ap11A42	PL	57	666	0.09	0.4077	0.0100	0.0532	0.0010	0.39	0.0530	0.0005	347	7	334	6	330	22	101
ap11A43	PL	48	575	0.08	0.3913	0.0096	0.0531	0.0009	0.33	0.0535	0.0005	335	7	333	5	352	21	95
ap11A79	PL	66	734	0.09	0.3973	0.0098	0.0541	0.0009	0.33	0.0532	0.0005	340	7	340	5	336	20	101
ap11A92	PL	65	736	0.09	0.3971	0.0114	0.0547	0.0010	0.31	0.0537	0.0006	340	8	343	6	359	27	96
ap12A05	PL	54	616	0.09	0.4098	0.0103	0.0543	0.0008	0.28	0.0532	0.0006	349	7	341	5	338	25	101

Notes:

[1] 'File name' is the lab ID of the raw data file for each individual analysis

[2] interpolated using the within run average count rates of 91500 zircon and the Th and U concentrations (Wiedenbeck et al., 1995)

[3] Measured isotopic ratios determined using the LAMDATE data reduction program for LA-ICPMS (Kosler et al. 2008b).

[4] 'Rho' is the correlation coefficient between the two U/Pb isotope ratios, calculated as the ratio of the covariance to the product of the standard deviations for each ratio.

[5] 'U-Pb/Pb-Pb concordancy (%) is a measure of U-Pb discordancy

Table S2.2: Zircon Lu-Hf LA-MC-ICPMS analysis of standard reference materials

file name[1]	sample	age[2]	^{176}Hf (V)	^{176}Lu/^{177}Hf	2SE	^{176}Yb/^{177}Hf	2SE	^{178}Hf/^{177}Hf	2SE	^{176}Hf/^{177}Hf	2SE	ε_{Hf}[4]	2SE
11oc02b01	Plesovice	336.9	3.23	0.000102	0.000003	0.003574	0.000111	1.467270	0.000049	0.282464	0.000028	-11.4	1.0
11oc02b02	Plesovice	336.9	3.80	0.000057	0.000000	0.001848	0.000015	1.467268	0.000037	0.282477	0.000024	-10.9	0.8
11oc03b03	Plesovice	336.9	3.02	0.000083	0.000001	0.002913	0.000029	1.467222	0.000047	0.282462	0.000026	-11.4	0.9
11oc04b16	Plesovice	336.9	2.89	0.000074	0.000002	0.002611	0.000062	1.467263	0.000044	0.282488	0.000037	-10.5	1.3
11oc04b28	Plesovice	336.9	3.35	0.000062	0.000001	0.001987	0.000030	1.467242	0.000038	0.282490	0.000031	-10.4	1.1
11oc04c01	Plesovice	336.9	2.62	0.000176	0.000001	0.006066	0.000022	1.467234	0.000046	0.282496	0.000031	-10.2	1.1
11oc04c02	Plesovice	336.9	2.48	0.000172	0.000001	0.005949	0.000026	1.467272	0.000053	0.282476	0.000037	-10.9	1.3
11oc04c03	Plesovice	336.9	2.78	0.000093	0.000001	0.003263	0.000054	1.467230	0.000056	0.282474	0.000026	-11.0	0.9
11oc04c04	Plesovice	336.9	2.63	0.000127	0.000003	0.004284	0.000084	1.467232	0.000044	0.282486	0.000030	-10.6	1.0
11oc04c18	Plesovice	336.9	3.48	0.000099	0.000003	0.003412	0.000105	1.467282	0.000047	0.282492	0.000038	-10.4	1.4
11oc04c19	Plesovice	336.9	3.43	0.000121	0.000002	0.004238	0.000076	1.467261	0.000048	0.282468	0.000041	-11.2	1.5
11oc04c20	Plesovice	336.9	3.50	0.000070	0.000001	0.002478	0.000039	1.467255	0.000046	0.282477	0.000029	-10.9	1.0
11oc04c25	Plesovice	336.9	3.05	0.000103	0.000001	0.003600	0.000031	1.467241	0.000068	0.282484	0.000034	-10.7	1.2
11oc04c26	Plesovice	336.9	3.22	0.000118	0.000001	0.004271	0.000021	1.467252	0.000042	0.282497	0.000038	-10.2	1.4
11oc04c27	Plesovice	336.9	3.62	0.000098	0.000002	0.003528	0.000076	1.467252	0.000038	0.282483	0.000037	-10.7	1.3
11oc04c28	Plesovice	336.9	3.15	0.000102	0.000000	0.003784	0.000020	1.467230	0.000050	0.282477	0.000035	-10.9	1.3
11oc04d01	Plesovice	336.9	2.98	0.000125	0.000003	0.004249	0.000117	1.467238	0.000046	0.282486	0.000032	-10.6	1.1
11oc04d02	Plesovice	336.9	3.10	0.000120	0.000001	0.004135	0.000048	1.467233	0.000036	0.282481	0.000027	-10.8	1.0
11oc04d03	Plesovice	336.9	3.00	0.000066	0.000001	0.002133	0.000037	1.467291	0.000059	0.282474	0.000034	-11.0	1.2
11oc04d16	Plesovice	336.9	3.03	0.000065	0.000001	0.002109	0.000046	1.467283	0.000039	0.282470	0.000027	-11.2	1.0
11oc04e01	Plesovice	336.9	2.84	0.000089	0.000001	0.003077	0.000026	1.467298	0.000056	0.282488	0.000022	-10.5	0.8
11oc04e14	Plesovice	336.9	2.83	0.000068	0.000000	0.002302	0.000026	1.467239	0.000058	0.282475	0.000034	-11.0	1.2
11oc04e27	Plesovice	336.9	2.74	0.000154	0.000001	0.005367	0.000038	1.467255	0.000041	0.282478	0.000022	-10.8	0.8
11oc04e37	Plesovice	336.9	2.72	0.000170	0.000005	0.005862	0.000179	1.467219	0.000045	0.282483	0.000028	-10.7	1.0
									mean	**0.282480**	**0.000031**	**-10.8**	**1.1**
									2SD	**0.000019**			
									(Slama et al., 2008)	0.282482	0.000013		
11oc04b04	R33	419.8	2.32	0.002112	0.000125	0.055574	0.003463	1.467280	0.000049	0.282763	0.000039	-0.8	1.4
11oc04b29	R33	419.8	2.31	0.001315	0.000023	0.031984	0.000692	1.467281	0.000067	0.282750	0.000041	-1.2	1.5
11oc04c08	R33	419.8	2.60	0.001041	0.000059	0.024532	0.001331	1.467249	0.000044	0.282762	0.000030	-0.8	1.1
11oc04c09	R33	419.8	2.63	0.001390	0.000031	0.033263	0.000819	1.467299	0.000044	0.282757	0.000036	-1.0	1.3
11oc04c23	R33	419.8	3.90	0.001454	0.000056	0.031196	0.001121	1.467310	0.000062	0.282770	0.000031	-0.5	1.1
11oc04c24	R33	419.8	2.96	0.001677	0.000002	0.040396	0.000103	1.467281	0.000052	0.282762	0.000030	-0.8	1.1
11oc04c39	R33	419.8	3.01	0.001666	0.000017	0.038845	0.000371	1.467257	0.000051	0.282752	0.000043	-1.2	1.5
11oc04d04	R33	419.8	2.98	0.000829	0.000019	0.019885	0.000441	1.467203	0.000039	0.282748	0.000026	-1.3	0.9
11oc04d17	R33	419.8	2.42	0.001214	0.000022	0.029113	0.000406	1.467253	0.000051	0.282756	0.000029	-1.0	1.0
11oc04d20	R33	419.8	2.85	0.001468	0.000020	0.035766	0.000472	1.467258	0.000048	0.282766	0.000030	-0.7	1.1
11oc04e02	R33	419.8	2.87	0.001471	0.000056	0.034182	0.001133	1.467252	0.000053	0.282772	0.000031	-0.5	1.1
11oc04e15	R33	419.8	2.36	0.001133	0.000012	0.027757	0.000302	1.467254	0.000042	0.282760	0.000031	-0.9	1.1
11oc04e28	R33	419.8	2.51	0.001627	0.000073	0.036008	0.001805	1.467224	0.000057	0.282759	0.000032	-0.9	1.1
11oc04e38	R33	419.8	1.75	0.001228	0.000083	0.030710	0.002191	1.467168	0.000054	0.282771	0.000035	-0.5	1.2
									mean	**0.282761**	**0.000033**	**-0.9**	**1.2**
									2SD	**0.000015**			
									(Vervoort, 2010)	0.282767	0.000018		
11oc04b06	91500	1056	1.75	0.000245	0.000000	0.005863	0.000025	1.467230	0.000056	0.282297	0.000039	-17.2	1.4
11oc04b07	91500	1056	1.81	0.000240	0.000000	0.005817	0.000026	1.467215	0.000060	0.282312	0.000033	-16.7	1.2
11oc04b17	91500	1056	1.70	0.000241	0.000000	0.005830	0.000033	1.467312	0.000060	0.282311	0.000041	-16.8	1.4
11oc04b30	91500	1056	1.68	0.000244	0.000001	0.005938	0.000040	1.467197	0.000058	0.282317	0.000038	-16.5	1.4
11oc04c05	91500	1056	1.55	0.000239	0.000001	0.005818	0.000032	1.467290	0.000068	0.282290	0.000037	-17.5	1.3
11oc04c06	91500	1056	1.71	0.000240	0.000001	0.006105	0.000096	1.467223	0.000081	0.282306	0.000045	-16.9	1.6
11oc04c07	91500	1056	1.90	0.000241	0.000000	0.005936	0.000030	1.467278	0.000055	0.282301	0.000037	-17.1	1.3
11oc04c21	91500	1056	2.39	0.000238	0.000000	0.005847	0.000074	1.467279	0.000067	0.282317	0.000031	-16.6	1.1
11oc04c40	91500	1056	2.06	0.000241	0.000001	0.005882	0.000085	1.467267	0.000063	0.282306	0.000033	-16.9	1.2
11oc04d05	91500	1056	1.30	0.000241	0.000001	0.005788	0.000054	1.467261	0.000105	0.282298	0.000058	-17.2	2.1
11oc04d18	91500	1056	1.73	0.000241	0.000001	0.005747	0.000031	1.467231	0.000043	0.282314	0.000039	-16.7	1.4
11oc04d19	91500	1056	1.73	0.000239	0.000000	0.005733	0.000031	1.467252	0.000055	0.282311	0.000044	-16.8	1.6
11oc04e03	91500	1056	1.61	0.000241	0.000001	0.005731	0.000025	1.467227	0.000059	0.282309	0.000041	-16.8	1.4
11oc04e16	91500	1056	1.63	0.000240	0.000000	0.005801	0.000025	1.467231	0.000061	0.282300	0.000033	-17.2	1.2
11oc04e29	91500	1056	1.61	0.000242	0.000000	0.005721	0.000024	1.467293	0.000055	0.282301	0.000033	-17.1	1.2
11oc04e39	91500	1056	1.67	0.000239	0.000001	0.005787	0.000032	1.467180	0.000062	0.282305	0.000039	-17.0	1.4
									mean	**0.282306**	**0.000039**	**-16.9**	**1.4**
									2SD	**0.000015**			
									(Blichert-Toft, 2008)	0.282308	0.000006		

Notes:

[1] 'File name' is the lab ID of the raw data file for each individual analysis

[2] ^{207}Pb/^{206}Pb age in millions of years (this study).

[3] The ^{176}Hf/^{177}Hf values are calculated using a Lu decay constant of 1.865 x 10^{-11} (Soderlund et al. 2004)

[4] Epsilon Hf values are calculated with ^{176}Hf/^{177}Hf and ^{176}Lu/^{177}Hf (CHUR) values of 0.282785 and 0.0336, respectively (Bouvier et al. (2008)).

Supplemental File S4-3: Fiskenæsset and Nunataarsuk Pb isotope compositions

Table S4-3.1: An-contents, Pb concentration and LA-MC-ICPMS Pb isotope compositions for the Fiskenæsset anorthosite complex, south West Greenland

Sample	file name[1]	spot size (um)[2]	AVG An-number[3]	AVG Pb (ppm)[4]	$^{206}Pb/^{204}Pb$	1SD	$^{207}Pb/^{204}Pb$	1SD	$^{208}Pb/^{204}Pb$	1SD	$^{207}Pb/^{206}Pb$	1SD	$^{208}Pb/^{206}Pb$	1SD
Lower Leucogabbro														
159430a	je29b12	40	85.4	9.0	13.132	0.106	14.337	0.096	32.695	0.217	1.096	0.002	2.502	0.005
	je29b16	40	86.4	9.7	13.250	0.115	14.488	0.098	33.200	0.241	1.094	0.002	2.512	0.005
	je29b17	40	86.2	9.2	13.238	0.147	14.504	0.147	33.064	0.331	1.095	0.003	2.504	0.008
	je29b22	40	86.3	9.1	13.079	0.111	14.276	0.099	32.648	0.216	1.095	0.002	2.501	0.006
	je29b23	40	86.8	9.0	13.127	0.117	14.423	0.105	32.885	0.244	1.095	0.002	2.506	0.005
	je29b24	40	86.6	8.9	13.068	0.119	14.375	0.109	32.862	0.238	1.098	0.003	2.517	0.006
	je29b28	40	87.4	9.2	13.111	0.126	14.361	0.109	32.740	0.265	1.097	0.003	2.505	0.005
	je29b29	40	87.8	8.2	13.105	0.134	14.365	0.118	32.722	0.265	1.095	0.003	2.498	0.006
	je29b30	40	87.1	8.8	13.149	0.123	14.471	0.114	33.028	0.265	1.092	0.003	2.497	0.006
	je29b35	40	87.2	9.0	13.169	0.146	14.350	0.138	32.961	0.284	1.089	0.003	2.492	0.007
	je29b36	40	86.5	9.2	13.152	0.120	14.370	0.104	32.816	0.231	1.089	0.002	2.484	0.006
		mean	86.7	9.0	13.144		14.393		32.875		1.094		2.502	
		SD (1s)	0.7	0.4	0.058		0.070		0.174		0.003		0.009	
		%RSD (1s)	0.8%	4.2%	0.4%		0.5%		0.5%		0.3%		0.4%	
Lower Leucogabbro														
159430b	ju03c05	69	80.6	9.6	13.092	0.120	14.388	0.077	32.951	0.261	1.098	0.001	2.524	0.003
	ju03c06	69	86.5	8.2	13.058	0.122	14.406	0.079	33.022	0.263	1.100	0.001	2.526	0.003
	ju03c10	69	87.0	7.9	13.030	0.127	14.377	0.085	33.026	0.275	1.101	0.001	2.533	0.003
	ju03c11	69	86.8	8.1	13.051	0.121	14.430	0.080	33.170	0.267	1.102	0.001	2.533	0.003
	ju03c12	69	86.7	8.4	13.065	0.124	14.434	0.083	33.064	0.279	1.101	0.001	2.533	0.003
	ju03c16	69	86.6	8.5	13.087	0.122	14.412	0.079	33.248	0.265	1.099	0.001	2.536	0.003
	ju03c17	69	87.1	8.3	13.147	0.123	14.444	0.083	33.307	0.271	1.097	0.001	2.531	0.003
	ju03c22	69	87.1	8.2	13.089	0.128	14.331	0.083	32.921	0.273	1.100	0.001	2.523	0.003
	ju03c23	69	86.7	8.3	13.117	0.126	14.392	0.083	33.007	0.274	1.096	0.001	2.519	0.003
	ju03c24	69	86.4	8.2	13.097	0.119	14.343	0.079	32.942	0.263	1.096	0.001	2.525	0.003
	ju03c28	69	n/a	n/a	13.165	0.120	14.430	0.081	33.201	0.265	1.096	0.001	2.528	0.003
	ju03c29	69	n/a	n/a	13.179	0.121	14.451	0.078	33.164	0.264	1.096	0.001	2.520	0.003
		mean	86.1	8.4	13.098		14.403		33.085		1.099		2.527	
		SD (1s)	2.0	0.5	0.046		0.039		0.129		0.002		0.006	
		%RSD (1s)	2.3%	5.6%	0.4%		0.3%		0.4%		0.2%		0.2%	
Lower Leucogabbro														
159437	no15c10	99	86.4	4.3	13.107	0.082	14.364	0.068	32.658	0.165	1.101	0.002	2.505	0.004
	no15c11	99	86.6	4.1	13.071	0.084	14.300	0.071	32.638	0.169	1.103	0.002	2.505	0.004
	no15c12	99	87.4	3.2	13.130	0.077	14.419	0.065	32.880	0.155	1.101	0.002	2.508	0.003
	no15c16	99	87.9	2.7	12.951	0.076	14.312	0.066	32.590	0.148	1.104	0.001	2.512	0.003
	no15c17	99	87.2	2.2	12.813	0.077	14.112	0.068	32.227	0.152	1.102	0.002	2.511	0.003
	no15c23	99	87.1	2.3	12.811	0.094	14.060	0.088	32.074	0.210	1.099	0.002	2.503	0.004
	no15c24	99	87.1	2.8	13.042	0.086	14.302	0.070	32.593	0.166	1.098	0.002	2.501	0.004
	no15c28	99	87.2	2.3	12.984	0.077	14.313	0.071	32.442	0.145	1.098	0.002	2.509	0.004
	no15c29	99	86.8	1.8	12.946	0.124	14.165	0.111	32.349	0.273	1.094	0.002	2.498	0.004
	no15c30	99	87.3	1.8	12.976	0.100	14.302	0.091	32.389	0.202	1.102	0.002	2.497	0.004
	no15c34	99	88.1	1.8	13.059	0.090	14.425	0.079	32.786	0.175	1.106	0.002	2.517	0.005
	no15c35	99	87.0	2.1	13.094	0.076	14.450	0.070	32.899	0.154	1.101	0.002	2.506	0.004
	no15c36	99	87.2	2.6	13.085	0.074	14.459	0.067	32.882	0.151	1.101	0.002	2.511	0.003
	no15c41	99	86.6	3.3	13.004	0.076	14.328	0.055	32.646	0.145	1.102	0.002	2.513	0.003
	no15c46	99	85.9	4.4	13.010	0.070	14.326	0.060	32.714	0.140	1.103	0.001	2.518	0.003
		mean	87.0	2.8	13.006		14.309		32.584		1.101		2.508	
		SD (1s)	0.6	0.9	0.097		0.118		0.246		0.003		0.006	
		%RSD (1s)	0.6%	32.0%	0.7%		0.8%		0.8%		0.3%		0.3%	
Middle Gabbro														
159444	ju04d05	69	87.8	1.5	13.096	0.100	14.329	0.112	32.463	0.257	1.091	0.002	2.479	0.004
	ju04d06	69	88.3	1.4	13.063	0.084	14.179	0.109	32.122	0.256	1.091	0.003	2.469	0.005
	ju04d11	69	88.4	1.2	13.061	0.085	14.171	0.086	32.419	0.219	1.081	0.003	2.477	0.005
		mean	88.2	1.4	13.073		14.226		32.334		1.088		2.475	
		SD (1s)	0.3	0.1	0.020		0.089		0.186		0.006		0.006	
		%RSD (1s)	0.3%	10.1%	0.1%		0.6%		0.6%		0.5%		0.2%	
Middle Gabbro														
159448	je27a10	49	89.9	3.4	13.369	0.173	14.484	0.173	32.971	0.369	1.084	0.005	2.467	0.011
	je27a11	49	90.0	3.5	13.340	0.180	14.621	0.165	32.993	0.394	1.087	0.005	2.466	0.011
	je27a12	49	90.0	3.4	13.312	0.175	14.377	0.155	32.749	0.363	1.085	0.004	2.470	0.011
	je27a23	49	89.6	3.6	13.358	0.185	14.456	0.172	32.694	0.394	1.088	0.005	2.452	0.011

je27a24	50	90.6	4.6	14.358	1.185	15.456	1.172	33.694	1.394	2.088	1.005	3.452	1.011
je27a29	49	89.8	3.5	13.216	0.227	14.593	0.254	32.561	0.512	1.092	0.005	2.468	0.012
je27a34	49	89.5	3.1	13.262	0.179	14.333	0.167	32.358	0.366	1.080	0.005	2.447	0.012
je27a35	49	89.4	3.3	13.214	0.166	14.297	0.153	32.232	0.339	1.087	0.005	2.445	0.012
je27a42	49	89.3	3.3	13.253	0.175	14.411	0.168	32.483	0.400	1.086	0.004	2.446	0.012
	mean	89.8	3.5	13.409		14.559		32.748		1.197		2.568	
	SD (1s)	0.4	0.4	0.361		0.354		0.437		0.334		0.332	
	%RSD (1s)	0.4%	12.6%	2.7%		2.4%		1.3%		27.9%		12.9%	
Upper Leucogabbro													
124613 ju06a05	69	86.1	2.0	13.192	0.097	14.351	0.120	32.560	0.318	1.091	0.004	2.482	0.012
ju06a06	69	86.8	1.9	13.224	0.107	14.370	0.121	32.448	0.346	1.079	0.004	2.454	0.011
ju06a10	69	87.4	1.7	13.092	0.092	14.409	0.121	32.572	0.306	1.097	0.004	2.496	0.011
ju06a11	69	87.6	1.8	13.032	0.105	14.406	0.130	32.560	0.328	1.102	0.004	2.493	0.011
ju06a12	69	87.7	1.7	13.078	0.095	14.270	0.121	32.582	0.304	1.095	0.004	2.494	0.011
ju06a16	69	87.4	1.7	13.197	0.114	14.398	0.148	32.845	0.348	1.093	0.004	2.490	0.011
ju06a17	69	87.5	1.7	13.105	0.108	14.360	0.134	32.627	0.347	1.098	0.004	2.489	0.011
ju06a18	69	87.2	1.7	13.193	0.105	14.327	0.141	32.571	0.344	1.094	0.004	2.486	0.011
ju06a23	69	87.6	1.7	13.104	0.110	14.266	0.138	32.682	0.339	1.090	0.004	2.491	0.011
ju06a24	40	85.8	1.8	13.138	0.109	14.311	0.138	32.707	0.347	1.094	0.004	2.499	0.011
ju06a28	69	84.0	1.7	13.101	0.114	14.213	0.143	32.344	0.365	1.087	0.004	2.483	0.012
ju06a29	69	83.7	1.8	13.173	0.133	14.301	0.158	32.458	0.369	1.088	0.005	2.476	0.012
ju06a30	69	81.0	1.9	13.234	0.088	14.284	0.121	32.702	0.307	1.089	0.004	2.467	0.011
	mean	86.1	1.8	13.143		14.328		32.589		1.092		2.485	
	SD (1s)	2.1	0.1	0.063		0.061		0.130		0.006		0.013	
	%RSD (1s)	2.4%	6.0%	0.5%		0.4%		0.4%		0.5%		0.5%	
Upper Leucogabbro													
124665 no10a17	99	87.2	0.88	12.939	0.099	14.070	0.108	31.979	0.250	1.087	0.003	2.481	0.004
no10a18	99	87.8	0.84	13.429	0.096	14.639	0.107	33.327	0.255	1.090	0.004	2.480	0.005
no10a22	99	88.1	0.81	13.095	0.110	14.172	0.122	32.665	0.301	1.085	0.004	2.481	0.005
no10a23	99	88.0	0.84	13.175	0.123	14.319	0.132	32.714	0.301	1.090	0.004	2.492	0.006
no10a24	99	87.6	0.86	13.127	0.101	14.369	0.113	32.556	0.247	1.092	0.003	2.476	0.005
no10a29	99	88.2	0.86	13.413	0.090	14.661	0.105	33.385	0.235	1.095	0.004	2.489	0.005
no10a30	99	88.2	0.94	13.130	0.098	14.271	0.108	32.508	0.248	1.085	0.003	2.477	0.005
no10b06	99	88.2	0.94	13.049	0.128	14.218	0.141	32.287	0.333	1.085	0.003	2.485	0.005
no10b11	99	88.2	0.78	13.177	0.141	14.491	0.148	32.765	0.339	1.096	0.003	2.492	0.006
no10b12	99	88.7	0.79	13.168	0.122	14.319	0.131	32.612	0.334	1.093	0.003	2.479	0.006
no10b16	99	88.6	0.76	13.283	0.135	14.438	0.154	32.909	0.367	1.084	0.002	2.471	0.005
no10b17	99	88.7	0.89	13.391	0.191	14.530	0.175	32.952	0.418	1.092	0.003	2.472	0.006
	mean	88.1	0.9	13.198		14.375		32.722		1.089		2.481	
	SD (1s)	0.5	0.1	0.152		0.183		0.396		0.004		0.007	
	%RSD (1s)	0.5%	6.8%	1.2%		1.3%		1.2%		0.4%		0.3%	
Upper Leucogabbro													
125765 ju06d05	69	85.1	3.4	13.172	0.132	14.439	0.145	32.817	0.318	1.094	0.003	2.497	0.004
ju06d06	69	85.1	3.6	13.098	0.114	14.333	0.120	32.724	0.255	1.094	0.002	2.492	0.005
ju06d10	69	85.4	3.5	13.095	0.099	14.319	0.106	32.811	0.225	1.089	0.002	2.494	0.004
ju06d11	69	84.4	3.5	13.106	0.113	14.307	0.120	32.617	0.271	1.093	0.002	2.484	0.004
ju06d12	69	85.2	3.4	13.322	0.113	14.560	0.122	33.108	0.262	1.094	0.003	2.484	0.005
ju06d16	69	86.1	3.3	13.209	0.096	14.383	0.101	32.936	0.228	1.089	0.002	2.497	0.004
ju06d17	69	85.7	3.3	13.141	0.099	14.397	0.107	32.692	0.226	1.096	0.002	2.499	0.005
ju06d24	69	85.2	3.4	13.290	0.111	14.456	0.116	32.830	0.245	1.090	0.002	2.486	0.004
	mean	85.3	3.4	13.179		14.399		32.817		1.092		2.492	
	SD (1s)	0.5	0.1	0.088		0.085		0.153		0.003		0.006	
	%RSD (1s)	0.6%	3.1%	0.7%		0.6%		0.5%		0.2%		0.3%	
Upper Leucogabbro													
125767 ju19b06	99	87.2	2.3	13.233	0.125	14.452	0.134	33.018	0.307	1.094	0.003	2.495	0.007
ju19b10	99	87.5	2.4	12.827	0.106	14.047	0.112	32.175	0.270	1.095	0.003	2.509	0.006
ju19b11	99	87.8	3.1	13.137	0.098	14.439	0.109	32.979	0.255	1.092	0.003	2.505	0.006
ju19b12	109	87.4	3.8	13.118	0.088	14.303	0.099	32.610	0.225	1.095	0.003	2.506	0.005
ju19b16	109	87.5	3.8	13.161	0.090	14.362	0.101	32.949	0.239	1.095	0.003	2.500	0.005
ju19b17	109	87.6	3.9	13.111	0.105	14.338	0.118	32.980	0.280	1.093	0.003	2.504	0.005
ju19b18	109	87.3	3.7	13.132	0.085	14.395	0.096	32.773	0.217	1.093	0.003	2.498	0.005
ju19b23	109	87.0	4.4	13.043	0.124	14.286	0.129	32.641	0.325	1.099	0.003	2.505	0.007
ju19b24	109	87.7	4.4	13.006	0.076	14.244	0.084	32.567	0.196	1.095	0.002	2.512	0.004
ju19b28	109	87.0	4.7	12.949	0.106	14.055	0.113	32.370	0.258	1.097	0.003	2.501	0.007
ju19b29	109	87.2	4.7	12.977	0.083	14.238	0.091	32.638	0.213	1.098	0.003	2.516	0.005
ju19b30	109	87.2	4.8	13.024	0.079	14.266	0.088	32.853	0.206	1.096	0.002	2.511	0.004
ju19b34	109	87.1	5.3	13.223	0.080	14.456	0.088	33.055	0.205	1.094	0.002	2.504	0.005
ju19b35	109	86.6	5.1	13.044	0.079	14.272	0.087	32.724	0.204	1.092	0.002	2.512	0.004
ju19b36	109	86.6	5.1	13.210	0.077	14.453	0.086	33.028	0.203	1.092	0.002	2.503	0.004

ju19b40	109	87.2	5.2	13.121	0.078	14.426	0.087	32.950	0.204	1.094	0.002	2.506	0.004
ju19b41	109	86.6	5.2	13.182	0.086	14.482	0.093	33.019	0.215	1.096	0.003	2.501	0.005
ju19b46	109	86.3	5.1	13.090	0.080	14.342	0.088	32.798	0.204	1.096	0.002	2.511	0.005
ju19b47	109	86.7	4.8	13.079	0.077	14.389	0.087	32.806	0.201	1.097	0.002	2.515	0.005
ju19b52	109	87.0	4.9	13.161	0.077	14.402	0.085	33.063	0.200	1.092	0.003	2.509	0.005
ju19b53	109	87.8	4.9	13.091	0.084	14.367	0.091	32.905	0.209	1.095	0.002	2.517	0.005
ju19b54	109	n/a	n/a	13.116	0.083	14.428	0.090	33.013	0.215	1.101	0.002	2.528	0.005
	mean	87.2	4.4	13.092		14.338		32.814		1.095		2.508	
	SD (1s)	0.4	0.9	0.096		0.119		0.236		0.002		0.007	
	%RSD (1s)	0.5%	20.3%	0.7%		0.8%		0.7%		0.2%		0.3%	
Upper Leucogabbro													
125469 no15b10	69	87.3	5.9	13.201	0.091	14.445	0.086	32.934	0.190	1.095	0.002	2.497	0.004
no15b11	69	87.3	5.9	12.890	0.079	14.101	0.073	32.222	0.154	1.099	0.002	2.506	0.004
no15b12	69	87.9	6.1	12.886	0.085	14.090	0.077	32.088	0.172	1.097	0.002	2.497	0.004
no15b16	69	87.1	6.2	13.153	0.094	14.402	0.096	32.789	0.214	1.098	0.002	2.501	0.004
no15b17	69	87.6	5.8	13.081	0.076	14.331	0.065	32.709	0.159	1.095	0.002	2.500	0.004
no15b18	69	87.6	6.0	13.103	0.080	14.359	0.074	32.671	0.161	1.098	0.002	2.504	0.004
no15b23	69	86.4	6.3	13.063	0.080	14.340	0.073	32.594	0.161	1.101	0.002	2.501	0.004
no15b24	69	86.6	6.3	12.944	0.086	14.239	0.082	32.333	0.182	1.099	0.002	2.502	0.004
no15b28	69	87.2	6.1	13.098	0.076	14.379	0.069	32.743	0.156	1.098	0.002	2.503	0.004
no15b29	69	88.1	6.0	13.076	0.083	14.314	0.071	32.661	0.163	1.095	0.002	2.495	0.004
no15b30	69	86.5	6.4	13.148	0.074	14.457	0.063	32.719	0.155	1.096	0.002	2.500	0.004
no15b34	69	86.2	6.5	13.113	0.075	14.354	0.064	32.719	0.148	1.100	0.002	2.505	0.004
no15b35	69	85.1	6.6	13.146	0.077	14.386	0.068	32.813	0.156	1.099	0.002	2.500	0.004
no15b36	69	80.1	6.8	13.150	0.085	14.424	0.077	32.805	0.174	1.097	0.002	2.498	0.004
	mean	86.5	6.2	13.075		14.330		32.629		1.098		2.501	
	SD (1s)	2.0	0.3	0.099		0.114		0.243		0.002		0.003	
	%RSD (1s)	2.3%	4.8%	0.8%		0.8%		0.7%		0.2%		0.1%	
Upper Leucogabbro													
159394 ju18a22	59	85.9	8.6	13.213	0.126	14.413	0.133	32.896	0.310	1.086	0.004	2.483	0.006
ju18a23	59	85.9	8.1	13.264	0.126	14.499	0.131	33.094	0.301	1.094	0.003	2.494	0.006
ju18a24	59	86.3	8.5	13.282	0.104	14.443	0.115	32.984	0.256	1.090	0.002	2.487	0.005
ju18a28	59	85.9	8.7	13.321	0.113	14.496	0.128	33.271	0.285	1.094	0.003	2.499	0.005
ju18a29	59	86.0	8.8	13.354	0.104	14.475	0.118	33.233	0.263	1.087	0.002	2.493	0.005
ju18a34	49	86.1	8.3	13.194	0.117	14.484	0.131	32.687	0.288	1.090	0.003	2.485	0.005
ju18a35	59	84.9	8.5	13.273	0.111	14.521	0.121	32.996	0.271	1.092	0.002	2.492	0.005
ju18a36	59	86.2	8.7	13.236	0.106	14.532	0.117	33.107	0.265	1.094	0.002	2.503	0.005
ju18a40	59	85.1	9.5	13.093	0.117	14.190	0.128	32.506	0.284	1.085	0.003	2.484	0.005
ju18a41	59	n/a	9.3	13.102	0.131	14.329	0.151	32.674	0.339	1.094	0.004	2.503	0.007
ju18a46	59	n/a	9.2	13.224	0.109	14.436	0.120	32.771	0.270	1.088	0.003	2.481	0.005
ju18a47	59	83.0	8.8	13.211	0.104	14.442	0.115	32.882	0.257	1.091	0.002	2.491	0.005
ju18a48	59	85.2	8.8	13.259	0.117	14.477	0.126	33.142	0.290	1.088	0.003	2.494	0.006
ju18a52	59	84.8	8.7	13.275	0.108	14.563	0.120	33.153	0.264	1.097	0.003	2.503	0.005
ju18a53	59	84.8	8.8	13.144	0.105	14.373	0.119	32.763	0.262	1.092	0.003	2.494	0.005
ju18a58	59	84.7	8.1	13.268	0.110	14.518	0.121	32.901	0.271	1.095	0.002	2.496	0.005
ju18a59	59	85.3	9.3	13.371	0.108	14.666	0.120	33.208	0.268	1.090	0.003	2.483	0.005
ju18a60	59	82.0	9.2	13.371	0.129	14.518	0.145	33.158	0.327	1.088	0.003	2.481	0.006
ju18a64	59	n/a	9.5	13.172	0.111	14.382	0.124	32.641	0.280	1.095	0.003	2.481	0.005
ju18a65	59	n/a	8.6	13.142	0.140	14.450	0.163	33.024	0.369	1.089	0.004	2.500	0.007
	mean	85.1	8.8	13.238		14.460		32.955		1.091		2.491	
	SD (1s)	1.2	0.4	0.082		0.097		0.222		0.003		0.008	
	%RSD (1s)	1.4%	4.8%	0.6%		0.7%		0.7%		0.3%		0.3%	
Upper Leucogabbro													
159452 ju06c05	69			13.306	0.126	14.452	0.107	32.710	0.245	1.083	0.002	2.456	0.004
ju06c06	69	82.9	3.4	13.373	0.120	14.557	0.102	32.801	0.234	1.088	0.002	2.460	0.003
ju06c10	69	83.7	3.3	13.322	0.129	14.425	0.108	32.635	0.244	1.083	0.002	2.452	0.003
ju06c11	69	86.9	3.3	13.465	0.132	14.656	0.115	33.139	0.257	1.085	0.002	2.462	0.003
ju06c12	69	86.9	3.1	13.452	0.135	14.562	0.120	32.834	0.264	1.085	0.002	2.455	0.003
ju06c16	69	86.9	3.1	13.185	0.130	14.382	0.115	32.345	0.250	1.088	0.002	2.463	0.004
ju06c17	69	83.0	3.3	13.198	0.126	14.295	0.106	32.482	0.247	1.083	0.002	2.463	0.004
ju06c18	69			13.361	0.130	14.463	0.111	32.743	0.252	1.083	0.002	2.455	0.004
ju06c23	69			13.273	0.125	14.318	0.102	32.429	0.241	1.076	0.002	2.436	0.005
ju06c24	69			13.394	0.134	14.475	0.130	32.721	0.289	1.086	0.002	2.455	0.005
	mean	85.0	3.2	13.333		14.458		32.684		1.084		2.456	
	SD (1s)	2.1	0.1	0.096		0.112		0.229		0.003		0.008	
	%RSD (1s)	2.4%	3.3%	0.7%		0.8%		0.7%		0.3%		0.3%	
Anorthosite													
124652 ju03b05	69	84.6	3.7	12.917	0.103	14.220	0.087	32.445	0.237	1.099	0.001	2.514	0.003
ju03b06	69	85.2	3.5	12.942	0.111	14.262	0.094	32.552	0.256	1.098	0.001	2.515	0.003

ju03b10	69	84.8	3.5	12.920	0.130	14.217	0.111	32.488	0.282	1.098	0.001	2.516	0.003
ju03b11	69	80.9	3.7	12.856	0.109	14.155	0.092	32.292	0.250	1.101	0.001	2.518	0.003
ju03b12	69	81.2	3.4	12.913	0.113	14.262	0.088	32.543	0.247	1.101	0.002	2.523	0.004
ju03b16	69	81.3	4.0	12.915	0.119	14.222	0.094	32.507	0.260	1.100	0.001	2.519	0.003
ju03b23	69	82.1	3.5	12.894	0.107	14.209	0.095	32.765	0.246	1.097	0.001	2.531	0.003
ju03b24	69	86.4	3.6	12.894	0.102	14.206	0.084	32.758	0.233	1.098	0.001	2.522	0.003
ju03b28	69	87.3	3.6	12.910	0.102	14.238	0.094	32.642	0.237	1.097	0.002	2.526	0.003
ju03b29	69	87.1	3.5	12.909	0.123	14.225	0.103	32.610	0.270	1.098	0.001	2.520	0.003
ju03b34	69	86.8	3.2	12.975	0.116	14.287	0.100	32.777	0.261	1.101	0.001	2.529	0.003
ju03b35	69	86.0	3.6	12.955	0.135	14.230	0.110	32.697	0.291	1.100	0.002	2.523	0.004
ju03b36	69			13.039	0.108	14.347	0.091	32.872	0.244	1.101	0.001	2.523	0.003
ju03b41	69			12.949	0.112	14.244	0.095	32.654	0.253	1.101	0.001	2.521	0.003
ju03b42	69	85.9	3.3	13.010	0.097	14.375	0.083	33.024	0.226	1.102	0.001	2.532	0.003
	mean	84.6	3.6	12.933		14.247		32.642		1.100		2.522	
	SD (1s)	2.4	0.2	0.047		0.055		0.183		0.002		0.005	
	%RSD (1s)	2.8%	5.3%	0.4%		0.4%		0.6%		0.2%		0.2%	
Anorthosite													
125760 jc28a10	40	85.4	8.7	12.810	0.111	14.132	0.105	32.202	0.270	1.103	0.004	2.513	0.009
jc28a12	40	86.1	8.7	12.844	0.111	14.208	0.120	32.326	0.294	1.098	0.004	2.502	0.009
jc28a16	40	84.8	9.0	13.238	0.120	14.529	0.124	33.168	0.297	1.097	0.005	2.503	0.009
jc28a17	40	84.7	6.4	13.250	0.141	14.384	0.122	33.097	0.308	1.087	0.004	2.498	0.008
jc28a18	40	83.9	7.3	13.146	0.127	14.527	0.122	32.916	0.305	1.103	0.005	2.513	0.010
jc28a28	40	82.1	8.6	13.121	0.133	14.408	0.125	32.924	0.306	1.099	0.004	2.505	0.009
jc28a29	40	84.3	7.6	13.072	0.126	14.277	0.132	32.693	0.331	1.095	0.005	2.508	0.009
jc28a34	40	83.2	7.8	12.904	0.123	14.373	0.122	32.669	0.288	1.103	0.004	2.518	0.009
jc28a35	40	82.6	8.4	12.935	0.130	14.307	0.127	32.479	0.321	1.094	0.004	2.504	0.009
	mean	84.1	8.1	13.035		14.350		32.719		1.098		2.507	
	SD (1s)	1.3	0.9	0.167		0.134		0.337		0.005		0.007	
	%RSD (1s)	1.6%	10.6%	1.3%		0.9%		1.0%		0.5%		0.3%	
Anorthosite													
125763 no11a10	69	83.6	4.8	13.173	0.091	14.450	0.080	33.031	0.214	1.099	0.002	2.509	0.005
no11a11	69	86.1	4.6	13.189	0.081	14.496	0.073	33.169	0.195	1.101	0.002	2.514	0.005
no11a12	69	86.4	4.4	13.133	0.085	14.406	0.077	32.965	0.207	1.099	0.002	2.515	0.005
no11a16	69	86.4	4.4	13.024	0.085	14.303	0.075	32.825	0.206	1.096	0.002	2.516	0.005
no11a17	69	86.8	4.3	13.118	0.086	14.409	0.077	33.042	0.208	1.101	0.002	2.517	0.005
no11a18	69	86.1	4.2	13.101	0.087	14.341	0.080	32.880	0.217	1.097	0.002	2.515	0.005
no11a23	69	87.1	4.3	13.045	0.089	14.369	0.077	32.790	0.219	1.104	0.002	2.519	0.005
no11a24	69	86.9	4.1	13.133	0.088	14.407	0.078	32.946	0.207	1.100	0.002	2.524	0.005
no11a28	69	86.9	4.5	12.962	0.100	14.265	0.095	32.378	0.239	1.101	0.003	2.511	0.007
no11a29	69	86.7	4.3	12.866	0.091	14.126	0.083	32.424	0.213	1.099	0.002	2.520	0.005
no11a30	69	86.4	4.5	12.893	0.084	14.163	0.081	32.415	0.206	1.099	0.002	2.515	0.005
no11a34	69	86.2	4.5	13.024	0.083	14.290	0.074	32.694	0.200	1.103	0.002	2.523	0.005
no11a35	69	86.4	4.7	12.961	0.088	14.238	0.079	32.575	0.212	1.100	0.002	2.518	0.005
no11a36	69	86.0	5.1	13.030	0.088	14.309	0.086	32.752	0.208	1.098	0.002	2.514	0.005
no11a41	69	86.5	4.9	13.070	0.091	14.364	0.086	32.777	0.220	1.100	0.002	2.506	0.005
no11a42	69	85.6	4.9	13.177	0.091	14.432	0.083	32.969	0.219	1.098	0.002	2.510	0.005
no11a46	69	84.3	5.0	13.136	0.092	14.447	0.085	32.967	0.213	1.097	0.002	2.512	0.005
no11a47	69	n/a	n/a	13.073	0.085	14.383	0.077	32.800	0.201	1.103	0.002	2.520	0.005
	mean	86.1	4.6	13.062		14.344		32.800		1.100		2.516	
	SD (1s)	0.9	0.3	0.095		0.100		0.229		0.002		0.005	
	%RSD (1s)	1.1%	6.5%	0.7%		0.7%		0.7%		0.2%		0.2%	
Anorthosite													
159455 ju06b06	69	79.3	9.4	13.181	0.084	14.382	0.095	33.016	0.303	1.093	0.003	2.510	0.003
ju06b10	69	81.1	8.8	13.177	0.089	14.484	0.101	33.044	0.311	1.096	0.003	2.512	0.004
ju06b11	69	80.2	8.6	13.036	0.085	14.384	0.100	32.861	0.309	1.099	0.004	2.515	0.004
ju06b12	69	81.4	8.5	13.158	0.085	14.462	0.097	33.043	0.306	1.099	0.004	2.513	0.003
ju06b16	69	80.3	n/a	13.064	0.087	14.362	0.099	32.853	0.310	1.100	0.004	2.516	0.004
ju06b17	69	79.0	8.7	13.118	0.085	14.419	0.098	32.920	0.309	1.099	0.004	2.511	0.004
ju06b18	69	82.4	8.3	13.119	0.088	14.452	0.098	32.969	0.310	1.101	0.003	2.512	0.004
ju06b23	69	85.0	8.2	13.092	0.085	14.413	0.098	32.932	0.306	1.102	0.004	2.515	0.004
ju06b24	69	85.9	7.7	13.086	0.086	14.372	0.100	32.871	0.306	1.100	0.004	2.511	0.004
ju06b28	69	86.3	8.3	13.001	0.086	14.273	0.099	32.555	0.306	1.102	0.003	2.515	0.004
ju06b29	69	85.6	8.2	12.982	0.086	14.341	0.097	32.617	0.308	1.103	0.004	2.516	0.003
ju06b30	69	86.1	8.5	13.003	0.087	14.308	0.099	32.563	0.309	1.103	0.004	2.510	0.003
ju06b34	69	86.0	8.1	13.115	0.085	14.418	0.097	32.942	0.307	1.098	0.004	2.513	0.004
ju06b35	69	85.8	8.1	13.071	0.084	14.397	0.096	32.846	0.304	1.100	0.004	2.515	0.004
ju06b40	69	85.7	8.5	13.198	0.090	14.492	0.100	33.123	0.314	1.099	0.003	2.510	0.003
ju06b41	69	85.6	8.5	13.186	0.085	14.526	0.098	33.150	0.305	1.100	0.003	2.513	0.003
ju06b42	69	83.9	8.5	13.167	0.085	14.465	0.097	33.114	0.307	1.099	0.004	2.513	0.003
ju06b47	69	84.6	8.3	13.137	0.086	14.428	0.099	32.949	0.309	1.098	0.004	2.513	0.004
	mean	83.6	8.4	13.105		14.410		32.909		1.099		2.513	

SD (1s)	2.6	0.4	0.068	0.066	0.179	0.002	0.002
%RSD (1s)	3.2%	4.3%	0.5%	0.5%	0.5%	0.2%	0.1%

Notes:

[1] 'filename' is the name underwith each MC-LA-ICPMS Pb isotope analysis is saved

[2] laser spot size for MC-LA-ICPMS Pb isotope analysis

[3] determined by EPMA, method details given in Electronic Annex EA-1

[4] determined by LA-ICPMS, full method details given in Electronic Annex EA-1

Table S4-3.2: An-contents, Pb concentration and LA-MC-ICPMS Pb isotope compositions for the Nunataarsuk anorthosite complex, south West Greenland

Sample	file name[1]	spot size (um)[2]	AVG An-number[3]	AVG Pb (ppm)[3]	$^{206}Pb/^{204}Pb$	1SD	$^{207}Pb/^{204}Pb$	1SD	$^{208}Pb/^{204}Pb$	1SD	$^{207}Pb/^{206}Pb$	1SD	$^{208}Pb/^{206}Pb$	1SD
Lower Leucogabbro-anorthosite														
N03-06	ju25b18	99	78.7	3.9	12.876	0.108	14.019	0.106	32.618	0.254	1.094	0.002	2.550	0.005
	ju25b23	99	81.3	3.7	12.900	0.110	14.118	0.106	32.662	0.258	1.101	0.003	2.548	0.005
	ju25b24	99	81.3	3.9	12.803	0.112	14.083	0.115	32.657	0.270	1.097	0.002	2.545	0.005
	ju25b28	99	81.6	3.8	12.869	0.106	14.232	0.107	32.911	0.256	1.103	0.002	2.555	0.005
	ju25b29	99	79.9	4.0	12.832	0.105	14.077	0.104	32.610	0.249	1.097	0.002	2.544	0.005
	ju25b30	99	72.7	4.0	12.807	0.104	14.051	0.103	32.703	0.248	1.100	0.002	2.553	0.005
	ju25b42	99	75.3	4.0	12.808	0.105	13.999	0.105	32.642	0.251	1.092	0.002	2.543	0.005
	ju25b46	99	75.7	3.9	12.772	0.105	14.093	0.105	32.479	0.251	1.099	0.002	2.545	0.005
	ju25b47	99	77.6	4.2	12.847	0.107	14.134	0.104	32.732	0.252	1.099	0.002	2.547	0.005
	ju25b48	99	78.0	4.1	12.720	0.105	13.957	0.104	32.245	0.252	1.098	0.002	2.546	0.005
	ju25b52	99	76.7	4.2	12.912	0.106	14.040	0.105	32.541	0.252	1.087	0.002	2.522	0.005
	ju25b53	99	77.1	4.2	12.908	0.109	14.189	0.105	32.767	0.258	1.096	0.002	2.533	0.005
		mean	78.0	4.0	12.838		14.083		32.631		1.097		2.544	
		SD (1s)	2.7	0.2	0.059		0.078		0.164		0.004		0.009	
		%RSD (1s)	3.5%	4.0%	0.5%		0.6%		0.5%		0.4%		0.4%	
N03-10	ju19a24	99	n/a	n/a	12.844	0.116	14.136	0.105	32.932	0.274	1.094	0.002	2.554	0.005
	ju19a29	99	n/a	n/a	12.567	0.112	13.798	0.101	31.926	0.262	1.094	0.002	2.543	0.005
	ju19a35	99	n/a	n/a	12.709	0.124	13.872	0.117	32.331	0.298	1.089	0.003	2.543	0.006
	ju19a36	99	n/a	n/a	12.780	0.117	14.032	0.107	32.700	0.286	1.099	0.002	2.551	0.005
	ju19a42	99	n/a	n/a	12.786	0.112	14.125	0.101	32.651	0.265	1.095	0.002	2.550	0.005
	ju19a46	99	n/a	n/a	12.739	0.126	14.037	0.114	32.566	0.294	1.103	0.003	2.553	0.006
	ju19a48	99	n/a	n/a	12.736	0.115	13.946	0.106	32.449	0.277	1.096	0.002	2.541	0.006
	ju19a52	99	n/a	n/a	12.762	0.120	13.965	0.106	32.394	0.285	1.088	0.003	2.533	0.007
	ju19a59	99	78.6	2.4	12.725	0.116	13.945	0.106	32.418	0.276	1.092	0.002	2.536	0.006
	ju19a60	99	78.0	2.4	12.676	0.112	13.934	0.100	32.344	0.266	1.091	0.002	2.535	0.006
	ju19a64	99	76.5	2.5	12.570	0.111	13.736	0.100	32.070	0.267	1.097	0.002	2.555	0.005
	ju19a65	99	73.9	2.5	12.590	0.121	13.821	0.113	32.107	0.287	1.098	0.003	2.558	0.006
	ju19a66	99	75.9	2.7	12.604	0.115	13.812	0.101	32.172	0.267	1.102	0.002	2.560	0.006
		mean	76.6	2.5	12.699		13.935		32.389		1.095		2.547	
		SD (1s)	1.9	0.1	0.090		0.125		0.281		0.005		0.009	
		%RSD (1s)	2.4%	5.0%	0.7%		0.9%		0.9%		0.4%		0.4%	
N03-83c	jl11a011	99	n/a	n/a	12.447	0.121	13.845	0.110	32.493	0.230	1.113	0.004	2.612	0.005
	jl11a012	99	87.6	2.3	12.497	0.127	13.853	0.119	32.553	0.253	1.107	0.005	2.589	0.005
	jl11a017	99	88.0	2.3	12.470	0.125	13.956	0.119	32.457	0.251	1.115	0.004	2.595	0.005
	jl11a018	99	89.0	2.4	12.457	0.123	13.817	0.114	32.151	0.241	1.115	0.004	2.586	0.005
	jl11a022	99	88.4	2.4	12.556	0.127	14.093	0.119	32.419	0.254	1.123	0.005	2.584	0.005
	jl11a023	99	88.1	2.3	12.554	0.124	14.021	0.116	32.425	0.243	1.120	0.004	2.585	0.005
	jl11a024	99	84.3	3.3	12.408	0.122	13.948	0.112	32.301	0.235	1.125	0.004	2.602	0.005
	jl11a029	99	n/a	3.3	12.373	0.120	13.768	0.110	32.215	0.228	1.113	0.004	2.604	0.005
	jl11a030	99	89.2	2.4	12.438	0.123	13.885	0.114	32.151	0.239	1.112	0.004	2.586	0.005
	jl11a034	99	89.1	2.3	12.507	0.131	13.837	0.127	32.317	0.269	1.110	0.005	2.579	0.006
		mean	88.0	2.5	12.471		13.902		32.348		1.115		2.592	
		SD (1s)	1.6	0.4	0.059		0.101		0.143		0.006		0.010	
		%RSD (1s)	1.8%	17.0%	0.5%		0.7%		0.4%		0.5%		0.4%	
Upper Leucogabbro-anorthosite														
N03-09A	ju20a06	109	83.5	1.8	12.656	0.113	14.074	0.114	32.434	0.292	1.109	0.002	2.560	0.005
	ju20a10	109	83.5	1.5	12.608	0.118	14.025	0.114	32.298	0.288	1.107	0.002	2.562	0.005
	ju20a11	109	83.6	1.3	12.597	0.130	14.032	0.129	32.292	0.316	1.113	0.003	2.568	0.006
	ju20a18	109	82.4	1.3	12.554	0.123	13.843	0.121	32.215	0.307	1.103	0.003	2.560	0.006
	ju20a24	109	83.0	1.3	12.246	0.133	13.635	0.137	31.543	0.339	1.112	0.003	2.575	0.006
	ju20a28	109	82.9	1.4	12.429	0.141	13.903	0.141	32.053	0.353	1.119	0.004	2.589	0.007
	ju20a29	109	82.1	1.4	12.393	0.131	13.761	0.132	31.748	0.323	1.111	0.003	2.565	0.006
	ju20a30	109	82.3	1.4	12.623	0.141	14.076	0.151	32.608	0.365	1.104	0.004	2.568	0.006
	ju20a35	109	81.8	1.3	12.406	0.134	13.746	0.131	31.825	0.342	1.105	0.003	2.568	0.007
	ju20a36	109	n/a	n/a	12.534	0.162	13.938	0.171	32.015	0.414	1.109	0.004	2.560	0.008
	ju20a41	109	n/a	n/a	12.364	0.134	13.726	0.133	31.854	0.341	1.112	0.003	2.566	0.006
	ju20a42	109	n/a	n/a	12.411	0.118	13.814	0.119	32.050	0.301	1.110	0.003	2.575	0.006
		mean	82.8	1.4	12.485		13.881		32.078		1.110		2.568	
		SD (1s)	0.7	0.2	0.127		0.150		0.307		0.004		0.009	

		%RSD (1s)	0.8%	11.7%	1.0%		1.1%		1.0%		0.4%		0.3%	
N03-72	ju25a06	69	79.3	6.9	12.806	0.120	14.041	0.097	32.602	0.264	1.096	0.002	2.547	0.004
	ju25a10	69	81.5	6.4	12.859	0.125	14.137	0.107	32.754	0.282	1.102	0.002	2.545	0.004
	ju25a11	69	79.9	6.8	12.773	0.120	14.044	0.098	32.539	0.266	1.100	0.002	2.545	0.004
	ju25a12	69	82.2	6.5	12.736	0.121	13.977	0.097	32.509	0.267	1.102	0.002	2.550	0.004
	ju25a16	69	83.3	6.6	12.801	0.121	14.040	0.100	32.626	0.271	1.098	0.002	2.547	0.004
	ju25a17	69	81.7	6.8	12.754	0.124	14.077	0.103	32.555	0.276	1.102	0.002	2.556	0.004
	ju25a18	69	77.9	6.6	12.861	0.121	14.033	0.099	32.580	0.269	1.094	0.002	2.538	0.004
	ju25a30	69	76.2	6.6	12.697	0.129	13.984	0.108	32.366	0.288	1.102	0.003	2.547	0.006
	ju25a42	69	76.2	7.2	12.754	0.125	14.095	0.105	32.583	0.282	1.097	0.002	2.546	0.005
	ju25a46	69	76.1	n/a	12.779	0.123	14.100	0.104	32.484	0.277	1.102	0.002	2.541	0.004
	ju25a47	69	74.7	7.1	12.749	0.123	14.048	0.102	32.394	0.273	1.103	0.002	2.545	0.004
		mean	79.0	6.7	12.779		14.052		32.545		1.100		2.546	
		SD (1s)	3.0	0.3	0.050		0.048		0.108		0.003		0.005	
		%RSD (1s)	3.7%	3.8%	0.4%		0.3%		0.3%		0.3%		0.2%	
N03-81A	ju22a18	99	83.3	2.0	12.786	0.090	13.992	0.098	32.435	0.218	1.084	0.003	2.514	0.005
	ju22a28	99	85.2	2.1	12.729	0.086	13.864	0.093	31.926	0.204	1.092	0.002	2.523	0.005
	ju22a35	99	89.4	1.9	12.693	0.096	13.853	0.104	31.677	0.225	1.093	0.003	2.497	0.005
		mean	86.0	2.0	12.736		13.903		32.013		1.090		2.511	
		SD (1s)	3.1	0.1	0.047		0.078		0.386		0.005		0.013	
		%RSD (1s)	3.6%	5.5%	0.4%		0.6%		1.2%		0.4%		0.5%	

Notes:

[1] 'filename' is the name underwith each MC-LA-ICPMS Pb isotope analysis is saved

[2] laser spot size for MC-LA-ICPMS Pb isotope analysis

[3] determined by EPMA, method details given in Electronic Annex EA-1

[4] determined by LA-ICPMS, full method details given in Electronic Annex EA-1

Chapter 5: Summary

The Earth is differentiated into a mantle and crust but the timing and mechanism of these differentiation events is uncertain. Some researchers have argued for massive to moderate amounts of continental crust formation in the Archean while others have argued for large amounts of early mafic crust that was quickly recycled back into the deep mantle. The long-lived incompatible element depletion of the upper mantle provides some of the best evidence for the early crust because rocks older than ~3 Ga are rare in the present-day crust. A major limiting factor for studies of ancient crust-mantle differentiation is the pervasive metamorphism and secondary alteration affecting almost all Archean rock samples preserved today at the surface of the Earth. The significance of whole rock analyses of Archean rocks for trace elements and radiogenic isotopes is unclear, and debate over whether magmatic compositions are preserved by whole rocks is ongoing.

Advances in analytical equipment over the past 10 to 15 years, particularly LA-ICPMS and SIMS, have allowed earth scientists to take an alternative approach to geochemistry. Instead of analyzing bulk samples, scientists can utilize in-situ methods and target magmatic domains preserved in individual minerals, identified traditionally using a polarizing optical microscope and further characterized with BSE and CL imaging by scanning electron microscopy. It is expected these magmatic domains preserve initial parent-daughter isotope ratios, which provide information about magma sources.

It is recognized that tholeiites are the major product of mantle-derived magmatism

in the Archean. Unfortunately, the fine-grained minerals in these rocks are typically affected pervasively by secondary alteration and metamorphic reaction. In principle, magmatic minerals, or domains therein, may be preserved in Archean tholeiites and could be targeted for in-situ analysis. In practice, however, the small crystal size and extent of secondary processing makes this task difficult. A more attractive approach for in situ analysis is to use coarse-grained plutonic rocks with igneous domains that are more likely to be preserved and more easily identified within the larger crystals present.

Anorthosites are a distinct rock type of the Archean with characteristic plagioclase megacrysts that have long been interpreted as preserved igneous minerals. It has also become obvious that Archean anorthosites contain zircon, which can be used to establish robust crystallization ages for anorthosite complexes through U-Pb geochronology. The zircon also can provide insights into the nature of the source of anorthosite magmas using Lu-Hf isotopes. In-situ methods to determine the Hf isotope composition of zircons have expanded during the recent past due to development of LA-MC-ICPMS methods, which enable targeting of specific domains within a zircon crystal to focus on the characterization of a specific source. Hf isotopes in zircon are ideal tracers of mantle evolution and the timing of crust formation because of their low Lu/Hf (parent/daughter) ratio, requiring minimal correction for radiogenic in-growth, and the demonstrated ability of zircon to preserve initial isotope compositions through metamorphism and secondary alteration.

Although the Hf composition of zircon is a powerful isotopic tracer, a limitation of the Hf-zircon method is the inability to constrain both the $^{176}Lu/^{177}Hf$, characteristic of

the mantle and/or crustal sources, and the Hf depleted mantle model age (T_{DM}) of the host rocks of the zircon uniquely: one must be assumed to calculate the other. One approach used to constrain $^{176}Lu/^{177}Hf$ and T_{DM} is to link Hf isotope compositions and O-isotope compositions measured from the same zircon crystal. T_{DM} for zircon grains with "mantle-like" O-isotope compositions are calculated using $^{176}Lu/^{177}Hf$ ratios typical of mantle-derived mafic rocks or primitive granitoids, whereas zircon grains with "elevated" O-isotope ratios are modeled assuming the involvement of sedimentary sources, providing hybrid T_{DM} ages. In our approach, we use the timing of source extraction, T_{DM} for mantle-derived rocks such as Archean anorthosites, determined from the in-situ Pb isotope measurements of igneous plagioclase that crystallized from the same magmatic rock as zircon. The value for the T_{DM} is then used to constrain the $^{176}Lu/^{177}Hf$ of the zircon grains analyzed for Hf-isotopes and U-Pb age. The $^{176}Lu/^{177}Hf$ ratio is characteristic of mafic or more evolved sources. Pb isotopes in plagioclase are ideal tracers of crust and mantle evolution as well as sensitive indicators of igneous processes such as magma mixing and crustal contamination. Plagioclase also has the advantage of very low U concentrations requiring minimal correction for radiogenic in-growth. We specifically explored the possibility of using the Pb isotopic measurements in plagioclase from the same rock as the zircon in Archean anorthosites in order to constrain the mantle extraction age and nature of their sources.

The difficultly with measuring Pb isotopes in-situ in plagioclase is the low total Pb concentration, typically less than 15 ppm total Pb. At these levels, laser ablation measurements of the Pb isotope composition of plagioclase are not sufficiently precise

and accurate for studies of igneous geochemistry, using the faraday cup configuration that is standard on multi-collector ICPMS instruments. The integration of ion counters in the collector configuration of the MC-ICPMS can, however, enable in situ isotopic measurement of trace elements in minerals such as Pb isotopes in plagioclase. Ion counters have much greater signal to noise ratios than faraday detectors and a multi-ion counting system has the ability to measure the Pb isotope composition of plagioclase with low total Pb concentrations precisely and accurately. Drawbacks of ion counters are that they are much less stable than faraday detectors and, when the thesis was begun, there was no well-established method for laser ablation Pb isotope measurements using only ion counters in widespread use. A major goal of this thesis was therefore to develop such a method and apply it to Archean anorthosites.

Chapter 2 (thesis paper 1) was the first step in the development of the analytical method to measure in-situ Pb isotopes by LA-MC-ICPMS. The work explored the various aspects of measuring Pb isotopes of 'Pb-poor' (< 15 ppm total Pb) silicate glass standard reference materials. Glasses were chosen over natural minerals because of their presumed homogeneous geochemical and isotopic composition, avoiding the complicating effects of variations in natural minerals, and their well-established Pb isotope composition. The main challenges of making LA-MC-ICPMS Pb isotope measurements centered around the issues of correcting for the ^{204}Hg interference on the minor ^{204}Pb isotope; drift of the ion counters over the course of an analytical session; and the ability to properly correct for mass bias using external correction methods. Average Pb isotope ratios measured using 40 μm laser spots in this study for the MPI-DING

reference glasses T1-G (11.6 ppm total Pb) and ATHO-G (5.67 ppm total Pb) agree within 0.10 % and 0.15 % respectively of the preferred values. For silicate glasses with even lower Pb concentrations, MPI-DING KL2-G (2.07 ppm total Pb) and ML3B-G (1.28 ppm total Pb), measured Pb isotope ratios that include the minor 204-isotope agree within 0.75 % of the accepted values with typical precisions of < 0.85 % (RSD) using 69 μm spots; measured $^{207}Pb/^{206}Pb$ and $^{208}Pb/^{206}Pb$ are within 0.25% of preferred values with precisions of < 0.25% (RSD).

Chapter 3 (thesis paper 2) further explored the LA-MC-ICPMS Pb isotope method applied to in situ analyses addressing the issue of whether or not biases in instrument response, or "matrix effects", exist between silicate glasses and various minerals, specifically plagioclase and sulfides. The concern was that Pb isotope measurements on certain minerals might suffer from matrix effects unless the calibration standard was an exact matrix match to the target mineral of interest. Feldspar minerals and sulfides, two matrices with large differences in composition and ablation behavior, were chosen to determine the quality of data obtained when calibrating samples with standards having different physical and chemical characteristics. The work demonstrated that matrix matching was not required to accurately measure Pb isotopes in Pb-poor plagioclase and sulfide minerals and that silicate glass reference materials could be used as calibration standards to produce acceptable results for both feldspars and sulfides.

Chapter 4 (thesis paper 3) presented the results of Pb isotope measurements of plagioclase megacrysts from two Archean anorthosite complexes in south West Greenland. The Fiskenæsset and Nunataarsuk anorthosite complexes are two of the best

preserved Archean anorthosite complexes on Earth. In-situ U-Pb zircon geochronology by LA-ICPMS determined that both anorthosite complexes crystallized at ~ 2900 Ma and LA-MC-ICPMS Lu-Hf isotopic measurements of the zircon demonstrated that they also have a similar range of ε_{Hf} compositions. The ε_{Hf} values for both Fiskenæsset and Nunataarsuk fall between expected values for ~ 2900 Ma depleted mantle and a crustal component. The Pb isotope data for each anorthosite complex share a similar depleted mantle end member but diverge from this point in opposite directions, Fiskenæsset to more radiogenic Pb isotope crustal compositions and Nunataarsuk to less radiogenic Pb isotope crustal compositions. The Pb isotope data are used to constrain the timing of crust extraction for each anorthosite complex (Fiskenæsset = 3700 Ma; Nunataarsuk = 4200 Ma). This information is then used to calculate the $^{176}Lu/^{177}Hf$ for the crustal end member of each anorthosite complex. The calculated $^{176}Lu/^{177}Hf$ for Fiskenæsset and Nunataarsuk are characteristic of mafic crust (~ 0.03). The exciting implication of this result is that ancient, Hadean to Eoarchean mafic crusts survived for ~ 1 billion years within the Archean craton of south West Greenland, and are possibly still preserved in the Fiskenæsset and Nunataarsuk regions today.

Chapter 6: Bibliography

Albarede F., Telouk P., Blichert-Toft J., Boyet M., Agranier A. and Nelson B. (2004) Precise and accurate isotopic measurements using multiple-collector ICPMS. *Geochim. Cosmochim. Acta* **68**, 2725 – 2744.

Amelin Y., Lee D-C., Halliday A.N., and Pidgeon R.T. (1999) Nature of the Earth's earliest crust from hafnium sotopes in single detrital zircons. *Nature* **399**, 252 – 255.

Amelin Y., Lee D.-C. and Halliday A.N. (2000) Early-middle Archean crustal evolution deduced from Lu-Hf and U-Pb isotopic studies of single zircon grains. *Geochiim. Cosmochim. Acta* **64**, 4205 – 4225.

Andersen T., Andersson U.B., Graham S., Aberg G., and Simonsen S.L. (2009) Granitic magmatism by melting of juvenile continental crust: new constraints on the source of Palaeoproterozoic granitoids in Fennoscandia from Hf isotopes in zircon. *J. Geol. Soc. London* **166**, 233 – 247.

Andren H., Rodushkin I., Stenberg A., Malinovsky D. and Baxter D.C. (2004) Sources of mass bias and isotope ratio variation in multi-collector ICP-MS: optimization of instrumental parameters based on experimental observations. *J. Anal. At. Spectrom.* **19** 1217 – 1224.

Armstrong R.L. (1981) Radiogenic isotopes: the case for crustal recycling on a near-steady-state no-continental-growth. *Earth. Phil. Trans. Roy. Soc. London* **A301**, 443 – 472.

Ashwal L.D. (1993) Anorthosites. Springer-Verlag, New York, 422 p.

Ashwal L.D. (2010) The temporality of anorthosites. *Can. Min.* **48**, 711 – 728.

Ashwal L.D., Morrison D.A., Phinney W.C. and Wood J. (1983) Origin of Archean Anorthosites: Evidence from the Bad Vermilion Lake anorthosite complex, Ontario. *Contrib. Mineral. Petrol.* **82**, 259 – 272.

Ashwal L.D., Wooden J.L., Phinney W.C. and Morrison D.A. (1985) Sm-Nd and Rb-Sr isotope systematic of an Archean anorthosite and related rocks from the Superior Province of the Canadian Shield. *Earth Planet. Sci. Lett.* **74**, 338 – 346.

Ashwal L.D., Jacobsen S.B., Myers J.S., Kalsbeek F. and Goldstein S.J. (1989) Sm-Nd age of the Fiskenaesset Anorthosite Complex, West Greenland. *Earth Planet. Sci. Lett.* **91**, 261 – 270.

Baadsgaard H. and McGregor V.R. (1981) The U-Th-Pb systematics of zircons from the type Nuk Gneisses, Godthabsfjord, West Greenland. *Geochim. Cosmochim. Acta* **45**, 1099 – 1109.

Bachmann O., Dungan M.A. and Bussy R. (2005) Insights into shallow magmatic processes in large silicic magma bodies: the trace element record in the Fish Canyon magma body, Colorado. *Contrib. Mineral. Petrol.* **149**, 338 – 349.

Baker J., Peate D., Waight T. and Meyzen C. (2004) Pb isotopic analysis of standards and samples using a $^{207}Pb - ^{204}Pb$ double spike and thallium to correct for mass bias with a double-focusing MC-ICP-MS. *Chemical Geology*, **211**, 275 – 303.

Baker J., Stos S. and Waight T. (2006) Lead isotope analysis of archaeological metals by multiple-collector inductively coupled plasma mass spectrometry. *Archaeometry* **48**, 45 – 56.

Barling J. and Weis D. (2008) The influence of non-spectral matrix effects on the accuracy of Pb isotope ratio measurement by MC-ICP-MS. Implications for the external normalization method of instrumental mass bias correction. *J. Anal. At. Spectrom.* **23**, 1017-1025.

Barton Jr. J.M. (1996) The Messina layered intrusion, Limpopo belt, South Africa, an example on the in-situ contamination of an Archaean anorthosite complex by continental crust. *Precam. Res.* **78**, 139 – 150.

Barton J.M., Fripp R.E.P., Horrocks P. and McLean N. (1979) The geology, age and tectonic setting of the Messina layered intrusion, Limpopo Mobile Belt, Southern Africa. *Am. J. Sci.* **279**, 1108 – 1134.

Barton J.M., Ryan B. and Fripp R.E.P. (1983) Rb-Sr and U-Th-Pb isotopic studies of the Sand River Gneisses, Central Zone, Limpopo Mobile Belt. *Spec. Publ. Geol. Soc. S. Afr.* **8**, 9 – 18.

Bennett V.C. (2003) Compositional evolution of the mantle. In *The Mantle and Core Treatise on Geochemistry, v.2* (ed. R.W. Carlson). Elsevier, Amsterdam, pp. 493 - 515.

Bennett V.C., Nutman A.P. and McCulloch M.T. (1993) Nd isotopic evidence for transient, highly depleted mantle reservoirs in the early history of the Earth. *Earth Planet. Sci. Lett.* **119**, 299 – 317.

Bhaskar Rao Y.J., Chetty T.R.K., Janardhan A.S. and Gopalan K. (1996) Sm–Nd and Rb–Sr ages and P–T history of the Archean Sittampundi and Bhavani layered meta-anorthosite complexes in the Cauvery shear zone, South India: evidence for Neoproterozoic reworking of Archean crust. *Contrib. Mineral. Petrol.* **125**, 237-250.

Bhaskar Rao Y.J., Kumar A., Vrevsky A.B., Srinivasan R. and Anantha Iyer G.V. (2000): Sm–Nd ages of two meta-anorthosite complexes around Holenarsipur: constraints on the antiquity of Archean supracrustal rocks of the Dharwar Craton. *Proc. Indian Acad. Sci., Earth and Planetary Sci.* **109**, 57-65.

Black L.P., Moorbath S., Pankhurst R.J. and Windley B.F. (1973) $^{207}Pb/^{206}Pb$ whole rock age of the Archaean granulite facies metamorphic event in west Greenland. *Nature Phys. Sci.* **244**, 50 – 53.

Blichert-Toft J. (2008) The Hf isotopic composition of zircon reference material 91500. *Chem. Geol.* **253**, 252 – 257.

Blichert-Toft J. and Albarede F. (1994) Short-lived chemical heterogeneities in the Archean mantle with implications for mantle convection. *Science* **263**, 1593 – 1596.

Blichert-Toft J. and Albarede F. (2008) Hafnium isotopes in Jack Hills zircons and the formation of the Hadean crust. *Earth Planet. Sci. Lett.* **265**, 686 – 702.

Blichert-Toft J. and Puchtel I.S. (2010) Depleted mantle sources through time: Evidence from Lu-Hf and Sm-Nd isotope systematics of Archean Komatiites. *Earth Planet. Sci. Lett.* **297**, 598 – 606.

Blichert-Toft J., Arndt N.T. and Gruau G., (2004) Hf isotopic measurements on the Barberton komatiites: effects of incomplete sample dissolution and importance for primary and secondary magmatic signatures. *Chem. Geol.* **207**, 261 – 275.

Bouvier A., Vervoort J.D. and Patchett P.J. (2008) The Lu-Hf and Sm-Nd isotopic composition of CHUR: constraints from unequilibrated chondrites and implications for the bulk composition of terrestrial planets. *Earth Planet. Sci. Lett.* **273**, 48 – 57.

Bowring S.A. and Housh T. (1995) The Earth's early evolution. *Science*. **269**, 1535 – 1540.

Bridgwater D., Keto L., McGregor V.R. and Myers J.S. (1976) Archaean geniss complex of Greenland. *In* Geology of Greenland (eds. A. Escher and W.S. Watt), Grønlands geol. Unders. p. 18 – 75.

Burg J.P., Bodinier J.L., Chaudhry S., Hussain S., Dawood H. (1998) Infra-arc mantle-crust transition and intra-arc mantle diapers in the Kohistan complex (Pakistani Himalaya): petro-structural evidence. *Terra Nova* **10**, 74-80.

Burnett A., Kurtz A.C., Brabander D. and Shailer M. (2007) Dendrochemical Record of Historical Lead Contamination Sources, Wells G&H Superfund Site, Woburn, Massachusett. *J. of Environ. Qual.* **36**, 1488-1494.

Chase C.G. and Patchett P.J. (1988) Stored mafic/ultramafic crust and early Archean mantle depletion. *Earth Planet. Sci. Lett.* **91**, 66 – 72.

Chauvel C. and Blichert-Toft J. (2001) A hafnium isotope and trace element perspective on melting of the depleted mantle. *Earth Planet. Sci. Lett.* **190**, 137 – 151

Chu N.C., Taylor R.N., Chavagnac V., Nesbitt R.W., Boella R.M., Milton J.A., German C.R., Bayon G. and Burton K. (2002) Hf isotope ratio analysis using multi-collector inductibely coupled plasma mass spectrometry: an evaluation of isobaric interference corrections. *J. Anal. At. Spectrom.* **17**, 1567 – 1574.

Clift P.D. Van Long H., Hinton R., Ellam R.M., Hannigan R., Tan M.T. Blusztajn J. and Duc N.A. (2008) Evolving east Asian river systems reconstructed by trace element and Pb and Nd isotope variations in modern and ancient Red River-Song Hong sediments. *Geochem. Geophys. Geosyst.* **9**, Q04039, DOI:10.1029/2007GC001867.

Connolly J.A.D., Schmidt M.W., Solferino G. and Bagdassarov N. (2009) Permeability of asthenospheric mantle and melt extraction rates at mid-ocean ridges. *Nature* **462**, 209 – 212.

Connelly J.N. and Thrane K. (2005) Rapid determination of Pb isotopes to define Precambrain allochthonous domains: and example from West Greenland. *Geology* **33**, 953 – 956.

Cottle J.M., Horstwood M.S.A. and Parrish R.R. (2009) A new approach to single shot laser ablation analysis and its application to in situ Pb-U geochronology. *J. Anal. At. Spectrom.* **24**, 1355 – 1363.

Defant M.J., and Drummond M.S. (1990) Derivation of some modern arcs by melting of young subducted lithosphere. *Nature* **347**, 662 – 665.

DePaolo D.J. and Wasserburg G.J. (1976) Inferences about magma sources and mantle structure from variations of $^{143}Nd/^{144}Nd$. *Geophys. Res. Lett.* **3**, 743-746.

Doe B.R. (1962) Relationships of lead isotopes among granites, pegmatites and sulfide ores near Balmat, New York. *J. Geophys. Res.* **67**, 2895 – 2906.

Dymek R.F. and Owens B.R. (2001) Chemical assembly of Archean anorthosites from amphibolite-and granulite-facies terranes, SW Greenland. *Contrib. Mineral Petrol.* **141**, 513 – 528.

Eggins S.M., Kinsley L.P.J. and Shelley J.M.G. (1998) Deposition and element fractionation processes during atmospheric pressure laser sampling for analysis by ICPMS. *Appl. Surf. Sci.* **129**, 278 – 286.

Elburg M., Vroon P., van der Wagt B. and Tchalikian A. (2005) Sr and Pb isotopic composition of five USGS glasses (BHVO-2G, BIR-1G, BCR-2G, TB-1G, NKT-1G) *Chem. Geol.* **223**, 196 – 207.

Escher J.C. and Myers J.S. (1975) New evidence concerning the original relationships of early Precambrian volcanics and anorthosites in the Fiskenæsset region, southern west Greenland. Rapp. *Grønl. Geol. Unders. Bull.* **75**, 72 – 76.

Fandrich R., Gu Y., Burrows D. and Moeller K. (2007) Modern SEM-based mineral liberation analysis. *International Journal of Mineral Processing* **84 (1-4)**, 310 – 320.

Fletcher I.R., Rosman K.J.R. and Libby W.G. (1988) Sm-Nd, Pb-Pb, and Rb-Sr geochronology of the Manfred Complex, Mount Narryer, Western Australia. *Precamb. Res.* **38**, 343 – 354.

Flowerdew M.J., Millar I.L., Vaughan A.P.M., Horstwood M.S.A. and Fanning C.M. (2006) The source of granitic gneisses and migmatites in the Antarctic Peninsula: a combined U-Pb SHRIMP and laser ablation Hf isotope study of complex zircons. *Contrib. Mineral Petrol.* **151**, 751 – 768.

Frei R., Polat A. and Meibom A (2004) The Hadean upper mantle conundrum: Evidence for source depletion and enrichment from Sm-Nd, Re-Os, and Pb isotopic compositions in 3.71 Gy boninite-like metabaslts from the Isua Supracrustal Belt, Greenland. *Geochim. Cosmochim. Acta* **68**, 1645 – 1660.

Gagnevin D., Daly J.S., Waight T.E., Morgan D. and Poli G. (2005) Pb isotopic zoning of K-feldspar megacrysts determined by laser ablation multi-collector ICP-MS: insights into granite petrogenesis. *Geochim. Cosmochim. Acta* **69**, 1899 – 1915.

Galer S.J.G. and Goldstein S.L. (1996) Influence of accretion on lead in the Earth. *In* Earth processes: reading the isotopic code. (eds. A. Basu, S. Hart). American Geophysical Union, Washington, DC, pp 75 – 98.

Gancarz A.J. (1976) Isotopic systematic in Archean rocks, west Greenland. PhD thesis, California Institute of Technology, Pasadena, 378p.

Gerdes A. and Zeh A. (2009) Zircon formation versus zircon alteration – new insights from combined U-Pb and Lu–Hf in-situ LA-ICP-MS analyses, and consequences for the interpretation of Archaean zircon from the Central Zone of the Limpopo Belt. *Chem. Geol.* **261**, 230 – 243.

Gibson G.M. and Ireland T.R. (1999) Black Giants anorthosite, New Zealand: a Paleozoic analogue of Archean stratiform anorthosites and implications for the formation of Archean high grade gneiss terranes. *Geology* **27**, 131 – 134.

Griffin W.L. Pearson N.J. Belousova E. Jackson S.E. van Achterbergh E. O'Reilly S.Y. Shee S.R. (2000) The Hf isotope composition of cratonic mantle; LAM-MC-ICPMS analysis of zircon megacrysts in kimberlites. *Geochim. Cosmochim Acta.* **64**, 133 – 147.

Guillong M. and Günther D. (2002) Effect of particle size distribution on ICP-induced elemental fractionation in laser-ablation–inductively coupled plasma–mass spectrometry. *J. Anal. At. Spectrom.* **17**, 831 – 837.

Günther D. and Heinrich C.A. (1999) Enhanced sensitivity in laser ablation-ICP mass spectrometry using helium-argon mixtures as aerosol carrier. *J. Anal. At. Spectrom.* **14**, 1363 – 1368

Halter W.E., Pettke T. and Heinrich C.A. (2004) Laser–ablation ICP–MS analysis of silicate and sulfide melt inclusions in an andesitic complex I: analytical approach and data evaluation. *Contrib. Mineral. Petrol.* **147**, 385 – 396.

Hargraves R.B. (1986) Faster spreading or greater ridge length in the Archean? *Geology* **14**, 750 – 752.

Harrison T.M., Blichert-Toft J., Muller W., Albarede F., Holden P. and Mojzsis S.J. (2005) Heterogeneous Hadean Hafnium: evidence for continental crust at 4.4 to .5 Ga. *Science* **310**, 1947.

Harrison T.M., Schmitt A.K., McCulloch M.T. and Lovera O.M. (2008) Early (4.5 Ga) formation of terrestrial crust: Lu Hf, del ^{18}O, and Ti thermometry results for Hadean zircons. *Earth Planet. Sci. Lett.* **268**, 476 – 486.

Hawkesworth C.J., Dhuime B., Pietranik A.B., Cawood P.A., Kemp A.I.S. and Storey C.D. (2010) The generation and evolution of the continental crust. *J. Geol. Soc. Lon.* **167**, 229 – 248.

Hemming S.R. and Rasbury E.T. (2000) Pb isotope measurements of sanidine monitor standards: implications for provenance analysis and tephrochronology. *Chem. Geol.* **165**, 331 – 337.

Henderson P., Fishlock S.J. Laul J.C., Cooper T.D., Conrad R.L., Boynton W.V. and Schmitt R.A. (1976) Rare earth element abundances in rocks and minerals from the Fiskenæsset complex, West Greenland. *Earth Planet. Sci. Lett.* **30**, 37 – 47.

Hiess J., Bennett V.C., Nutman A.P. and Williams I.S. (2009) In situ U-Pb, O and Hf isotopic compositions of zircon and olivine from Eoarchaean rocks, West Greenland: New insights to making old crust. *Geochim. Cosmochim. Acta* **73**, 4489-4516.

Hoffmann J.E., Munker C., Polat A., Konig S., Mezger K. and Rosing M.T. (2010) Highly depleted Hadean mantle reservoirs in the sources of early Archean arc-like rocks, Isua supracrustal belt, wouthern West Greenland. *Geochim Cosmochin Acta.* **74**, 7236 – 7260.

Hofmann A.W. (2004) Sampling mantle heterogeneity through oceanic basalts: isotopes and trace elements. In *The Mantle and Core Treatise on Geochemistry, v.2* (ed. R.W. Carlson). Elsevier, Amsterdam, pp. 493 - 515.

Horn I., Rudnick R.L., McDonough W.F. (2000) Precise elemental and isotope ratio determination by simultaneous solution nebulization and laser ablation ICP-MS: application to U-Pb geochronology. *Chem. Geol.* **164**, 281 – 301.

Horstwood M.S.A., Foster G.L., Parrish R.R., Noble S.R. and Nowell G.M. (2003) Common-Pb corrected in situ U-Pb accessory mineral geochronology by LA-MC-ICP-MS. *J. Anal. Atom. Spectrom.* **18**, 837 – 846.

Housh T. and Bowring S.A. (1991) Lead isotopic heterogeneities within alkali feldspars: Implications for the determination of initial lead isotopic compositions. *Geochim. Cosmochim. Acta* **55**, 2309 – 2316.

Housh T.B., Bowring S.A. and Villeneuve M. (1989) Lead isotopic study of arc magmatism within early Proterozoic Wopmay Orogen, NW Canada: Role of continental crust in arc magmatism. *J. Geol.* **97**, 735 – 747.

Iizuka T., Komiya T., Johnson S.P., Kon Y., Maruyama S. and Hirata T. (2009) Reworking of Hadean crust in the Acasta gneisses, northwestern Canada: evidence from in situ Lu-Hf isotope analysis of zircon. *Chem. Geol.* **259,** 230 – 239.

Jackson S.E. (2008) Calibration strategies for elemental analysis by LA-ICP-MS. *In* Laser Ablation ICP-MS in the Earth Sciences: Current Practices and Outstanding Issues, v. 40 (ed. P.J. Sylvester). Mineralogical Association of Canada pp.

Jackson S.E. and Günther D. (2003) The nature and source of laser induced isotopic fractionation in laser ablation -multicollector-inductively coupled plasma-mass spectrometry. *J. Anal. At. Spectrom.* **18** 205 – 212.

Jaffey A.H., Flynn K.F., Glendenin L.E., Bentley W.C. and Essling A.M. (1971) Precision measurement of half-lives and specific activities of ^{235}U and ^{238}U. *Phys. Rev. C.* **4**, 1889 – 1906.

Jochum K.P., Dingwell D.B., Rocholl A., Stoll B., Hofmann A.W., Becker S., Besmehn A., Bessett D., Dietze H-J., Dulski P., Erzinger J., Hellebrand E., Hoppe P., Horn I., Janssens K., Jenner G.A., Klein M., McDonough W.F., Maetz M., Mezger K., Munker C., Nikogosian I.K., Pickhardt C., Raczek I., Rhede D., Seufert H.M., Simakin S.G., Sobolev A.V., Spettel B., Straub S., Vincze L., Wallianos A., Weckwerth G., Weyer S., Wolf D. and Zimmer M. (2000) The prepartion and preliminary characterization of eight geological MPI-DING reference glasses for in-situ microanalysis. *Geostandards Newsletter: The Journal of Geostandards and Geoanalysis*. **24**, 87 – 133.

Jochum K.P., Pfander J., Woodhead J.D., Willbold M., Stoll B., Herwig K., Amini M., Abouchami W. and Hofmann A.W. (2005) MPI-DING glasses: New geological reference materials for in situ Pb isotope analysis. *Geochem. Geophys. Geosys.* **6**, Q10008.

Jochum K.P., Stoll B., Herwig K., Amini M., Abouchami W. and Hofmann A.W. (2005) Lead isotope ratio measurements in geological glasses by laser ablation-sector field-ICP mass spectrometry (LA-SF-ICPMS). *Int. J. Mass Spectrom.* **242**, 281 – 289.

Jochum K.P, Stoll B., Herwig K., Willbold M., Hofmann A.W., Amini M., Aarburg S., Abouchami W., Hellerbrand E., Mocek B., Raczek I., Stracke A., Alard O., Bouman C., Becker S., Ducking M., Bratz H., Klemd R., deBruin D. Canil D., Cornell D., de Hoog C., Dalpe C., Danyushevsky L., Eisenhauer A., Gao Y., Snow J.E. Groschopf N., Gunther D., Latkoczy C., Gillong M., Hauri E.H., Hofer H.E., Lahaye Y., Horz K., Jacob D.E., Kasemann S.A., Kent A.J.R., Ludwig T., Zack T., Mason P.R.D., Meixner A., Rosner M., Misawa K., Nash B.P., Pfander J., Premo W.R., Sun W.D., Tiepolo M., Vannucci R., Vennemann T., Wayne D. and Woodhead J.D. (2006) *Geochem. Geophys. Geosyst.*, 2006, **7**, DOI: 10.1029/2005GC001060.

Jochum K.P., Stoll B., Herwig K. and Willbold M. (2006) Improvement of in situ Pb isotope analysis by LA-ICP-MS using a 193 nm Nd:YAG laser. *J. Anal. At. Spectrom.* **21**, 666 – 675.

Jochum K.P., Stoll B. Herwig K. and Willbold M. (2007) Validation of LA–ICP–MS trace element analysis of geological glasses using a new solid-state 193 nm Nd:YAG laser and matrix-matched calibration. *J. Anal. At. Spectrom.* **22**, 112 – 122.

Kalsbeek F. and Pidgeon R.T. (1980) The geological significance of Rb-Sr whole-rock isochrons of polymetamorphic Archean gneisses, Fiskenæsset area, southern West Greenland. *Earth Planet. Sci. Lett.* **50**, 225 – 237.

Kamber B.S. and Moorbath S (1998) Initial Pb of the Amitsoq gneiss revisited: implication for the timing of early Archaean crustal evolution in West Greenland. *Chem. Geol.* **150**, 19 – 41.

Kamber B.S., Collerson K.D., Moorbath S. and Whitehouse M.J. (2003) Inheritance of early Archaean Pb-isotope variability from long-lived Hadean protocrust. *Contrib. Mineral Petrol.* **145**, 25 – 46.

Kamber B.S., Whitehouse M.J., Bolhar R. and Moorbath S. (2005) Volcanic resurfacing and the early terrestrial crust: zircon U-Pb and REE constraints from the Isua Greenstone Belt, southern West Greenland. *Earth Planet. Sci. Lett.* **240**, 276 – 290.

Kemp A.I.S., Foster G.L., Schersten A. et al. (2009) Concurrent Pb-Hf isotope analysis of zircon by laser ablation multi-collector ICP-MS, with implications for the crustal evolution of Greenland and the Himalayas. *Chem. Geol.* **261**, 244 – 260.

Kemp A.I.S., Wilde S.A., Hawkesworth C.J., Coath C.D., Nemchin A., Pidgeon R.T., Vervoort J.D. and DuFrane S.A. (2010) Hadean crustal evolution revisited: New constraints from Pb-Hf isotope systematics of the Jack Hills zircons. *Earth Planet. Sci. Lett.* **296**, 45 - 56.

Kent A.J.R. (2008) In-situ analysis of Pb isotope ratios using laser ablation MC-ICP-MS: controls on precision and accuracy and comparison between Faraday cup and ion counting systems. *J. Anal. At. Spectrom.* **23**, 968 – 975.

Keulen N., Schersten A., Schumacher J.C., Næraa T. and Windley B.F. (2009) Geological observations in the southern West Greenland basement from Ameralik to Frederikshab Isblink in 2008. *Geo. Survey of Denmark and Greenland Bulletin* **17**, 49 – 52.

Keulen N., Næraa T., Kokfelt T., Schumacher J.C. and Schersten A. (2010) Zircon record of the igneous and metamorphic history of the Fiskenæsset anorthosite complex in southern West Greenland. *Geo. Survey of Denmark and Greenland Bulletin.* **20**, 67-70.

Kinney P.D., Williams I.S., Froude D.O., Ireland T.R. and Compston W. (1988) Early Archaean zircon ages from orthogneisses and anorthosites at Mount Narryer, Western Australia. *Precamb. Res.* **38**, 325 – 341.

Kosler J. (2008) Laser ablation sampling strategies for concentration and isotope ratio analyses by ICP-MS. *In* Laser Ablation ICP-MS in the Earth Sciences: Current Practices and Outstanding Issues, v. 40 (ed. P.J. Sylvester). Mineralogical Association of Canada pp. 79 – 92.

Kosler J. and Sylvester P.J. (2003) Present trends and the future of zircon in geochronology: laser ablation ICPMS. *In* Zircon, Vol. 53, Reviews in Mineralogy and Geochemistry (eds. J.M. Hanchar, P.W.O. Hoskin). Mineralogical Society of America. pp. 243 – 275.

Kosler J., Fonneland H., Sylvester P., Tubrett M. and Pederson R. (2002) U–Pb dating of detrital zircons for sediment provenance studies: a comparison of laser- ablation ICPMS and SIMS techniques. *Chem. Geol.* **182**, 605–618.

Kosler J., Pedersen R.B., Kruber C. and Sylvester P.J. (2005) Analysis of Fe isotopes in sulfides and iron meteorites by laser ablation high-mass resolution multi-collector-ICP mass spectrometry. *J.Anal. At. Spectrom.* **20**, 192 – 199.

Kosler J., Forst L. and Slama J. (2008) LAMDATE and LAMTOOL: Spreadsheet-based data reduction for laser ablation-ICPMS. *In* Laser Ablation ICP-MS in the Earth Sciences: Current Practices and Outstanding Issues, v. 40 (ed. P.J. Sylvester). Mineralogical Association of Canada pp. 315 - 317.

Kramers J.D. and Tolstikhin I.N. (1997) Two terrestrial lead isotope paradoxes, forward transport modeling, core formation and the history of the continental crust. *Chem. Geol.* **139**, 75 – 110.

Kroslakova I. and Günther D. (2007) Elemental fractionation in laser ablation–inductively coupled plasma–mass spectrometry: evidence for mass load induced matrix effects in the ICP during ablation of a silicate glass. *J. Anal. Atom. Spectrom.* **22**, 51 – 62.

Lahaye Y., Arndt N., Byerly G., Chauvel C., Fourcade S. and Gruau G. (1995) The invluence of alteration of the trace-element and Nd isotopic compositions of komatiites. *Chem. Geol.* **126**, 43 – 64.

Longerich H. (2008) Laser ablation-inductively coupled plasma-mass spectrometry (LA-ICP-MS); an introduction. *In* Laser Ablation ICP-MS in the Earth Sciences: Current Practices and Outstanding Issues, v. 40 (ed. P.J. Sylvester). Mineralogical Association of Canada p. 1 - 18.

Ludwig K. (2008) Isoplot 3, A Geochronological Toolkit for Microsoft Excel. Special Publication 1a. Berkeley Geochronology Center.

Ludwig K.R. and Silver L.T. (1977) Lead-isotope inhomogeneity in Precambrian igneous K-feldspars. *Geochim Cosmochim. Acta* **41**, 1457 – 1471.

Martin H. (1993) The mechanisms of petrogenesis of the Archean continental crust – comparison with modern processes. *Lithos* **30**, 373 – 388.

Martin H., (1995) Archaean grey gneisses and the generation of the continental crust. *In* Archaean Crustal Evolution, (ed. K.C. Condie). Elsevier pp. 205 – 260.

Mason P.R.D., Kosler J., De Hoog J.C.M., Sylvester P.J., Meffan-Main S. (2006) In-situ determination of sulfur isotopes in sulfur-rich materials by laser ablation multiple-collector inductively coupled plasma mass spectrometry (LA-MC-ICP-MS). *J. Anal. Atom. Spectrom.* **21**, 177 – 186.

Mathez E.A. and Waight T.E. (2003) Lead isotopic disequilibrium between sulfide and plagioclase in the Bushveld complex and the chemical evolution of large layered intrusions. *Geochim Cosmochim Acta* **67**, 1875 – 1888.

Mathez E.A. and Kent A.J.R. (2007) Variable initial Pb isotopic compositions of rocks associated with the UG2 chromitite, eastern Bushveld Complex. *Geochim. Cosmochim. Acta* **71**, 5514 – 5527.

McCulloch M.T. and Woodhead J.D. (1993) Lead isotopic evidence for deep crustal-scale fluid transport during granite petrogenesis. *Geochim. Cosmochim. Acta* **57**, 659 – 674.

McGill R.A.R., Pearce J.M., Fortey N.J., Watt J., Ault L. and Parrish R.R. (2003) Contaminant source apportionment by PIMMS lead isotope analysis and SEM image analysis. *Environ. Geochem. Health* **25**, 25 – 32.

Moorbath S. and Pankhurst R.J. (1976) Further rubidium-strontium age and isotopic evidence for the nature of late Archean plutonic event in West Greenland. *Nature*. **262**, 124 – 126.

Morrison D.A., Haskin L.A., Qiu Y.Z., Phinney W.C. and Maczuga D.E. (1985) Alteration in Archean anorthosite complexes. *Lunar and Planetary Science XVI.* Lunar Planet Inst, Houston, p. 589 – 590.

Mouri H., Whitehouse M.J., Brandl G. and Rajesh H.M. (2009) A magmatic age and four successive metamorphic events recorded in zircons from a single metaanorthosite sample in the Central Zone of the Limpopo Belt, South Africa. *J. Geol. Soc. London* **166**, 827 – 830.

Myers J.S. (1975) Igneous stratigraphy of Archaean anorthosite at Majorqap qava, near Fiskenæsset, South-West Greenland. *Rapp. Grønlands Geol. Unders.* **74**, 27p.

Myers J.S. (1976) Channel deposits of peridotite, gabbro and chromitite from turbidity currents in the stratiform Fiskenæsset anorthosite complex, southwest Greenland. *Lithos* **9**, 265 – 268.

Myers J.S. (1985) Stratigraphy and structure of the Fiskenaesset Complex, West Greenland. *Gronl. Geol. Unders. Bull.* **150**, 72p.

Myers J.S. (1988) Oldest known terrestrial anorthosites at Mount Narryer, Western Australia. *Precamb. Res.* **38**, 309 – 323.

Myers J.S. and Platt R.G. (1977) Mineral chemistry of layered Archean anorthosite at Majorqap qâva, near Fiskenaesset, southwest Greenland. *Lithos* **10**, 59 – 72.

Næraa T. and Schersten A. (2008) New zircon ages from the Tasiusarsuaq terrane, southern West Greenland. *Geol. Surv. Den. Greenland Bull.* **15**, 73 – 76.

Norman M., McCulloch M., O'Neill H. and Yaxley G. (2006) Manesium isotopic analysis of olivine by laser ablation multi-collector ICP-MS: Composition dependent matrix effects and a comparison of the Earth and Moon. *J. Analyt. Atom. Spectrom.* **21**, 50 – 54.

Novak M., Mikova J., Krachler M., Kosler J., Erbanova L., Prechova E., Jackova I. and Fottova D. (2010) Radial distribution of lead and lead isotopes in stem wood of Norway spruce: A reliable archive of pollution trends in Central Europe. *Geochim. Cosmochim. Acta* **74**, 4207 – 4218.

Nutman A.P., McGregor V.R., Friend C.R.L., Bennett V.C. and Kinny P.D. (1996) The Itsaq Gneiss Complex of southern West Greenland; the world's most extensive record of early crustal evolution (3900 – 3600 Ma). *Precambrian Res.* **78**, 1 – 39.

O'Neil J., Carlson R.W., Francis D. and Stevenson R.K. (2008) Neodymium-142 evidence for Hadean mafic crust. *Science* **321**, 1828 – 1831.

Oversby V.M. (1975) Lead isotopic systematics and ages of Archean acid intrusives in the Kalgoorlie Norseman area, western Australia. *Geochim. Cosmochim. Acta* **39**, 1107 – 1125.

Owens B.E. and Dymek R.F. (1997) Comparative petrology of Archean anorthosites in amphibolite and granulite facies terranes, WE Greenland. *Contrib. Mineral. Petrol.* **128**, 371 – 384.

Patchett P.J., Kouvo O., Hedge C.E. and Tatsumoto M. (1981) Evolution of continental crust and mantle heterogeneity: evidence from Hf isotopes. *Contrib. Mineral. Petrol.* **78**, 279 – 297.

Paul B., Woodhead J.D. and Hergt J. (2005) Improved in situ isotope analysis of low Pb materials using LA-MC-ICP-MS with parallel ion counter and Faraday detection. *J. Analyt. Atom. Spectrom.* **20**, 1350 – 1357.

Pearson N.J., Griffin W.L. and O'Reilly S. Y. (2008) Mass fractionation correction in laser ablation multiple-collector ICP-MS: precise and accurate in-situ isotope ratio measurement. *In* Laser Ablation ICP-MS in the Earth Sciences: Current Practices and Outstanding Issues, v. 40 (ed. P.J. Sylvester). Mineralogical Association of Canada p. 93 – 116.

Peck W.H. and Valley J.W. (1996) The Fiskenæsset Anorthosite Complex: stable isotope evidence for shallow emplacement into Archean oceanic crust. *Geology*, **24**, 523 – 526.

Pettingill H.S. and Patchett P.J. (1981) Lu-Hf total-rock age for the Amitsoq gneisses, West Greenland. *Earth Planet. Sci. Let.* **55**, 150 – 156.

Phinney W.C. (1982) Petrogenesis of Archean anorthosites. *In* Workshop on magmatic processes of early planetary crusts: magma oceans and stratiform layered intrusions. (eds. D. Walker, I.S. McCallum). Lunar Planet Inst Tech Rep 82 – 01, Lunar Planet Inst, Houston, p. 121 – 124.

Phinney W.C. and Morrison D.A. (1990) Partition coefficients for calcic plagioclase: implications for Archean anorthosites. *Geochim. Cosmochim. Acta.* **54**, 1639 – 1654.

Phinney W.C., Morrison D.A. and Maczuga D.E. (1988) Anorthosites and related megacrystic units in the evolution of Archean crust. *J. of Petrol.* **29**, 1283 – 1323.

Pidgeon R.T. and Kalsbeek, F. (1978) Dating of igneous and metamorphic events in the Fiskenaesset region of southern West Greenland. *Can. J. Earth Sci.* **15**, 2021 – 2025.

Pietranik A.B., Hawkesworth C.J., Storey C.D., Kemp A.I.S., Sircombe K.N., Whitehouse M.J. and Bleeker W. (2008) Episodic mafic crust formation from 4.5 to 2.8 Ga. New evidence from detrital zircons, Slave craton, Canada. *Geology*, **36**, 875 – 878.

Pietranik A.B., Hawkesworth C.J., Storey C., and Kemp T. (2009) Depleted mantle evolution and how it is recorded in zircon. *Geochim. Cosmochim. Acta* **73**, A1028.

Polat A., Hormann A.W., Munker C., Regelous M. and Appel P.W.U. (2003) Contrasting geochemical patterns in the 3.7 – 3.8 Ga pillow basalt cores and rims, Isua Greenstone Belt, southwest Greenland: Implications for postmagmatic alteration processes. *Geochim. Cosmochim. Acta.* **67**, 441 – 457.

Polat A., Appel P.W.U., Fryer B., Windley B., Frei R., Samson I.M. and Huang H. (2009) Trace element systematics of the Neoarchean Fiskenæsset anorthosite complex and associated met-volcanic rocks, SW Greenland: Evidenc for a magmatic arc origin. *Precamb. Res.* **175**, 87 – 115.

Polat A. Frei R. Schersten A. and Appel P.W.U. (2010) New age (ca. 2970 Ma), mantle source composition and geodynamic constraints on the Archean Fiskenæsset anorthosite complex, SW Greenland. *Chem. Geol.* **277**, 1 – 20.

Polat A., Fryer B.J., Appel P.W.U., Kalvig P., Kerrich R., Dilek Y., and Yang Z. (2011) Geochmistry of anorthositic differentiated sills in the Archean (~2970 Ma) Fiskenæsset Complex, SW Greenland: Implications for parental magma compositions, geodynamic setting, and secular heat flow in arcs. *Lithos* **123**, 50 – 72.

Riciputi L.R., Valley J.W. and McGregor V.R. (1990) Conditions of Archean granulite metamorphism in the Gadthab-Fiskenaesset region, southern West Greenland. *J. Meta. Geol.* **8**, 171 – 190.

Rivalenti G. (1976) Geochemistry of metavolcanic amphibolites from south-west Greenland. In *The Early History of the Earth* (ed. B.F. Windley). Wiley, London, pp. 213 – 223.

Rollinson H., Reid C. and Windley B. (2010) Chromitites from the Fiskenæsset anorthositic complex, West Greenland: clues to late Archaean mantle processes. In *The Evolving Continents: Understanding Processes of Continental Growth*, v. 338 (eds. T.M. Kusky, M.-G. Zhai, W. Xiao). Geological Society, London, pp. 197 – 212.

Rosholt J.N., Zartman R.E. and Nkomo I. T. (1973) Lead isotope systematics and uranium depletion in the Granite Mountains, Wyoming. *Geol. Soc. Amer. Bull.* **89**, 989 – 1002.

Rosman K.J.R. and Taylor P.D.P. (1997) Isotopic composition of the elements. *Pure Appl. Chem.* **70**, 217 – 236.

Rudnick R.L., McLennan S.M. and Taylor S.R. (1985) Large ion lithophile elements in rocks from high-pressure granulite facies terrains. *Geochim. Cosmochin. Acta* **49**, 645 – 655.

Segal I., Halicz L. and Platzner I.T. (2003) Accurate isotope ratio measurements of ytterbium by multiple collection inductively coupled plasma mass spectrometry applying erbium and hafnium in an improved double external normalization procedure. *J. Anal. Atom. Spec.* **18**, 1217 – 1223.

Simmons E.C., Hanson G.N. and Lumbers S.B. (1980) Geochemistry of the Shawmere anorthosite complex, Kapuskasing structural zone, Ontario. *Precam. Res.* **11**, 43 – 71.

Simonetti A., Heaman L.M., Hartlaub R.P., Creaser R.A., MacHattie T.G. and Bohm C. (2005) U-Pb zircon dating by laser ablation-MC-ICP-MS using a new multiple ion counting Faraday collector array. *J. Anal. At. Spectrom.* **20**, 677 – 686.

Simonetti A., Heaman L.M., Chacko T. and Banerjee N.R. (2006) In situ petrographic thin section U-Pb dating of zircon, monazite, and titanite using laser ablation-MC-ICP-MS. *Int. J. Mass. Spectrom.* **253**, 87 – 97.

Sisson T.W. and Grove T.L. (1993) Temperatures and H_2O contents of low NgO high-alumina basalts. *Contrib. Mineral. Petrol.* **113**, 167 – 184.

Slama J., Kosler J., Condon D.J., Crowley J.L., Gerdes A., Hanchar J.M., Horstwood M.S.A., Morris G.A., Nasdala L., Norberg N., Schaltegger U., Schoene B., Tubrett M.N. and Whitehouse M.J. (2008) Plesovice zircon – a new natural reference material for U-Pb and Hf isotopic microanalysis. *Chem. Geol.* **249**, 1 – 35.

Soderlund U., Patchett P.J., Vervoort J.D. and Isachsen C.E. (2004) the ^{176}Lu decay constant determined by Lu-Hf and U-Pb isotope systematics of Precambrian mafic intrusions. *Earth Planet. Sci. Lett.* **219**, 311 – 324.

Souders A.K. and Sylvester P.J. (2008a) Improved in situ measurements of lead isotopes in silicate glasses by LA-MC-ICPMS using multiple ion counters. *J. Anal. At. Spectrom.* **23**, 535 – 543. doi: 10.1039/b713934a

Souders A.K. and Sylvester P.J. (2008b) Use of multiple channeltron ion counters for LA-MC-ICPMS analysis of common lead isotopes in silicate glasses. *In* Laser Ablation ICP-MS in the Earth Sciences: Current Practices and Outstanding Issues, v. 40 (ed. P.J. Sylvester). Mineralogical Association of Canada p. 79 – 92.

Souders A.K. and Sylvester P.J. (2010) Accuracy and precision of non-matrix-matched calibration for lead isotope ratio measurements of lead-poor minerals by LA-MC-ICPMS. *J.Anal. At. Spectrom.* **25**, 975 – 988. doi: 10.1039/c002729D.6

Souders A.K., Sylvester P.J., Myers J.S. (*in review*) Mantle and crustal sources of Archean anorthosite: a combined in-situ isotopic study of Pb-Pb in plagioclase and Lu-Hf in zircon. *Geochim. Cosmochim Acta.*

Stacey J.S. and Kramers J.D. (1975) Approximation of terrestrial lead isotope evolution by a two-stage model. *Earth Planet. Sci. Lett.* **26**, 207 – 221.

Steele I.M., Bishop F.C., Smith J.V. and Windley B.F. (1977) The Fiskenæsset complex, West Greenland, Part III. Chemistry of silicates and oxide minerals from oxide bearing rocks, mostly from Qeqertarssuatsiaq. *Grønl. Geol. Unders Bull.*. **124**, 38p.

Stolper E. and Walker D. (1980) Melt density and the average composition of basalt. Ibid. **375**, 86 – 111.

Stracke A.M., Bizimis M. and Salters V.J.M. (2003) Recycling oceanic crust: Quantitative constraints. *Geochem. Geophys. Geosyst.* **4**, doi: 10.1020/2001GC000223.

Streckeisen A. (1976) To each plutonic rock its proper name. *Earth Sci. Rev.* **12**, 1 – 33.

Strom R.G. and Sprague A.L. (2003) Exploring Mercury: the iron planet. Springer-Verlag. 216p.

Sylvester P.J. (2008) Matrix effects in laser ablation ICP-MS. *In* Laser Ablation ICP-MS in the Earth Sciences: Current Practices and Outstanding Issues, v. 40 (ed. P.J. Sylvester). Mineralogical Association of Canada p. 79 – 92.

Sylvester P.J. and Ghaderi M. (1997) Trace element analysis of scheelite by excimer laser ablation–inductively coupled plasma–mass spectrometry (ELA–ICP–MS) using a synthetic silicate glass standard. *Chem. Geol.* **141**, 49–65.

Takagi D., Sato H. and Nakagawa M. (2005) Experimental study of a low alkali tholeiite at 1-5 kbar: optimal condition for the crystallization of high-An plagioclase in hydrous arc tholeiite. *Contrib. Mineral. Petrol.* **149**, 527 – 540.

Taylor G.J. (2009) Ancient lunar crust: origin, composition and implications. *Elements* **5**, 17 – 22.

Taylor S.R. and McLennan S.M. (1995) The geochemical evolution of the continental crust. *Rev. Geophys.* **33**, 241 – 265.

Taylor P.N., Moorbath S., Goodwin R. and Petrykowski A.C. (1980) Crustal contamination as an indicator of the extent of early Archean continental crust: Pb isotopic evidence from the late Archean gneisses of West Greenland. *Geochim. Cosmochim. Acta.* **44**, 1437 – 1453.

Tessalina S.G., Bourdon B., Van Kranendonk M., Birck J-L. and Philippot P. (2010) Influence of Hadean crust evident in basalts and cherts from the Pilbara Craton. *Nature Geosci.* **3**, 214 – 217.

Tolstikhin I.N., Kramers J.D., and Hofmann A.W. (2006) A chemical Earth model with whole mantle convection: the importance of a core-mantle boundary layer (D") and its early formation. *Chem. Geol.* **226**, 79 – 99.

Thirlwall M.F. and Anczkiewicz R. (2004) Multidynamic isotope ratio analysis using MC-ICP-MS and the causes of secular drift in Hf, Nd, and Pb isotope ratios. *Int. J. Mass Spec.* **235**, 59 – 81

Tyrrell S., Haughton P.D.W., Daly J.S., Kokfelt T.F. and Gagnevin D. (2006) The use of the common Pb isotope composition of detrital K-feldspar grains as a provenance tool and its application to Upper Carboniferous palaeodrainage, Northern England. *J. Sed. Res.* **76**, 324 – 345.

Tyrrell S., Leleu S., Souders A.K., Haughton P.D.W. and Daly J.S. (2009) K-feldspar sand-grain provenance in the Triassic, west of Shetland: distinguishing first-cycle and recycled sediment sources? **44**, 692 – 710.

Vervoort J.D. (2010) Hf Analysis in zircon by LA-MC-ICPMS: promise and pitfalls. *Geol. Soc. Amer. Abstracts with Program*. Paper No. 286-9.

Vervoort, J.D. and Blichert-Toft J. (1999) Evolution of the depleted mantle: Hf isotope evidence from juvenile rocks through time. *Geochim. Cosmochim. Acta*, **63**, 533 – 556.

Vervoort J.D., Patchett P.J., Gehrels G.E. and Nutman A.P. (1996) Constraints on early Earth differentiation from hafnium and neodymium isotopes. *Nature* **379**, 624 – 627.

Vry J.K. and Baker J.A. (2006) LA-MC-ICPMS Pb–Pb dating of rutile from slowly cooled granulites: Confirmation of the high closure temperature for Pb diffusion in rutile. *Geochim. Cosmochim. Acta* **70**, 1807 – 1820.

Waight T.E. and Lesher C.E. (2010) Pb isotopes during crustal melting and magma mingling – a cautionary tale form Miki Fjord macrodike, central east Greenland. *Lithos* **118**, 191 – 201.

Watson E.B. and Harrison T.M. (1983) Zircon saturation revisited: temperature and composition effects in a variety of crustal magma types. *Earth Planet. Sci. Lett.* **64**, 295-304.

Weaver B.L., Tarney J. and Windley B. (1981) Geochemistry and petrogenesis of the Fiskenæsset anorthosite complex, southern West Greenland: nature of the parent magma. *Geochim. Cosmochim. Acta*. **45**, 711 – 725.

Weaver B.L., Tarney J., Windley B. and Leake B.E. (1982) Geochemistry and petrogenesis of Archean metavolcanic amphibolites from Fiskenæsset, S.W. Greenland. *Geochim. Cosmochim. Acta*, **46**, 2203 – 2215.

Wiedenbeck M., Alle P., Corfu F. et al. (1995) Three natural zircon standards for U–Th–Pb, Lu–Hf, trace element and REE analyses. *Geostandards Newsletter* **19**, 1–23.

Wilde S.A., Valley J.W. Peck W.H. and Graham C.M. (2001) Evidence from detrital zircons for the existence of continental crust and oceans on the Earth 4.4 Ga ago. *Nature* **409**, 175 – 178.

Willigers B.J.A., Baker J.A., Krogstad E.J. and Peate D.W. (2002) Precise and accurate in situ Pb-Pb dating of apatite, monazite, and sphene by laser ablation multiple-collector ICP-MS. *Geochim. Cosmochim. Acta*, **66**, 1051 – 1066.

Wilson S.A., Ridley W.I. and Koenig A.E. (2002) Development of sulfide calibration standards for the laser ablation inductively-coupled plasma mass spectrometry technique. *J. Anal. At. Spectrom.* **17**, 4006 – 40.

Windley B.F. (1971) The stratigraphy of the Fiskenæsset anorthosite complex. *Gronl. Geol. Unders. Rapport* **35**, 19 – 21.

Windley B.F. and Garde A.A. (2009) Arc-generated blocks with crustal sections in the North Atlantic craton of West Greenland; new mechanism of crustal growh in the Archean with modern analogues. *Earth Sci. Rev.* **93**, 1 – 30.

Windley B.F., Herd R.K. and Bowden A.A. (1973) The Fiskenaesset complex, west Greenland. Part I: A preliminary study of the stratigraphy, petrology, and whole rock chemistry from Qeqertarssuatsiaq. *Gronl. Geol. Unders. Bull.*. No. 106, 54p.

Wohlgemuth-Ueberwasser C.C., Ballhaus C., Berndt J., Stotter nee Paliulionyte V. and Meisel T. (2007) Synthesis of PGE sulfide standards for laser ablation inductively coupled plasma mass spectrometry (LA-ICP-MS). *Contrib. Mineral. Petrol.* **154**, 607 – 617.

Wood J., Dekker J., Jansen J.G., Keay J.P. and Panagapko D. (1980) Mine Centre area geological map with marginal notes. *Ontario Ministry of Natural Resources, Ontario Geol. Survey Preliminary maps* 2201 and 2202.

Woodhead J., Hergt J., Meffre S., Large R.R. Danyushevsky L. and Gilber S. (2009) In situ Pb-isotope analysis of pyrite by laser ablation (multi-collector and quadrupole) ICPMS. *Chem. Geol.* **262**, 344 – 354.

Zeh A., Gerdes A., Barton Jr J. and Klemd R. (2010) U-Th-Pb and Lu-Hf systematics of zircon from TTG's, leucosomes, meta-anorthosites and quartzites of the Limpopo Belt (South Africa): Constraints for the formation, recycling and metamorphism of Palaeoarchaean crust. *Precam. Res.* **179**, 50 – 68.

APPENDIX

Chap. 15 from Mineralogical Association of Canada Short Course, Vancouver, B.C.

Souders A.K. and Sylvester P.J. (2008b) Use of multiple channeltron ion counters for LA-MC-ICPMS analysis of common lead isotopes in silicate glasses. *In* Laser Ablation ICP-MS in the Earth Sciences: Current Practices and Outstanding Issues, v. 40 (ed. P.J. Sylvester). Mineralogical Association of Canada p. 79 – 92.

INTRODUCTION

One of the most significant developments in laser ablation-inductively coupled plasma mass spectrometry (LA-ICP-MS) over the past decade has been the growth of in situ, high precision isotope ratio analyses of geological materials using multicollector (MC) magnetic sector instruments. A variety of isotopic systems have been investigated including boron (*e.g.* Tiepolo et al., 2006); magnesium (*e.g.* Norman et al., 2006); silicon (*e.g.* Chmeleff et al., 2008); sulfur (*e.g.* Mason et al., 2006); iron and copper (*e.g.* Graham et al., 2004); rubidium-strontium (*e.g.* Woodhead et al., 2005); samarium-neodymium (*e.g.* McFarlane & McCulloch, 2008); lutetium-hafnium (*e.g.* Iizuka & Hirata, 2005); rhenium-osmium (*e.g.* Pearson et al., 2002); uranium-lead (*e.g.* Simonetti et al., 2008) and U-series (*e.g.* Eggins et al., 2005). Most of these studies have focused on isotopes that are sufficiently abundant in the sample (*e.g.* Mg in olivine; S, Fe and Cu in sulfides, Nd in monazite; Hf in zircon) such that Faraday detectors can be used for ion collection.

There are many advantages of Faraday collection such as efficiency and uniform response (see Longerich, 2008 for further discussion) but their precision is severely compromised by resistor noise at low signal intensities, as are found during in situ analysis of isotopes of minor to trace elements in minerals and glasses. In these cases,

discrete-dynode, secondary electron multipliers (SEMs) or continuous-dynode, channel electron multipliers (CEMs or Channeltrons®) may be employed. Figure 1, for instance, illustrates the improved precision that can be attained on a ^{208}Pb signal of ~40,000 cps using a Channeltron ion counter (1.5% RSD) compared to Faraday detector (6.7% RSD).

In this short course volume, Simonetti et al. (2008) describe the use of SEMs in conjunction with Faradays for LA-MC-ICP-MS U-Pb geochronology. Here, we report on LA-MC-ICP-MS analyses for silicate glass standard reference materials (SRMs) using Channeltrons. Our results on these SRMs have already been reported elsewhere (Souders & Sylvester, 2008) but here we give more details on the analytical procedures used and principles behind them. The use of Channeltrons for LA-MC-ICP-MS is a relatively new development. Tiepolo et al. (2006) used Channeltrons for in situ boron-isotope measurements by LA-MC-ICP-MS. Cocherie & Robert (2008) reported combined Channeltron-Faraday measurements for LA-MC-ICP-MS U-Pb zircon geochronology.

PRINICPLES OF MULTI-ION COUNTING WITH ELECTRON MULTIPLIERS

Ion counting and the use of electron multipliers have been incorporated into mass spectrometry for almost 50 years to detect and measure ions of low- to moderate-intensity ion beams, that is, less than 10^6 counts per second (cps). The physical process that allows electron multipliers, or ion counters, to operate is secondary ion emission. The general principle of secondary electron emission is that a particle or ion impacts a high-voltage surface, or dynode, causing the release of secondary electrons from the outer layers of atoms. The number of electrons produced by an impact is dependant on the

type of particle hitting the surface (*i.e.* positive ion, negative ion, electron, etc.), the angle of contact between the particle and the surface, the mass and energy of the incoming particles and the condition of the surface. The electrons produced by this initial collision are directed down the detector by an electric potential gradient, generating even more secondary electrons each time a collision occurs between an electron and the dynode surface inside the detector. This amplification process is quite effective: some 10 thousand to 100 million electrons are produced from each ion. Eventually the electrons reach an output device at the end of the ion counter, where a resultant pulse is produced that is processed using digital electronics.

A schematic of a Channeltron continuous-dynode electron multiplier is shown in Figure 2. They consist of curved lead-silicate glass tubes that have the ability to detect both positive and negative ions, electrons and photons. A potential between ~2000 and 3200 V is applied to the top, or input end, of the CEM and decreases steadily to ground state at the output end of the detector. Secondary electrons generated at the input end of the detector are driven down the channel to a collector by the potential gradient generating even more secondary electrons each time the particles come in contact with the inner surface walls of the detector (Burle Technologies Inc., 2003). SEMs operate on the same principle as CEMs, but consist of discrete dynode plates (see Simonetti et al., 2008) rather than a continuous dynode.

Electron gains, or the output current divided by the input current (which are less than 100%), are a function of the application, the voltage applied to the detector and the length of the dynode surface within the detector. The voltage applied to each detector has

an effect on the impact energy of ions arriving at the detector, which in turn influences the electron gain of the detector. In order to maintain normal gains, it is important to make sure the operational voltage of the ion counter is set properly. It is also important to understand that ion counter gains change or "drift" with exposure to ion currents over time, even within a single analytical session of a few hours. The challenge for isotope ratio measurements using multiple ion counters (MICs) is that each Channeltron will see different count rates, which are largely a function of the relative abundances of the isotopes measured, and thus the cross-calibration normalization factors for the different gains between the detectors or "yields" will drift as well. If the drift is linear over time however it may be corrected using a standard – sample – standard bracketing technique assuming that the standard and sample drift in an analogous fashion (Tiepolo et al., 2006; Souders & Sylvester, 2008; Cocherie & Robert, 2008). Drift may also be corrected by normalization to the invariant ratio of an isotope pair that is analyzed at the same time as the unknown isotope ratio (*e.g.* Pearson et al., 2008). Possible concerns about differences in drift between the sample and an external reference material are eliminated if the invariant pair is of the same chemical element as the unknown isotope ratio pair (*e.g.* $^{179}Hf/^{177}Hf$ for $^{176}Hf/^{177}Hf$).

Linearity of the ion counters can become compromised by the accuracy of pulse pile up or "dead time" corrections at count rates exceeding approximately 300,000 cps. Thus it is recommended to adjust LA parameters (beam size, fluence, repetition rate) so that analytical work can be carried out at count rates below these levels. This is an unusual (but welcome) case in microbeam-based geoanalysis where the analytical

protocols for optimal data quality are in concert with the desire of the geologist to reveal fine scale heterogeneities in minerals by reducing the analytical volume as much as possible.

Tiepolo et al. (2006) have indicated that a "burn-in" period is needed for the stabilization of the gain factors for new Channeltrons. They suggested that Channeltrons become increasingly stable after exposure to more than 1.5 billion counts and have an operation voltage higher than 2300 V. Over months to years (depending on use), the surface of the detector where electron multiplication takes place will begin to degrade due to contamination from the vacuum system and as a result of ion impacts. The operational voltage of the detector will need to be increased in order to keep the impact energy of arriving particles constant and to maintain normal electron gains. Thus, it is advantageous to keep count rates low (<300,000 cps) not only to limit detector drift and potential dead time correction errors, but also in order to prolong the life-span of the ion counters before replacement becomes necessary.

PROCEDURES FOR LA-MC-ICP-MS ANALYSES OF PB-ISOTOPES USING MULTIPLE CHANNELTRONS

Instrumentation

In situ lead isotope measurements described in this chapter were performed on a Thermo Finnigan NEPTUNE double-focusing multi-collector (MC)-ICP-MS equipped with nine Faraday detectors and eight Channeltron ion counters. The ion counters are identical in size to the Faraday detectors and can be attached to the high or low mass side of a Faraday cup within the collector array (Schwieters et al., 2004). A generalized

schematic of the NEPTUNE MC-ICP-MS is shown in Figure 3. Normal instrument operating parameters and the collector configuration used in this study are provided in Tables 1 and 2, respectively. Five ion counters are attached to the low mass side of Faraday cup L4. They are used for the static, concurrent measurement of ^{202}Hg, ^{204}(Hg + Pb), ^{206}Pb, ^{207}Pb and ^{208}Pb. The ^{202}Hg measurement is used to correct for the isobaric interference of ^{204}Hg on ^{204}Pb. Mercury is a ubiquitous laboratory contaminant, present in the gas supplies for the ICP-MS and from other environmental sources that can coat surfaces of instrument components and sample mounts. It also can be a constituent of the sample matrix itself. To reduce levels of mercury in the argon gas, an activated charcoal filter made by Frontier GeoSciences Inc. is placed in the gas line to the ICP torch. The dry sorbent in the trap collects the vapor phase mercury present in both elemental and oxidized forms.

It is possible to monitor ^{235}U (simultaneously with the lead isotopes) in an ion counter attached to a high mass Faraday cup due to the mass dispersion provided by the dynamic zoom optics of the NEPTUNE system and the variable multi-collector array. In this chapter, however, ^{235}U data are not discussed because we are concerned only with describing lead isotope analyses in silicate glass SRMs of known composition. But the reader should keep in mind that ^{235}U data would be valuable for lead isotope investigations of minerals or glasses of unknown composition in which lead isotope ratios have been modified by the in-growth of radiogenic lead via the decay of uranium after crystallization, or in uranium-rich phases such as zircon measured for U-Pb geochronology.

A GeoLas laser ablation system is linked to the MC-ICP-MS for *in situ* analyses. This system includes a Lambda Physik ComPex Pro 110 ArF excimer laser operating at a wavelength of 193 nm and a pulse width of 20 ns. Typical operating conditions for the GeoLas system are included in Table 1. A laser fluence of approximately 5 J/cm^2 and a repetition rate of 10 Hz were used for all glass analyses. The spot size of the analyses ranged from 40 to 99 μm depending on the total Pb concentrations of the glasses. Samples were ablated in helium gas, which reduces sample re-deposition and elemental fractionation while increasing sensitivity for 193 nm ablation (Eggins *et al.*, 1998; Gunther and Heinrich, 1999). Mercury was filtered from the helium using gold-coated glass wool placed on the helium gas line feeding the ablation cell.

Long-term settings of Channeltrons

The dead time for each ion counter on our instrument is set to 70 ns at the recommendation of the manufacturer due to the tendency for Channeltrons to produce double-pulses, the second arriving 30 – 40 ns after the main pulse (Tiepolo et al. 2006). The dark noise and operation voltage for each ion counter are checked every few months. The typical dark noise measurement for a single ion counter has not exceeded 0.0060 cps. A plateau calibration curve (cps *vs.* voltage) is constructed to determine the operation voltage for each ion counter using a PCL script within the NEPTUNE operating software. This procedure is performed in solution mode for each ion counter individually. The calibration curve is constructed by focusing the ion beam into one ion counter while the operation voltage of that ion counter is increased in 20 V increments. The output signal for each step is recorded in counts per second. The operation voltage for each ion

counter is determined by observing the point, or bend in the curve where the change in signal intensity (cps) no longer significantly increases with a corresponding increase in the detector voltage. The operating voltage can be different for each ion counter so a plateau calibration curve must be constructed for each individual ion counter. Operating voltages for the Channeltrons in our laboratory were set at ~2100V when they were new and had reached ~3000 V when they first needed to be replaced.

Sample preparation

Sample preparation for LA-MC-ICP-MS is relatively straightforward. In the case here, small separates of the silicate glass SRMs were mounted in 10 or 25 mm rings using epoxy resin. Once the epoxy had cured, the mount was ground to a flat surface and polished using diamond abrasive, exposing a cross-section of each glass. The mounts fit inside circular cavities of the polycarbonate holders fashioned for the laser ablation cell.

The SRMs discussed here are USGS BCR2-G and MPI-DING T1-G, ATHO-G, KL2-G and ML3B-G, made by fusion of natural rocks. BCR2-G, KL2-G and ML3B-G all have basaltic compositions whereas T1-G is a quartz-diorite and ATHO-G is a rhyolite. Each glass has well-defined lead isotope ratios and chemical composition, with total lead concentrations ranging from ~1 to 11 ppm (Jochum et al. 2000; Jochum et al. 2005a; Jochum et al. 2006a).

Tasks for set-up of an analytical session of isotope ratio measurements

Figure 4 is a flow chart documenting the step-by-step tasks that an analyst needs to do each day that LA-MC-ICP-MS analyses are to be carried out. To begin, great care must be given to eliminate any potential contamination from the ambient environment on the surfaces of components of the ICP-MS instrument (ablation cell, transfer tubing, torch, cones, etc.) and the samples themselves. This is particularly true of lead and other "sticky" metals that are ubiquitous contaminants in laboratory settings. It is true that laboratory contaminants can be removed from the surface of sample mounts by "pre-ablation" for a few seconds before the "analytical ablation" is carried out but since this only disperses contaminants into the sample introduction system where they may be released during subsequent analyses, we emphasize careful cleaning instead.

Our epoxy mounts are cleaned in an ultrasonic bath for approximately 15 min with double-distilled water, deionized and purified (to 18 $M\Omega\ cm^{-1}$) by a Milli-Q water system. The surface of each mount is then scrubbed with double-distilled, ~8 N HNO_3 followed by a Milli-Q water rinse. The mount is left to dry in a positive-pressure air box prior to loading into the laser ablation sample cell. The ICP torch, injector, quartz shield, glass T-piece used to mix the He and Ar gases, and sampler and skimmer cones are all cleaned prior to each analytical session as well. Torch parts and glassware are soaked in a ~0.5 N HNO_3 bath and subsequently rinsed with double-distilled ~8N HNO_3 followed by a Milli-Q water rinse. Residue from prior ablations was removed from both the sample and skimmer cones with a cotton-topped applicator and each cone was rinsed with deionized water prior to installation on the instrument.

The next steps in the daily set-up involve instrument tuning and determinations of yields (cross-calibration normalization factors) for the Channeltrons, which are both done in solution mode prior to *in situ* laser analyses. On the NEPTUNE, after a typical 30 to 45 minute warm-up period, gas flow, torch position, and lens focus potentials are all first adjusted for maximum sensitivity as well as optimal peak shape and peak overlap using the Faraday detectors and aspirating a 10 ppb Pb NBS 981 solution (Table 2). Typical sensitivity is 28 mV or ~1,750,000 cps (1 mV is ~62,500 cps) per ppb ^{208}Pb. Following a brief wash-out with dilute HNO_3, the collector array is repositioned for the collection of ^{202}Hg, ^{204}(Hg + Pb), ^{206}Pb, ^{207}Pb, and ^{208}Pb in the 5 MICs attached to the low-mass end of Faraday cup L4 (Table 2).

Determination of the ion counter yields is shown schematically in Figure 5. This process is similar to determining the gain for a Faraday collector but instead of an electronic pulse being sent through each detector, the relative yield of each ion counter is determined by a dynamic peak jumping method which sequentially places a reference signal of ~100,000 cps into each of the 8 ion counters by changing the mass setting for the center Faraday cup. The relative yield value for each ion counter is determined in solution mode to maximize signal stability and attain the best precision. The dynamic cycle is repeated 10 times using an integration time of 8 sec. The relative yield value for each ion counter to be used in the analytical session (IC1 – IC5 in the case of lead isotopes) is then determined by normalizing the average of the measured signal intensities for each ion counter to the average response of IC1. If the relative yield values are not within 80% of IC1, the operation voltage on the ion counter is adjusted.

After another brief wash-out period, the instrument is switched to laser ablation mode and rechecked for sensitivity on a known reference material and, if necessary, retuned. Under dry plasma conditions a typical sensitivity of 23,000 cps per ppm ^{208}Pb for *in situ* analyses of BCR2-G (~11 ppm total Pb) with a 40 μm laser spot is achieved using our instrumentation. Signal intensities during *in situ* analysis are typically less then ~5 mV, or ~312,500 cps, in all ion counters (for BCR2-G with a 40 μm spot, ~230,000 cps ^{208}Pb is typical). Ion counter backgrounds are usually less than 1000 cps for all the lead isotopes.

Analytical routine

The duration of each standard and sample analysis in our experiments is ~ 120 seconds or 120 cycles using an integration time of ~1 sec/cycle. The first 30 seconds (cycles) are used to measure the background count rates with the laser off followed by 60 seconds of laser ablation monitoring of the ^{202}Hg, ^{204}Pb, ^{206}Pb, ^{207}Pb and ^{208}Pb isotopes followed by a 30 second wash-out.

Standard – sample – standard bracketing is employed to correct for instrumental mass fractionation in the argon plasma and other components of the ICP (e.g., the transfer lenses), as well as for detector drift. The lead isotopic system does not have an invariant isotopic pair that can be used to monitor fractionation and drift. Also, the configuration of ion counters on our instrument does not allow us to monitor mass bias and drift relative to an aspirated thallium tracer solution of known isotopic composition or measured $^{202}Hg/^{200}Hg$ using the MICs in static mode (Pearson *et al.*, 2008). For bracketing, the lead isotope measurement of every three unknown samples are preceded

and followed by three measurements of the bracketing standard, BCR2-G. Souders and Sylvester (2008) discussed the suitability of BCR2-G as a bracketing standard for in situ lead isotope measurements including its homogeneity (which, on the micron-scale, is better than 1% for lead isotope ratios with ^{204}Pb and as good as 0.15% for ^{207}Pb/^{206}Pb), and give the calibration values used for lead isotope ratios in this material.

On-line corrections for yield, dark noise and dead time are performed using the NEPTUNE software prior to downloading the measured mass intensities into an Excel spreadsheet for off-line subtraction of mean gas background intensities from the time-resolved signal intensities for each isotope, ^{204}Hg interference corrections on ^{204}Pb (described below), lead isotope ratio calculations, and instrumental mass bias corrections (Albarede *et al.*, 2004). Lead isotope ratios determined for the set of three BCR2-G standards run before and after each set of 3 unknowns are averaged together. The lead isotope ratios for the unknowns are linearly interpolated, anchored by the average value of the three standards.

As noted above, bracketing with an external standard can be carried out by simple interpolation only if drift in the measured isotopic ratios of the standard are linear over the course of an analytical session, and there are no differences in mass bias between the standard matrix and the sample matrix. Figure 6 illustrates how the Channeltrons used for ^{206}Pb (IC3) and ^{208}Pb (IC5) drifted for BCR2-G, ML3B-G, KL2-G and ATHO-G SRMs over the course of two experiments separated by five months in our laboratory. ^{208}Pb is about twice as abundant as ^{206}Pb in the SRMs and thus the efficiency of IC5 decreases more rapidly than IC3 as it is exposed to greater total counts over time than

IC3. The $^{208}Pb/^{206}Pb$ ratio decreases accordingly but in a linear fashion that is consistent for all four SRM glasses. It is particularly noteworthy that ATHO-G, a rhyolite glass, exhibits similar drift behavior as BCR2-G, ML3B-G and KL2-G, which are basalt glasses. This gives us some confidence that BCR2-G can be effectively used as a bracketing standard for lead isotope measurements in unknown glasses of basalt to rhyolite composition. Note that the total drift of the Channeltrons was much greater in the later experiment (May 2007) than in the earlier one (December 2006). This may reflect the fact that the operation voltage settings for the ion counters had not been recently calibrated before the May 2007 experiment, in contrast to the December 2006 experiment.

Interference corrections for mercury on ^{204}Pb

The main motivation for using multicollector ICP-MS instruments for measurements of lead isotope ratios rather than single collector instruments is the potential to determine ratios involving the minor ^{204}Pb isotope much more precisely. The ability to measure lead isotope ratios involving ^{204}Pb is particularly difficult in lead – poor samples due to its low relative abundance (~1.4 % of all common lead) and the isobaric interference from ^{204}Hg mentioned above. The interference from ^{204}Hg is potentially very significant for laser analyses where target materials contain more than ~10 ppm Hg, and even for materials with less Hg where lead concentrations are very low (< 5 ppm total Pb).

We have explored two methods for interference corrections for ^{204}Hg on ^{204}Pb, which are detailed in Figure 7 and in Souders and Sylvester (2008). In Method 1, which

is very similar to the off-line 204-correction procedure presented in Horstwood *et al.* (2003) and Paul *et al.* (2005), gas background subtraction removes the ^{204}Pb and ^{204}Hg in the gas from the ^{204}(Hg + Pb) measurement, and any residual ^{204}Hg derived from the sample itself is calculated from the ^{204}Hg/^{202}Hg and the background-corrected ^{202}Hg measurement in the sample. ^{204}Hg/^{202}Hg is ideally calculated from the relative natural abundances of the mercury isotopes and a mass bias factor (β) determined from the observed ^{202}Hg/^{200}Hg, measured in the gas background at the start of a day's laser ablation session using a cup configuration in which ^{200}Hg is collected in IC1 and ^{202}Hg in IC2. With our instrumentation, however, we could not measure ^{202}Hg/^{200}Hg in the ion counters accurately (possibly due to an isobaric interference on ^{202}Hg). We thus had to simply assume that ^{204}Hg/^{202}Hg had the natural ratio recommended by IUPAC (Rosman and Taylor, 1997).

In Method 2, the ^{204}Hg/^{202}Hg of the gas background is determined from measurements of ^{202}Hg, ^{204}(Hg+Pb) and ^{208}Pb made with the laser off prior to each analysis. For each gas background measurement cycle, ^{204}Pb is calculated from the measured ^{208}Pb and ^{208}Pb/^{204}Pb, assuming that the actual isotopic composition of lead in the gas is given by the ^{208}Pb/^{204}Pb for modern lead (^{208}Pb/^{204}Pb = 38.63 +/- 0.98; Stacey and Kramers, 1975). The ^{204}Hg in the gas is then determined by subtraction of the calculated ^{204}Pb from the measured ^{204}(Hg + Pb), and a calculated ^{204}Hg/^{202}Hg in the gas is derived using the measured ^{202}Hg in the gas. With both ^{204}Pb and ^{204}Hg/^{202}Hg in the gas now established, the ^{204}Pb for each laser ablation measurement cycle is determined by subtracting ^{204}Hg from the measured ^{204}(Hg + Pb) using the measured ^{202}Hg during laser

ablation and the average $^{204}Hg/^{202}Hg$ for the gas background. The resulting ^{204}Pb is then background corrected using the average ^{204}Pb calculated for the gas background. Souders and Sylvester (2008) tested both methods and found that Method 2 gave somewhat more precise results for their data sets. They also showed that while within-run fluctuations in the mass bias factor (β) calculated from $^{202}Hg/^{200}Hg$ in Method 1 will have little affect on the accuracy of the final lead isotope results for most natural silicate glasses, which have $^{204}Hg/^{204}Pb$ ratios of less than 0.5, data quality will be degraded for minerals (notably some sulfides) with $^{204}Hg/^{204}Pb$ intensities greater than ~2 (Figure 8). Therefore Method 2 is preferred for determining lead isotope ratios from LA-MC-ICP-MS data.

ION COUNTER LINEARITY

The linearity of each of ion counters IC2 – IC5 as a function of count rate is shown for both solution and laser analysis in Figures 9 and 10, respectively. In the solution experiment, a series of SRM 981 dissolutions with total lead concentrations from 0.025 to 0.1 ppb were analyzed. Signal intensities varied from a few hundred counts per second for ^{204}Pb to ~120,000 cps for ^{208}Pb (Fig. 9A-D). All results are well-correlated ($r^2 > 0.99$) showing a linear increase in count rate with increasing Pb concentration. The laser linearity test was performed by ablating BCR2-G for 60 seconds and varying the total volume of material ablated by changing the diameter of the laser spot while keeping the laser energy (3 J/cm^2) and laser repetition rate (10 Hz) constant. Lead count rates ranged from ~300 cps (20 μm spot) to ~4000 cps (109 μm spot) for ^{204}Pb, to ~7000 cps (20 μm spot) to ~130,000 cps (109 μm spot) for ^{208}Pb (Fig. 10A-D). This is associated

calculated laser pit volumes of ~18,000 μm^3 to ~575,000 μm^3 respectively. Again, the results are well-correlated ($r^2 > 0.99$) with count rates increasing linearly with increasing spot size.

The co-linearity of the ion counters as a function of count rate is illustrated for both solution (Fig. 9E-H) and laser ablation (Fig. 10E–H) analyses using $^{208}Pb/^{204}Pb$ (IC5/IC2) and $^{207}Pb/^{206}Pb$ (IC4/IC3) ratios. The figures plot the data both before (E-F) and after (G-H) mass bias corrections were applied and are shown relative to the preferred values of each of SRM 981 (Baker et al. 2004) and BCR2-G (http://georem.mpch-mainz.gwdg.de). The results of the solution and laser analyses show that within the range of lead concentrations and amounts of ablated material that were evaluated, the mass bias corrected lead isotope ratios match the preferred values to better than ~0.2% for the solution data and to within ~0.7 to 1% for the laser data. The somewhat better accuracy for the solution data compared to the laser data reflect additional sources of error in laser analyses beyond ion counter co-linearity. These additional errors are probably associated with the generation, transport and vaporization of laser-derived aerosols.

ACCURACY AND PRECISION OF SILICATE GLASS ANALYSES

Souders and Sylvester (2008) reported lead isotope ratios for the silicate glass SRMs T1-G (11.6 ppm total Pb), ATHO-G (5.67 ppm total Pb), KL2-G (2.07 ppm total Pb) and ML3B-G (1.38 ppm total Pb), measured using the methods discussed in this chapter (Figure 11). Results for T1-G and ATHO-G agree, on average, with the preferred values to within 0.10% and 0.15%, respectively, using 40 μm laser ablation spots. For

KL2-G and ML3B-G, measured mean $^{208,207,206}Pb/^{204}Pb$ ratios are within 0.75% of the accepted values using 69 μm spots, whereas measured mean $^{207}Pb/^{206}Pb$ and $^{208}Pb/^{206}Pb$ ratios are within 0.45% of preferred values. For the glasses with the lowest concentrations of lead, Method 2 for the mercury interference correction produces somewhat more accurate and precise results than Method 1.

Figure 12 provides a comparison between the external precision of $^{207}Pb/^{206}Pb$ and $^{208}Pb/^{204}Pb$ ratios determined by Souders and Sylvester (2008) with the combined SEM-Faraday, LA-MC-ICP-MS measurements of Paul *et al.* (2005) and Simonetti *et al.* (2005) and the single-SEM-collector, LA- sector field (SF)-ICP-MS data of Jochum *et al.* (2005b) and Jochum *et al.* (2006b). For laser spot sizes between 90 to 120 μm, the external precision of the multi-Channeltron LA-MC-ICP-MS measurements of Souders and Sylvester (2008) for both the $^{207}Pb/^{206}Pb$ and $^{208}Pb/^{204}Pb$ ratios in the SRMs with the lowest lead concentrations, KL2-G and ML3B-G, show a distinct improvement when compared to the measurements made with the combined SEM-Faraday LA-MC-ICP-MS and single-SEM-collector LA-SF-ICP-MS methods. For 40 and 50 μm spots on the SRMs with somewhat more lead, ATHO-G and T1-G, there is improvement in the precision on $^{208}Pb/^{204}Pb$ ratios for the data of Souders and Sylvester (2008) compared to the single-SEM-collector data, but not in the precision on $^{207}Pb/^{206}Pb$ ratios. The results attest to the particular improvement in external precision that can be achieved for lead isotope ratios involving ^{204}Pb when ion counters are used to collect all 4 lead isotopes in lead-poor samples. With multicollector cup configurations that include Faraday

detectors, it is necessary to produce a signal of at least ~5mV (~310,000 cps) to preserve acceptable levels of precision.

Souders and Sylvester (2008) compared the theoretical and observed limits of precision for the multiple Channeltron measurements for lead isotopes using the observed internal precision for the silicate SRMs glasses that they analyzed, plotted as a function of total ^{208}Pb intensity (Figure 13). Theoretical limits of precision are governed by Poisson counting statistics, detector dark noise, the uncertainty on the measurement of the blank, and uncertainties associated with ion counter gains and the correction for the isobaric interference of ^{204}Hg on the 204-mass. Theoretical precision degrades rapidly at total ^{208}Pb intensities of less than 1 mV (~62,500 cps). The minimum theoretical limits of precision for lead isotope ratios measured using multiple Channeltrons are approached at lower total ^{208}Pb count rates than for Faraday-SEM cup configurations (*e.g.* Paul *et al.* 2005). This is because the uncertainty budget of the multiple Channeltron method is dominated by uncertainties in the ion counter gains, which are large only at very low ^{208}Pb count rates. Internal precision of measured lead isotope ratios in the silicate glass SRMs plot well above the theoretical curves. This reflects additional errors not included in the theoretical calculations, including possible matrix effects associated with the laser-produced aerosols, spot-to-spot heterogeneity in the lead isotopic composition of the BCR2-G calibrant and fluctuations in mass bias factors over short time scales (*i.e.* between individual analyses).

Kent (2008) has recently compared analytical uncertainties for LA-MC-ICP-MS measurements of lead isotope ratios using a combined Faraday-SEM detector array (with

the discrete-dynode ion counters used for ^{204}Pb, ^{202}Hg and ^{200}Hg) to those made using solely Faraday cups. He found that at signal intensities of 5 mV or ~310,000 cps for ^{204}Pb, the precision on measurements using an ion counter for ^{204}Pb are significantly better than those using a Faraday cup for ^{204}Pb. However, the use of a parallel Faraday-SEM configuration introduces an additional error of ±0.3% (2*s*) associated with the measurement of differences in gain between the ion counters and Faraday cups, which is required for determination of $^{208,207,206}Pb/^{204}Pb$ ratios. Thus, Kent (2008) argued that improvements in the precision on $^{208,207,206}Pb/^{204}Pb$ ratios are realized with the combined Faraday-SEM detector array only when measuring intensities of less than 2 mV or ~130,000 cps ^{204}Pb in an ion counter.

Kent (2008) compared the precision on $^{208}Pb/^{204}Pb$ ratios as a function of lead count rates, with measured intensities of ^{204}Pb as low as ~7000 cps in an ion counter, and ~4000 cps in a Faraday. At these very low intensities, his data show uncertainties on $^{208}Pb/^{204}Pb$ of about ±0.8% (2*s*) for the ion counter measurement and about ±10% (2*s*) for the Faraday measurement. Our multiple Channeltron data for lead isotope ratios cover an even lower range of ^{204}Pb intensities (~200 to 4000 cps) so we have compared our data to Kent's in Figure 14. The plot illustrates the potential improvements in precision that can be attained by employing multiple Channeltrons for LA-MC-ICP-MS in samples that have very low lead concentrations, or require analysis at a very fine spatial resolution, and thus remove only very small aliquots of the target matrix during laser ablation. Particularly important applications in the Earth sciences that may be developed in the

coming years are *in situ* analyses of fluid inclusions (Pettke, 2008) and melt inclusions (Mason *et al.*, 2008).

THE FUTURE

LA-MC-ICP-MS with Faraday cup collection has changed geoanalysis fundamentally in recent years by providing Earth scientists with the ability to determine precise isotopic ratios of major and minor elements in minerals *in situ*. Whereas geologists were once trying to understand isotopic variations only on the scale of whole rock samples, they now are increasingly analyzing and modeling isotopic variations on the mineral scale, and debating the significance of those models, in ever more detail.

The development of ion counters for LA-MC-ICP-MS opens up the possibility of determining precise isotopic ratios of trace elements in minerals *in situ*, thereby expanding the data sets available to the Earth scientist significantly. We can look forward confidently to exciting new applications in accessory mineral geochronology and thermochronology, sedimentary provenance, and petrogenesis in the years to come. Proper use of LA-MC-ICP-MS instruments equipped with multiple Channeltron detectors will be essential part of this development.

REFERENCES

Albarede, F., Telouk, P., Blichert-Toft, J., Boyet, M., Agranier, A. & Nelson, B. (2004) Precise and accurate isotopic measurements using multiple-collector ICPMS. *Geochim. Cosmochim. Acta*, **68**, 2725 – 2744.

Baker, J., Peate, D., Waight, T. & Meyzen, C. (2004) Pb isotopic analysis of standards and samples using a $^{207}Pb - ^{204}Pb$ double spike and thallium to correct for mass bias with a double-focusing MC-ICP-MS. *Chemical Geology*, **211**, 275 – 303.

Burle Technologies, Inc. (2003): Channeltron Electron Multiplier, Handbook for Mass Spectrometry Applications, 64 pp.
(www.burle.com/cgi-bin/byteserver.pl/pdf/ChannelBook.pdf)

Chmeleff, J., Horn, I, Steinhoefel, G & Von Blanckenburg, F. (2008): In situ determination of precise stable Si isotope ratios by UV-femtosecond laser ablation high-resolution multi-collector ICP-MS. *Chem. Geol. 249*, 155-166.

Cocherie, A. & Robert, M. (2008): Laser ablation coupled with ICP-MS applied to U–Pb zircon geochronology: A review of recent advances. *Gondwana Research*, doi:10.1016/j.gr.2008.01.003.

Eggins, S.M., Kinsley, L.P.J. & Shelley, J.M.G. (1998): Deposition and element fractionation processes during atomospheric pressure laser sampling for analysis by ICP-MS. *Appl. Surf. Sci.*, **127 – 129**, 278 – 286.

Eggins, S.M., Grun, R., Mcculloch, M.T., Pike, A.W.G., Chappell, J., Kinsley, L., Mortimer, G., Shelley, M., Murray-Wallace, C.V. & Taylor, L (2005): In situ U-series dating by laser ablation multi-collector ICPMS: new prospects for Quaternary geochronology. *Quat. Sci, Rev*, **24**, 2523-2538.

GEOREM, Max-Planck-Institute data base for geological and environmental reference materials, http://georem.mpch-mainz.gwdg.de/.

Graham, S., Pearson, N.J., Jackson, S.E., Griffin, W.L. & O'reilly, S.Y. (2004): Tracing Cu and Fe from source to porphyry: in situ determination of Cu and Fe isotope ratios in sulfides from the Grasberg Cu-Au deposit. *Chemical Geology*, **207**, 147-169.

Gunther, D. & Heinrich, C.A. (1999): Enhanced sensitivity in laser ablation-ICP mass spectrometry using helium-argon mixtures as aerosol carrier. *J. Anal. At. Spectrom.*, **14**, 1363 – 1368.

Horstwood, M.S.A., Foster, G.L., Parrish, R.R., Noble, S.R. & Nowell, G.M. (2003): Common-Pb corrected *in situ* U-Pb accessory mineral geochronology by LA-MC-ICP-MS. *J. Anal. At. Spectrom.*, **18**, 837 – 846.

Iizuka, T. & Hirata, T. (2005): Improvements of precision and accuracy in in situ Hf isotope microanalysis of zircon using the laser ablation-MC-ICPMS technique. *Chemical Geology* 220, 121-137.

Jochum, K.P., Dingwell, D.B., Rocholl, A., Stoll, B., Hofmann, A.W., Becker, S., Besmehn, A., Bessette, D., Dietze, H.-J., Dulski, P., Erzinger, J., Hellebrand, E., P. Hoppe, Horn, I., Janssens, K., Jenner, G.A., Klein, M., Mcdonough, W.F., Maetz, M., Mezger, K., Munker, C., Nikogosian, I.K., Pickhardt, C., Raczek, I., Rhede, D., Seufert, H.M., Simakin, S.G., Sobolev, A.V., Spettel, B., Straub, S., Vincze, L., Wallianos, A., Weckwerth, G., Weyer, S., Wolf, D. & Zimmer, M. (2000): The preparation and preliminary characterization of eight geological MPI-DING reference glasses for in situ microanalysis. *Geostand. Newsl.* **24**, 87 – 133.

Jochum, K.P., Pfander, J., Woodhead, J.D., Willbold, M., Stoll, B., Herwig, K., Amini, M., Abouchami, W. & Hofmann., A.W. (2005a): MPI-DING glasses: New geological reference materials for in situ Pb isotope analysis. *Geochem. Geophys. Geosyst.*, **6**, DOI: 10.1029/2005GC000995, Q10008.

Jochum, K.P., Stoll, B., Herwig, K., Amini, M., Abouchami, W. & Hofmann, A.W. (2005b): Lead isotope ratio measurements in geological glasses by laser ablation-sector field-ICP mass spectrometry (LA-SF-ICPMS). *Int. J. Mass Spectrometry*, **242**, 281 – 289.

Jochum, K.P., Stoll, B., Herwig, K., Willbold, M., Hofmann, A.W., Amini, M., Aarburg, S., Abouchami, W., Hellebrand, E., Mocek, B., Raczek, I., Stracke, A., Alard, O., Bouman,C., Becker, S., Ducking, M., Bratz, H., Klemd, R., De Bruin, D., Canil, D., Cornell, D., De Hoog, C., Dalpe, C., Danyushevsky, L., Eisenhauer, A., Gao, Y., Snow, J.E., Groschopf, N., Gunther, D., Latkoczy, C., Guillong, M., Hauri, E.H., Hofer, H.E., Lahaye, Y., Horz, K., Jacob, D.E., Kasemann, S.A., Kent, A.J.R., Ludwig, T., Zack, T., Mason, P.R.D., Meixner, A., Rosner, M., Misawa, K., Nash, B.P., Pfander, J., Premo, W.R., Sun, W.D., Tiepolo, M., Vannucci, R., Vennemann, T., Wayne, D. & Woodhead, J.D. (2006a): MPI-DING reference glasses for in situ microanalysis: New reference values for element concentrations and isotope ratios. *Geochem. Geophys, Geosyst.*, **7**, DOI: 10.1029/2005GC001060.

Jochum, K.P., Stoll, B., Herwig, K. & Willbold, M. (2006B): Improvement of *in situ* Pb isotope analysis by LA-ICP-MS using a 193 nm Nd:YAG laser. *J. Anal. At. Spectrom.*, **21**, 666 – 675.

Kent, A.J.R. (2008): *In-situ* analysis of Pb isotope ratios using laser ablation MC-ICP-MS: Controls on precision and accuracy and comparison between Faraday cup and ion counting systems. *J. Anal. At. Spectrom.*, 2008, DOI: 10.1039/b801046c.

Longerich, H.L. (2008): Laser Ablation-Inductively Coupled Plasma-Mass Spectrometry (LA-ICP-MS); An Introduction. *In* Laser-Ablation–ICP–MS in the Earth Sciences (P. Sylvester, ed.). *Mineralogical Association of Canada Short Course Series Volume* **40**, xxxx.

Mason, P.R.D., Kosler, J., De Hoog, J.C.M., Sylvester, P.J. & Meffan-Main, S. (2006): In situ determination of sulfur isotopes in sulfur-rich materials by laser ablation multiple-collector inductively coupled plasma mass spectrometry (LA-MC-ICP-MS). *J. Anal. At. Spectrom.*, **21**, 177–186.

Mason, P.R.D., Nikogosian, I.K. & Vanbergen, M.J. (2008): Major and trace element analysis of melt inclusions by laser ablation ICP–MS. *In* Laser-Ablation–ICP–MS in the Earth Sciences (P. Sylvester, ed.). *Mineralogical Association of Canada Short Course Series Volume* **40**, xxxx.

Mcfarlane, C. & Mcculloch, M. (2008): Sm–Nd and Sr isotope systematics in LREE-rich accessory minerals using LA–MC–ICP–MS. *In* Laser-Ablation–ICP–MS in the Earth Sciences (P. Sylvester, ed.). *Mineralogical Association of Canada Short Course Series Volume* **40**, xxxx.

Norman, M., Mcculloch, M., O'neill, H. & Yaxley, G. (2006). Magnesium isotopic analysis of olivine by laser-ablation multi-collector ICP-MS: Composition dependent matrix effects and a comparison of the Earth and Moon. J. Anal. At. Spectrom. *21*, 50-54.

Paul, B., Woodhead, J.D. & Hergt, J. (2005): Improved *in situ* isotope analysis of low-Pb materials using LA-MC-ICP-MS with parallel ion counter and Faraday detection. *J. Anal. At. Spectrom.*, **20**, 1350 – 1357.

Pearson, N.J., Alard, O., Griffin, W.L., Jackson, S.E. & O'reilly, S.Y. (2002): In situ measurement of Re-Os isotopes in mantle sulfides by laser ablation multicollector inductively coupled plasma mass spectrometry: Analytical methods and preliminary results. *Geochimica et Cosmochimica Acta*, **66**, 1037-1050.

Pearson, N.J., Griffin, W.L. & O'reilly, S. Y. (2008): Mass fractionation correction in laser ablation multiple-collector ICP-MS: precise and accurate in-situ isotope ratio measurement. *In* Laser-Ablation–ICP–MS in the Earth Sciences (P. Sylvester, ed.). *Mineralogical Association of Canada Short Course Series Volume* **40**, xxxx.

Pettke, T. (2008): Analytical protocols for element concentration and isotope ratio measurements in fluid inclusions by LA–(MC–)ICP–MS. *In* Laser-Ablation–ICP–MS in the Earth Sciences (P. Sylvester, ed.). *Mineralogical Association of Canada Short Course Series Volume* **40**, xxxx.

Rosman, K.J.R. & Taylor, P.D.P. (1997): Isotopic compositions of the elements. *Pure Appl. Chem.*, **70**, 217-236.

Schwieters, J.B., Bouman,C., Tuttas, C. & Wieser, M. (2004): A new tool for in situ isotopic analysis of small samples: multiple ion counting – ICPMS and – TIMS. *Geochim. Cosmochim. Acta*, **68 (Suppl 1)**, A60.

Simonetti, A., Heaman, L.M., Chacko, T. & Banerjee, N.R. (2005): U-Pb zircon dating by laser ablation-MC-ICP-MS using a new multiple ion counting Faraday collector array. *J. Anal. At. Spectrom.*, **20**, 677 – 686.

Simonetti, A., Heaman, L.M. & Chacko, T. (2008): Use of discrete-dynode secondary electron multipliers with Faradays – A '*reduced volume*' approach for *in-situ* U-Pb dating of accessory minerals within petrographic thin section by LA-MC-ICP-MS. *In* Title of Short Course (P.J. Sylvester, ed.). *Mineralogical Association of Canada Short Course Series Volume* **XX** (this volume).

Souders, A.K. & Sylvester, P.J. (2008): Improved *in situ* measurements of lead isotopes in silicate glasses by LA-MC-ICPMS using multiple ion counters. *J. Anal. At. Spectrom.* **23**, 535 – 543.

Stacey, J.S. & J.D., Kramers (1975): Approximation of terrestrial lead isotope evolution by a two-stage model. *Earth Planet. Sci. Lett.*, **26**, 207 – 221.

Tiepolo, M. Bouman C., Vannucci, R. & Schwieters, J. (2006): Laser ablation multicollector ICPMS determination of $\delta^{11}B$ in geological samples. *Appl. Geochem.* **21**, 788 – 801.

Woodhead, J.D., Swearer, S., Hergt, J. & Maas, R. (2005): *In situ* Sr-isotope analysis of carbonates by LA–MC–ICP–MS: interference corrections, high spatial resolution and an example from otolith studies. *J. Analytical Atomic Spectrometry* **20**, 22-27.

Table 1 Typical operating conditions for the Finnigan Neptune MC-ICPMS and GeoLas laser ablation system

Finnigan Neptune MC-ICPMS	
Operation power	1200 W
HV	10 kV
Cool gas flow	16 l min^{-1}
Auxiliary gas flow	0.7 l min^{-1}
Carrier gas (Ar) flow rate	0.9 l min^{-1}
Cones	Ni (H skimmer cone)
GeoLas laser ablation system	
Lambda Physik Compex Pro 110 ArF excim	193 nm
Laser fluence	~5 J cm^{-2}
Spot size	40 - 99 μm
Repetition rate	10 Hz
He gas to cell	1.2 l min^{-1}

Table 2 Finnigan Neptune collector assignments for Pb isotope analysis

Collector[a]	IC1	IC2	IC3	IC4	IC5	L4	L3	L2	L1	C	H1	H2	H3	IC6	H4	IC7	IC8
Ion Counters																	
isotope	^{202}Hg	^{204}(Hg+Pb)	^{206}Pb	^{207}Pb	^{208}Pb					219.68				^{235}U			
Faraday																	
isotope						^{200}Hg	^{202}Hg	^{204}(Hg+Pb)		^{206}Pb	^{207}Pb	^{208}Pb					

[a] L4 to L1, C, and H1 to H4 are Faraday cups. IC1 to IC5 are ion counters fixed to Faraday cup L4. IC6 is an ion counter fixed to Faraday cup H3. IC7 and IC8 are ion counters fixed to Faraday cup H4.

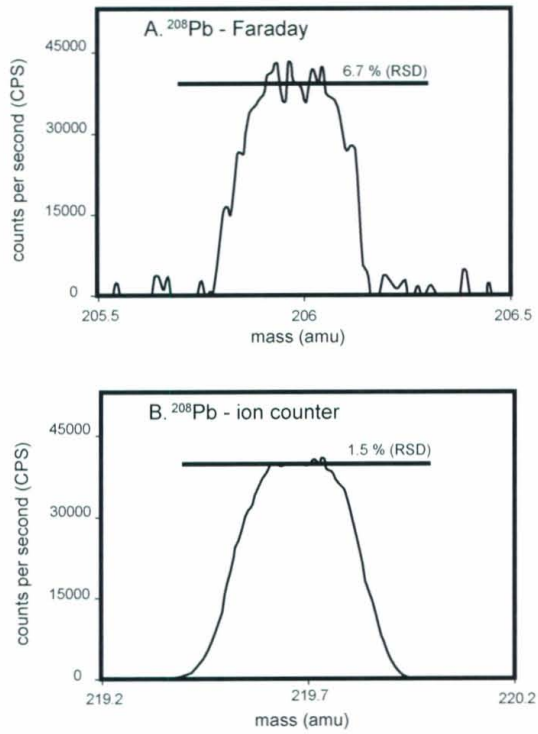

Fig. 1. Peak shapes of 208Pb from a SRM 981standard solution of 0.5 ppb total Pb concentration measured on a (A) Faraday detector and a (B) Channeltron ion counter. The x-axis corresponds to the mass range over which the peak was measured with the center value representing the axial mass of the collector array. The noise level for the plateau of the 208Pb signal collected in the Faraday detector (6.71 % RSD, 1-sigma) is over four times that of the noise level for the plateau of the 208Pb signal collected in the ion counter (1.5 % RSD, 1-sigma).

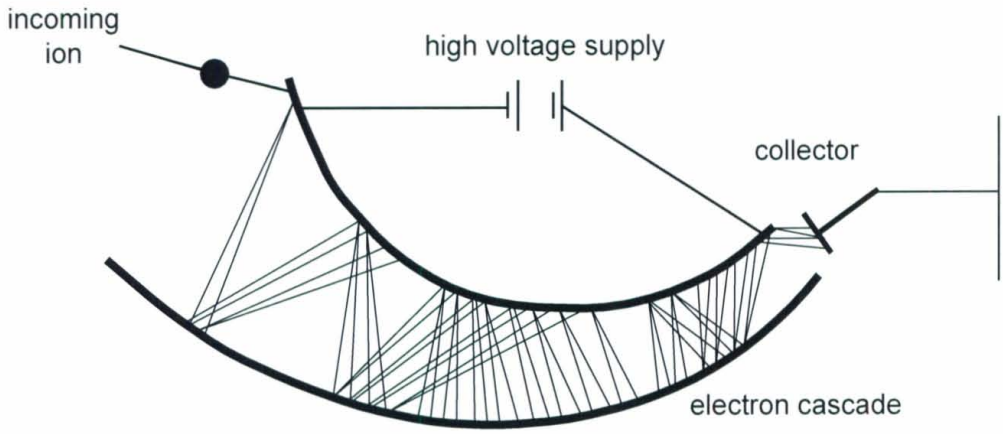

Continuous dynode electron multiplier

Fig. 2. Example of a continuous-dynode electron multiplier (modified from Montaser, 1998). Secondary electrons are produced when ions impact the high-voltage surfaces while traveling down the channel.

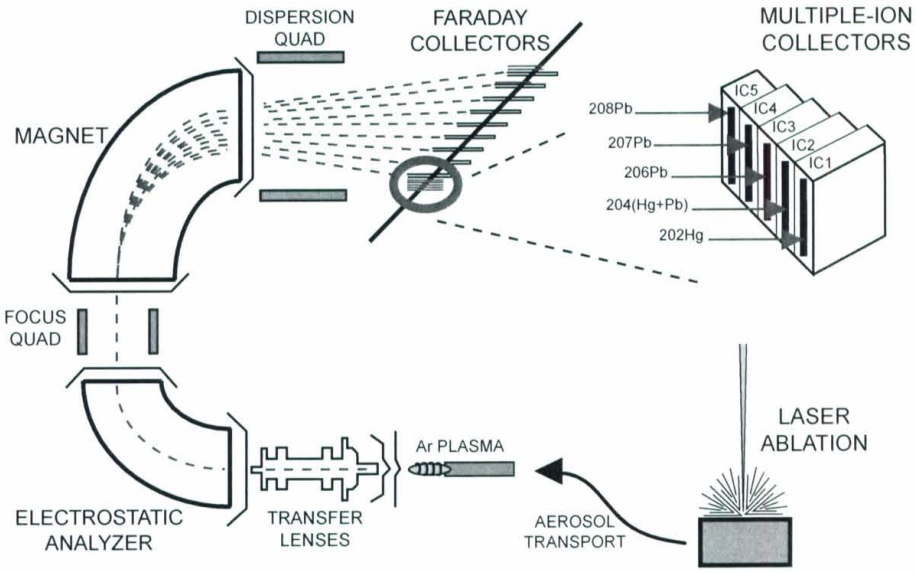

Fig. 3. Generalized illustration of the Finnigan NEPTUNE multi-collector inductively coupled plasma mass spectrometer.

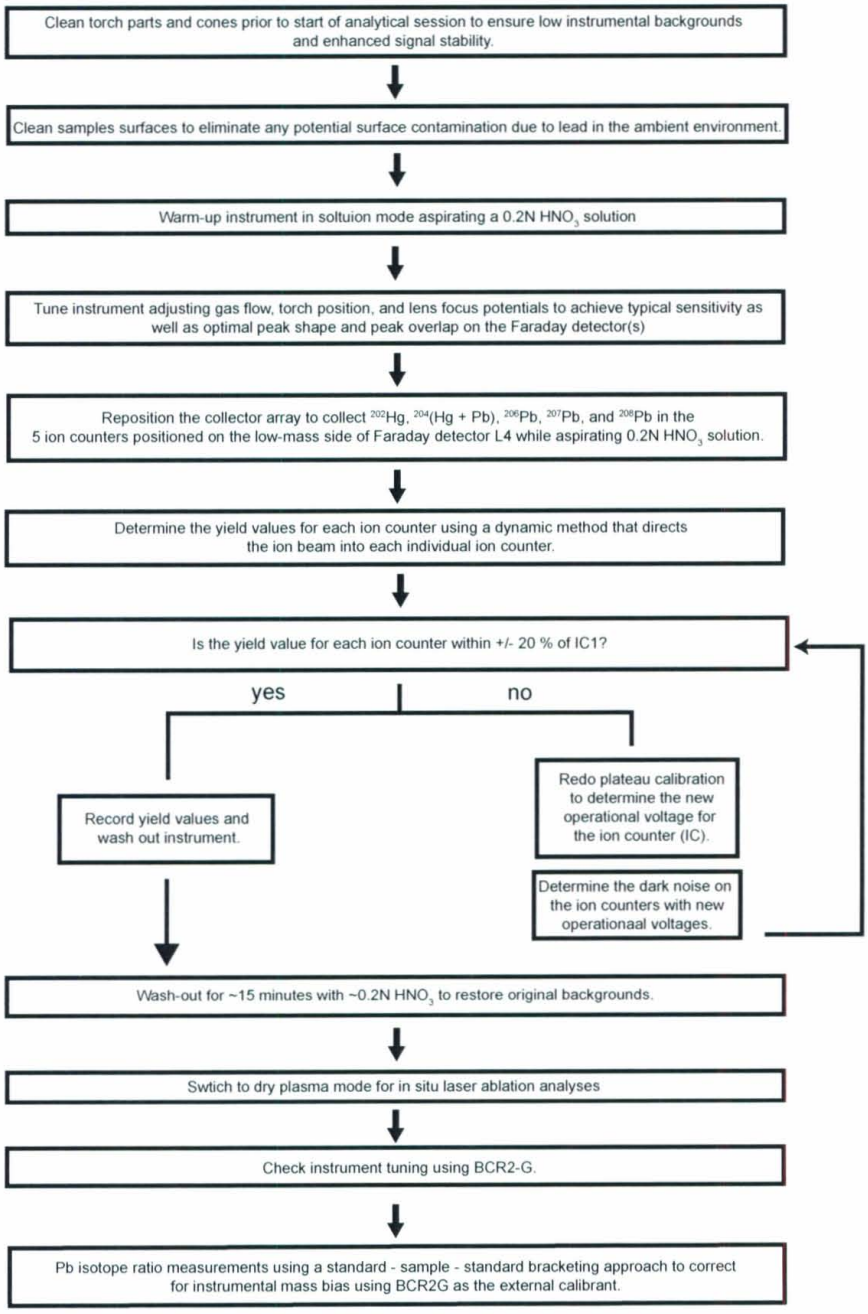

Fig. 4. Flow chart describing the daily analytical set-up for Pb isotope analyses using multiple ion counters.

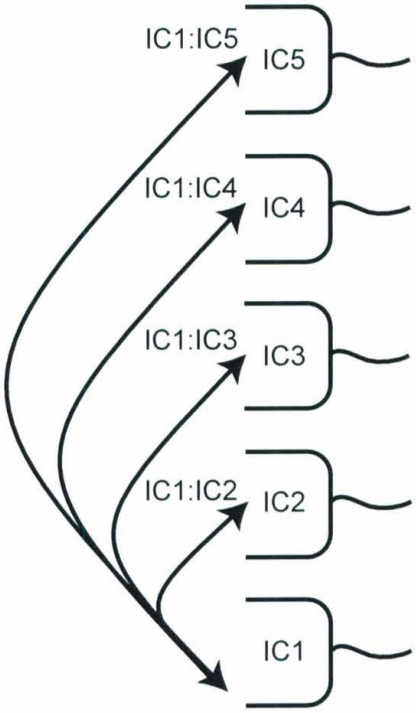

Fig. 5. Illustration depicting how the yield cross-calibration factors for each ion counter are determined. An ion beam of ~100 000 counts is directed into each individual ion counter 10 times over the course of the yield calibration. The beam intensity is measured using an ~8 sec integration time. To determine the yield factor, the measured beam intensities of ion counters 2 – 5 (IC2 – IC5) are recorded and normalized to the measured ion beam intensity of ion counter 1 (IC1).

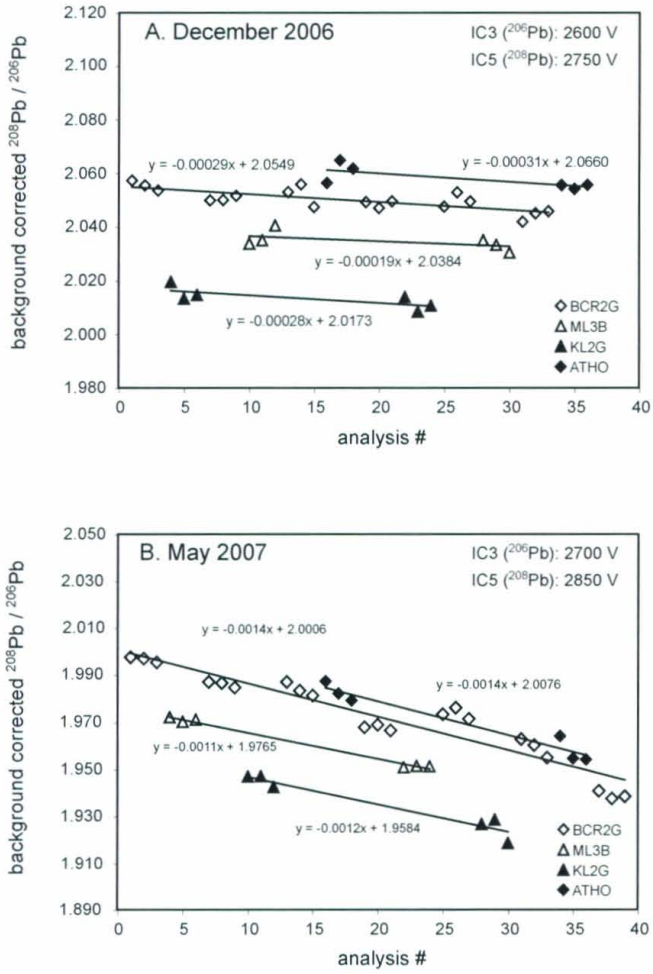

Fig. 6. Decrease in the measured (uncorrected) $^{208}Pb/^{206}Pb$ ratio within sequences of analyses consisting of 4 different silicate glass SRMs performed in (A) December 2006 and (B) May 2007, the latter with collector voltages set somewhat higher. The decrease is due largely to drift in ion counter yields. The slopes of the linear regressions fit to the drift are similar for all materials, independent of composition, indicating that BCR2-G may be used effectively as the bracketing standard for the other silicate glasses. The time interval covered by the December 2006 and May 2007 experiments is 85 and 90 minutes, respectively.

DATA REDUCTION METHODS

On-line yield, dark noise and dead time corrections made on each measurement cycle for the 90 second analysis using the NEPTUNE software.

Download .EXP file to formatted Excel worksheet.

Select gas background interval for ^{202}Hg, $^{204}(Hg + Pb)$, ^{206}Pb, ^{207}Pb, and ^{208}Pb

METHOD 1

Average signal intensities from the selected gas background interval.

Mean gas gackground subtracted from each ^{202}Hg, $^{204}(Hg + Pb)$, ^{206}Pb, ^{207}Pb, and ^{208}Pb measurement cycle in laser ablation interval.

^{204}Pb during the ablation interval calculated by subtracting ^{204}Hg from the $^{204}(Hg + Pb)$ using the natural $^{204}Hg/^{204}Hg$ ratio (~0.2301) and the background corrected ^{202}Hg.
e.g. $^{204}Pb = {}^{204}(Hg + Pb)_{bg.corr} - (^{202}Hg_{bg.corr} * 0.2301)$

Pb isotope ratios calculated from each measurement cycle during laser ablation

2-sigma outlier rejection performed on calculated Pb isotope ratios.

Pb isotope ratios averaged for selected laser ablation interval

METHOD 2

Calculate factor to determine the difference between the measured $^{208}Pb/^{204}Pb$ in the gas background and the $^{208}Pb/^{204}Pb$ value for modern Pb ($^{208}Pb/^{204}Pb$ ~38.63) for each background measurement cycle.
$f = 38.63 / (^{208}Pb/^{204}Pb)_{bg.\ meas}$

Factor (f) used to calculate the ^{204}Pb in measured $^{204}(Hg + Pb)_{bg}$ for each background measurement cycle.
$^{204}Pb_{bg} = {}^{204}(Hg + Pb)_{bg.\ meas} / f$

$^{204}Hg/^{202}Hg$ calculated for the gas background for each background measurement cycle.
$^{204}Hg/^{202}Hg = [^{204}(Hg + Pb)_{bg} - {}^{204}Pb_{bg}] / {}^{202}Hg_{bg.\ meas}$

Calculated $^{204}Hg/^{204}Hg$ and ^{204}Pb, and measured ^{206}Pb, ^{207}Pb, ^{208}Pb averaged over selected background interval.

Each laser ablation measurement cycle background corrected by subtracting the average background ^{206}Pb, ^{207}Pb, ^{208}Pb.

^{204}Hg removed from $^{204}(Hg + Pb)_{meas}$ by using the measured ^{202}Hg for each laser ablation measurement cycle and the calculated average $^{204}Hg/^{204}Hg$ for the gas background.
e.g. $^{204}Pb_{bg.corr} = {}^{204}(Hg + Pb)_{meas} - (^{202}Hg_{meas} * {}^{204}Hg/^{202}Hg_{bg.calc}) - {}^{204}Pb_{bg.calc}$

Pb isotope ratios calculated for each measurement cycle during laser ablation

2-sigma outlier rejection performed on calculated Pb isotope ratios.

Pb isotope ratios averaged for selected laser ablation interval

Fig. 7. Comparison of the two data reduction strategies presented in this chapter. Method 2 is the reduction method favored by the authors and used for routine daily Pb isotope analyses using multiple ion counters.

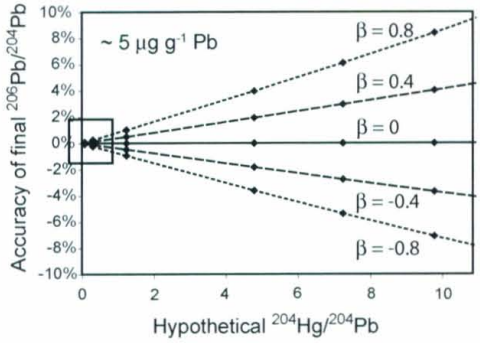

Fig. 8. Plot of accuracy of the final $^{206}Pb/^{204}Pb$ as a function of hypothetical $^{204}Hg/^{204}Pb$ and various mass bias factors (β) for a material of approximately 5 µg g-1 Pb. The box highlights the typical Hg/Pb ratios for silicate glasses used in our study, which is < 0.5. (From Souders and Sylvester, 2008).

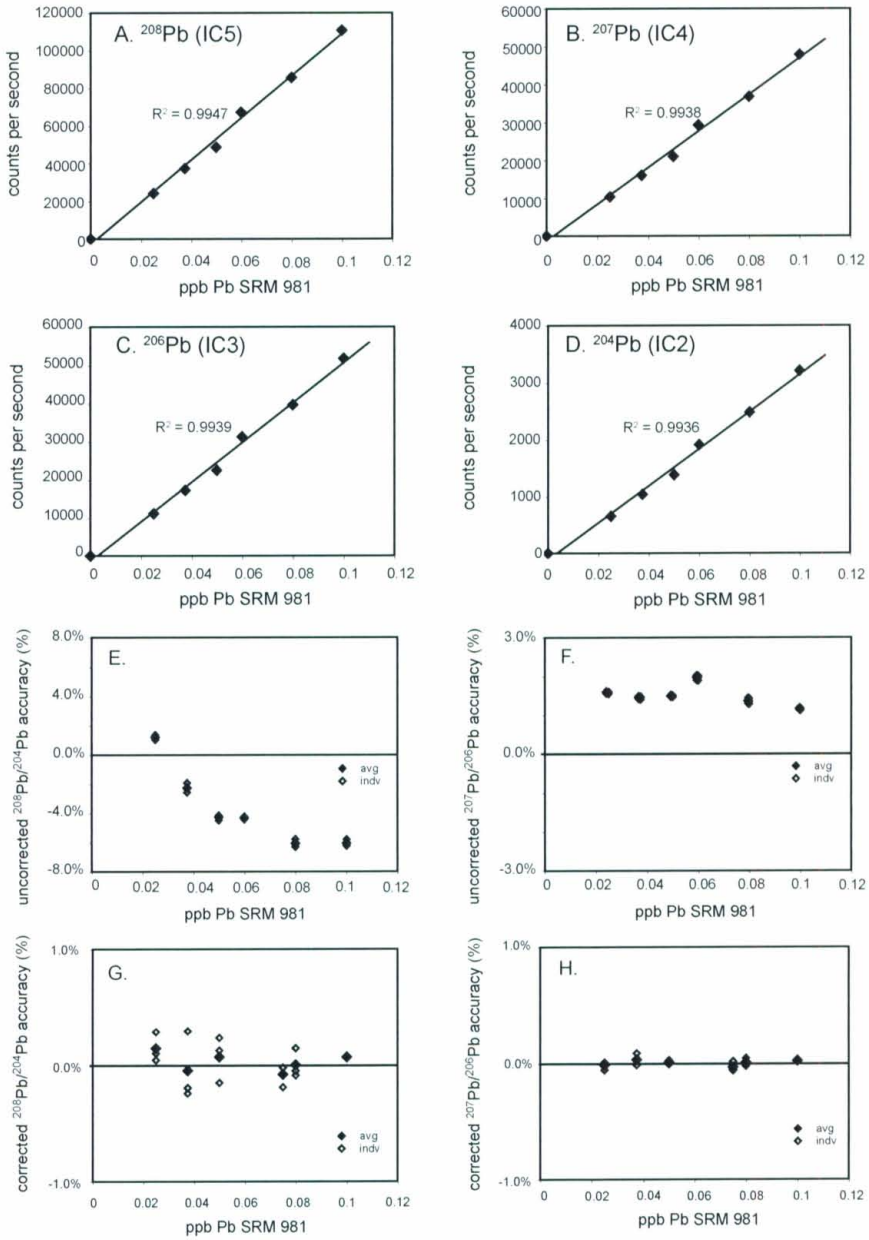

Fig. 9. Channeltron linearity in solution mode. (A-D) Graphs showing the linear increase in measured intensities (cps) for each Pb isotope as the total Pb concentration of a SRM 981 standard solution is increased. A concentrated 'mother' solution was diluted with varying amounts of ~0.2 % HNO3 to make all solutions used in the experiment. Each point represents the average background corrected count rate of 3 analyses of the same SRM 981 solution. (E-H) Plots displaying the accuracy of the measured, uncorrected $^{208}Pb/^{204}Pb$ (E) and $^{207}Pb/^{206}Pb$ (F) ratios, and the mass bias corrected $^{208}Pb/^{204}Pb$ (G) and $^{207}Pb/^{206}Pb$ (H) ratios for various total Pb concentrations of standard solution SRM 981. Solid diamonds represent the accuracy of the average of three lead isotope ratio measurements of the same SRM 981 solution. The open diamonds are the accuracy of each individual measurement of the same standard solution. The preferred values for SRM 981 from Baker et al. (2004) were used to calculate the mass bias corrected lead isotope ratios used in plots G and H, the accuracy results in plots E-H.

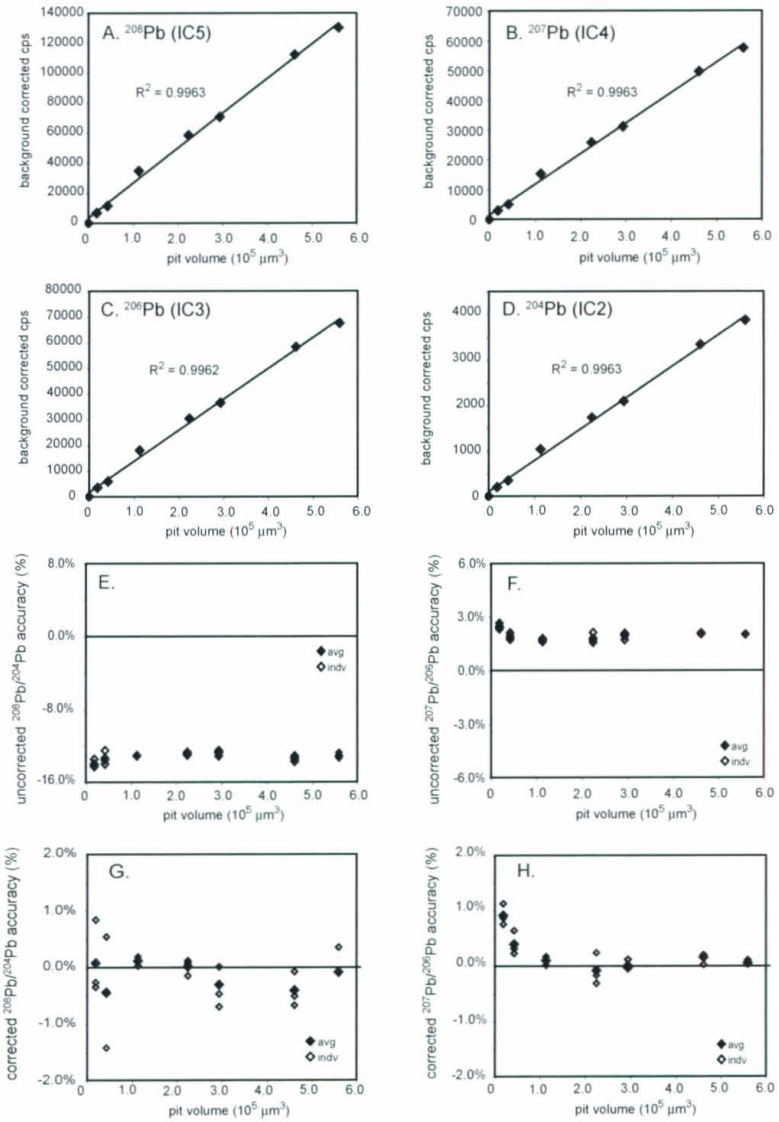

Fig. 10. Channeltron linearity in laser ablation mode. (A-D) Plots of background corrected count rates for each lead isotope over a range of laser ablation pit volumes. Variation in the volume of material ablated was produced by adjusting the laser spot size while keeping the laser energy (3 J/cm^2) and repetition rate (10 Hz) constant. Each point represents the average background corrected count rate of three 60 second laser analyses of BCR2-G at a single spot size. The volume of material ablated was estimated using a drill rate of ~1 µm/sec. (E-H) Plots showing the accuracy of the background corrected $^{208}Pb/^{204}Pb$ and $^{207}Pb/^{206}Pb$ ratios (E-F) and the mass bias corrected $^{208}Pb/^{204}Pb$ and $^{207}Pb/^{206}Pb$ ratios (G-H) for an increasing range of laser ablation pit volumes. Solid diamonds represent the accuracy of the average of three lead isotope ratio measurements performed under the same laser ablation conditions. The open diamonds represent each individual analysis. Method 2 outlined in this paper and the preferred values for BCR2-G given in GeoREM (http://georem.mpch-mainz.gwdg.de/) were used to calculate the mass bias corrected lead isotope ratios used in plots G and H, the accuracy results in plots E-H.

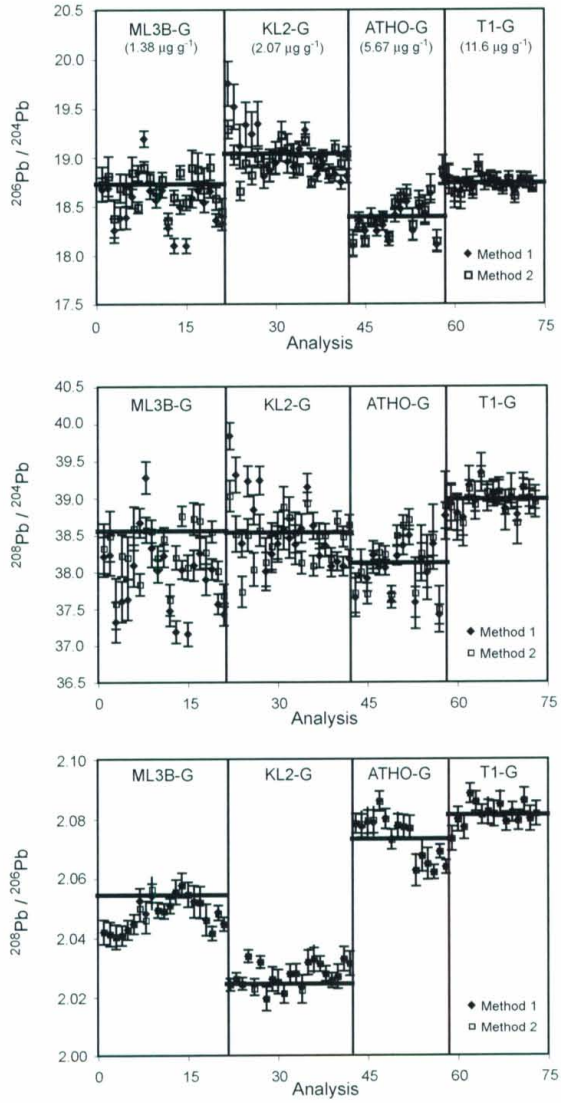

Fig. 11. LA-MC-ICPMS analysis of lead isotope ratios in silicate glass SRMs ML3B-G, KL2-G, ATHO-G and T1-G, arranged from left to right in order of increasing lead concentration. S olid horizontal lines indicate the preferred lead isotopic values for each glass given in GeoREM (http://georem.mpch-mainz.gwdg.de/). Lead isotope ratios for each analysis are calculated using both Method 1 (filled diamonds) and Method 2 (open squares). There is general agreement between the Method 1 and 2 results and the preferred values for the glasses with higher lead concentrations (ATHO-G and T1-G) for the $^{206}Pb/^{204}Pb$, $^{208}Pb/^{204}Pb$ and 208Pb/206Pb. There is more scatter and larger discrepancies between the two methods for the two glasses with lower concentrations (ML3B-G and KL2-G) but, in general, Method 2 produces more accurate and precise results than Method 1. (From Souders and Sylvester, 2008).

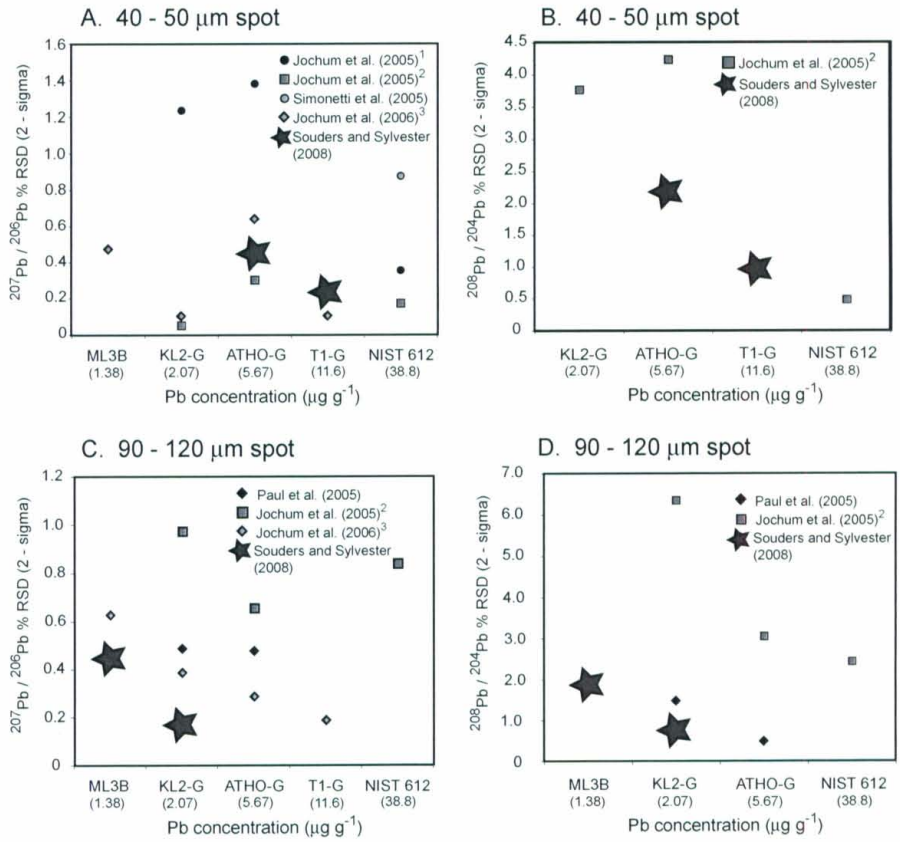

Fig. 12. Comparison of the external precision on $^{207}Pb/^{206}Pb$ and $^{208}Pb/^{204}Pb$ ratios in a silicate glass SRMs as a function of spot size in Souders and Sylvester (2008) and other LA-MC-ICP-MS and single-collector LA-SF-ICP-MS investigations. (A) and (B) compare analyses using spot sizes ranging from 40 to 50 μm, while (C) and (D) compare the reproducibility of measurements using spot sizes between 90 and 120 μm.

1Measurements using Escan mode.

2Measurements using combined Escan and Bscan modes.

3Only 193nm laser data considered.

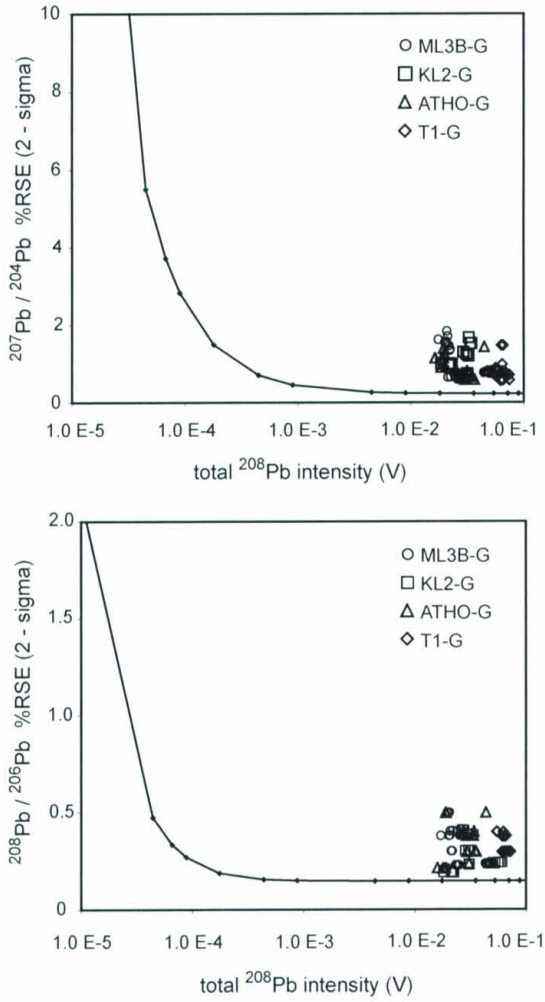

Fig. 13. Theoretical limits of precision, expressed as % RSE (2-sigma), for the measurement of lead isotope ratios using MICs are defined by the solid line. The observed internal precision on the lead isotope ratio measurements of Souders and Sylvester (2008) for the MPI-DING silicate glasses are also shown. Uncertainties due to counting statistics, dark noise, background subtraction, ion counter yield, and the ^{204}Hg correction on the 204-mass are all included in the calculation of the theoretical curves. (From Souders and Sylvester, 2008).

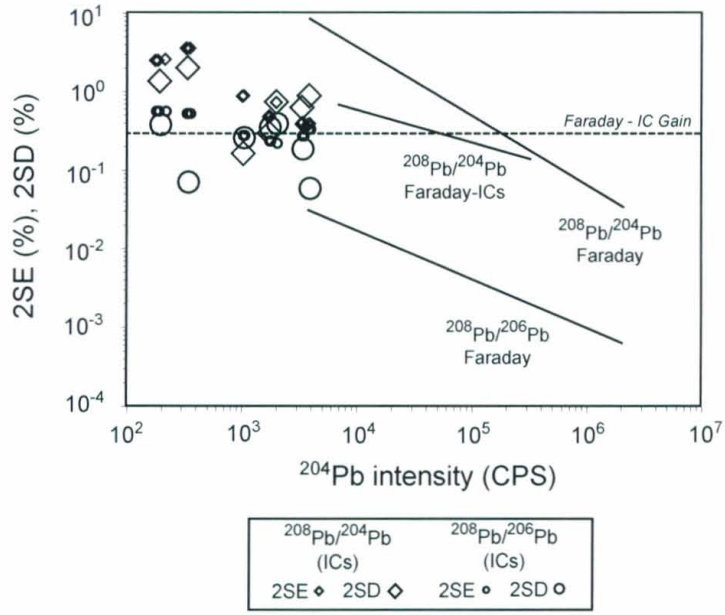

Fig. 14. Plot of observed measurement precision and ^{204}Pb average signal intensity (cps) for replicate analyses of BCR2-G. Variations in the observed count rates were produced by changing the laser spot size. The points represent the 2SE (%) and 2SD (%) for mass bias corrected ^{208}Pb/^{204}Pb and ^{208}Pb/^{206}Pb ratios where all lead isotopes of interest were measured on ion counters. The standard error of the mean (2SE (%)) was calculated for each individual analysis of BCR2-G consisting of 30 seconds of background measurement followed by 60 seconds of laser ablation followed by 30 seconds of wash-out. The standard deviation (2SD (%)) was calculated for the 3 replicate analyses for each laser spot size. The solid lines are the observed measurement precision trends for lead isotope ratios using both Faraday-Faraday and Faraday-ion counter cup configurations from Kent (2008) for NIST 610 SRM and the dashed line is the analytical uncertainty for Faraday-ion counter cross calibration (gain). The uncertainty on the Faraday-ion counter gain is the greatest source of error for measurements below this line. It is only a very low count rates that analytical precision is improved using multiple ion counters to measure lead isotope ratios involving ^{204}Pb.